2013

Magnetic deflections of ultra-high energy cosmic rays from Centaurus A

Azadeh Keivani
Louisiana State University and Agricultural and Mechanical College

MAGNETIC DEFLECTIONS OF ULTRA-HIGH ENERGY COSMIC RAYS FROM CENTAURUS A

A Dissertation

Submitted to the Graduate Faculty of the
Louisiana State University and
Agricultural and Mechanical College
in partial fulfillment of the
requirements for the degree of
Doctor of Philosophy

in

The Department of Physics and Astronomy

by
Azadeh Keivani
B.S., Sharif University of Technology, 2008
M.S., Louisiana State University, 2012
December 2013

To my family, for their endless love and support.
To my love, for all the wonderful moments we have together.

Acknowledgements

I would like to thank my advisor, Dr. James Matthews, for his excellent ideas, great support and unlimited encouragement. Thanks for always being so understanding during my graduate school days. I would also like to thank Dr. Glennys Farrar for her collaboration, brilliant ideas, encouragement, and time for all the Skype meetings and helpful discussions.

I would especially like to thank Dr. Michael Sutherland for his limitless helps in every step of my work from the beginning to the end. It is very enjoyable working with a smart person like you; thanks for being supportive.

I would also like to thank my committee members, Dr. Ravi Rau, Dr. Gabriela González, Dr. Geoffrey Clayton, and Dr. David Koppelman for their time and support. I would especially like to thank Dr. Rau for his wonderful weekly informal seminars for graduate students and also for his great discussions about everything in physics. Thanks for always having an open door and your help throughout my graduate studies.

This work was supported by the Louisiana State University Flagship Assistantship, the Department of Physics and Astronomy at the Louisiana State University, and the Department of Energy under grants DE-0009926 and DE-FG02-91-EF0617. Resources supporting this work were provided by the NASA High-End Computing (HEC) Program through the NASA Advanced Supercomputing (NAS) Division at Ames Research Center, consisting of time on the Pleiades supercomputing cluster awarded to Glennys Farrar. I additionally acknowledge the Pierre Auger Collaboration for providing me great opportunity to work with brilliant people from all over the world.

I am so grateful that I have had so many great teachers and advisors in my life. I would especially like to thank Dr. Jalal Samimi and Dr. Mahmoud Bahmanabadi for introducing me to the world of cosmic ray physics and providing me research opportunities and for their unlimited encouragements. I would also like to acknowledge my former lab mates, Dr. Farzaneh Sheidaei, Dr. Viviana Scherini, and Dr. Guofeng Yuan for teaching me valuable lessons and for their great friendship and Dr. Jonathan Roberts for his helpful collaboration.

There are too many friends who had great influences in my life to name them all individually, but I would like to thank Shiva for always being there; Ghazaleh for the great moments we had during our undergraduate years; Marjan for being a true friend in the most important years of my life; Elham who has always been my physics fellow and a lovely friend, and my many classmates both at Sharif and LSU.

I would like to give special acknowledgements to my parents, Gholamreza Kaivani and Marzieh Fooladi, who always encouraged me to learn science and provided me the best educational opportunities. I would also like to thank my sister, Saeide Kaivani, who always encouraged me to achieve my goals. My family's support and encouragement indeed made it possible to travel this road.

I would like to express my love and deep appreciation to my fiancé, Ashkan Balouchi, who has always been there in every aspect of my life. I am so glad that you are a smart physicist that we could have so many useful and awesome discussions. Thanks for being so understanding and supportive during all the years of my undergraduate and graduate studies, including the two years of long distance relationship. I am also very thankful for all your help with my dissertation. Your support and encouragement is indeed the greatest.

Table of Contents

List of Tables

List of Figures

Abstract

The origin and mass composition of ultra-high energy cosmic rays (UHECRs) are among the mysteries of particle astrophysics. Since UHECRs are mostly or entirely charged particles, they will be deflected in cosmic magnetic fields on their way to Earth. UHECR deflections in the Galactic magnetic fields (GMF) should be considered to identify their origin and nature.

The calculated Galactic magnetic deflections of UHECRs from a source strongly depend on the GMF model. I use the recent GMF model of Jansson and Farrar (JF12), a 35-parameter model which includes coherent, striated and random components and is constrained by WMAP7 Galactic synchrotron emission map and more than forty thousand extragalactic rotation measures. I develop a new method of implementing a random field using a Kolmogorov spectrum and scale it with the JF12 random component strengths.

Simulated UHECRs are propagated through the GMF using the publicly available propagation code *CRT*. These particles are simulated from Centaurus A, which is the nearest AGN to Earth. I identify the expected arrival direction loci of UHECRs in the JF12 GMF model for different rigidities (energy divided by charge) between 2 and 100 EV (1 EV $\equiv 10^{18}$ V) to determine whether Centaurus A could be a significant source of the UHECR excess reported by Pierre Auger Observatory. I calculate the excess of event arrival directions, with respect to isotropic expectations, for cases of pure protons, pure iron, and a mixture.

I also develop a method for identifying the mass composition of UHECRs under specific source and GMF hypotheses. Comparing Auger observations with simulations of different rigidities leads to the identification of the charges of the events. Consistent simulated rigidities are found for each Auger event based on their overlap probabilities. The charge of each event is the measured energy divided by the rigidity of the most consistent simulation.

Including a Kolmogorov random field component to the JF12 regular component does not significantly change the results of propagation at high rigidities whereas at low rigidities it smears the arrival distributions of events to such an extent that deflection studies can become difficult.

1. Introduction

One of the fundamental open problems in astrophysics is to find the origin of ultra-high energy cosmic rays (UHECRs). The arrival directions of these particles would point back to their astrophysical sources if either the particles were neutral or there were no magnetic fields along their path. UHECRs are believed to be charged particles such as protons or heavier nuclei, so they are deflected when traversing the magnetic fields on their way to Earth. Studying cosmic magnetic fields is crucial for UHECR source identification.

There are two kinds of magnetic fields that could affect the trajectories of cosmic rays at these energies: Galactic and extragalactic. Since the Galactic magnetic field (GMF), typically of the order of few μG, is unable to confine the UHECRs to within the Galaxy, UHECRs are likely extragalactic. Extragalactic magnetic field strengths are usually estimated to be three orders of magnitude smaller than their GMF counterpart. UHECR deflection magnitudes due to the extragalactic magnetic fields could be negligible relative to the GMF deflection magnitude if the particles do not travel far in the intergalactic medium. This is a more accurate assumption at higher energies (E $>$ 50 EeV) where flux suppression occurs. Based on the GZK effect (Greisen, 1966; Zatsepin & Kuz'min, 1966), an ultra-high energy proton can interact with cosmic microwave background (CMB) photons resulting in energy loss and flux suppression. Particles with energies above about 50 EeV should therefore arrive from relatively nearby distances (smaller than 100 Mpc).

In this dissertation, I consider the effect of GMF on the propagation of UHECRs. The GMF is typically comprised of two components: regular (coherent) and random (incoherent) fields. There are many different GMF models. These models have common properties such as having large scale regular field lines that follow the spiral structure. In some models, there are field reversals between the spiral arms. The coherent field also exists in the Galactic halo (away from the Galactic plane) in most of the recent models. Random fields may likely originate from supernova explosions in the Galaxy and have typical scale lengths of $\sim$ 100

pc. The GMF, besides changing UHECR arrival directions, can also produce multiple images of sources (known as lensing effects) which are dependent on the particle energy.

Magnetic deflections are strongly model dependent, particularly for the random component. Developing a more realistic magnetic field model, especially the random component, is crucial. A recent model by Jansson and Farrar (JF12) (Jansson & Farrar, 2012a,b) includes both GMF components and has been fitted to all the available extragalactic rotation measures and the WMAP7 Galactic synchrotron emission map (Gold et al., 2011). In this dissertation, I use the JF12 GMF model and develop a new method of implementing random field. A Kolmogorov spectrum is used to generate the random field. I simulate and propagate UHECRs through the GMF using the publicly available propagation code *CRT* (Sutherland et al., 2010).

There are many different source candidates for UHECRs including Active Galactic Nuclei (AGN). Among all known AGN, Centaurus A (Cen A) is the nearest to Earth. Cen A is about 3.8 Mpc away and possesses very large radio lobes that make it a very interesting object for many astrophysical studies including UHECRs. The Pierre Auger Observatory has reported an excess in a somewhat broad region around Cen A for events with energies above 55 EeV. This provides a motivation to study cosmic ray trajectories from Cen A to see if it could be a significant source of UHECRs in the context of the JF12 GMF model.

Another important mystery in UHECR physics is the mass composition. The Pierre Auger observatory measures particle energies accurately but is not sensitive to their types or their charges. I simulate UHECRs with different rigidities (energy divided by charge) and compare them with Auger data. I develop a method to identify the mass composition of UHECRs by comparing the event energies with simulation rigidities.

In Chapter 2, I give a brief introduction to UHECRs, discussing their probable sources and acceleration sites, their observed flux and detection methods of the extensive air showers induced by their passage through the atmosphere. Chapter 3 describes the Pierre Auger Observatory and its recent results. Chapter 4 details different GMF models and the histor-

ical observational methods that were used to study them. It also compares the results of propagating simulated UHECRs through different GMF models. In Chapter 5, I explain the development of a Kolmogorov random field and present tests and verification. The UHECR tracking methods and the results of full-sky simulations are presented in Chapter 6. These results represent new modern estimates of UHECR deflection behavior in a complete (coherent plus incoherent) GMF model. The main results of this work are shown in Chapter 7 including the identification of the arrival directions of simulated UHECRs from Cen A, estimates of simulation event excesses around Cen A, and the mass identification method and application to Auger data. Conclusions are presented in Chapter 8.

2. Ultra-High Energy Cosmic Ray Physics

2.1 Introduction

Cosmic rays are charged particles coming from outer space. These particles span a wide range of energy from about 1 MeV to above 10^{20} eV. Although more than 100 years have passed since the discovery of cosmic rays, there are still many outstanding questions, especially at ultra-high energies ($E \geq 10^{18}$ eV $\equiv$ 1 EeV). One significant question concerns the origin of ultra-high energy cosmic rays (UHECRs). Other important questions are what their acceleration mechanism and mass composition are. Below I describe the history of cosmic rays, the known properties, and what yet needs to be discovered.

2.2 History

Victor Hess (Hess, 1912) has been attributed with the discovery of cosmic rays when he took several balloon flights in 1912 up to 5 km altitudes to measure the ionization level in the atmosphere; he discovered that this ionization increases with altitude. He concluded this radiation came from outer space. Scientists had previously thought that the natural radioactivity in Earth was the origin of the radiation. Hess was awarded the Nobel Prize in 1936 for his discovery of cosmic radiation. The term "cosmic rays" was first used by Robert Milikan, who is famous for his oil-drop experiment that calculated the charge of the electron. Cosmic ray physics brought many important discoveries in the 20th century. Some examples are the discovery of positron in 1932 (Anderson, 1933), muon in 1936 (Neddermeyer & Anderson, 1937), and pion in 1947 (Lattes et al., 1947).

In 1939, Pierre Auger and Roland Maze discovered time coincidences in the arriving cosmic rays suggesting they were initiated by a single event. Auger called this an "extensive air shower" (Auger et al., 1939) (EAS). To record the cosmic ray arrival times, they used Wilson chambers and Geiger-Müller tubes separated by large distances. Coincidences were observed for separations up to about 300 m. They concluded that the detected particles were some secondary particles initiated by an interaction high in the atmosphere of a primary

particle that could have an energy as high as 10^{15} eV, which was far higher than the MeV laboratory energies at the time.

The story of high energy cosmic rays continued to a new phase when John Linsley observed an air shower initiated by a particle of 10^{20} eV, the highest observed energy up to that point in 1963 (Linsley, 1963). He observed this event with the detectors at Volcano Ranch array in New Mexico, which was the first large scale surface array experiment designed to measure high energy cosmic rays. Linsley's observations suggested the possibility of extra-galactic sources for these cosmic rays. The ground-based experiments continued worldwide to detect the high and ultra-high energy cosmic rays. Important experiments since then are Haverah Park (UK) (Ave et al., 2002), SUGAR (Australia) (Winn et al., 1986), Yakutsk (Russia) (Vernov et al., 1971), AGASA (Japan) (Chiba et al., 1992), the Telescope Array (USA) (Teshima et al., 1992), and the Pierre Auger Observatory (Argentina) (Dova, 2003).

The fluorescence technique was proposed by Greisen in 1967 to complement the surface array technique for detection of cosmic ray air showers. This technique uses the Earth's atmosphere as a calorimeter so that when the high energy cosmic rays excite atmospheric nitrogen, the molecules emit fluorescence light. The first detection of air fluorescence was also done at the Volcano Ranch array by physicists from University of Utah (Bergeson et al., 1977). Since then, the Fly's Eye Experiment (Baltrusaitis et al., 1985) continued using this technique at Utah, followed by HiRes (Bird et al., 1994), and now the Telescope Array. The Pierre Auger Observatory and the Telescope Array currently use both techniques covering the sky of southern and northern hemispheres, respectively. The design and operation of the Pierre Auger Observatory is the subject of Chapter 3. JEM-EUSO is a new type of observatory that will be placed on the international space station and is designed to detect the most energetic cosmic rays in the universe. JEM-EUSO will observe the fluorescence light in the Earth's atmosphere (JEM-EUSO Collaboration, 2013).

2.3 Flux

A complete energy spectrum over a broad energy range has been produced after about 100 years of cosmic ray experiments. The cosmic ray flux is well measured for energies below 10^{19} eV. Figure 2.1 shows the energy spectrum of cosmic rays from about 10^8 eV to more than 10^{20} eV. The cosmic ray flux generally follows a power law

$$\frac{dN}{dE} \propto E^{-\gamma}, \tag{2.1}$$

where γ is the spectral index varying between 2.6 and 3.2 depending on the energy. A hardening is located around 4 EeV, known as the *ankle* of the spectrum. There is also a flux suppression observed above 50 EeV that will be discussed in Section 2.5. As shown, the flux uncertainty becomes larger above about 10 EeV. Also, the flux has decreased to 1 particle per km^2 per year around the ankle. The flux further decreases at higher energies; for example, the cosmic ray flux is roughly 1 particle per km^2 per century around 10^{20} eV.

2.4 Origin

There are two different classes of theoretical models explaining the observed energy of cosmic rays. They are termed "bottom-up" and "top-down" models. In bottom-up models, particles are generated with lower energies but accelerated to higher energies using conventional physics, whereas in top-down models the particles are initially generated at energies above ultra-high energies. The bottom-up method is now more generally accepted, in part because of recent studies imposing severe constraints on top-down models (Pierre Auger Collaboration, 2009).

2.4.1 Acceleration

There are two ways that a particle can accelerate in the bottom-up model. One is acceleration due to an electromotive force associated with the time variation of magnetic fields. Charged particles can then accelerate by the induced electric fields. However there is no large scale

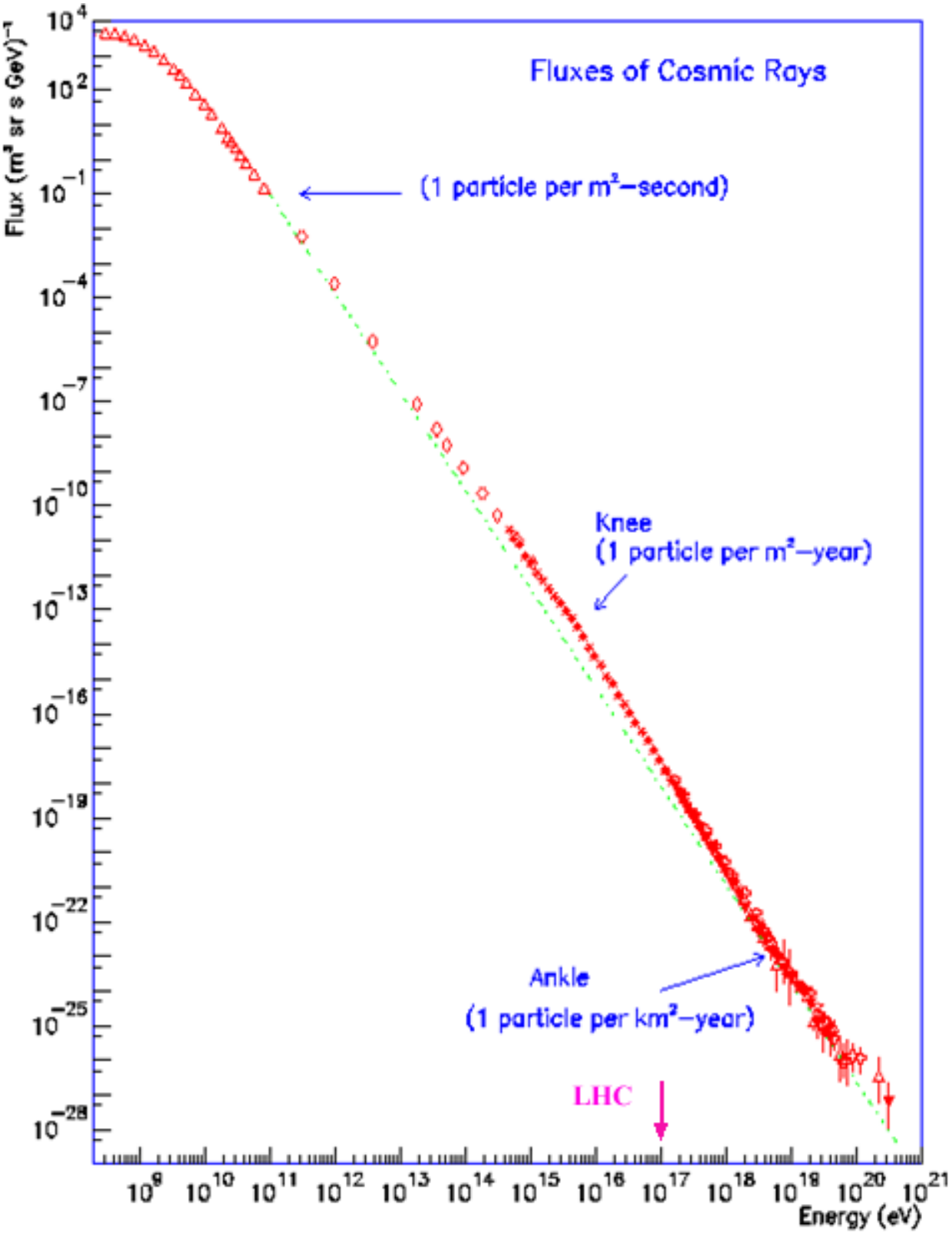

Figure 2.1: Observed energy spectrum of cosmic rays from 10^8 eV to 10^{21} eV (Cronin et al., 1997). The spectrum follows a power law with an index of roughly ≈ -3. The laboratory energy of the CERN Large Hadron Collider (the largest man-made accelerator) is marked with a pink arrow.

electric field in the cosmological distances and cosmic plasmas do not allow high voltages to be maintained (Fraschetti, 2008). The other is acceleration from interaction with a diffuse plasma shock that is termed Fermi acceleration (Fermi, 1949). Fermi suggested that a charged particle in a plasma may eventually gain energy by being repeatedly reflected by a magnetic mirror, meaning a particle with appropriate velocity and angle is reflected from a denser magnetic field region. Each interaction increases the particle energy $\Delta E = \xi E$, where ξ is a proportionality constant related to properties of the shock front. In Fermi's original model, particles were accelerated in collisions with moving plasma "clouds", giving $\xi \approx \beta^2$, where β is the cloud speed in units of "c". Later, it was found that strong shock waves give more efficient acceleration, with $\xi \approx \beta$. The energy spectrum of particles that escape the acceleration region follows a power law, $N(> E) \propto E^{-\gamma}$, where γ is the power law index.

Magnetic fields at the source confine the cosmic rays up to some maximum energy. The maximum energy can be estimated from the Larmor radius, $E_{\max} = \beta(Ze)BR$, where Ze is the charge of the particle, B is the magnetic field strength in the shock and R is the Larmor radius. Based on the magnetic field strength B and the scale size R, one can define the possible astrophysical accelerators in a technique first developed by A.M. Hillas (Hillas, 1984). Figure 2.2 shows a Hillas plot for a variety of possible sources of cosmic rays at different energies and source environments.

2.4.2 Source Candidates

It is thought that the sources of cosmic rays with energies below the ankle are Galactic supernova shocks. Sources of cosmic rays with energies above the ankle are still one of the biggest mysteries in astrophysics. There are some arguments that the origin of ultra-high energy cosmic rays is extragalactic since the galactic magnetic fields appear to have insufficient strength to contain these particles (Hillas, 1984). A proton of EeV energy would have a Larmor radius of 400 pc in a uniform magnetic field of 3 μG. The Larmor radius is proportional to the energy of the particle and so reaches scales of tens of kpc at higher

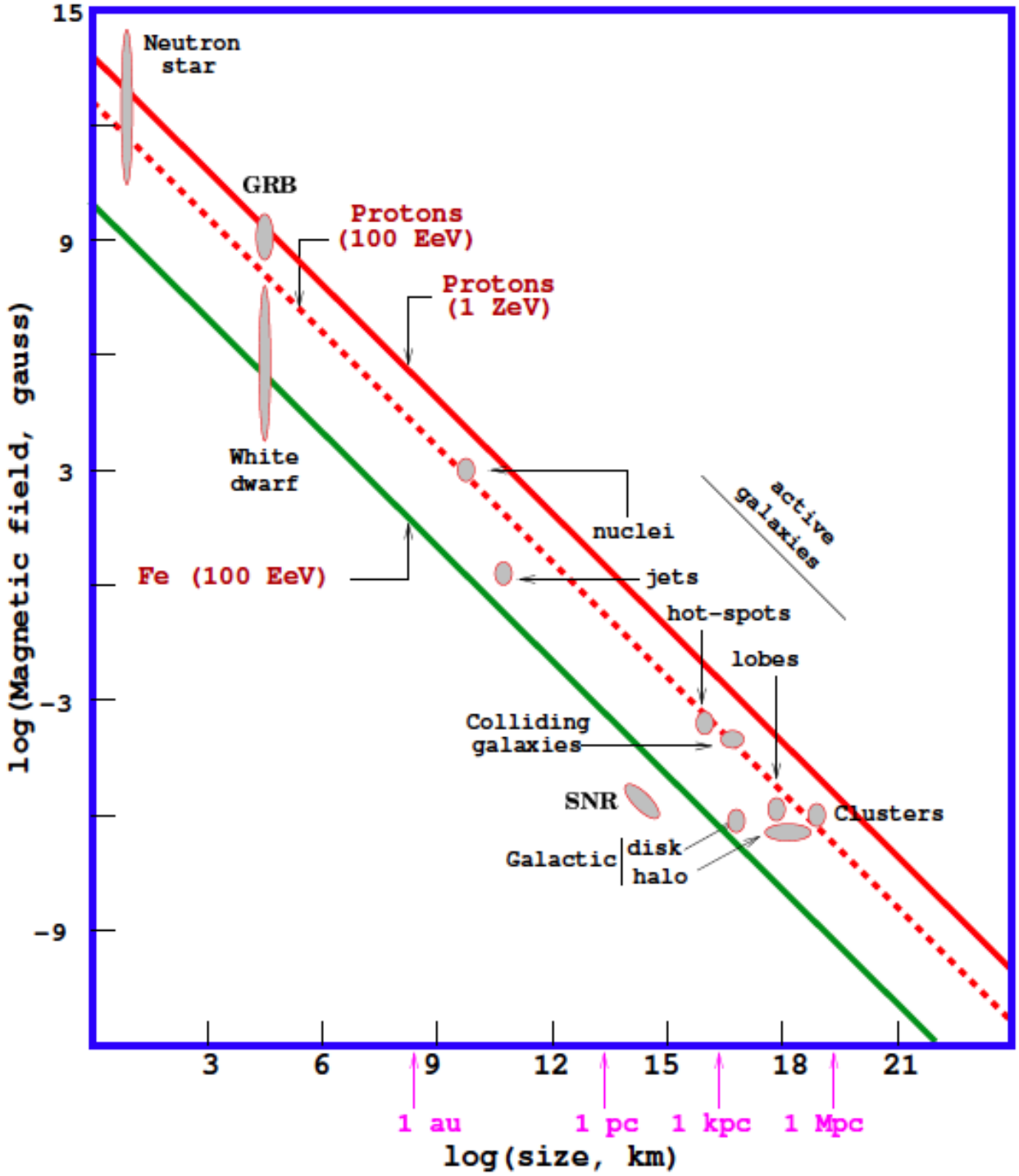

Figure 2.2: Hillas plot showing the magnetic field versus the scale size of the possible astrophysical sources of accelerating UHECRs. The candidates below the diagonal lines from top to bottom can not accelerate protons above 10^{21} eV, protons above 10^{20} eV, and iron nuclei above 10^{20} eV, respectively. From (Anchordoqui et al., 2003).

energies, which would then exceed the diameter of the Galactic disk. Here I introduce the probable sources of UHECRs.

Active Galactic Nuclei (AGN) are thought to be possible sources of UHECRs. AGN cores with a magnetic field of the order of 10^3 G and a size of the order of 10^{-5} pc are capable of accelerating these particles to ultra-high energies (see Figure 2.2). They produce enormous luminosity and electromagnetic fields. AGN jets with dimensions of the order of a fraction of a parsec and magnetic field strength of the order of a few Gauss are also capable of accelerating protons to energies up to 10^{20} eV (Letessier-Selvon & Stanev, 2011).

One problem with AGN is that they have large photon densities around their central engine that could interact with cosmic rays before they leave the AGN resulting in flux suppression at the source. If the cosmic rays are heavier nuclei, then the situation is even worse since they have smaller interaction lengths (Protheroe, 1999). One idea is that the protons interacting with the ambient photons would create neutrons that escape the AGN. These neutrons then decay to protons outside of the source, which still possess ultra-high energies. Most AGN are located at cosmological distances greater than 10 Mpc so the resulting flux suppression and energy losses (see Section 2.5) would significantly affect the energy spectrum.

Radio galaxies are another class of source candidates. They are active galaxies with radio emission appearing as lobes connected to the central galaxy which are also endpoints of jets. Typical radio galaxies have a size of the order of $10^3 \sim 10^6$ pc and a magnetic field of $10 \sim 10^3\,\mu$G (Letessier-Selvon & Stanev, 2011). The shock waves appearing in the lobe regions make the charged particles radiate synchrotron emissions. A popular radio galaxy candidate is Centaurus A that I will describe in more detail in Chapter 7.

Gamma Ray Bursts (GRBs) could be another source of UHECRs. GRBs are transient energetic events that last between tens of ms to few minutes, releasing a total energy of about 10^{51} ergs (Fishman & Meegan, 1995; Mészáros, 2002). The connection of GRBs to UHECRs have been suggested in different studies (Waxman, 1995; Vietri, 1996; Milgrom &

Usov, 1995). Most GRBs are at far cosmological distances, which would result in a much lower cosmic ray flux (Mészáros, 2002). In addition, the cosmological magnetic deflections of charged cosmic rays in transit to Earth would induce a time delay between the observed photons and cosmic ray signals (Mészáros, 2002). There has been no correlation between GRBs and UHECRs so far (Mirabal & Oya, 2010).

2.5 Energy Loss

After the discovery of the cosmic microwave background (CMB) in 1964, Greisen in the US and Zatsepin and Kuzḿin in the USSR investigated the propagation of UHECRs in extragalactic space (Greisen, 1966; Zatsepin & Kuz'min, 1966) and independently realized that high energy protons could interact with CMB photons resulting in energy loss and flux suppression. Photo-pion production is the dominant source of energy loss for the high energy protons which proceeds as,

$$\begin{aligned} p + \gamma_{CMB} &\rightarrow p + \pi^0 \\ &\rightarrow n + \pi^+. \end{aligned} \tag{2.2}$$

This process has a threshold at the Δ^+ resonance (1232 MeV) with a maximum cross section there of ≈ 500 μb. At higher center-of-mass energies the cross section drops to about 100 μb. The number density of the CMB photons $n_{\rm CMB}$ is about 400 cm^{-3}. The mean free path for a photon-proton interaction depends on the particle energy and is of the order of $\lambda = (\sigma_{\rm p\gamma} n_{\rm CMB})^{-1} \approx 10$ Mpc for a 10^{20} eV proton, where $\sigma_{\rm p\gamma}$ is the cross section of proton-photon interaction. Conservation of momentum implies that the proton loses about 20% of its energy with each interaction. Energy loss continues until the proton reaches the GZK threshold energy which is about 5×10^{19} eV.

There is another energy loss mechanism for a lower energy proton through the Bethe-Heitler pair production,

$$p + \gamma_{CMB} \rightarrow p + e^+ + e^-. \tag{2.3}$$

The energy loss at each pair production interaction would only be about 0.1% since $2m_e/m_p \approx 0.1\%$, so this would be only a minor effect compared to photo-pion production above the threshold energy.

Heavier nuclei also go through the energy loss processes mainly via photo-disintegration through interaction with the CMB and background infrared radiation. The thresholds for such processes increase with the energy of the nucleus. Iron nuclei have a threshold very similar to that of protons in photo-pion production.

2.6 Magnetic Deflections

2.6.1 Galactic Magnetic Deflection

Magnetic fields of the Milky Way influence the trajectories of the charged particles. Cosmic ray deflections depend on the charge of the particle and its energy as given by the relativistic Lorentz force $\mathrm{d}(\gamma m\vec{v})/\mathrm{d}t = q\vec{v} \times \vec{B}$. One needs to correct for magnetic deflections when studying UHECR sources using their observed arrival directions. One method is backtracking cosmic rays through the Galactic magnetic field. The method was first discussed in (Flückiger et al., 1991) for a different study. Unfortunately there is no commonly accepted Galactic magnetic field (GMF) model yet. But there are several different models with common properties that will be fully discussed in Chapter 4. Stanev (Stanev, 1997) performed an analysis with different GMF configurations and found that some observed events lie closer to the supergalactic plane and some fall further away. Medina Tanco et al. (Medina Tanco et al., 1998) also assumed a field model consistent with both Stanev's and Beck's models (Beck et al., 1994) to track the UHECR protons and iron nuclei. They found that magnetic deflections are significantly larger than previously believed.

Harari et al. (Harari et al., 2000, 1999) revised Stanev's model (see Section 4.3) and showed the possibility of seeing multiple images and lensing effects. They found that the lensing could affect the energy spectrum, since the lower energy particles are deflected more. They also did other studies including turbulent GMF (Harari et al., 2002) and confirmed

the magnification effects. Prouza and Smída (Prouza & Smida, 2003) also propagated the cosmic rays in GMF and concluded that directions of cosmic rays are incompatible with nearby Galactic neutron stars. They also confirmed the previous studies.

Tinyakov and Tkachev (Tinyakov & Tkachev, 2002) tracked the observed cosmic rays by the AGASA experiment and found a correlation with extragalactic objects known as BL Lacs. This was later shown to be strongly GMF model dependent by Kachelries et al. (Kachelries et al., 2007). They also confirmed that the GMF plays a significant role in correlation studies. Takami et al. (Takami et al., 2006) also studied the AGASA data and simulations through magnetic fields to determine a source density limit.

As discussed above, using a realistic GMF model is extremely important in UHECR propagation and therefore in source identification. In this dissertation, the most recent GMF model (JF12) is used for propagation of UHECRs in addition to developing a more realistic turbulent GMF model.

2.6.2 Extragalactic Magnetic Deflection

Magnetic fields in extragalactic space may also influence the trajectories of charged particles. The magnetic field strength in the extragalactic medium is believed to be of order nG (Dolag et al., 2004; Dar & De Rújula, 2005). The Larmor radius of a particle with energy E in EeV and charge Z traversing an extragalactic magnetic field with strength B in nG is given by

$$R \approx 1.1 \left(\frac{1}{Z}\right) \left(\frac{E}{\mathrm{EeV}}\right) \left(\frac{\mathrm{nG}}{B}\right) \mathrm{Mpc}. \tag{2.4}$$

In the voids between large scale structures, the magnetic field consists of small turbulent fields or is essentially non-existent. In most cosmic ray propagation studies, the extragalactic magnetic field is considered to be negligible relative to the Galactic magnetic field. However, if the coherence length and rms strength of the extragalactic magnetic field is small, it could affect the propagation of UHECRs by smearing their observed arrival directions. The strength and structure of the extragalactic magnetic fields are not well known and different

studies show upper and lower limits that can vary by several orders of magnitude (Dolag et al., 2011).

2.7 Extensive Air Showers

Pierre Auger in 1939 found that cosmic rays with energies above 10^{18} eV interact with the atmospheric molecules and produce extensive air showers of particles and photons. Figure 2.3 shows a schematic diagram of an EAS. Depending on the type of the initial particle, the air shower will develop with both hadronic and electromagnetic cascades. Figure 2.4 shows schematic diagrams of these two showers.

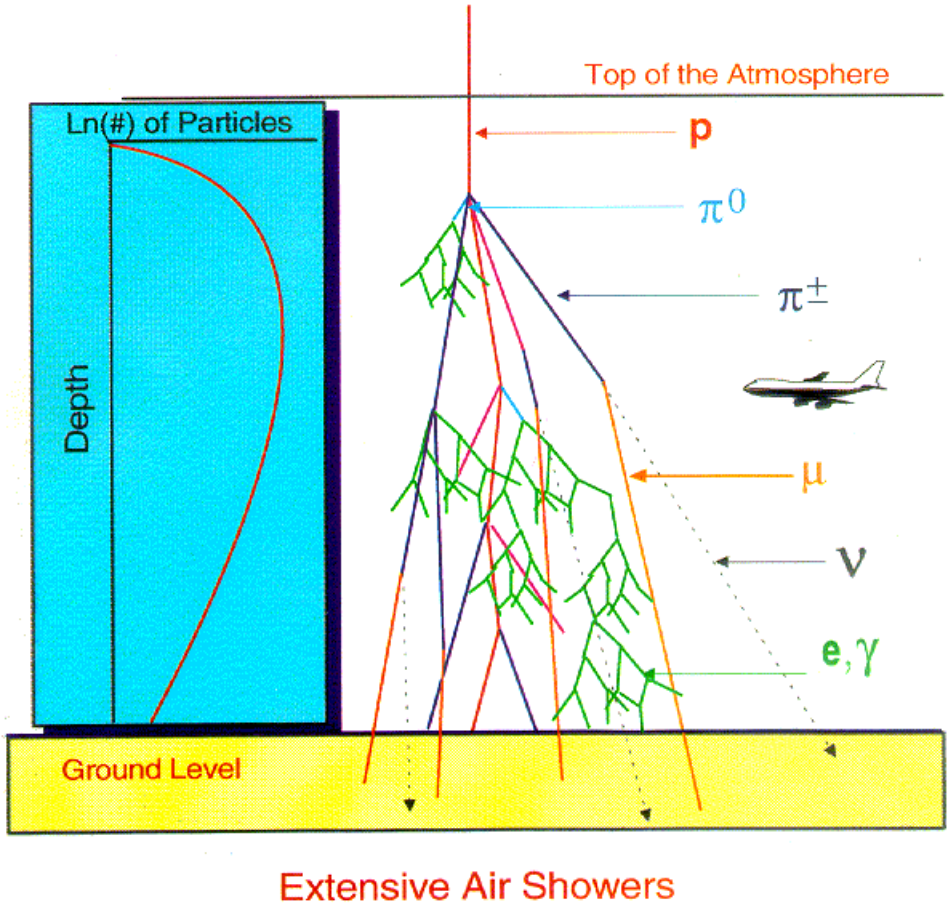

Figure 2.3: Schematic diagram of the formation and development of an EAS. On the left, the number of particles first increases to reach a maximum and then decreases with atmosphere depth. The image on the right shows the evolution and major interactions of an EAS initiated by a proton. The image is from the University of Adelaide astrophysics group website.

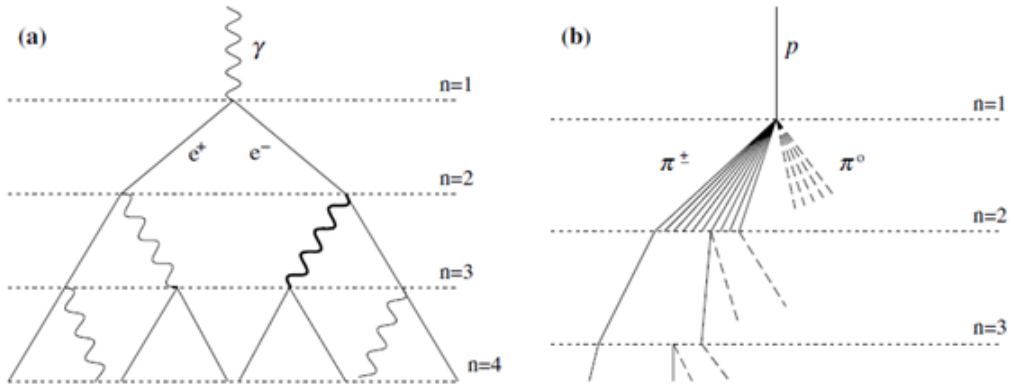

Figure 2.4: Schematic diagram of (a) electromagnetic and (b) hadronic air showers. The dashed line indicates neutral pions and the solid line indicates charged pions. From (Matthews, 2005).

2.7.1 Electromagnetic Showers

An electromagnetic shower is induced by a photon. Its development has two particle processes: electron-positron pair production and bremsstrahlung. When a photon hits an atmospheric nucleus (A) such as oxygen or nitrogen, it can convert into electron-positron pairs.

$$\gamma + A \rightarrow e^+ + e^- + A. \tag{2.5}$$

In order for this process to happen, the photon needs to have a minimum energy of $2m_e c^2 = 1.022$ MeV. The produced electron or positron will continue until it scatters off from a charged particle (B) to lose energy and emit a photon. The process generates bremsstrahlung radiation,

$$e^{\pm} + B \rightarrow e^{\pm} + B + \gamma. \tag{2.6}$$

A simple model of electromagnetic shower development was given by Heitler in 1954 (Heitler, 1954), in which he assumed every interaction has the same interaction length λ and every step causes the shower particles to lose half of their energies into daughter particles. Suppose the initial photon has an energy E_0 when it first interacts. This interaction would

transfer half of this energy to the produced electron and half to the positron. The produced pair would travel another interaction length until each emits a photon, losing half of their own energies. These processes generate 2^n particles after n steps with each particle having an energy of $E_0/2^n$ and will continue until the energies of individual particles reach a critical energy E_c. The critical energy is at the point where the electron energy loss by Bremsstrahlung will be less than that from ionization. The value of E_c in air is 85 MeV (Matthews, 2005; Beringer et al., 2012).

The depth of shower maximum for an electromagnetic air shower, $X^{\gamma}_{\max}$, can be estimated as

$$X^{\gamma}_{\max} = \lambda \ln(E_0/E_c), \tag{2.7}$$

and the number of particles at shower maximum, $N^{e}_{\max}$, can be calculated as

$$N^{e}_{\max} = E_0/E_c. \tag{2.8}$$

These two formulae from the Heitler model suggest that in electromagnetic EAS, the maximum number of particles is proportional to the initial energy and the depth of shower maximum is proportional to the logarithm of the primary energy.

2.7.2 Hadronic EAS

The hadronic EAS can be induced by either a proton or heavier nucleus. In both cases, the first interaction happens when the primary particle hits an atmospheric nucleus, such as nitrogen or oxygen and produces pions ($\pi^{\pm}$, π^0), kaons ($K^{\pm}$), and secondary nuclei with significant fractions of the primary particle energy. The secondary particles continue interacting in the atmosphere as long as they have sufficient energies and small interaction lengths.

Neutral pions immediately decay into two photons $\pi^0 \rightarrow \gamma+\gamma$, feeding the electromagnetic component of the air shower. The $\pi^{\pm}$ decay into muons and neutrinos $\pi^{\pm} \rightarrow \mu^{\pm} + \nu$. The

produced neutrinos have essentially no interactions while carrying away a significant amount of the primary energy. Charged kaons also produce muons and neutrinos $K^{\pm} \rightarrow \mu^{\pm} + \nu$ or charged and neutral pions $K^{\pm} \rightarrow \pi^{\pm} + \pi^{0}$. The branching ratio for these two interactions is 63.5% to 21.2% (Rao & Sreekantan, 1998). The pion and kaon interactions produce the most important observable part of the EAS, the muon. Muons have a relatively large interaction length and lifetime of $\sim 2.2 \times 10^{-6}$ s.

J. Matthews (Matthews, 2005) extended Heitler's toy model to describe the hadronic EAS, enabling methods to distinguish a shower initiated by a proton from that by a heavier nucleus. The model, as shown in Figure 2.4(b), divides the atmosphere into layers of fixed thickness $\lambda_{\mathrm{I}} \ln 2$, where λ_{I} is the interaction length of the strongly interacting particles. $\lambda_{\mathrm{I}} \approx 120\,\mathrm{g/cm^2}$ for pions in the atmosphere. The model assumes λ_{I} is constant, which is a fairly good approximation for interactions between 10 and 1000 GeV. In this model, every hadron produces N_{ch} charged pions and $N_{\mathrm{ch}}/2$ neutral pions in each interaction per layer. As discussed previously, π^0 decays to photons and initiates electromagnetic showers immediately. On the other hand, the $\pi^{\pm}$ will travel through another layer and interact. This process will continue until $\pi^{\pm}$ reach a critical energy E_c^{π} and decay to muons and neutrinos. Here, E_c^{π} is considered to be 20 GeV and $N_{ch} = 10$ appropriate in the range from 1 GeV to 10 TeV.

Assume a proton with an initial energy E_0 hits the atmosphere. After n atmospheric layers, there will be $N_{\pi} = (N_{\mathrm{ch}})^n$ charged pions. If the energy is divided equally in all pions, the charged pions carry $\frac{2}{3}$ of the total energy and the remainder $\frac{1}{3}$ goes into electromagnetic showers via the π^0 decay. The energy per charged pion after the n^{th} interaction is therefore

$$E_{\pi} = E_0 / \left(\frac{3}{2} N_{ch}\right)^n . \tag{2.9}$$

The number of interactions before E_π falls below the critical energy E_c^π is

$$n_c = \frac{\log_{10}[E_0/E_c^\pi]}{\log_{10}[\frac{3}{2}N_{ch}]} = 0.85\ \log_{10}[E_0/E_c^\pi]. \tag{2.10}$$

Since the number of produced muons in the $\pi^\pm$ decay is the same as the charged pions, the primary energy can be estimated by the energy carried by pions and electromagnetic particles as

$$E_0 = E_c N_e + E_c^\pi N_\mu \approx 0.85\,(N_e + 24N_\mu)\,\mathrm{GeV}. \tag{2.11}$$

So, the primary energy can be calculated by measuring the N_e and N_μ regardless of the primary particle type and fluctuation.

From the result of Equation 2.10, the number of muons created in the shower is obtained as

$$N_\mu = N_\pi = (N_{ch})^{n_c} = (N_{ch})^{0.85\ \log_{10}[E_0/E_c^\pi]} = (E_0/E_c^\pi)^{0.85} \approx 10^4 \left(\frac{E_0}{\mathrm{PeV}}\right)^{0.85}. \tag{2.12}$$

The number of electrons can be obtained as a function of primary energy as

$$N_e \approx 10^6 \left(\frac{E_0}{\mathrm{PeV}}\right)^{1.03}. \tag{2.13}$$

If the primary particle is a heavier nucleus than proton, then superposition approximation can be used, meaning a nucleus with mass A can be represented by A showers of E_0/A, where E_0 is the primary energy. This reduces the depth of maximum development to $X_{\max}^A = X_{\max} - X_0 \ln A$, where X_0 is the first interaction length of proton. This indicates that air showers starting by heavy nuclei will reach maximum development higher in the atmosphere than a proton-initiated air shower. In addition, the muon content will be larger in a nuclei-initiated air shower since the shower begins at a lower energy, so less energy will be transferred to the electromagnetic component. The muon content of a nuclei-initiated shower compared

to a proton can be estimated as $N_\mu^A = A^{0.15} N_\mu^p$ (Matthews, 2005). The A exponent of 0.15 results mainly from the fraction of pions that are charged ($\approx 2/3$).

2.8 Composition

The composition of UHECRs is not very well known because of their very low flux. But for cosmic rays below 10^{14} eV, one can directly measure the composition by placing detectors above the atmosphere in balloons or satellites. Figure 2.5 shows the composition of cosmic rays at lower energies. About 79% of the nuclei are free protons (shown as hydrogen), 15% are helium and the rest are either heavier elements or electrons. The abundances of some common heavier elements, such as carbon, oxygen, magnesium, silicon, and iron are very similar to that in the solar system. However, there are over-abundances of some rare elements, such as lithium, beryllium, and boron in cosmic ray composition. These rare elements are produced when heavier elements such as carbon, nitrogen, and oxygen disintegrate during collisions with the interstellar gas.

The composition of UHECR is another story. The most popular candidates are protons and iron nuclei, since they have the highest binding energy and are least probable to disintegrate during their propagation through space. But the possibility of existence of other elements provides motivation to study the EAS in great detail. Neutrinos and photons are other possible candidates that would either be created as secondary particles from the decay of pions during the GZK process or from "exotic" processes. Photons at ultra-high energies would undergo the pair production process, therefore they travel over small ranges (<10 Mpc). Neutrinos, on the other hand, travel very large distances before any interaction, because of their very small cross sections. I will discuss the observational limits on the photon and neutrino fluxes later in Chapter 3.

Recent results of mass composition studies using data from HiRes, Telescope Array and Pierre Auger Observatory lead to inconsistent conclusions (Telescope Array Collaboration and Pierre Auger Collaboration, 2013). But it should be noted that the comparison is not

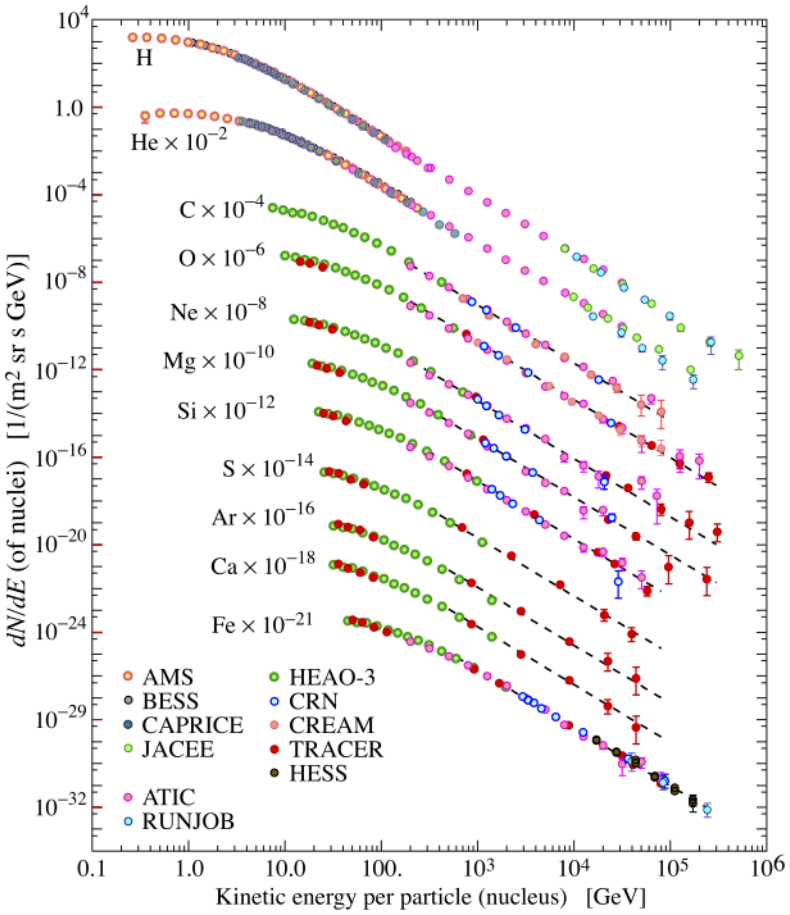

Figure 2.5: Cosmic ray composition with energies between 10^9 eV and 10^{14} eV. Plot by P. Boyle and D. Müller. From (Beringer et al., 2012).

exact because of the differences between the acceptance and resolution of the experiments. Measurement of the chemical composition of UHECRs in an event-by-event basis is difficult due to the low energy flux at these energies. But the composition can be studied with indirect methods such as measuring the depth of shower maximum ($X_{\max}$). The $X_{\max}$ study at the Pierre Auger Observatory and its results will be discussed in Section 3.3.3.

3. Pierre Auger Observatory

3.1 Overview

Section 2.3 discussed the flux of cosmic rays above 1 EeV which is extremely low. Therefore, in order to detect the UHECRs, a large area is covered with the detectors. There are a few large cosmic ray observatories on Earth that detect UHECRs. The largest one is the Pierre Auger Observatory that has been built to collect UHECRs in an area of about 3000 km^2 (see Figure 3.1). To have a sense of how big this area is, if it is compared to the state of Rhode Island, Pierre Auger Observatory is slightly larger. It is located near the town of Malargüe in Mendoza, Argentina (35.2° S, 69.5° W) at 1400 m above the sea level. There are two different techniques used for the detection of UHECRs at Auger that I will describe in the following section. Although the construction of the observatory was completed in mid-2008, it has been taking data continuously since January 2004.

3.2 Detectors

Pierre Auger Observatory is called a "hybrid" detector because it uses two different techniques. The Surface Detector (SD) array is comprised of more than 1660 water Cherenkov detectors arranged in a hexagonal grid with 1.5 km spacing. The Fluorescence Detector (FD) is comprised of four buildings each containing 6 fluorescence telescopes overlooking the SD. Each telescope has a 30° × 30° field of view. Figure 3.2 shows a full view of the observatory with images of the four fluorescence telescope buildings at the corners of the figure. Figure 3.3 shows a water Cherenkov detector overlooked by one of the fluorescence telescope buildings.

3.2.1 Surface Detector

An individual surface detector is a cylindrical tank filled with about 12 thousand liters of purified water and outfitted with electronics. Each station has diameter of 3.6 m and a height of 1.55 m. But only up to about 1.2 m of its height is filled with water. The thickness of the

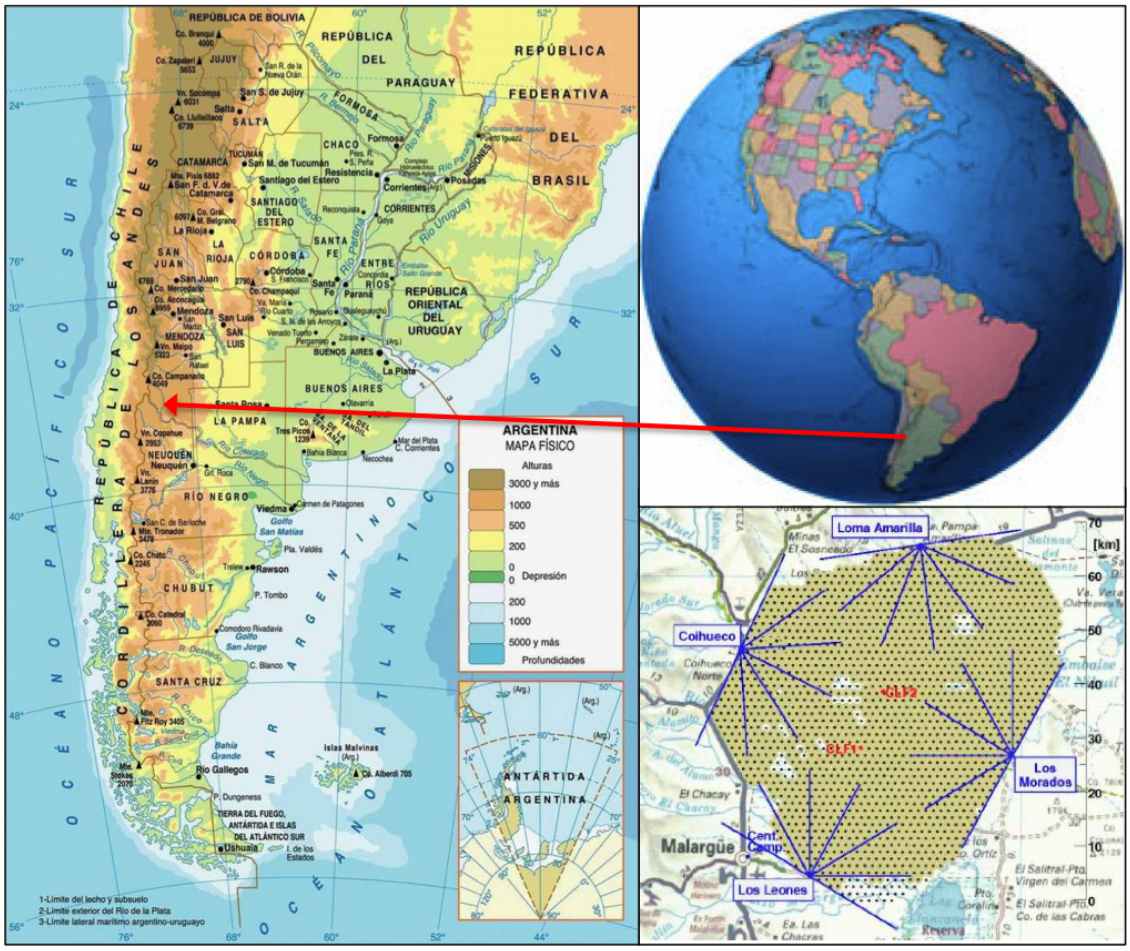

Figure 3.1: Location of the Pierre Auger Observatory near Malargüe in Mendoza, Argentina. The lower right figure shows the layout of the observatory.

tank is 13 mm. Water Cherenkov detectors detect Cherenkov light produced by energetic particles moving faster than the speed of light in water. The advantage of using purified water is that it reduces the Cherenkov light attenuation. The detector is built with polyethylene that can bear the weight of three people working on top of it. Most importantly, it stands still for long terms of operation, while keeping the solar panels stable even in strongest winds at the site.

This light is detected by three 9-inch Photomultiplier Tubes (PMTs) Photonis XP1805 that are located on top of the detector at a distance of 1.2 m from the center and is converted to a digital signal at 40 MHz by a Flash Analog to Digital Converter (FADC). The PMT signals are then sent to the Central Data Acquisition System (CDAS) by a radio communi-

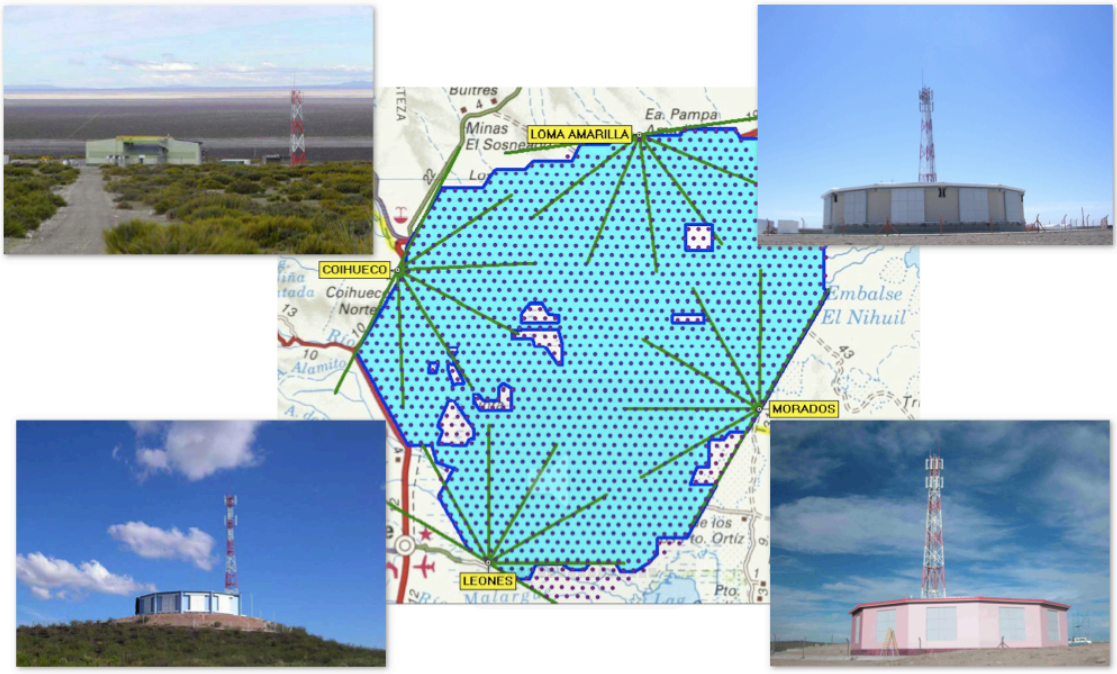

Figure 3.2: Map of the Pierre Auger Observatory: The dots are the locations of the surface detectors and the green lines show the pointing direction of each of the fluorescence telescopes. As a scale, each green line is about 20 km.

cation system at the observatory main campus. Signals are measured in vertical equivalent muon (VEM), that is the average signal response of a muon passing vertically through a tank. The random atmospheric muons produce a peak in the charge distribution, which is proportional to a vertical muon signal. You can see a detailed picture of one of the SDs in Figure 3.4. Each SD operates with its own electronics powered by solar panels and they work on a 100% duty cycle.

3.2.2 Surface Detector Event Reconstruction

Here I describe how to reconstruct the energy of an air shower detected by the SDs. An important parameter in reconstructing the energy is the shower front. The shower geometry can be obtained because the shower front hits different detectors at different times. As a first approximation, the shower front is assumed to be planar as shown in Figure 3.5. The shower axis can be determined by fitting station arrival times to a plane-wave moving at the speed of light. First the barycenter (the origin from which all the distances are measured)

Figure 3.3: A water Cherenkov detector and one of the four buildings containing fluorescence telescopes.

of a signal-weighted sum is measured

$$\vec{x}_0 = \frac{1}{W} \sum_i \sqrt{S_i}\ \vec{x}_i, \tag{3.1}$$

where S_i is the Cherenkov signal for station i at time t_i and position $\vec{x}_i$, and W is $\sum_j \sqrt{S_j}$. The barycentric time would then be

$$t_0 = \frac{1}{W} \sum_i \sqrt{S_i}\ t_i. \tag{3.2}$$

The shower position in the barycentric coordinate system is described as

$$\vec{x}_i = \vec{x}_0 - c(t_i - t_0)\hat{a}, \tag{3.3}$$

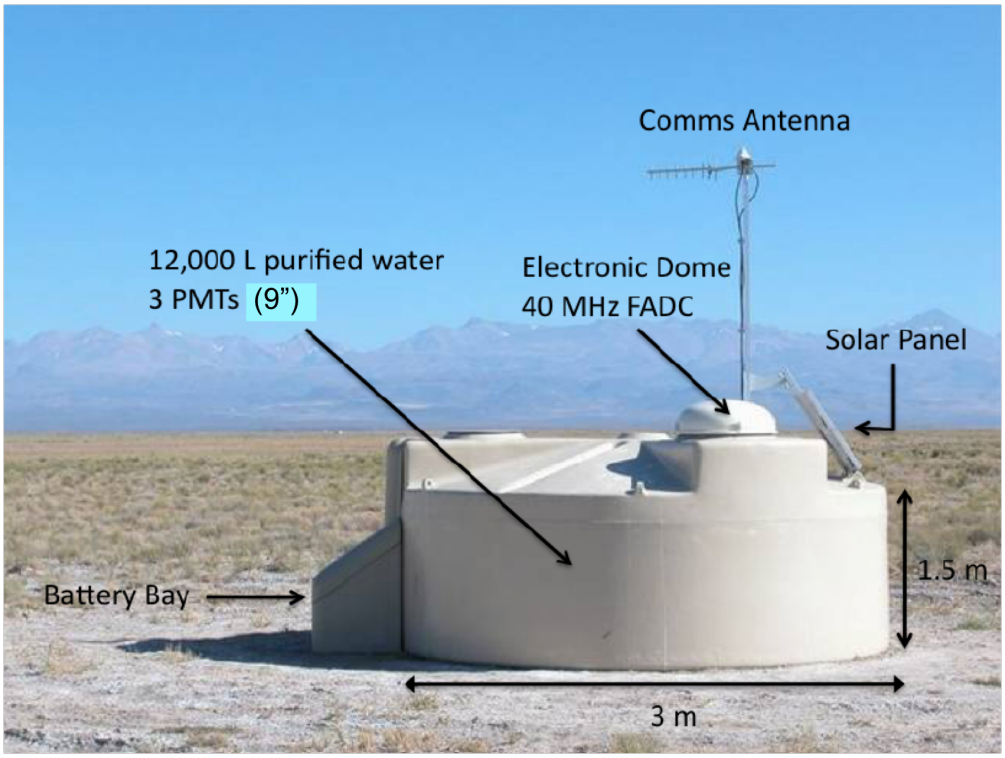

Figure 3.4: Surface detector (SD) with a diameter about 3 m and a height of 1.5 m. The SDs are also called water Cherenkov detectors that are filled with 12,000 L purified water and overlooked by three PMTs. The solar panel, battery bay, and communication antenna are also shown.

where $\hat{a}$ is the shower axis unit vector. From this equation, the time that the shower front reaches any of the stations is derived

$$t_i(\vec{x}_i) = t_0 - \frac{1}{c}(\vec{x}_i - \vec{x}_0) \cdot \hat{a}. \tag{3.4}$$

The shower axis is then determined by minimizing the square of the difference between the predicted time $t_i(\vec{x}_i)$ and the measured time t_i,

$$\chi^2 = \sum_{i=1}^{n} \frac{1}{\sigma^2(t_i)}(t_i - t_i(\vec{x}_i))^2 = \sum_{i=1}^{n} \frac{1}{\sigma^2(t_i)}[t_i - t_0 + \frac{1}{c}(\vec{x}_i - \vec{x}_0) \cdot \hat{a}]^2, \tag{3.5}$$

where n is the number of triggered stations and $\sigma^2(t_i)$ is the timing uncertainty of station i. Since the real showers possess curved shower fronts, the above calculated barycenters are

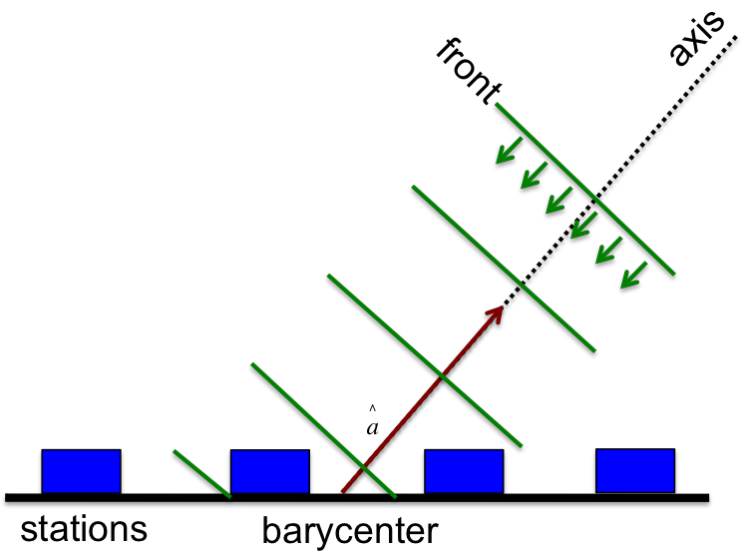

Figure 3.5: An extensive air shower hits the SDs. Shower front reaches the detectors at different arrival times.

then used as seed values for a second fit to a non-planar shower front to better estimate the core location. Signals and barycenter core location are then used to determine the Lateral Distribution Function (LDF) of the event. The LDF is used to determine the expected signal size of a station located at a distance of 1000 m from the shower core (S(1000)). The LDF used at Auger is given by a standard NKG function (Kamata & Nishimura, 1958; Greisen & Wilson, 1956)

$$S(r) = S(1000)(\frac{r}{1000\text{ m}})^{\beta}(\frac{r+r_s}{1000\text{ m}+r_s})^{\beta+\gamma} \tag{3.6}$$

where β is a function of zenith angle θ, $\beta = a + b(\sec\theta - 1)$, and γ represents the scale of flattening of the LDF. r_s is a fixed parameter (= 700 m) to distinguish the slopes of muonic and electromagnetic component LDFs.

The parameter S(1000) depends on the zenith angle of the shower. In order to remove this dependency, S_{38} is usually used as an energy estimator. The signal S(1000) is corrected to what it would have been if the shower had arrived at 38° based on the observations of how showers diminish. The energy related to each S_{38} is calculated based on the calibration of

the SD with the fluorescence detector reconstructed energy, using hybrid events. Figure 3.6 shows the correlation between S_{38} and the fluorescence detector (FD) reconstructed energy.

3.2.3 Fluorescence Detector

There are four fluorescence sites named Los Leones, Los Morados, Loma Amarilla, and Coihueco (see Figure 3.2). In each of these sites, there are 6 fluorescence telescopes overlooking the array of surface detectors. Figure 3.7 shows a schematic downward view of these telescopes. The control room and other parts of the building are also shown in this figure. Each of the six telescopes has a field of view of $30° \times 30°$, so it will be overlooking the SDs at an angle of 180°. A schematic view of a fluorescence detector is shown in Figure 3.8. The fluorescence light passes through a large UV filter and an optical corrector ring ("Schmit optics") that corrects for spherical aberration. The light is then reflected and focused by a 13.4 m^2 mirror with a focal length of 1 m to a camera with 440 PMTs. The signals collected are digitized every 100 ns. Once the signals pass the triggers (Pierre Auger Collaboration, 2010c, 2013), they are sent to the data acquisition system (DAQ). The fluorescence light is produced due to the excitation of atmospheric nitrogen molecules by the charged particles. The wavelength of the produced fluorescence light is mainly between 300 nm and 430 nm (Figure 3.9). The number of fluorescence photons is proportional to the energy deposit of the shower particles. The timing and intensity of light are measured by these telescopes. FDs work only on clear moonless nights, since the fluorescence light signal is very weak. It limits the time for this detection to about 13% of the total observation up-time.

Only FD events that also trigger the SD are kept for further analysis; these are called hybrid events. Although only a small fraction of the whole data set, they are very good crosschecks of these two independent techniques.

3.2.4 Fluorescence Detector Event Reconstruction

Reconstruction of the event energy requires the knowledge of shower geometry, since the photon flux observed at the detector should be related to the photons emitted from the

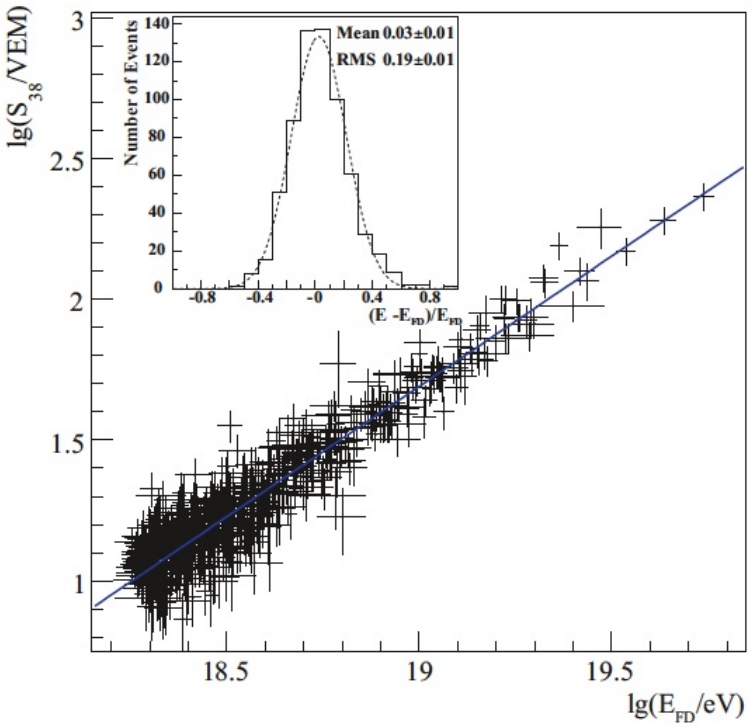

Figure 3.6: Correlation between $\log(S_{38})$ and the FD reconstructed energy $\log(E_{FD})$. The fractional dispersion is shown in the small plot. From (Pierre Auger Collaboration, 2008).

shower. Shower geometry consists of the shower detector plane (SDP), the angle that shower axis make with the horizontal plane χ_0, and the distance to the detector R_p. The SDP contains the shower axis and the FD as shown in Figure 3.11. The first step is to determine the SDP that is simply a fit to the pointing directions of each triggered pixel, weighted by the size of the signal (Pierre Auger Collaboration, 2004). The SDP can be determined by minimizing

$$\chi^2 = \sum_{i=1}^{n} S_i[\vec{n}_{SDP} \cdot \vec{r}_i]^2, \tag{3.7}$$

where n is the number of triggered pixels, S_i is the signal of pixel i for weighting purpose, $\vec{n}_{SDP}$ is the normal vector of SDP and $\vec{r}_i$ is the pointing direction of pixel i.

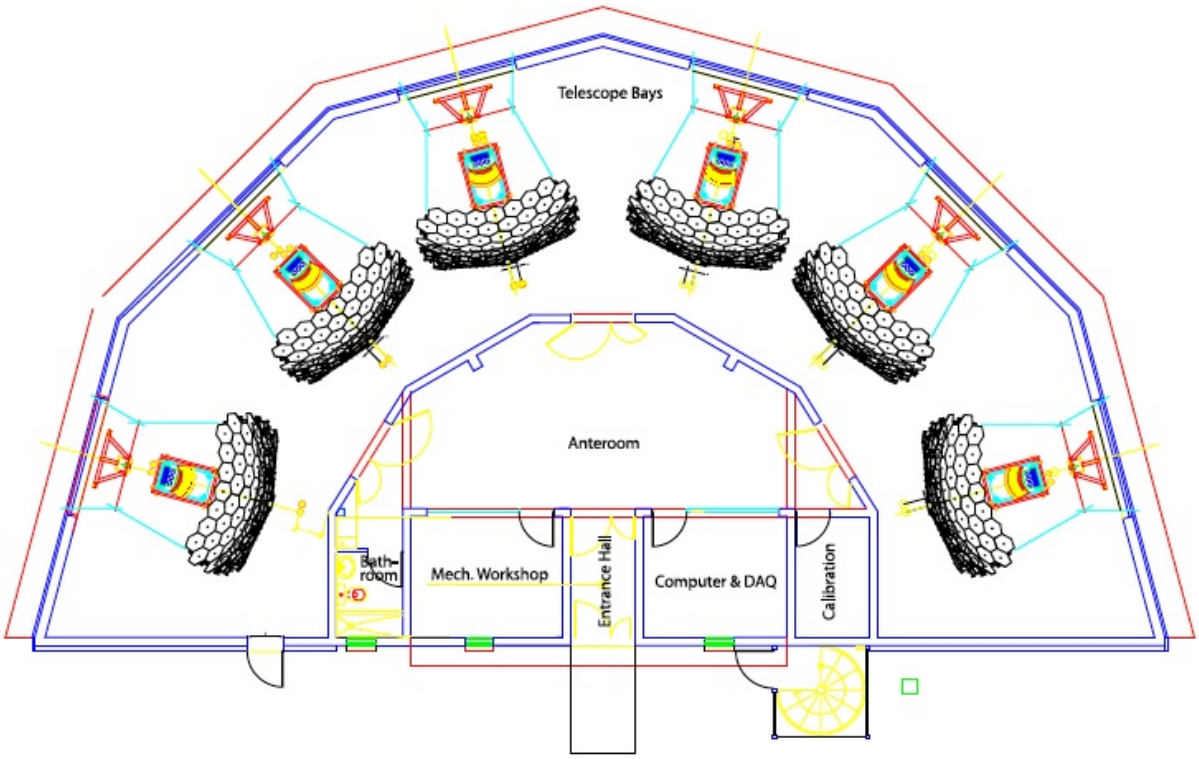

Figure 3.7: A downward view of the six telescopes in each FD site. The schematic of the computer room and other parts of the building is also shown.

The timing information is then used from each pixel to determine the shower axis. The expected arrival time of the light in pixel i is given by

$$t_i = t_0 + \frac{R_p}{c} \tan \frac{(\chi_0 - \chi_i)}{2}, \tag{3.8}$$

where c is the speed of light, χ_i is the angle of elevation of pixel i and t_0 is the time at which the shower crosses the closest point on the shower axis to the detector. The sum of the square of time difference between measurement and expectation is minimized by varying the assumed shower axes,

$$\chi^2 = \sum_{i=1}^{n} \frac{[T_i - t_i]^2}{\sigma_{t_i}}, \tag{3.9}$$

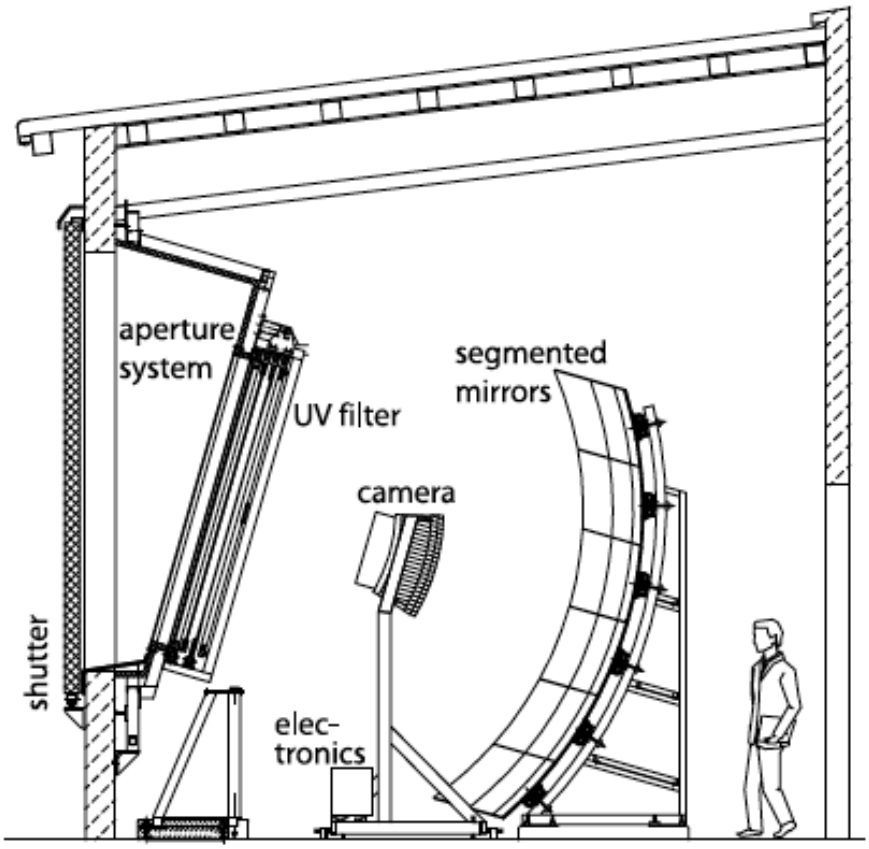

Figure 3.8: A schematic view of a fluorescence detector.

where T_i is the expected time for "test" shower axis and t_i is the measured time for that pixel and σ_i is the uncertainty in its value. The t_0, R_p and χ_0 are then found by this minimization.

Most of the FD events are also detected by the SD (hybrid events), so the information from the SD can also help to improve the accuracy of shower geometry determination. Also some showers are detected by more than one FD. In such cases, the intersection of the two SDPs can define the shower axis. The hybrid geometry reconstruction has an angular accuracy of about 0.6° above 1 EeV in terms of arrival direction and a resolution of 50 m in the shower core location (Pierre Auger Collaboration, 2010b).

Defining the shower geometry would take us to the second step, which is calculating the primary particle's energy. To do this, the light collected by the PMTs should be converted to the energy deposit into the atmosphere as a function of slant depth. The FD shower profile

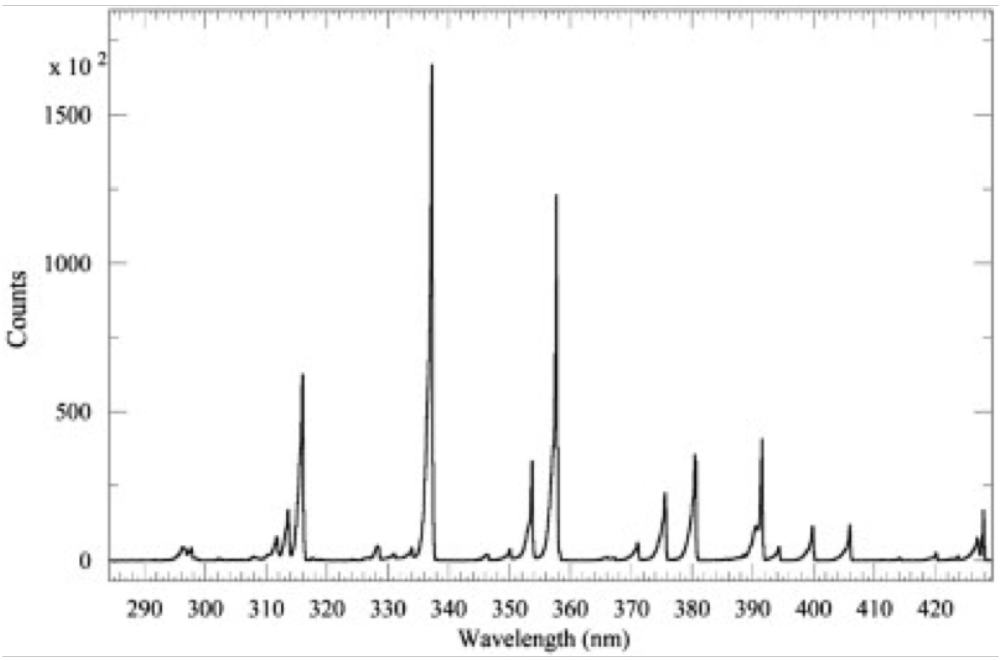

Figure 3.9: The wavelength of the produced fluorescence light is mainly between 300 nm and 430 nm.

is then reconstructed by fitting a function. Integrating the shower profile that is fitted by a Gaisser-Hillas function (Gaiser & Hillas, 1977) ($f_{GH}(x)$) gives the primary shower energy, as the energy deposit during the shower development is proportional to the emitted fluorescence light:

$$E_{FD} = \int_0^\infty f_{GH}(x)\,\mathrm{d}x. \tag{3.10}$$

Finally, some corrections need to be applied from the simulations, since the energy carried away by neutrinos and high energy muons will be missed in the shower profile analysis. However, this correction depends on the mass composition of the primaries and the interaction models. Assuming an equally mixed composition of protons and iron nuclei, the average missing energy correction is about 12% for a primary energy of 10^{19} eV. There are other sources of systematic uncertainties of FD, such as the absolute fluorescence yield, absolute calibration of FD and the reconstruction method uncertainties including the effects of pressure, temperature and humidity of the air. The total systematic uncertainty of FD is about

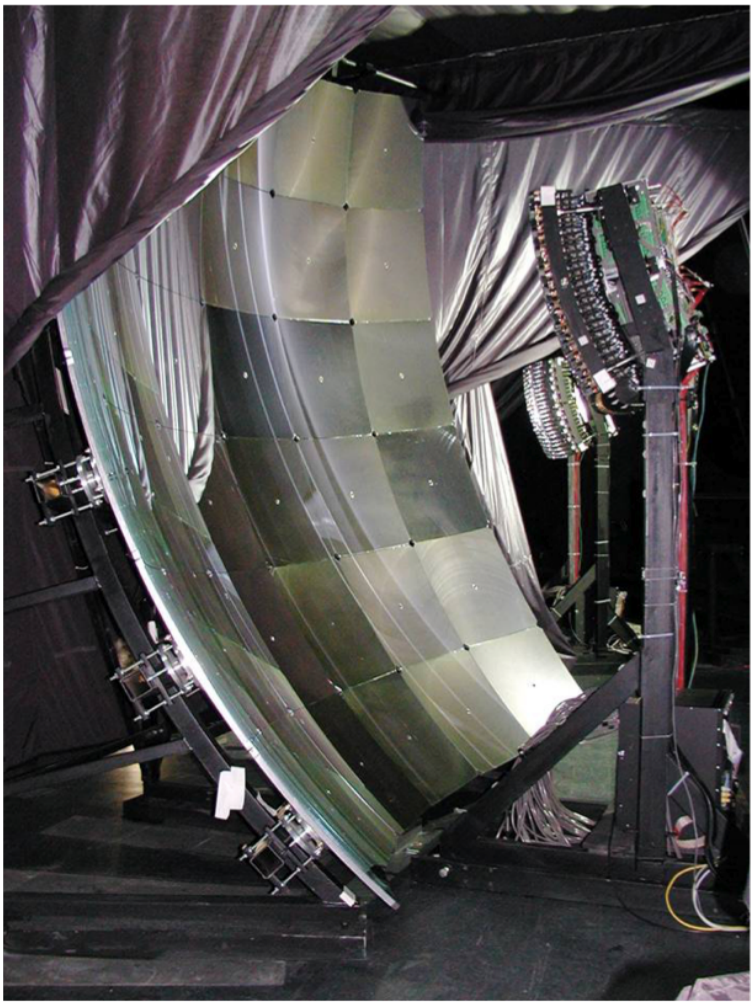

Figure 3.10: A real image of inside of a fluorescence telescope. The six mirrors are overlooked by 440 PMTs, on the right of the image.

14%, which is larger than the systematic error of SD that is 5% (Barbosa et al., 2004; Pierre Auger Collaboration, 2013).

Figure 3.12 summarizes the discussion in this section. It is taken from the online event display. The top left image shows the fluorescence light track of a real event recorded by FD camera. The track is from top to bottom with colors showing the time sequence. The top right image shows correlation between the triggered pixel time (t) and the pixel pointing direction (χ) as described in geometrical reconstruction. The bottom left is the typical shower profile reconstruction fitted with a Gaiser-Hillas function. The bottom right image

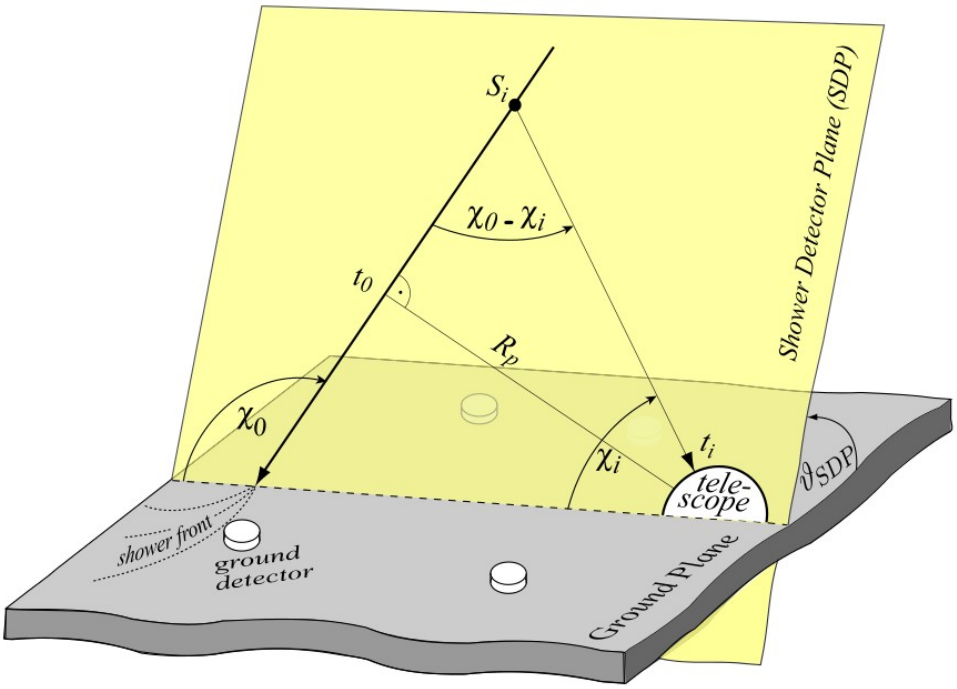

Figure 3.11: Shower detector plane, from (Kuempel et al., 2008). Also see (Sokolsky, 1989).

summarizes all the event information, such as the event time, energy, $X_{\max}$, direction and location.

3.3 Results

Auger has been operating and collecting data since 2004. The construction of the observatory was completed in 2008 and since then it has been fully operational. Auger has collected more UHECRs than any other cosmic ray experiment with its accurate hybrid technique. There have been several exciting published results mostly since after the completion of the observatory. I will cover the most important of these results in the following sections.

3.3.1 Energy Spectrum

The energy spectrum of cosmic rays at the very high energies is not completely understood. One of the main goals of Auger is to study the flux at these energies. To measure the flux, the hybrid data and the SD-only data are combined using a maximum likelihood method. The SD energy estimator S(1000) is calibrated using the hybrid events. So they have the

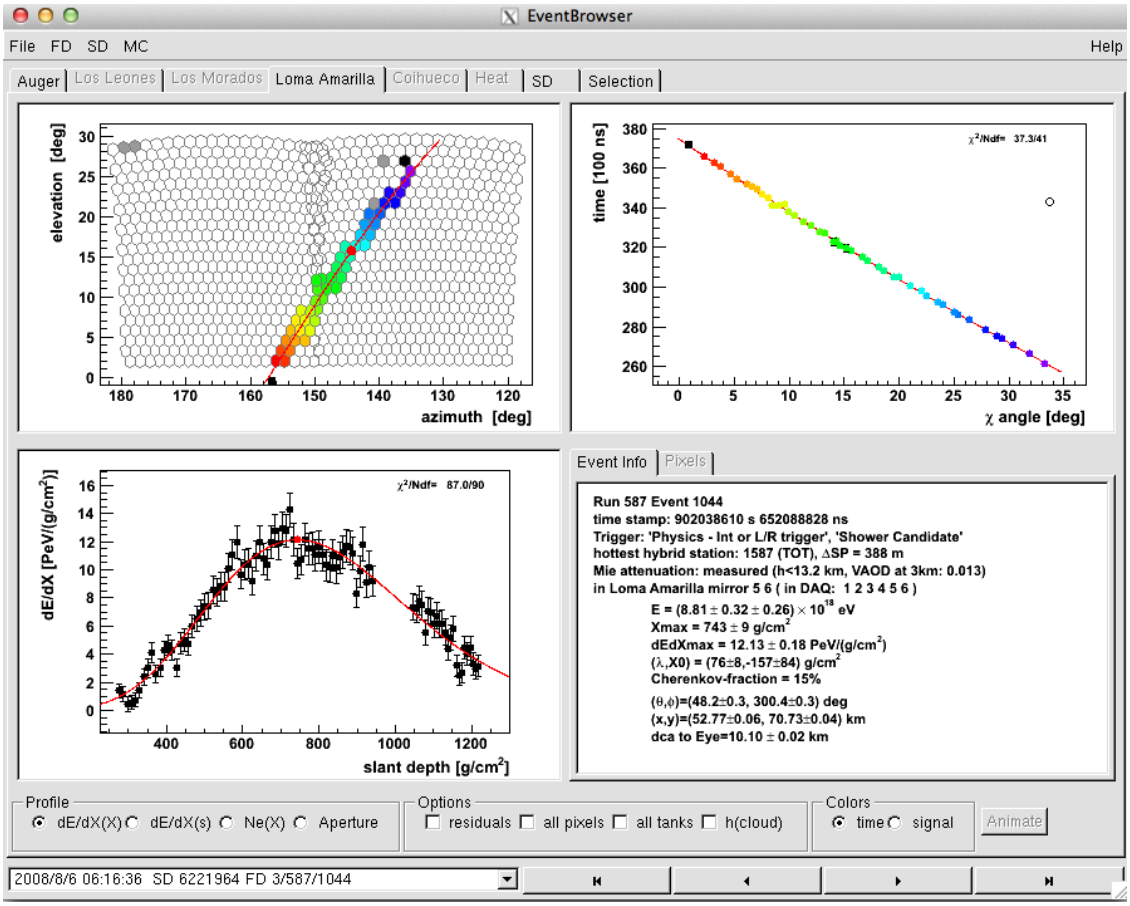

Figure 3.12: Reconstruction of an event with an energy of $(8.81 \pm 0.32) \times 10^{18}$ eV recorded by FD. Top left: the fluorescence light track recorded by FD camera. The track starts from top with color of the pixels showing the time sequence. Top right: reconstruction of geometry: correlation between the pixel triggered time and the pixel pointing direction. Bottom left: Fitting a Gaiser-Hillas function on the shower profile. The vertical axis is deposited energy and the horizontal axis is the atmospheric slant depth. Bottom right: summary of the event information, such as the event time, energy, $X_{\max}$, direction and location.

same systematic uncertainties, but they have different normalization uncertainties, which is about 6% for the SD and 10% for hybrid data at 10^{18} eV. The data used here is from January 2004 to December 2012 (Pierre Auger Collaboration, 2013).

Figure 3.13 shows the energy spectrum from Auger data. The flux is multiplied by E^3 to exhibit a flatter spectrum, so that the variations due to the ankle and high energy suppression from the other regions of the plot are enhanced. Auger energy spectrum is fitted with two functions; (i) three broken power laws ($J(E) \propto \mathrm{E}^{-\gamma}$, where γ is the power law index) and (ii) two power laws plus a continuous function decreasing smoothly with energy

at the highest energies. There are two breaks evident at $\log_{10}(E/\text{eV}) = 18.61 \pm 0.01$ and $\log_{10}(E/\text{eV}) = 19.61 \pm 0.03$. The power index changes from 3.26 ($\pm$ 0.04) to 2.55 ($\pm$ 0.04) at the first break which is the so-called ankle of the spectrum. This change in the spectral index may be due to the transition between Galactic and extragalactic sources. It could also happen due to a change in spectrum at the source (Creusot, 2012). The second change occurs at around 4×10^{19} eV with an spectral index of 4.3 ($\pm$0.2). This break is consistent with the GZK flux suppression. There is also the possibility of some physical phenomena at the source causing this break. The systematic uncertainty of the energy scale is 14% as shown in the figure.

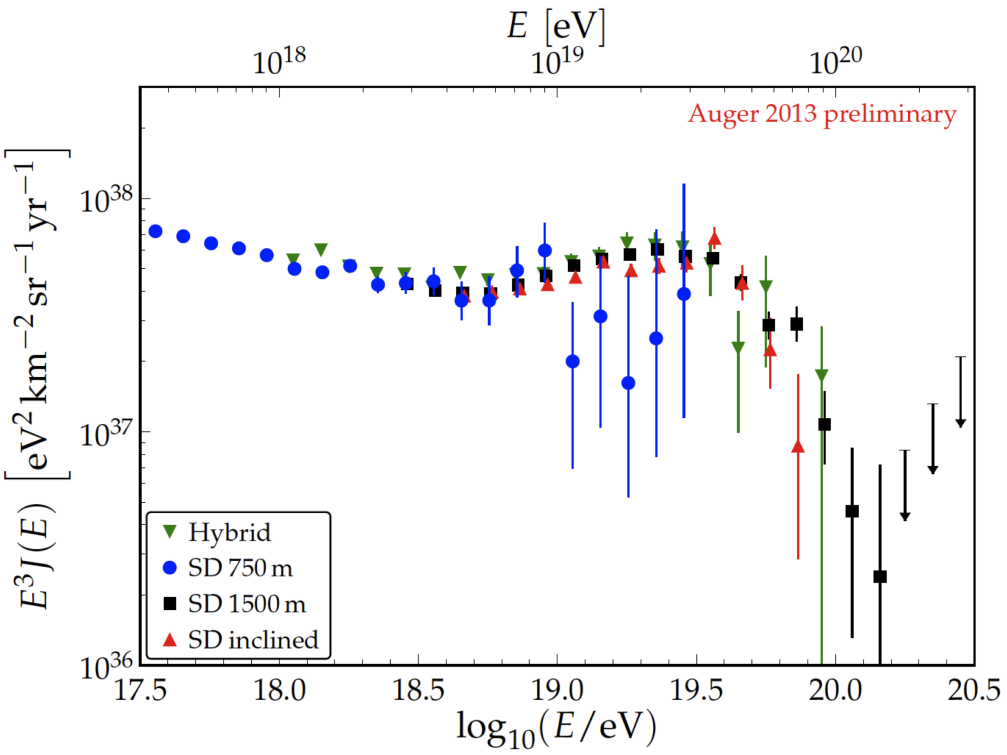

Figure 3.13: Energy spectra, corrected for energy resolution, derived from SD and from hybrid data.

3.3.2 Anisotropy

The most important question to answer at Auger is to find the origin of the UHECRs. The GZK effect implies that the UHECRs detected at Earth should be coming from a relatively

nearby distance (within 100 Mpc) (Roulet, E. for the Pierre Auger Collaboration, 2011). Most of the UHECRs are charged particles, so they are deflected in cosmic magnetic fields. The deflection angle for the highest energy protons are small so that one could neglect the effect of magnetic fields for sources in "GZK sphere". But for most rigidities of interest, the magnetic fields play an important role in the amount of deflection and so in source identification. I discuss this effect in full details in Chapters 4, 5, 6, and 7, which is the main work of this dissertation. In the previous studies at Auger, the effect of magnetic fields were not considered. Therefore, one method to look for UHECR origins is to seek correlations between the cosmic rays arrival directions and source candidates.

In 2007, the Pierre Auger Collaboration found a correlation between the arrival direction of the detected UHECRs above 5.5×10^{19} eV and the active galactic nuclei (AGN) of the Veron-Cetty-Veron (VCV) catalog (Véron-Cetty & Véron, 2006; Pierre Auger Collaboration, 2007). The correlation study was performed by looking for the probability (P) that k or more events out of total n events from an isotropic flux be within an angular separation of ψ of any of the AGN. P is given by the cumulative binomial distribution

$$P = \sum_{i=k}^{n} \binom{n}{i} p^i \, (1-p)^{n-i}, \tag{3.11}$$

where p is the exposure-weighted fraction of the sky accessible to Auger that is within ψ of AGN (Pierre Auger Collaboration, 2007).

Using the data between 1 January 2004 and 26 May 2006, a scan for the minimum of P was performed in three-dimensional parameter space defined by maximum ψ, maximum redshift $z_{\rm max}$ and minimum energy threshold $E_{\rm th}$. A minimum probability was found for the following parameter values: $\psi = 3.1^\circ$, $z_{\rm max} = 0.018$ (or equivalently maximum distance of 75 Mpc), and $E_{\rm th}$=56 EeV. With these parameters, 69% of the UHECR events correlated with one of the AGN of the VCV catalog, where 21% is expected from isotropy.

A more recent analysis shows a lower correlation fraction, decreased from 69% to about 38% (Pierre Auger Collaboration, 2010d). This number is still above the 21% expected from isotropy. The sky map of the arrival directions of the events with energies higher than 55 EeV and the positions of the AGNs within 75 Mpc is shown in Figure 3.14 in Galactic coordinates.

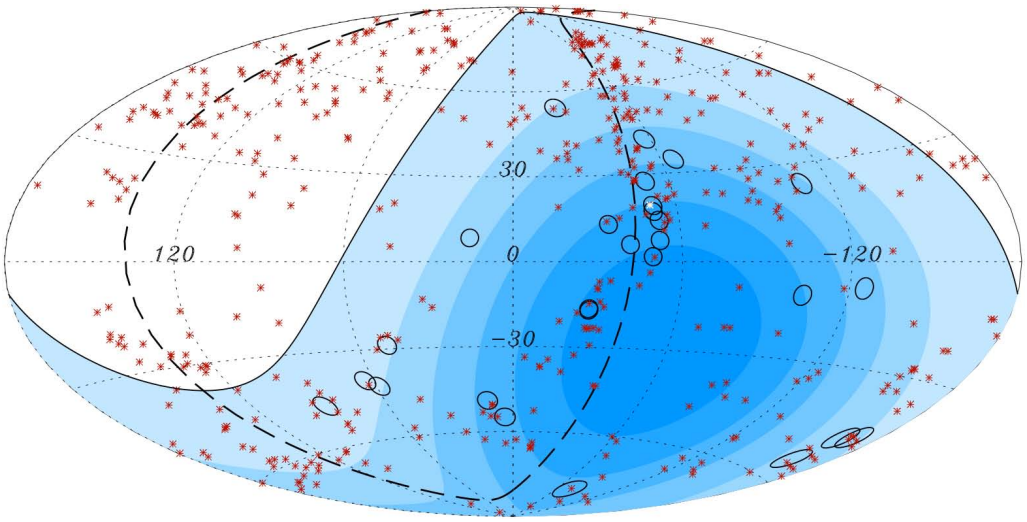

Figure 3.14: Aitoff projection of the celestial sphere in Galactic coordinates with circles of radius 3.1° centered at the arrival directions of the 27 cosmic rays with highest energy detected by the Pierre Auger Observatory. The positions of the 472 AGN (318 in the field of view of the Observatory) with $D < 75$ Mpc from VCV catalog are indicated by red asterisks. The solid line represents the border of the field of view (zenith angles smaller than 60°). Darker color indicates larger relative exposure. Each colored band has equal integrated exposure. The dashed line is the supergalactic plane. Centaurus A is marked in white.

3.3.3 Mass Composition

Particle air showers initiated by heavy elements reach their maximum number of particles higher in the atmosphere due to their larger cross-section. By studying the position of the shower maxima ($X_{\max}$) one expects to be able to infer the mass composition, since heavy nuclear primaries will interact higher in the atmosphere. The FD at Auger measures the longitudinal shower profile; therefore, we are able to calculate the average $X_{\max}$ for showers in a narrow range of primary energy E. The generalized Heitler model indicates that the

$\langle X_{\max} \rangle$ depends on the composition, the energy and the hadronic model used:

$$\langle X_{\max} \rangle = \alpha(\ln E - \langle \ln A \rangle) + \beta, \tag{3.12}$$

where $\langle \ln A \rangle$ is average of the logarithm of mass of the primary particle, E is the energy of the primary particle and α and β are model dependent parameters as described in (Matthews, 2005; Heitler, 1954).

Figure 3.15 shows the observed average of $X_{\max}$ as well as its fluctuation as a function of energy (Pierre Auger Collaboration, 2010a). Auger data (from December 2004 to March 2009) has been compared with four different air shower simulations using different hadronic interaction models. There is a tendency at higher energies to meet the models for heavier elements in both the $X_{\max}$ and rms($X_{\max}$). This suggests that the cosmic ray primaries at higher energies may be heavier elements such as iron rather than protons.

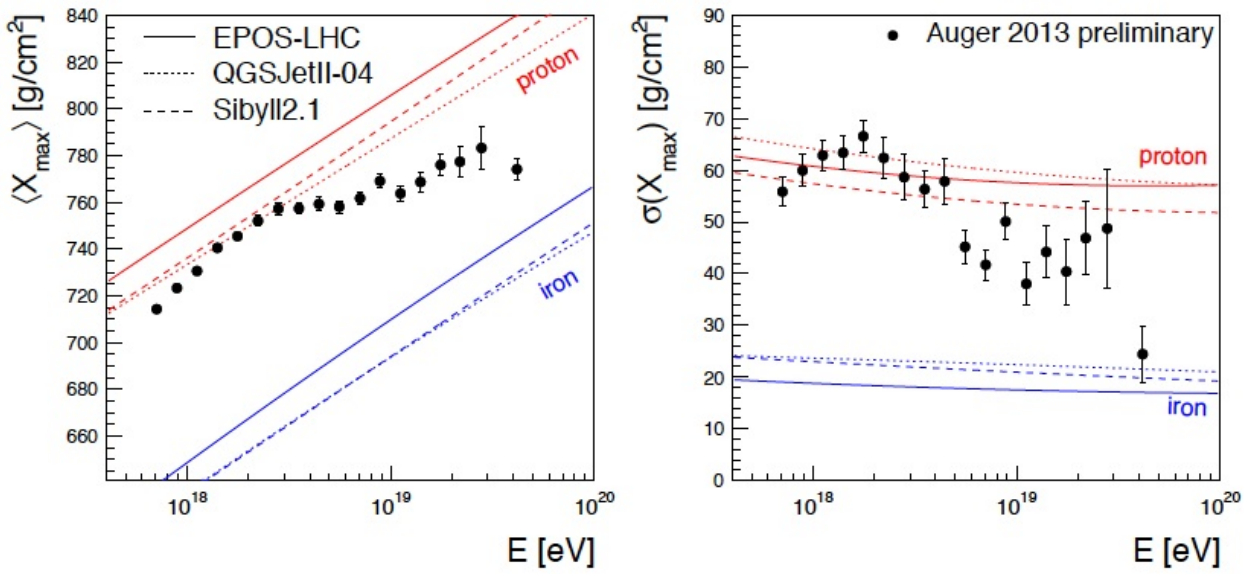

Figure 3.15: The average of shower maximum $\langle X_{\max} \rangle$ vs. energy is shown on the left and its fluctuation rms($X_{\max}$) vs. energy is shown on the right. The lines show the predicted hadronic models.

3.3.4 Photons and Neutrinos

Although neutrino and photon detection is not a primary goal of Auger, such detection may provide useful information about the cosmic ray origins. Neither photons nor neutrinos have been identified in the primary flux of cosmic rays. However, Auger has established stringent limits on their presence.

Neutrinos are weakly interacting particles and can penetrate deep into matter. "Horizontal showers" (zenith angle larger than 60°) induced by neutrinos may be observed by both detection techniques at Auger. There are two types of neutrino showers; downward-going and Earth-skimming as shown in Figure 3.16. The downward-going ν shower is when a neutrino interacts in the atmosphere and the Earth-skimming ν shower is when a neutrino interacts in the Earth crust. In addition to the high inclination, another signature of the ν showers is that they may interact very deeply in the atmosphere, and thus be distinguishable from hadronic showers. A number of shower front properties also can be used to distinguish the ν showers. Auger data has placed a flux limit on neutrinos above an EeV. Figure 3.17 shows these limits to the diffuse flux of UHEνs for downward-going and Earth-skimming ν from Auger. Limits from other experiments have been plotted for comparison.

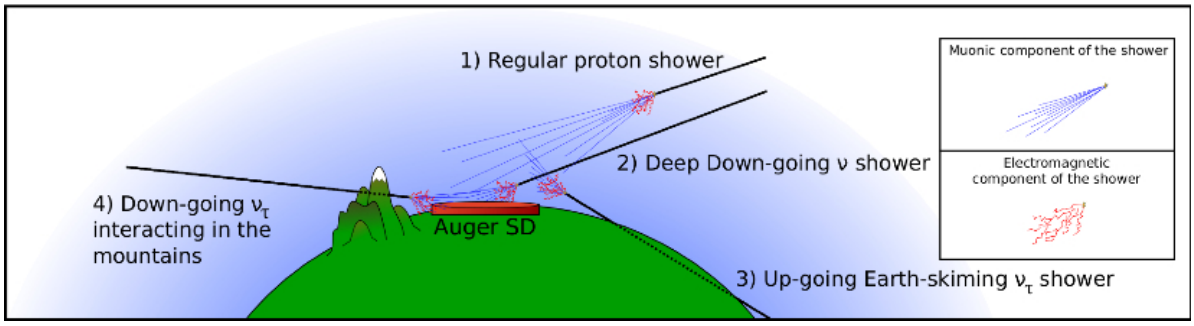

Figure 3.16: This image shows the different categories of ν showers, the downward-going and Earth-skimming in comparison to the regular proton shower.

Photon primaries are expected to produce showers deeper in the atmosphere than the protons or iron. The $X_{\max}$ is about 200 to 300 g/cm^2 larger than that for proton and iron showers. Photon-induced showers do not shed much energy into hadronic channels as they

develop, as happens in proton- or nuclei-induced showers. Therefore, the electromagnetic shower has more energy and will penetrate more deeply than do proton or nuclear showers.

The energy attenuation length of EeV photons is of the order of few Mpc. Therefore, photons can be produced as by products of the GZK process from interactions of protons with interstellar matter, or from the top-down scenarios (as discussed in Section 2.4.1). Photon flux limits can be established by observing the longitudinal development of the air showers with hybrid detection (Pierre Auger Collaboration, 2009). The derived flux limits at Auger compared to previous experiments and model predictions are shown in Figure 3.18 (Settimo, 2011). The black arrows show the flux limits from the ground array and the blue arrows show the flux limits above 2, 3, 5, and 10 EeV from the hybrid data. A1 and A2 are limits from the experiment AGASA, Y is the limits from the experiment Yakutsk, and AY shows the limits from AGASA-Yakutsk data. HP indicates the Haverah Park experimental data. The colored lines are predictions from top-down models and the shaded area is the expected GZK photon fraction (Settimo, 2011).

3.3.5 Proton-Air Cross-Section

The energies of the particles detected at Auger are higher than any particle accelerator on Earth. This fact provides a motivation to find the proton-proton cross section at the higher energies from the cosmic ray data. The proton-air cross section has been measured at the center-of-mass energy of 57 TeV. This cross section is derived from the measurement of the depth of shower maxima.

Proton showers interact lower in the atmosphere relative to larger nuclei and therefore the maximum of a proton-initiated shower is a larger value ($X_{\max}$). To deal with more of the proton showers, the analysis is restricted to the energy interval 10^{18} to $10^{18.5}$ since the shape of the $X_{\max}$ distribution is compatible with a large fraction of protons. There is also a good amount of recorded events at this energy interval. The average center-of-mass energy of a proton interacting with a nucleon is 57 TeV at this energy.

The approach to calculate the proton-air cross-section is to first measure an air shower observable sensitive to the cross section, and second to convert this observable to the cross section. The tail of the $X_{\max}$ distribution can well be fitted with an exponential function $dN/dX_{\max} \propto \exp(-\frac{X_{\max}}{\Lambda_\eta})$, where Λ_η is the defined observable and η denotes the fraction of most deeply penetrating air showers used. Figure 3.19 shows the $X_{\max}$ distribution where an unbinned likelihood fit obtains $\Lambda_\eta = 55.8 \pm 2.3$ g/cm^2.

Having the observable Λ_η, it can be converted to the proton-air cross section ($\sigma_{\mathrm{p-air}}$), using the Monte Carlo air shower simulations. Λ_η is directly related to $\sigma_{\mathrm{p-air}}$ as can bee seen in Figure 3.20. Four popular hadronic models are QGSJET01 (Kalmykov & Ostapchenko, 1993), QGSJETII.3 (Ostapchenko, 2006), SIBYLL2.1 (Ahn et al., 2009) and EPOS1.99 (Werner et al., 2006). The average value of cross section from all four models is the final proton-air cross-section,

$$\sigma_{\mathrm{p-air}} = [505 \pm 22(\mathrm{stat})^{+28}_{-36}(\mathrm{syst})]\,\mathrm{mb}. \tag{3.13}$$

The proton-air cross-section can be converted to proton-proton cross section using the Glauber model (Glauber & Matthiae, 1970). The inelastic cross-section is

$$\sigma^{\mathrm{inel}}_{\mathrm{p-p}} = [92 \pm 7(\mathrm{stat})^{+9}_{-11}(\mathrm{syst}) \pm 7(\mathrm{Glauber})]\,\mathrm{mb}, \tag{3.14}$$

and total proton-proton cross-section is

$$\sigma^{\mathrm{tot}}_{\mathrm{p-p}} = [133 \pm 13(\mathrm{stat})^{+17}_{-20}(\mathrm{syst}) \pm 16(\mathrm{Glauber})]\,\mathrm{mb}. \tag{3.15}$$

These results agree with a straightforward extrapolation of the LHC energies to 57 TeV for limited models as shown in Figure 3.21. More details can be found at (Pierre Auger Collaboration, 2012).

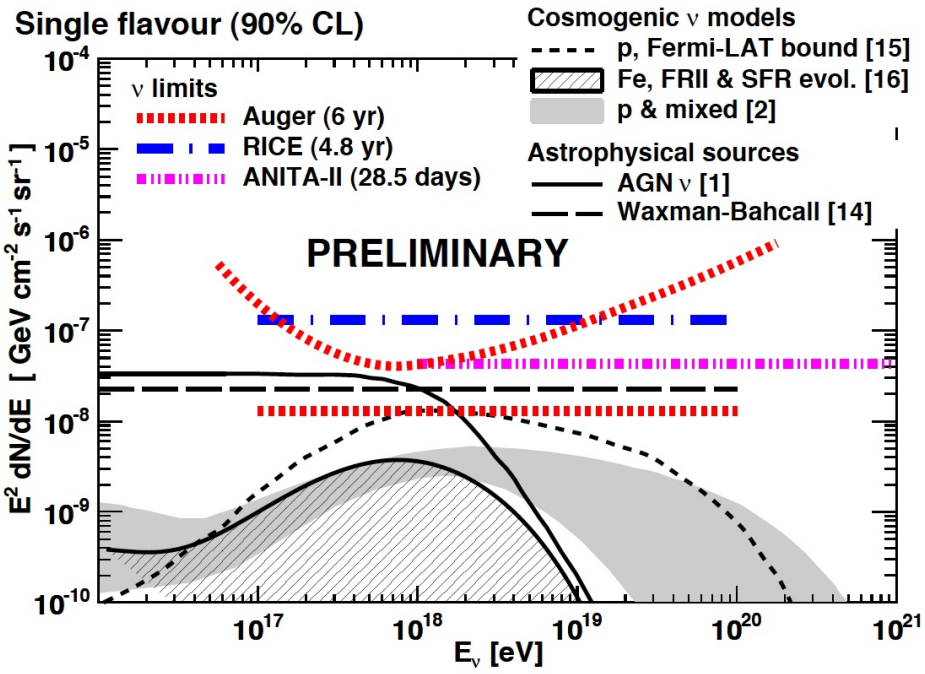

Figure 3.17: Neutrino flux limits from Auger for down-going and earth-skimming ν showers. The limits from other experiments are shown for comparison. For more information about the plot, see (Pierre Auger Collaboration, 2013).

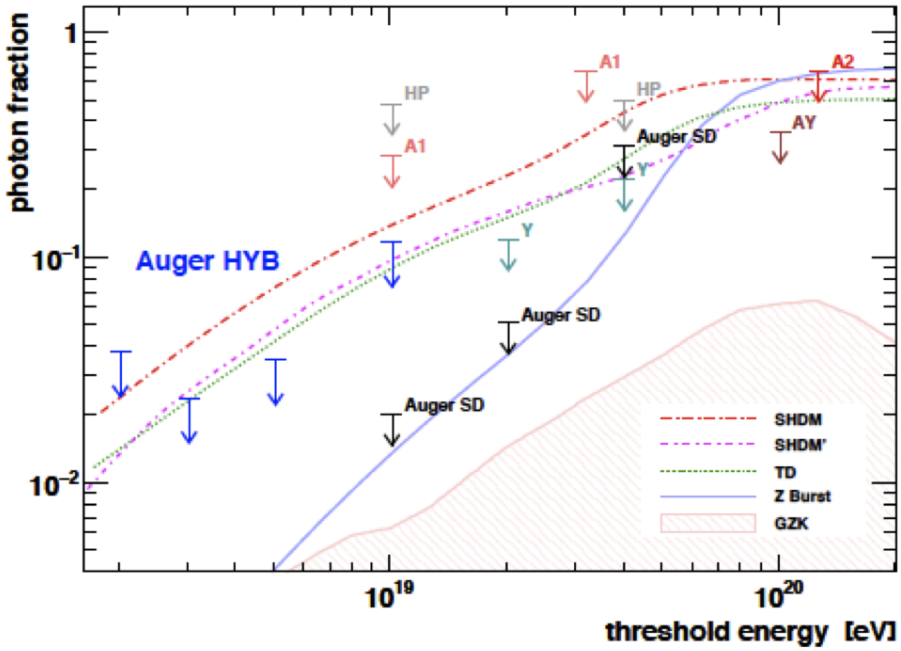

Figure 3.18: Upper limits of the photon fraction in the cosmic ray flux are shown versus the threshold energy. The black arrows are limits from the SD, and blue shows the limits above 2, 3, 5, and 10 EeV from hybrid data. This is compared with other experiments: A1 and A2 are limits from AGASA, AY shows the limits from AGASA-Yakutsk, Y is Yakutsk and HP is from Haverah Park. The shaded region is the expected GZK photon fraction and the lines indicate prediction from top-down models.

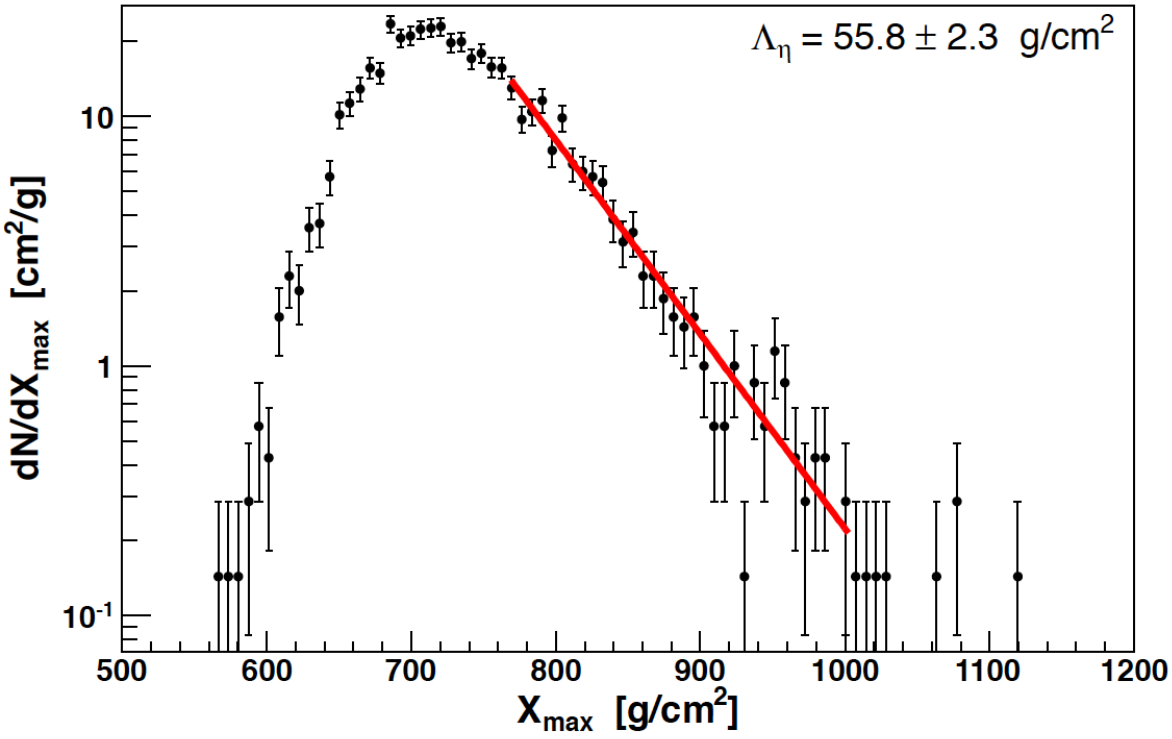

Figure 3.19: $X_{\max}$ distribution. Unbinned likelihood fit to obtain Λ_η (thick line).

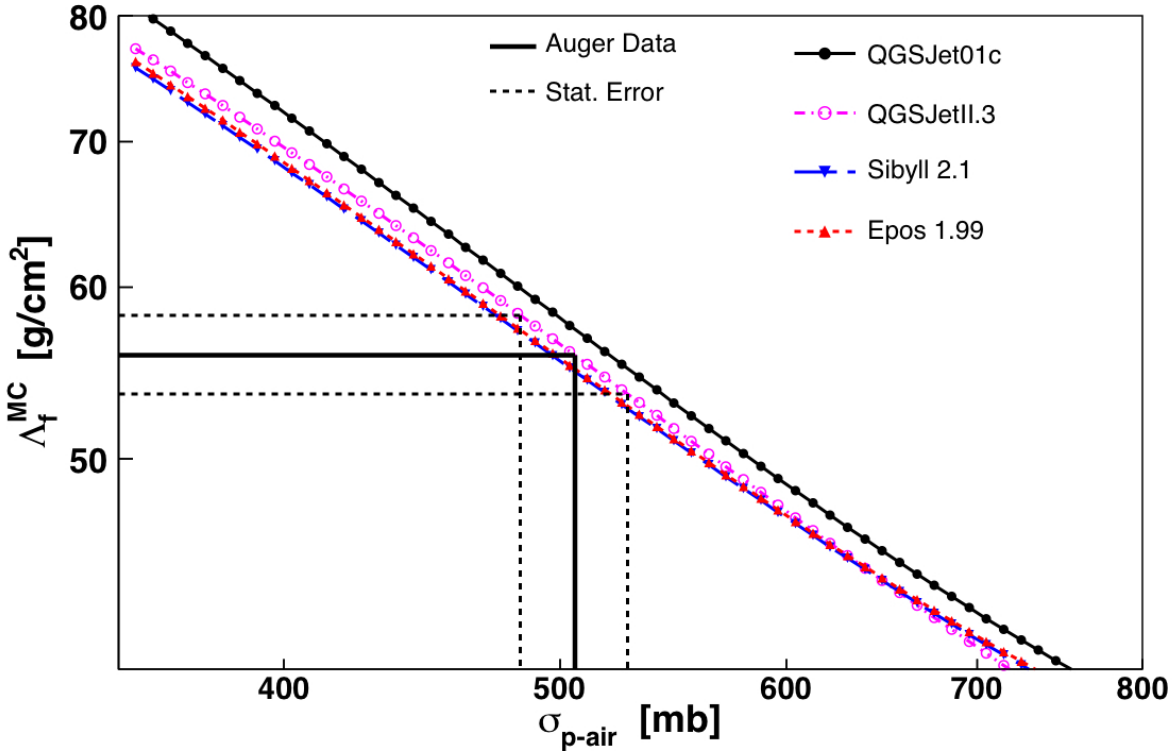

Figure 3.20: The conversion between Λ_η and $\sigma_{\mathrm{p-air}}$ for different simulation models. As an example the conversion of the measurement Λ_η with the QGSJetII model is shown.

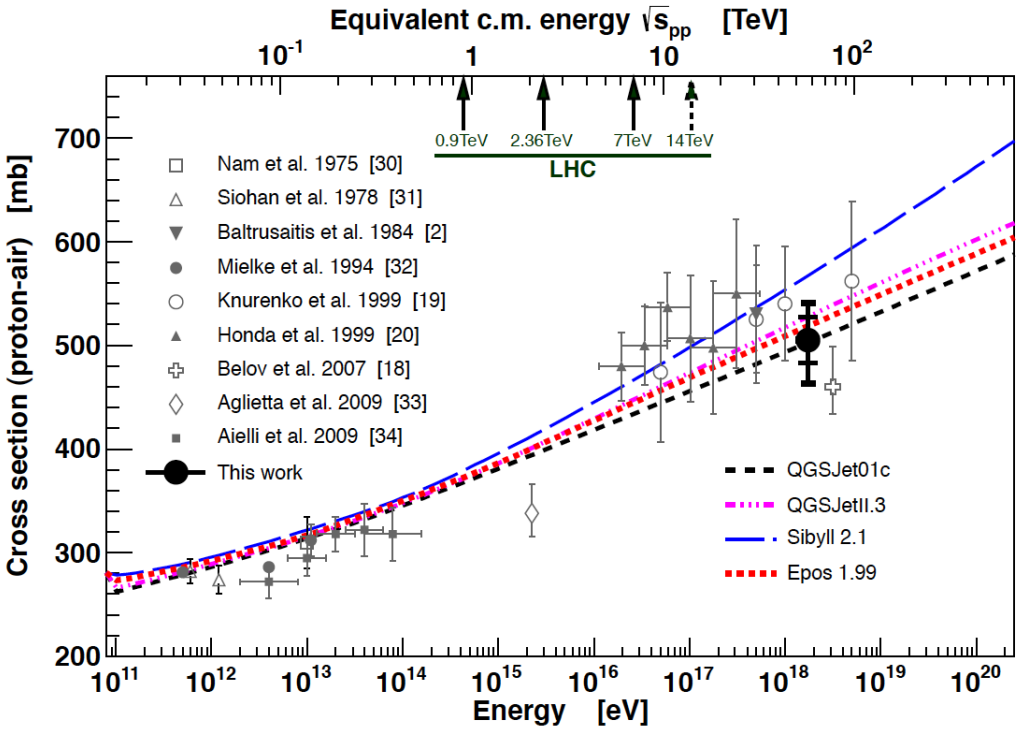

(a) proton-air cross section

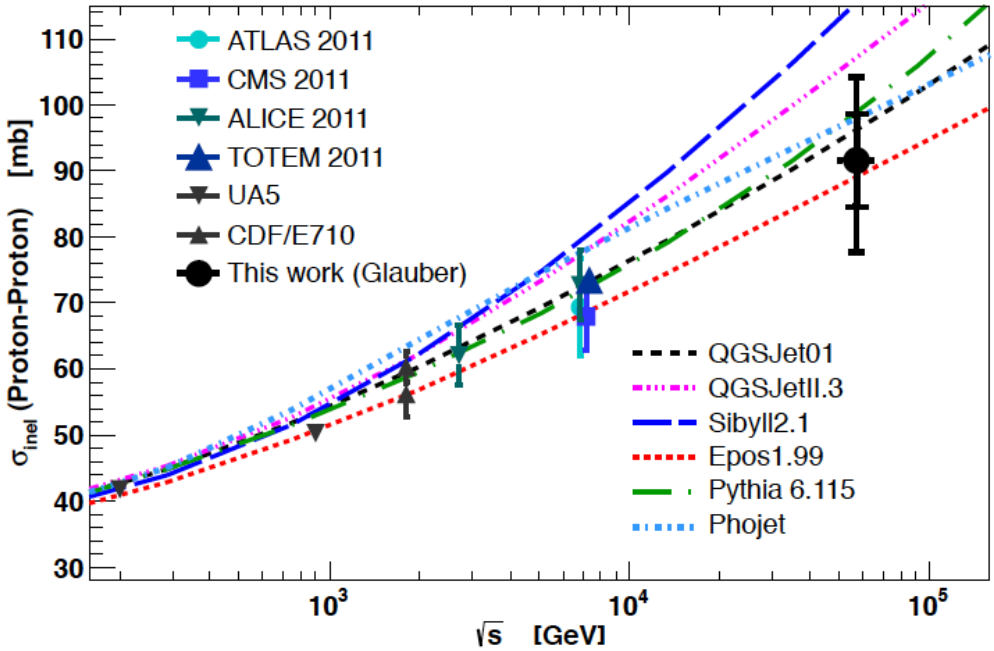

(b) proton-proton cross section

Figure 3.21: Auger $\sigma_{\mathrm{p-air}}$ and $\sigma^{\mathrm{inel}}_{\mathrm{p-p}}$ compared with different model predictions and other published results from previous experiments. The inner error bars are statistical while the outer ones include all systematic uncertainties. From (Pierre Auger Collaboration, 2012).

4. Galactic Magnetic Field

4.1 History

It was about 64 years ago that Alfven and Fermi were discussing the presence of a 10 μG magnetic field in the galaxy that confines the cosmic rays (Alfvén, 1949; Fermi, 1949). Fermi in his paper hypothesized that the cosmic rays originate in interstellar space where according to Alfven there are wandering magnetic fields. At about the same time, Hall and Hiltner observed the polarization of starlight in the magnetic field of the galaxy. Hiltner in his paper indicates that the measured polarization of the starlight should not arise in the atmosphere of the stars, but has to be related to the intervening interstellar medium (Hiltner, 1949). In the same journal, Hall confirms Hiltner's results (Hall, 1949). Later in 1951, Davis and Greenstein made the first model of interstellar magnetic field allowing the use of polarization data (Davis, Leverett & Greenstein, 1951). In 1967, Jones and Spitzer showed that a 3 μG field could explain the observed polarization (Jones & Spitzer, Lyman, 1967). Lyne and Smith were the first to use the Faraday rotation of the polarized radio emission from pulsars to measure the electron density and the magnetic field along the line of site (Lyne & Smith, 1968). Davies used the Faraday rotation of polarized extragalactic radio sources to conclude that there is a large-scale, regular magnetic field in our galaxy (Davies, 1968). Verschuur (1968) was the first to discover the Zeeman splitting in interstellar gas of neutral hydrogen (Verschuur, 1969), a relatively long time after Bolton and Wild suggested that an interstellar Zeeman effect should be observable (Bolton & Wild, 1957). A value of 2.2 μG was derived from pulsar data by Manchester in 1973 (Manchester, 1973). Mathewson and Ford in 1974 (Mathewson & Ford, 1970) and Ellis and Axon in 1978 (Ellis & Axon, 1978) produced maps of optical vectors vs. galactic coordinates (Figure 4.1). These maps showed a field structure with loops and spurs out of the plane but only within a kpc or less. Beuermann et al. (1985) studied the synchrotron emission from the galaxy and found that the magnetic field is oriented predominantly along the disk (Beuermann et al., 1985). They also observed a small scale chaotic component in addition to the regular component of the spurs and loops.

4.2 Observational Methods

Observational methods can be divided into four categories: polarization of starlight, Synchrotron emission, Faraday rotation, and Zeeman splitting. Below I explain a short description of each of these methods used historically to observe the galactic magnetic field.

4.2.1 Polarization of Starlight

Starlight polarization is due to preferential absorption by dust grains aligned with magnetic field lines. The component of the light parallel to the long axis of the dust grain will be absorbed, so the light will be linearly polarized along the direction of the field (Figure 4.2.). Observation of this polarization led to the conclusion that the local interstellar magnetic field is oriented in the plane of the galaxy. See Figure 4.1.

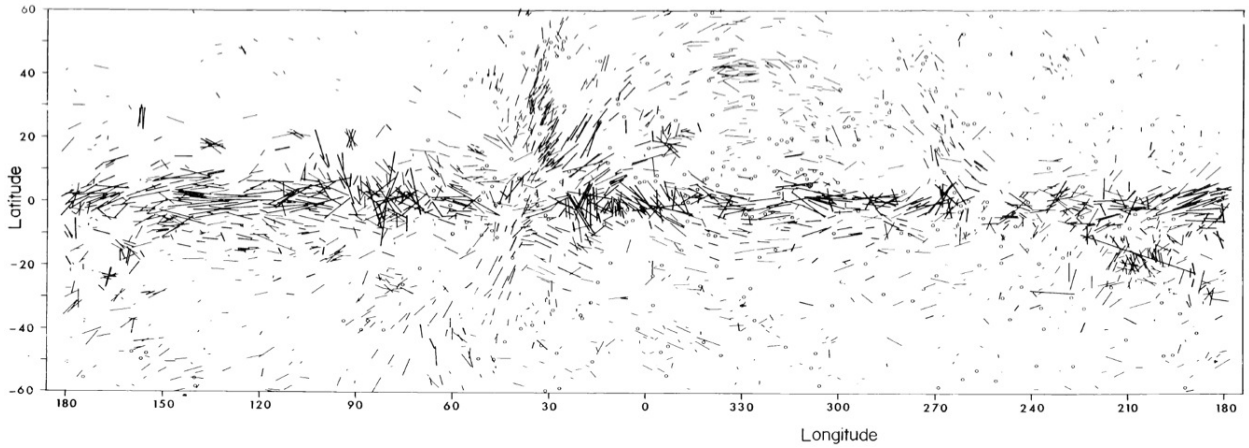

Figure 4.1: From (Mathewson & Ford, 1970). Optical polarization measurements in Galactic coordinates. The orientation of the lines represent the direction of the linearly polarized electric field vector of the starlight. The observed stars are located at the center of each line. The length of each line is proportional to the percentage polarization.

4.2.2 Synchrotron Emission

Relativistic charged particles such as electrons spiral around the magnetic field lines and radiate synchrotron radiation. This radiation is polarized in the plane perpendicular to the magnetic field. Synchrotron emission spectrum follows a power law decay with a varying spectral index depending on the type of the original radio source.

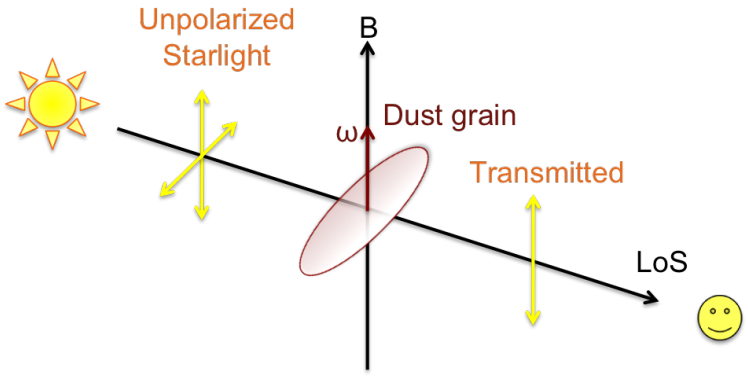

Figure 4.2: Illustration of starlight polarization.

4.2.3 Faraday Rotation

Faraday rotation of starlight polarization results from light passing through a plasma and magnetic fields. The rotation is related to the wavelength of the light by

$$\Delta\Theta = RM\ \lambda^2, \tag{4.1}$$

where RM is the rotation measure and is related to the electron density (n_e) and the line of sight component of the magnetic field ($B_{||}$) as follows,

$$RM = 0.81 \int n_e\ B_{||}\ dl\ [\text{rad m}^{-2}]. \tag{4.2}$$

In this equation, n_e is in cm^{-3}, $B_{||}$ is in μG and dl is the integration step in pc. An illustration of Faraday rotation is show

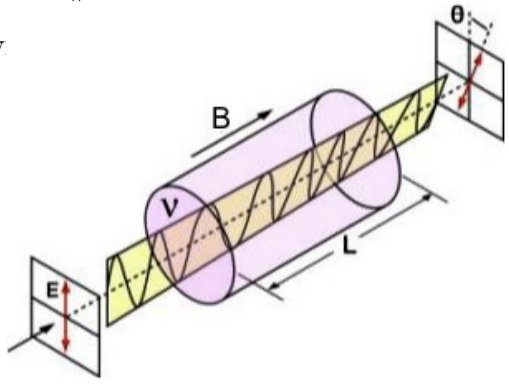

Figure 4.3: Illustration of Faraday Rotation.

Measuring the polarization rotation angles at multiple wavelengths and using data on the galactic free electron distribution make it possible to estimate the galactic magnetic field. The regions with ionized gas or plasma, such as pulsars or extragalactic radio sources, are good sources for Faraday rotation measurements.

4.2.4 Zeeman Splitting

Zeeman splitting is the splitting of atomic energy levels in the presence of a magnetic field. Even with a weak magnetic field, the 21 cm line can be split into three components. In 1959, Galt et al., determined the strength of the galactic magnetic field had an upper limit of 5 μG in clouds of neutral hydrogen toward Cassiopeia A. Since Verschuur (1969) discovered the Zeeman splitting of interstellar HI, many other observations have been taken, indicating a few μG field strength in regions with gas densities between 1 and 100 cm^{-3}. A good historical review written by Verschuur can be found in (Verschuur, 1979).

One limitation of this method is that it gives no information about the direction of the field. Measurements are difficult since it needs regions with high HI densities and small 21-cm line widths.

4.3 Models of the Magnetic Field of the Galaxy

Different models of the GMF have been proposed based on observational data. Most of these models have a few properties in common including a large scale regular component in the galaxy and the presence of a turbulent magnetic field. Most models have magnetic field lines following the spiral arms of the galaxy. However the scale and structure of the magnetic arms are not completely understood.

Common models include variants of the so-called symmetric spiral. As shown in Figure 4.4, the fields follow the spiral arms. If one observes field reversals as one travels radially outward (left side of Figure 4.4), the geometry is termed bisymmetric (BSS); if not (right side of Figure 4.4) then it is called axisymmetric (ASS). Furthermore, depending on the sym-

metry above and below the galactic disk, there is a dipole-type field labeled by "_A" which indicates antisymmetry, and a quadrupole-type field labeled by "_S" which is symmetric.

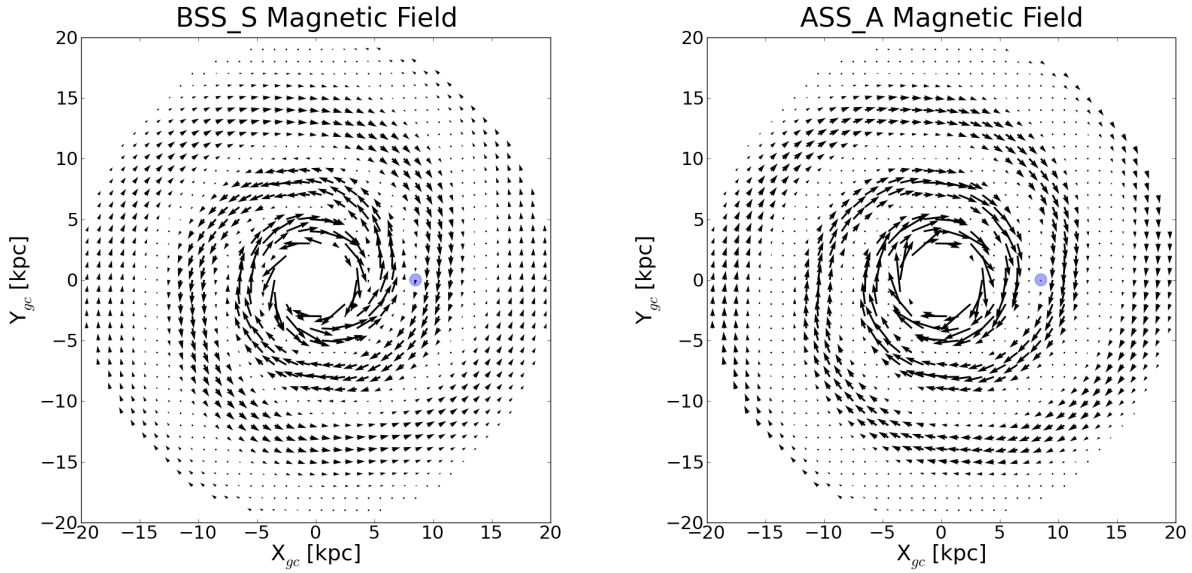

(a) (b)

Figure 4.4: Direction and Strength of the (a) BSS_S and (b) ASS_A field types in the disk of the Galaxy. The filled circle is the location of the sun.

Stanev (Stanev, 1997) built two extreme combinations of these GMF models - BSS_A and ASS_S. The BSS_A has an odd parity and field reversals, while ASS_S is without field reversals and with even parity. In his models, the solar system is at a Galactocentric distance $R = 8.5$ kpc with a field strength of $\sim 2\mu$G in direction of $\ell \approx 90°$. The GMF is taken to have a "pitch angle" $p = -10°$. Pitch angle refers to the space angle difference between the magnetic field vector and a reference direction; this direction is $\ell = 90°$ in most GMF models. In the BSS_A model there are two reversals at $\ell = 0°$ at a distance of 0.5 kpc and ~ 3 kpc. For the bisymmetric model in the Galactic plane the field strength at a point (ρ, ϕ) is

$$B(\rho, \phi) = B_0(\rho) \cos(\phi - \beta \ln(\frac{\rho}{\rho_0})), \tag{4.3}$$

where ρ_0 is the Galactocentric distance of the location with maximum field strength at $\ell = 0°$, which is equal to 10.55 kpc in this model and $\beta = \frac{1}{\tan p} = -5.67$. $B_0(\rho)$ is taken to be $\frac{3R}{\rho}$ μG

and the field extends to $\rho = 20$ kpc. The same equation is true for ASS_S model, except that only the absolute value of the cosine is acceptable.

Although there is no z component in this basic field model, the field strength in the Galactic halo is very important for cosmic ray particle trajectories. The field strength above and below the plane follow

$$|B(r,\theta,z)| = |B(r,\theta)| \exp -(\frac{|z|}{z_0}), \tag{4.4}$$

where $z_0 = 1$ kpc for $|z| < 0.5$ kpc and $z_0 = 4$ kpc for $|z| > 0.5$ kpc.

Another formalization of the symmetric spiral field models is done by Harari et al. (Harari et al., 1999), which is very similar to Stanev model with some corrections to the halo magnetic field in order to avoid spurious effects due to discontinuities in the field. A more complete GMF model is given by Sun et al. (Sun et al., 2008), which combines an ASS field with galactocentric annuli where the field reverses direction and also contains a toroidal halo component. They used the available rotation measures, linear polarization, and total synchrotron intensities. Pshirkov et al. (Pshirkov et al., 2011) favor a field consisting of symmetric spiral disk and antisymmetric halo component using rotational measures of extragalactic radio sources. A new more complete GMF model has been presented by Jansson and Farrar (Jansson & Farrar, 2012b) which includes three components: the regular, the random and a striated random component. This model has been fitted to all the available radio observations as will be discussed in more detail in the following section.

4.4 Jansson-Farrar Galactic Magnetic Field Model

The Jansson-Farrar (JF12) GMF model is more generalized compared to the previous models, in the sense that the field out of the plane has a component perpendicular to the plane and a "striated" random field component. They use the most updated WMAP7 Galactic Synchrotron Emission map and more than forty thousand extragalactic rotation measures to constrain the parameters of the GMF model. The Faraday rotation measures and polarized

synchrotron radiation are the best available constraints on the large scale GMF. The JF12 fits the observations better than all of the previous models. Below, I will describe this field model in more detail. The first part is about the large-scale regular field, the second part describes the striated random field and the third part explains the small-scale random field.

4.4.1 Large-Scale Regular Field

The large-scale regular field is modeled separately with three components: a disk, a toroidal halo, and an out-of-plane component. To let the parameters of each component be defined independently, each of the three components is divergenceless. The large-scale regular field contributes to all the observables, I, PI and RM, where I is the total synchrotron emission, PI is polarized synchrotron emission and RM is the Faraday rotation measure.

Disk Component

The disk field is defined for radius between 3 kpc and 20 kpc, in the x-y plane. In the annular region between 3 kpc and 5 kpc, the field is purely azimuthal with a field strength of $b_{\rm ring}$. There are eight spiral regions between 5 kpc and 20 kpc. The dividing lines between these regions follow the equation $r = r_{-x} \exp(\phi \tan(90 - i))$, where i is the pitch angle and equals 11.5°. r_{-x} is the value of the radius where a spiral crosses the negative x-axis (r_{-x} = 5.1, 6.3, 7.1, 8.3, 9.8, 11.4, 12.7, 15.5 kpc for the 8 arms). The field strength at each spiral arm is defined at r=5 kpc and falls off as $1/r$. The direction of the field in this region is $\hat{b} = \sin(i)\ \hat{r} + \cos(i)\ \hat{\phi}$. The strength of the 8th arm is found from the other 7 arms as $b_8 = -\sum_{i=1}^{7} f_i b_i / f_8$, where f_i is the relative cross-sectional areas of the spirals at a fixed radius. The disk component is multiplied by (1 - $L(z, h_{\rm disk}, \omega_{\rm disk})$), where

$$L(z, h, \omega) = (1 + e^{-2(|z|-h)/\omega})^{-1}, \tag{4.5}$$

$h_{\rm disk}$ is the height parameter and $\omega_{\rm disk}$ sets the width of the transition region.

Toroidal Halo Component

The JF12 halo component is toroidal (see Figure 4.5) or purely azimuthal. It is defined as

$$B_{\phi}^{tor}(r,z) = e^{-|z|/z_0} L(z, h_{\text{disk}}, \omega_{\text{disk}}) \times \begin{cases} B_n(1 - L(r, r_n, \omega_h)), \text{if } z > 0 \\ B_s(1 - L(r, r_s, \omega_h)), \text{if } z < 0 \end{cases} \tag{4.6}$$

The field amplitude and the radial extent is different in north and south. ω_h is the cut off width of the halo field.

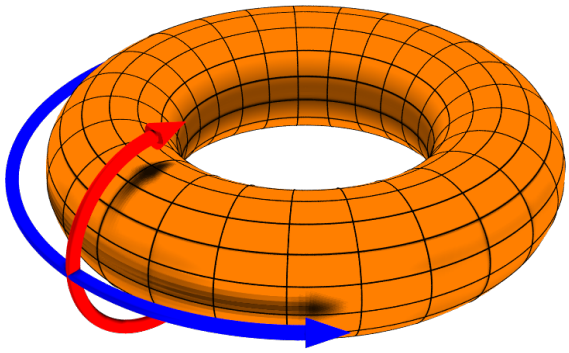

Figure 4.5: From (Burke, 2006): An image depicting the poloidal (red) and toroidal (blue) directions.

Out-of-Plane Component

An out-of-plane component has been added to the halo component in this new model. It is similar to the so-called X-shaped field structures seen in edge-on observation of some galaxies. This component is chosen to be axisymmetric and poloidal (see Figure 4.5). Figure 4.6 shows an example of X-shaped field. The field at each position (r, z) is specified in terms of r_p, the radius at which the field line passing through (r, z) crosses the plane $z = 0$.

The field outside a galactocentric radius of 5 kpc has a constant elevation angle (Θ_X^0) with respect to the mid-plane. For smaller radius, the elevation angle is linear with radius,

becoming vertical at the center. The field strength in the mid-plane is defined by

$$b_X(r_p, z = 0) = B_X \, e^{-r_p/r_X}, \tag{4.7}$$

where B_X is the amplitude of the field at $(r = 0, z = 0)$.

In the region with constant elevation angle, the field strength is $b_x(r_p)r_p/r$, with $r_p = r - |z|/\tan(\Theta_X^0)$. In the region with varying elevation angle, the field strength is $b_x(r_p)(r_p/r)^2$, with $r_p = r\ r_X^c/(r_X^c + |z|/\tan(\Theta_X^0))$ and $\Theta_X(r, z) = \tan^{-1}(|z|/(r - r_p))$. Altogether the out-of-plane component has four free parameters: B_X, Θ_X^0, r_X^c and r_X.

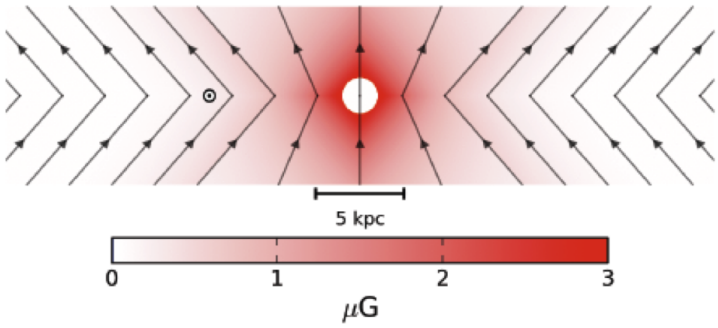

Figure 4.6: From (Jansson & Farrar, 2012a): An x-z slice of the galaxy showing only the out-of-plane component. This component is also called the X-shaped field component.

4.4.2 Striated Random Field

In the JF12 GMF model, a new component of the random field, termed "striated", has been added to the regular component based on theoretical considerations. The general orientation of this field is aligned along a particular axis over a large scale but its strength and specific orientation varies over small scales. It is possible that striated fields can be produced by levitation of bubbles of hot plasma carrying trapped randomly oriented fields away from the disk, or by differential rotation of small scale random fields, or both (Jansson & Farrar, 2012a). The strength of this striated component is proportional to the regular field strength with a factor ($\beta = 1.38 \pm 0.41$) as $B_{\rm stri}^2 = \beta B_{\rm reg}^2$ (Jansson & Farrar, 2012a).

The striated component is always aligned along the regular field vector, but may be parallel or anti-parallel.

The striated random field is used only for a brief portion of my study in Section 6.2. A specific implementation of the striated field in the *CRT* propagation code (version 3.0) follows. A cubic grid of size 100 pc is embedded within the Galaxy. Since the Galaxy is considered to be a sphere with a radius of 20 kpc, there will be approximately 64 million small cubes. A (+1) or a (-1) is randomly assigned to each cube to define the orientation of striated field vector relative to the orientation of the regular field vector. The magnetic field strength at each point in the Galaxy will then be scaled with $1 \pm \sqrt{\beta}$ where $\pm$ depends on the assigned sign of the current cube. As there are still large uncertainties in the properties of striated fields in the Galaxy, this model is used in combination with the regular and small scale random components only in Section 6.2. I do not include it in the GMF model used for propagation of cosmic rays in most parts of this dissertation.

4.4.3 Galactic Random Field

In this dissertation, I use two methods to generate the Galactic random field (GRF). One method was initially used for forward-tracking the UHECRs from Cen A. In this method, random spherical cells are assigned everywhere in the Galaxy with Gaussian random fields. The other method is mainly used in the back-tracking of UHECRs and is a grid method with the field following a Kolmogorov spectrum. The forward-tracking and back-tracking results using both random field methods will be fully described in Chapters 6 and 7.

In the following section, the first method that was initially coded in *CRT* will be described. The second method will be discussed in a separate Chapter (5) to fully explain the model I have made and all the tests done showing its truth.

GRF: The first method

Here I describe how the *CRT* code (version 3.0) was initially generating random magnetic field based on the JF12 model. In this code the volume of the Galaxy is taken to be a cube

of sides 40 kpc centered on the Galactic Center (GC). This cube is sub-divided into 64000 blocks, each with a side 1 kpc. Unique spherical magnetic cells are randomly distributed among and within these blocks. The user is capable of defining the number of desired cells to be generated inside the whole Galaxy. This division allows for simple and easy tracking of the independent magnetic cells in the *CRT* framework.

The size of each cell instance is sampled from a Gaussian distribution described by a mean of 0.06 kpc and a width of $\sigma = 0.025$ kpc. Cells positions are distributed randomly and uniformly throughout a 20 kpc spherical volume centered on the GC.

The magnitude of the random magnetic field within a cell instance is determined from separate disk ($B'_{\rm disk}$) and halo ($B'_{\rm halo}$) components. The total magnitude is found by $\sqrt{B'^2_{\rm disk} + B'^2_{\rm halo}}$. $B'_{\rm disk}$ and $B'_{\rm halo}$ are assigned values sampled from Gaussian distributions with mean zero. For the random halo component, the rms value (σ) is $B_0 \exp(-\frac{r}{r_0}) \times \exp(-0.5\,(\frac{z}{z_0})^2)$ where r and z are the galactocentric distance and height above the Galactic plane respectively. Also r_0 and z_0 are the exponential scale length and Gaussian scale height respectively. The values of the best-fit parameters of the random field with 1σ intervals can be found in Table 1 of (Jansson & Farrar, 2012b). For the random disk component, the base rms value is dependent on the cell position since different values are associated with the structures of the regular disk component. For $r < 5$ kpc (within the molecular ring), a base rms value of $b_{\rm int}$=7.691 is used. For $r > 5$ kpc (within the spiral arms), different base rms values are associated for each of the 8 arms. The base rms value is then multiplied by $\frac{5}{r} \exp(-\frac{1}{2}\,(\frac{z}{z_0^{\rm disk}})^2)$ to determine the rms value for the Gaussian distribution.

The calculation of the random magnetic field vector involves iteration over a list of individual cell field vectors. During the generation of the random field instance, for each block *CRT* determines and assigns a list of unique cells contained within that block. The instantaneous position of the particle maps to a specific 1 kpc^3 block and list of magnetic cells. During each tracking step *CRT* loops over only those cells to determine which cells contribute to the total field vector at the particle position resulting in significant time savings.

4.5 Comparing Galactic Magnetic Field Models

The JF12 GMF model is the newest and the most complete GMF model so far. But before that, there were other carefully studied proposed GMF models. I did an analysis to compare the effects of these different GMF models on UHECRs, by looking at the sky maps of deflected cosmic rays and the energy spectrum in each model.

Here I study five variations: ASS_A, ASS_S, BSS_A, BSS_S and another one combining an ASS field with galactocentric annuli where the field reverses direction, called ARING. I have used the specific models of Stanev (Stanev, 1997), as described in (Harari et al., 1999) and (Sun et al., 2008).

I start by simulating 10^4 events from each of the locations of AGN in the VCV catalog with redshift $z \leq 0.018$. Separate cases of protons and iron nuclei are considered. Particle energies are sampled from an energy spectrum following $\frac{dN}{dE} \propto E^{-\gamma}$ between 55 and 150 EeV with $\gamma = 2$. The particles are propagated without accounting for energy loss through each of the five GMF models described above using the *CRT* code.

In this analysis I took the following values for the parameters of the GMF. The magnitude of the field vector in the solar local vicinity has been taken to be 2 μG. The field has a pitch angle of -10°. The galactocentric distance of the location of maximum field strength along the line connecting the Sun and the galactic center is to be 10.55 kpc. Along the z direction there are two attenuation decay lengths and a transition point where one changes to the other. In this study the first scale length has been taken to be 1 kpc, the second is 4 kpc with the transition located 1 kpc from the plane.

4.5.1 Anisotropy

Forward-tracking the simulated particles through the GMF models, I get a new distribution of particles in the sky. Figure 4.7 shows the sky map of the observed directions of the particles after propagation in BSS_S GMF model and the locations of the AGN. In Figure 4.8, each of the observed particles has been connected to its original source with a blue line.

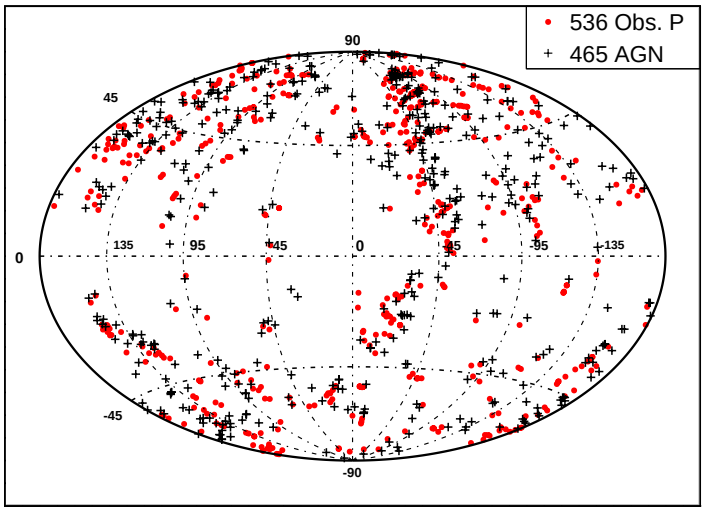

(a) Proton

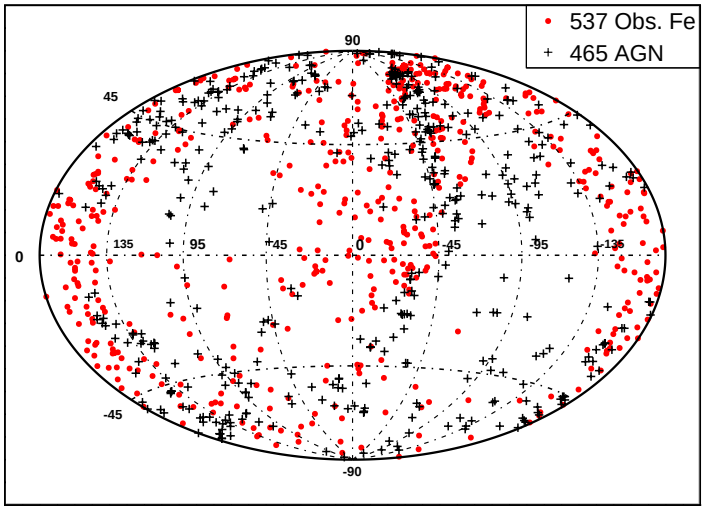

(b) Iron

Figure 4.7: Sky map of the observed (a) protons and (b) iron nuclei deflected in the BSS_S GMF model, shown in Galactic coordinates. The black plus signs (+) indicate the locations of the AGN and the red circles are the observed events.

I compare the propagation results with other GMF models, as shown in the Figures 4.9 - 4.12. These figures show that regardless of the model I use, the deflections are large enough to influence the source identification, so it is necessary to account for these deflections.

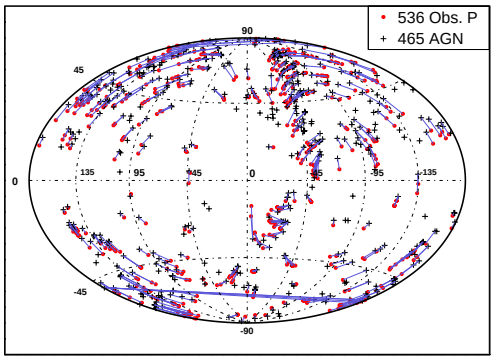

(a) Proton

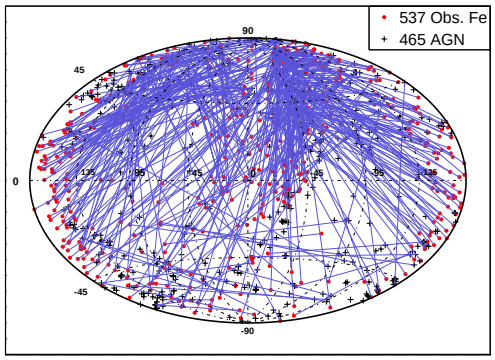

(b) Iron

Figure 4.8: Same plot as in Figure 4.7. The blue lines connect each particle to its original injected position.

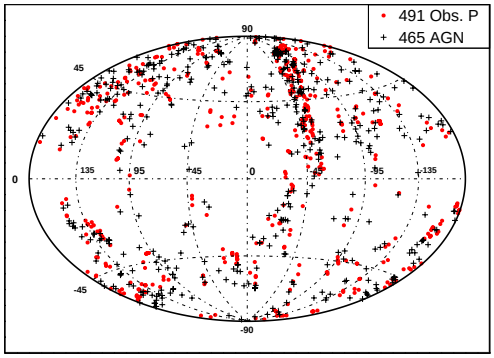

(a) Proton

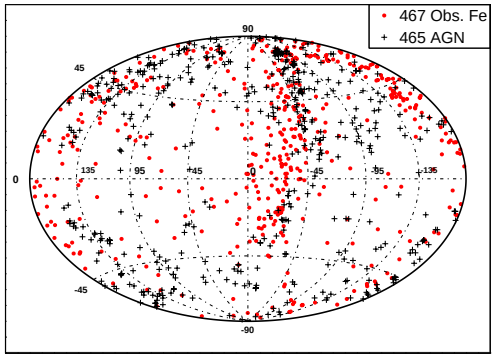

(b) Iron

Figure 4.9: Same plot as in Figure 4.7 for BSS_A GMF model.

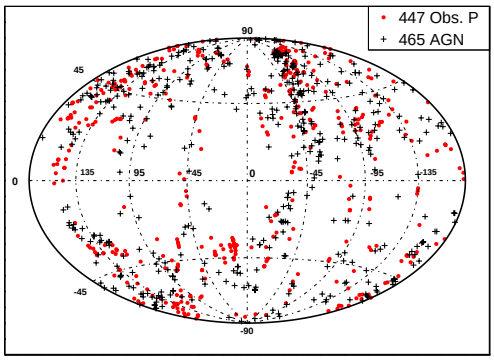

(a) Proton

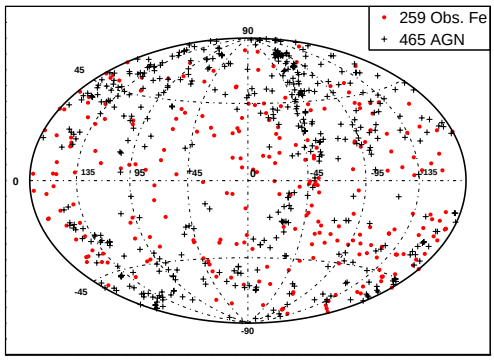

(b) Iron

Figure 4.10: Same plot as in Figure 4.7 for ASS_S GMF model.

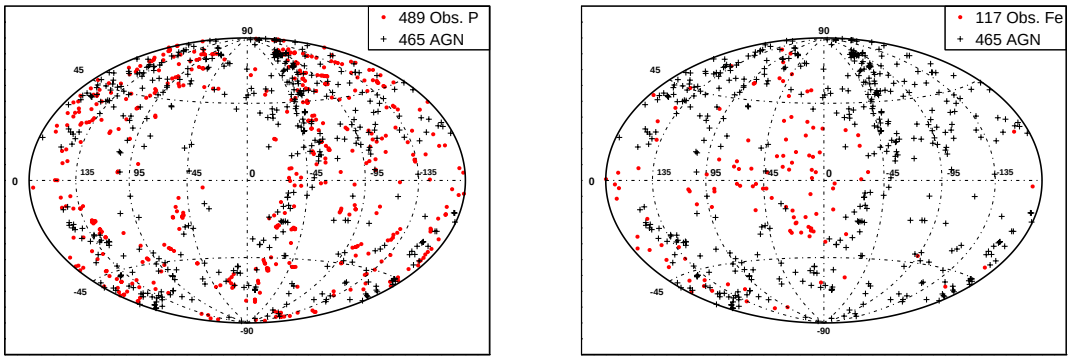

(a) Proton (b) Iron

Figure 4.11: Same plot as in Figure 4.7 for ASS_A GMF model.

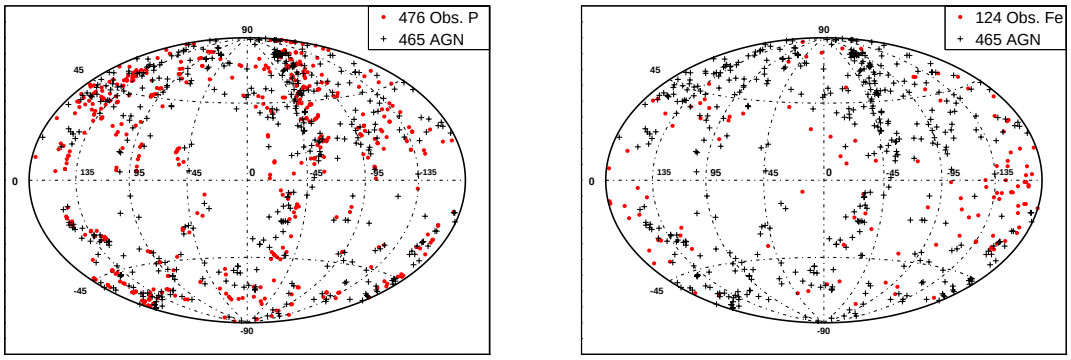

(a) Proton (b) Iron

Figure 4.12: Same plot as in Figure 4.7 for ARING GMF model.

On the other hand, the deflection patterns show the results are strongly model dependent, emphasizing the importance of a better understanding of the GMF and using the model that best fits the observational data.

Table 4.1 summarizes the results of propagating the particles in different GMF models. The first and second columns show the GMF model and cosmic ray primary type. Columns 3 and 4 are the total number of observed events at Earth (N_1) and the average deflection angles between the source position and arrival direction (Δ). Column 5 gives the average value of the *smallest* separation angle between events and all of the AGN (Θ). The quantity N_2 in the sixth column denotes the number of events with $\Theta < 3.1°$. These are defined to be *correlating* events, and the last column shows the fraction of these (f) with respect to the

total observed number N_1. The statistical errors on N_1 and N_2 are considered to calculate the error on f shown in the last column. An isotropic distribution of arrival directions would have correlation fraction of $\sim 23\%$. In all cases the ratio of protons correlating is well above isotropy, while it is much less so for iron.

The same study has been done for the portion of sky seen by Pierre Auger Observatory. Figure 4.13 shows the sky map of the observed particles deflected in the BSS_S field model only for Auger exposure.

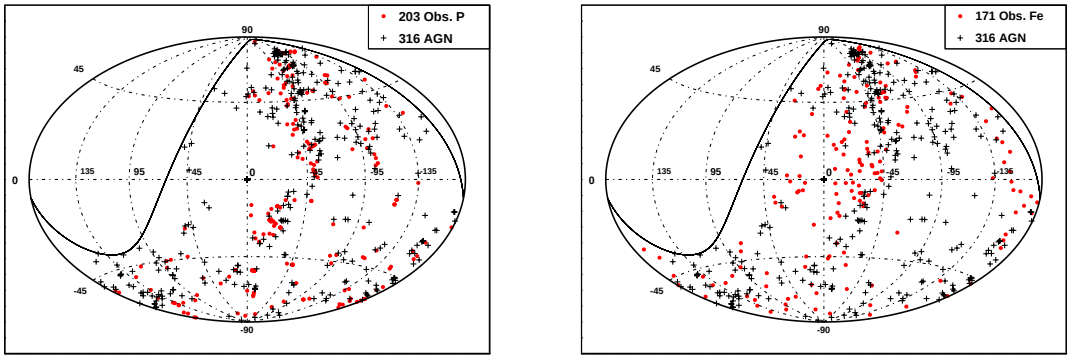

(a) Proton (b) Iron

Figure 4.13: Auger exposure: sky map of the observed (a) protons and (b) iron nuclei deflected in the BSS_S GMF model, shown in Galactic coordinates. The black plus signs (+) indicate the locations of the AGN and the red circles are the observed events.

The results for Auger sky is shown in Table 4.2. The results of the last columns of Table 4.1 and Table 4.2 are compared in Table 4.3 and it does not show a significant difference in the correlation fractions.

Since the results of this study indicate that understanding magnetic field is crucial for UHECR source identification, there is the need of using the best available model in addition to improve the current GMF models.

4.5.2 Observed Energy Spectrum

Since magnetic fields more strongly deflect lower energy particles, the observed energy spectrum may be altered with respect to the source spectrum. Figure 4.14(a) shows the observed spectrum for protons in the BSS_S GMF model compared to the input spectrum with spec-

Table 4.1: Results of propagating UHECRs in different GMF models for the whole sky.

GMF	Particles	N_1	Δ	Θ	N_2	f (%)
BSS_S	Proton	536	6.6°	3.3°	282	53 ±4
BSS_S	Iron	537	64.4°	6.2°	160	30 ±3
BSS_A	Proton	491	7.6°	3.4°	260	53 ±4
BSS_A	Iron	467	49.5°	5.8°	151	32 ±3
ASS_S	Proton	447	9.9°	4.5°	198	44 ±4
ASS_S	Iron	259	85.6°	7.0°	57	22 ±3
ASS_A	Proton	489	9.0°	4.6°	175	36 ±3
ASS_A	Iron	117	75.3°	10.2°	19	16 ±4
ARING	Proton	476	5.8°	3.5°	255	54 ±4
ARING	Iron	124	84.4°	6.9°	31	25 ±5

Table 4.2: Results of propagating UHECRs in different GMF models for Auger sky.

GMF	Particles	N_3	Δ	Θ	N_4	f' (%)
BSS_S	Proton	203	6.6°	3.4°	103	51 ±6
BSS_S	Iron	171	70.1°	7.3°	50	29 ±5
BSS_A	Proton	181	8.7°	3.6°	93	51 ±6
BSS_A	Iron	171	51.5°	6.2°	55	32 ±5
ASS_S	Proton	156	11.1°	4.9°	63	40 ±6
ASS_S	Iron	113	85.8°	6.7°	22	19 ±4
ASS_A	Proton	175	8.8°	4.7°	57	33 ±5
ASS_A	Iron	38	69.8°	12°	4	10 ±5
ARING	Proton	163	6.2°	3.6°	85	52 ±7
ARING	Iron	42	85.4°	6.3°	9	22 ±8

Table 4.3: Comparing the results for the whole sky with Auger sky.

GMF	Particles	f (%)	f' (%)
BSS_S	Proton	53 ±4	51 ±6
BSS_S	Iron	30 ±3	29 ±5
BSS_A	Proton	53 ±4	51 ±6
BSS_A	Iron	32 ±3	32 ±5
ASS_S	Proton	44 ±4	40 ±6
ASS_S	Iron	22 ±3	19 ±4
ASS_A	Proton	36 ±3	33 ±5
ASS_A	Iron	16 ±4	10 ±5
ARING	Proton	54 ±4	52 ±7
ARING	Iron	25 ±5	22 ±8

tral index of $\gamma = 2.0$. The observed spectrum is fitted, giving a value of $\gamma_{fit} = 2.24 \pm 0.15$. So, with $\Delta\gamma = 0.24 \pm 0.15$ the observed proton energy spectrum is slightly steeper (softer) than the initial spectrum. On the other hand, Figure 4.14(b) shows the observed energy spectrum for iron nuclei with $\Delta\gamma = -0.34 \pm 0.15$, which means a slightly flatter (harder) energy spectrum. The spectral indices do not appear to have changed significantly.

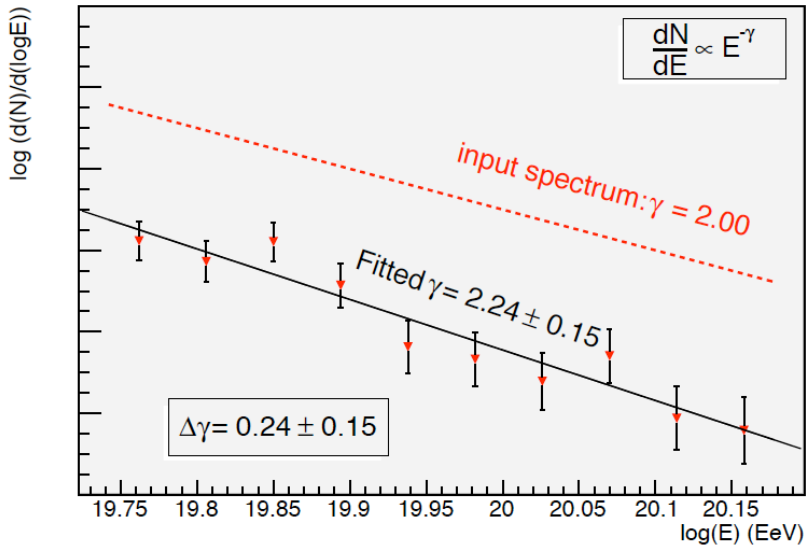

(a) Proton

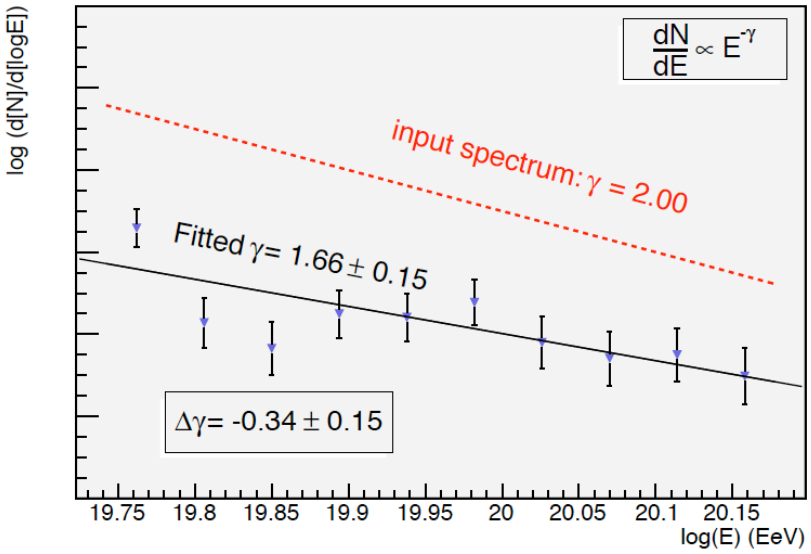

(b) Iron

Figure 4.14: Observed energy spectrum for (a) proton and (b) iron nuclei in the BSS_S GMF model. The dashed line indicates the input spectrum with an spectral index of 2. the solid line is a fit to the simulated data. The y-axis has an arbitrary scale.

For the other GMF models the observed energy spectrum is consistent with the BSS_S case, steeper for proton and flatter for iron nuclei. Considering only the first six bins ($E < 10^{20}$ eV), no significant difference in γ_{fit} is observed for the lower energies with the present statistics. If I apply the same method only for the events correlating with an AGN, the same general behavior is observed, which is a steeper observed energy spectrum for protons and a flatter one for iron nuclei.

5. Kolmogorov Random Field

5.1 Introduction

In this chapter, I will describe how I implement the random field in JF12 Galactic magnetic field (GMF) model. There are different methods to model random fields in the Galaxy. The general structure of JF12 random field component has been described in Chapter 4. Also, one primary method to generate random fields was discussed in Section 4.4.3. Here I use the Kolmogorov spectrum to make a more realistic random field model. The created magnetic field will be scaled with the JF12 random field parameters at the end.

First I will introduce the Kolmogorov turbulence and the general characteristics of a Kolmogorov spectrum in Section 5.2. Then I will explain modeling the Kolmogorov random field in Section 5.3. And finally I show the results of testing this model in Section 5.4.

5.2 Kolmogorov Turbulence

The *Kolmogorov scaling law* describes turbulence in fluids (Kolmogorov, 1941, 1991). A stable (or at least persistent) turbulent fluid in three dimensions is seen as a collection of little swirling vortices or "eddies" of various sizes. This complex, swirling motion also can be described as a superposition of waves of many different wavelengths λ or wavenumbers $k = 2\pi/\lambda$.

Consider only the group of waves that have wavenumbers in a small range $k \rightarrow k + dk$. The Kolmogorov law says that the energy contained in this group is proportional to $k^{-5/3}$. Kolmogorov obtained this relation using dimensional arguments. There still is no rigorous derivation of it. Nevertheless it is confirmed by experiment (Moisy et al., 1999), as long as k is neither too big nor too small. Why those limits? The size of an eddy (the contributing wavelengths) can't be larger than the overall size of the fluid. Eddies also break up into smaller eddies, but at some critically small size an eddy dissipates, giving up its energy as heat; eddies smaller than this won't be seen.

To get a picture of the physical process that Kolmogorov imagined, first visualize a collection of spinning eddies. Each one has some kinetic energy. Kolmogorov assumed that larger eddies break up into several smaller ones. This means that energy is exchanged between the eddies but only in one direction: larger eddies give their energy to smaller ones, but no energy is transferred the other way.

If there is no external input of energy into the system, the fluid will eventually become a large number of very small eddies. When their sizes are reduced to the critical limit, they will cease exchanging energy and instead dissipate it (in the form of heat) because of viscous forces.

Without external energy input, the turbulence of the fluid will then die out. So a "stable" but turbulent fluid needs energy input. In such a fluid, the rate ϵ at which energy is injected (in Joules/sec) should equal the rate at which it is viscously dissipated by the smallest eddies.

Let the magnitude of velocity at any spatial location $\vec{x}$ in a fluid be described by a field $u(\vec{x})$. One could describe the field as a (Fourier) superposition of waves:

$$u(\vec{x}) = \int_0^\infty A_k \mathrm{e}^{-i\vec{k}\cdot\vec{x}}\, \mathrm{d}^3k, \tag{5.1}$$

where A_k is the amplitude of a wave with wavenumber k. Having an eddy with characteristic size r, the waves that construct it are dominated by those with wavelength $\lambda \sim r$, so waves and eddy sizes can be associated by $k = 2\pi/r$.

Divide up our fluid into groups of similarly-sized eddies. The larger ones will transfer their energy to the next smaller sized group. The rate that this happens (J/s) should be the same as ϵ, to match either the overall energy input rate or dissipation loss rate.

Suppose an eddy with size r (maybe the radius or circumference) has a characteristic speed v as it spins. I would like to estimate how long it takes to lose its kinetic energy. That time is probably similar or proportional to the time for a rotation, $\tau \sim r/v = 2\pi/kv$. Since the energy (per unit mass) of an eddy is $\sim v^2$, the energy loss rate for a group of eddies with

this size and speed is

$$\epsilon \sim \frac{v^2}{\tau} \sim \frac{v^2}{1/kv} \sim kv^3, \tag{5.2}$$

where ϵ is a constant, the overall energy input rate.

Let the total kinetic energy carried by the group of waves with $k \rightarrow k + dk$ be written as $E(k)\ dk$. Note that $E(k)$ is a kind of "density" with units of (energy)/(wavenumber) $\sim v^2/k$. So use the expression for ϵ in Equation 5.2 to get

$$E(k)dk \sim \frac{v^2}{k}dk \sim \frac{(\epsilon/k)^{2/3}}{k}dk \sim \epsilon^{2/3}k^{-5/3}dk. \tag{5.3}$$

This is the famous Kolmogorov result.

Returning to Equation 5.1 above, the question is how the energy is distributed among the individual waves? If the turbulence is isotropic, then for any particular value of k, there will be many different waves, each with the same amplitude A_k, but pointing in different directions (k_x, k_y, k_z). The number of distinct waves with $k \rightarrow k + dk$ is proportional to a volume in k-space: $4\pi k^2 dk$. The energy contained in this *group* is given by Equation 5.3, so the mean energy of an individual wave is

$$\langle A_k^2 \rangle \sim \frac{\epsilon^{2/3}k^{-5/3}dk}{4\pi k^2 dk} \sim k^{-11/3},$$

where the general fact that the energy of a wave is proportional to the square of its amplitude has been used.

5.3 Kolmogorov Random Field Model

Here I use a Kolmogorov spectrum to model the random field component of the Galactic magnetic field (GMF). A Kolmogorov spectrum is $\propto k^{-5/3}$, where k is the modulus of wave vector as in Equation 5.3. The power spectrum of a random field with a Kolmogorov

spectrum is proportional to $k^{-5/3}$ and the amplitude of its Fourier modes is, as shown earlier,

$$\langle \mathbf{B}(\mathbf{k})^2 \rangle \propto |\mathbf{k}|^{-11/3}. \tag{5.4}$$

I model the random field by considering a three dimensional grid of N points per side in real space. The basic idea in generating the random magnetic field is to superpose a finite number of plane waves with different wavevectors. I first precompute the field in Fourier space (k space) and then to speed up the calculations, I use the Fast Fourier Transform (FFT) to compute the resulting field in real space.

Here the wavevector components in the Fourier space are called (k_1, k_2, k_3) and is given at each grid point (m, n, p) as

$$k_1(m, n, p) = \frac{m\ k_{\max}}{N/2}, \tag{5.5}$$

$$k_2(m, n, p) = \frac{n\ k_{\max}}{N/2}, \tag{5.6}$$

$$k_3(m, n, p) = \frac{p\ k_{\max}}{N/2}, \tag{5.7}$$

where $k_{\max}$ is the largest wavevector modulus. The wave vector moduli in Fourier space, $|\mathbf{k}|=\sqrt{k_1^2 + k_2^2 + k_3^2}$, should satisfy $k_{\min} \leq |\mathbf{k}| \leq k_{\max}$, where

$$k_{\min} = 2\pi/\lambda_{\max}, \tag{5.8}$$

$$k_{\max} = 2\pi/\lambda_{\min}, \tag{5.9}$$

in which $\lambda_{\min}$ and $\lambda_{\max}$ are the extrema in scales of variation present in the field therefore only $|\mathbf{k}|$ values that satisfy the above limits would be used for the field calculation.

The relation 5.4 can be written as an equation using a scaling factor β at each point in the Fourier space as follows:

$$\sigma^2_{m,n,p} = |\mathbf{B}(m,n,p)|^2 = \beta|\mathbf{k}(m,n,p)|^{-11/3} = \beta(k_1^2(m,n,p) + k_2^2(m,n,p) + k_3^2(m,n,p))^{-11/6}. \tag{5.10}$$

Here, I assume β is equal to one, since I later will scale the magnetic field strength with the JF12 GMF model at each point in the Galaxy. I draw random numbers from a Gaussian distribution with mean zero and variance $\sigma^2_{m,n,p}$. The average of squared value of the generated random numbers, $\langle|\mathbf{B}|^2\rangle$, is then equal to the variance, $\sigma^2_{m,n,p}$. This way I have picked the norm of the random magnetic field at each point in Fourier space, such that its mean value follows the Kolmogorov spectrum.

Since the magnetic field should be divergence free at each point in the real space ($\nabla\cdot\mathbf{B} = 0$ in real space), it implies that $\mathbf{B}(\mathbf{k}) \cdot \mathbf{k} = 0$ in the Fourier space. Together with the norm of the magnetic field I generated above, I will have the following two equations:

$$B_1^2 + B_2^2 + B_3^2 = |\mathbf{B}|^2 = B^2, \tag{5.11}$$

$$B_1k_1 + B_2k_2 + B_3k_3 = 0. \tag{5.12}$$

There are three unknowns in the above two equations, so I need to define one of them randomly. B_1 and B_2 in terms of B_3 can be written as

$$B_1 = \frac{-B_2k_2 - B_3k_3}{k_1}, \tag{5.13}$$

$$B_2 = \frac{-B_3k_2k_3 \pm k_1\sqrt{B^2(k_1^2+k_2^2) - B_3^2(k_1^2+k_2^2+k_3^2)}}{k_1^2+k_2^2}. \tag{5.14}$$

To make the term under the square root to be larger than or equal to 0 in Equation 5.14, I choose B_3 randomly in the following range

$$-\sqrt{\frac{B^2(k_1^2+k_2^2)}{k_1^2+k_2^2+k_3^2}} \leq B_3 \leq \sqrt{\frac{B^2(k_1^2+k_2^2)}{k_1^2+k_2^2+k_3^2}}. \tag{5.15}$$

One could instead randomly choose B_1 or B_2 and then find the other two unknowns. In order to make everything completely random, I pick one of the six possible permutations of choosing B_1, B_2, or B_3 in a random order for each grid point.

Now that I have found the three components of magnetic field in the Fourier space, I perform an inverse Fast Fourier Transform (FFT) using the FFTW package (Frigo & Johnson, 2005) to find the field in real space. The FFT integrates from 0 to 2π: 0 to π is corresponding to the positive values of k and π to 2π is related to negative k. I am only interested in producing real random fields, so I should symmetrize our magnetic field function in the Fourier space therefore I only calculate the field for (0, π) or in other words $(0, N/2)$ and set the field in the other half $(N/2, N)$ equal to the equivalent values in the first half. This means in three dimensions, I construct 1/8th of the cube and set the rest equal to its corresponding values. This way, performing FFT on the magnetic field function would give us the real magnetic field components in the real space. At the end, before printing out the field components, I normalize them by the calculated $B_{\rm rms}$ of all the grid points in order to make $B_{\rm rms}$=1 in the cube. The values of B_x, B_y, and B_z are saved into a file that can be used in the next step during the propagation of cosmic rays.

The next step is to fill the Galaxy with this constructed cube of size L. The method I follow here is to fill the whole Galaxy with the same repeating cube but with a different orientation. There are 6 ways to orient a cube, so I again randomly assign integer numbers from 1 to 6 to each cube and rotate that accordingly in order to have a complete isotropic field in the real space. Other suggested methods are as follows: (1) repeat the cube without orientation through the Galaxy, (2) fill the Galaxy isotropically with j different random

cubes instead of one repeating cube, (3) generate cubes with different sizes relative to their positions in the Galaxy, for example the size of the cube could increase exponentially based on its distance from the plane of the Galaxy. However, each of these methods have their own difficulties that would make using them inefficient in this work. The first method does not orient the cube throughout the Galaxy, so the field might not be completely isotropic in the Galaxy. The second and third proposed methods require huge computer memory since one needs to keep the information of all different realizations assigned to each cube (A single cube with 512 points on each side and length of 5.12 kpc, requires about 4 GB of memory).

I have coded and implemented the described method in *CRT*. The user can choose values for the cube size (L_x, L_y, L_z), the number of grid points (N_1, N_2, N_3), the minimum and the maximum wavelengths ($\lambda_{\rm min}$, $\lambda_{\rm max}$), and two filenames. These files contain the vector (B_x, B_y, B_z) at each grid point in the cube and the random numbers assigned to the cube for orientation purpose. This way the full random field realization in the Galaxy is saved and one can use it for different purposes, such as tracking multiple particles in the same field in different simulations.

Choosing the right values for generating a random field is an important part of the study and mainly depends on the cosmic rays energy range I am interested in and also the coherence length of the astrophysical phenomena occurring in the Galaxy. In general, $\lambda_{\rm min}$ corresponds to the damping scale of the turbulent field that could be as low as an astronomical unit (Giacinti et al., 2012). Also $\lambda_{\rm min}$ should be smaller than the Larmor radius of a cosmic ray particle to avoid losing important wavemodes around the Larmor size. The Larmor radius of a proton with energy of 1 EeV in a 1 μG field is 1 kpc, where an iron nucleus with the same energy would have a radius of curvature of about 38 pc. In practice, one can neglect the modes with spatial scales much smaller than the Larmor radius, since the trajectory of the cosmic rays in the random field are less sensitive to them. But to be on the safe side, $\lambda_{\rm min}$ will still be sufficiently small compared to the Larmor radius of cosmic rays in this study (for $E > 1$ EeV). In addition, it should be noticed that $\lambda_{\rm min}$ is comparable to the size of

grid spcaing (L/N). Overall, the precise value of $\lambda_{\min}$ will not noticeably affect the results since less magnetic energy is concentrated in the modes with small λ (large wave numbers) compared to large λ.

The maximum wavelength should be of the order of the spatial turbulent scale lengths that are found in the Galaxy. The random fields in the Galaxy are usually due to different phenomena including supernova explosions and other outflows that result in scale lengths of about 100 pc (Gaensler & Johnston, 1995; Haverkorn et al., 2008; Jansson & Farrar, 2012b). One good choice for $\lambda_{\max}$ would then be 100 pc. The correlation length L_c of the field with Kolmogorov spectrum defined in (Harari et al., 2002) is

$$L_c = \frac{L_{\max}}{5} \frac{1 - (L_{\min}/L_{\max})^{5/3}}{1 - (L_{\min}/L_{\max})^{2/3}}, \tag{5.16}$$

therefore a value of 100 pc for $\lambda_{\max}$ corresponds to a coherence length of about 25 pc for our random field.

To choose the cube size and the number of grid points, I consider two points. First I do not want a small cube to repeat several times in the Galaxy and to minimize the effect of the randomness. Second I cannot computationally afford having a cube of the Galaxy size with reasonable grid spacings. I tried different sets of (N, L) values and found that $(N = 512, L = 5.12$ kpc) is a reasonable choice. With these values the grid spacing would be 10 pc, which is also a reasonable size based on the discussions on $\lambda_{\min}$ and Larmor radius of cosmic rays. Also modes with the largest spatial variations of $\approx \lambda_{\max}$ should have only a few oscillations in the cube (Giacinti et al., 2012). So $\lambda_{\max} = 100$ pc is a reasonable value relative to the cube size.

5.4 Model Test

To test my model, I pick different values for $N = (N_1, N_2, N_3)$, $L = (L_x, L_y, L_z)$, $\lambda_{\min}$, and $\lambda_{\max}$ as shown in Table 5.1. Overall nine different realizations will be tested. I first plot the histograms of B_x, B_y, B_z, and $|\mathbf{B}|$ for the grid points in the cube for each case to verify if

they have similar distributions up to statistical fluctuations. Notice that the magnetic field values in the cube are not scaled with the JF12 parameters as this is done during actual propagation. I expect that the general behavior should be independent of N, L, $\lambda_{\rm min}$, and $\lambda_{\rm max}$.

As an example, Figure 5.1 shows two plots of histograms of B_x, B_y, B_z with different $\lambda_{\rm max}$ values, where N, L, and $\lambda_{\rm min}$ are constant (realizations 1 and 2). To check if the two plots of this figure have similar distributions, I calculate the differences in each bin separately for B_x, B_y, and B_z distributions as shown in Figure 5.2. The differences are divided by the total count number of data points to normalize the histogram. I see that the normalized differences are very small and at most of the order of 1%. Similar tests are performed for other values of N and L as in Figures 5.3 and 5.4 comparing realizations 3, 4, and 5, and Figures 5.5 and 5.6 comparing realizations 6, 7, and 9.

I can also change the value of $\lambda_{\rm min}$ and keep the N, L, and $\lambda_{\rm max}$ fixed. The B_x, B_y, and B_z distributions are shown in Figure 5.7 for realizations 7 and 8. The normalized differences versus the $\mathbf{B}$ components are shown in Figure 5.8. I conclude that the strengths of the field components in the cube have symmetric and isotropic distributions which were expected for a random field.

The histogram of the norm of the magnetic field ($|\mathbf{B}| = \sqrt{B_x^2 + B_y^2 + B_z^2}$) for every point in the cube is plotted in Figure 5.9 comparing realizations 2, 4, and 7. Three cases that are plotted have different N and L values but same $\lambda_{\rm min}$ and $\lambda_{\rm max}$ as indicated in figures. The general behavior of $|\mathbf{B}|$ is found to be the same, regardless of the cube size and number of grid points. I should restate that the magnetic field strength in this cube is normalized in such a way that $B_{\rm rms} = 1$.

Another test I perform for the cube is plotting the power spectrum for few values of N and L. Figure 5.10 shows the power law spectrum in k_1, k_2, and k_3 for realizations 2, 4, and 7 in log-log scale. These plots show that $|\mathbf{B}|^2$ is isotropic in k_1, k_2, and k_3. In Figure 5.11, I have shown the power spectrum in $k = |\mathbf{k}|$ in Fourier space for realizations 2, 4, and 7 in

log-log scale. Here the average value of $|\mathbf{B}|^2$ over all the points with similar k is calculated and plotted versus k. Figure 5.12 shows the power spectrum in k for different values of $\lambda_{\max}$ in log-log scale, where N, L, and $\lambda_{\min}$ are constant for realizations 6, 7, and 9. It shows the cutoffs for small k values happen at $2\pi/\lambda_{\max}$, which was expected.

All these plots show that the generated random field is isotropic in x, y, and z components. Also, the power spectrum is what I expect with its minimum and maximum cutoffs and the shape of the spectrum follows $k^{-11/3}$ Kolmogorov spectrum as shown in Figure 5.13 for realization 7.

After checking the modeled random field in the cube, I need to check it everywhere in the Galaxy. I plot the histograms of B_x, B_y, B_z, and $|\mathbf{B}|$ for the positions in whole Galaxy with spacing of 100 pc in each dimension as shown in Figures 5.15, 5.14 for realizations 2, 4, and 7. The magnetic field components plotted here have been scaled with the JF12 random field strengths (Jansson & Farrar, 2012b) and the values are in μG.

Table 5.1: Kolmogorov random field realizations.

Realization	N_1	N_2	N_3	L_x(kpc)	L_y(kpc)	L_z(kpc)	$\lambda_{\min}$(kpc)	$\lambda_{\max}$(kpc)
1	128	128	128	1.28	1.28	1.28	0.005	0.05
2	128	128	128	1.28	1.28	1.28	0.005	0.1
3	256	256	256	2.56	2.56	2.56	0.005	0.05
4	256	256	256	2.56	2.56	2.56	0.005	0.1
5	256	256	256	2.56	2.56	2.56	0.005	0.2
6	512	512	512	5.12	5.12	5.12	0.005	0.05
7	512	512	512	5.12	5.12	5.12	0.005	0.1
8	512	512	512	5.12	5.12	5.12	0.01	0.1
9	512	512	512	5.12	5.12	5.12	0.005	0.2

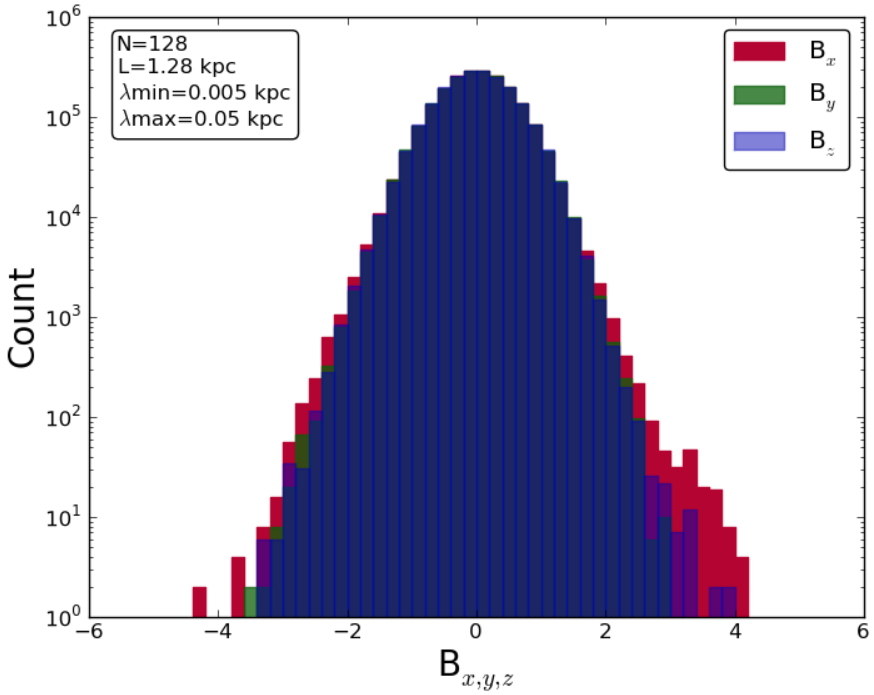

(a) $\lambda_{\max} = 0.05$ kpc

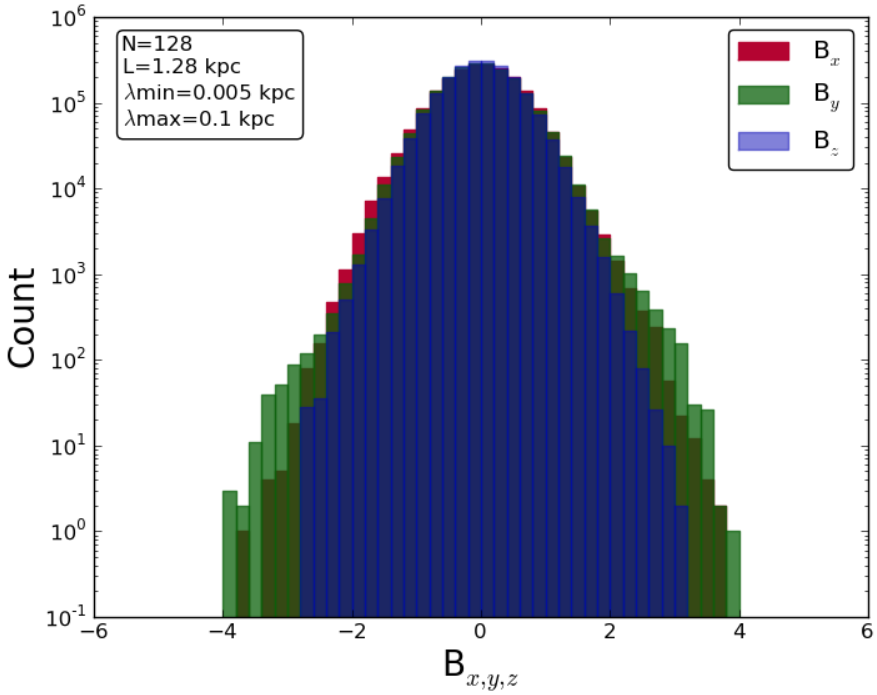

(b) $\lambda_{\max} = 0.1$ kpc

Figure 5.1: Histograms of B_x, B_y and B_z in the cube: N=128, L=1.28 kpc, $\lambda_{\min} = 0.005$ kpc, and (a) $\lambda_{\max} = 0.05$ kpc, (b) $\lambda_{\max} = 0.1$ kpc. The B values in the cube are not scaled with the JF12 parameters therefore they are shown in arbitrary units.

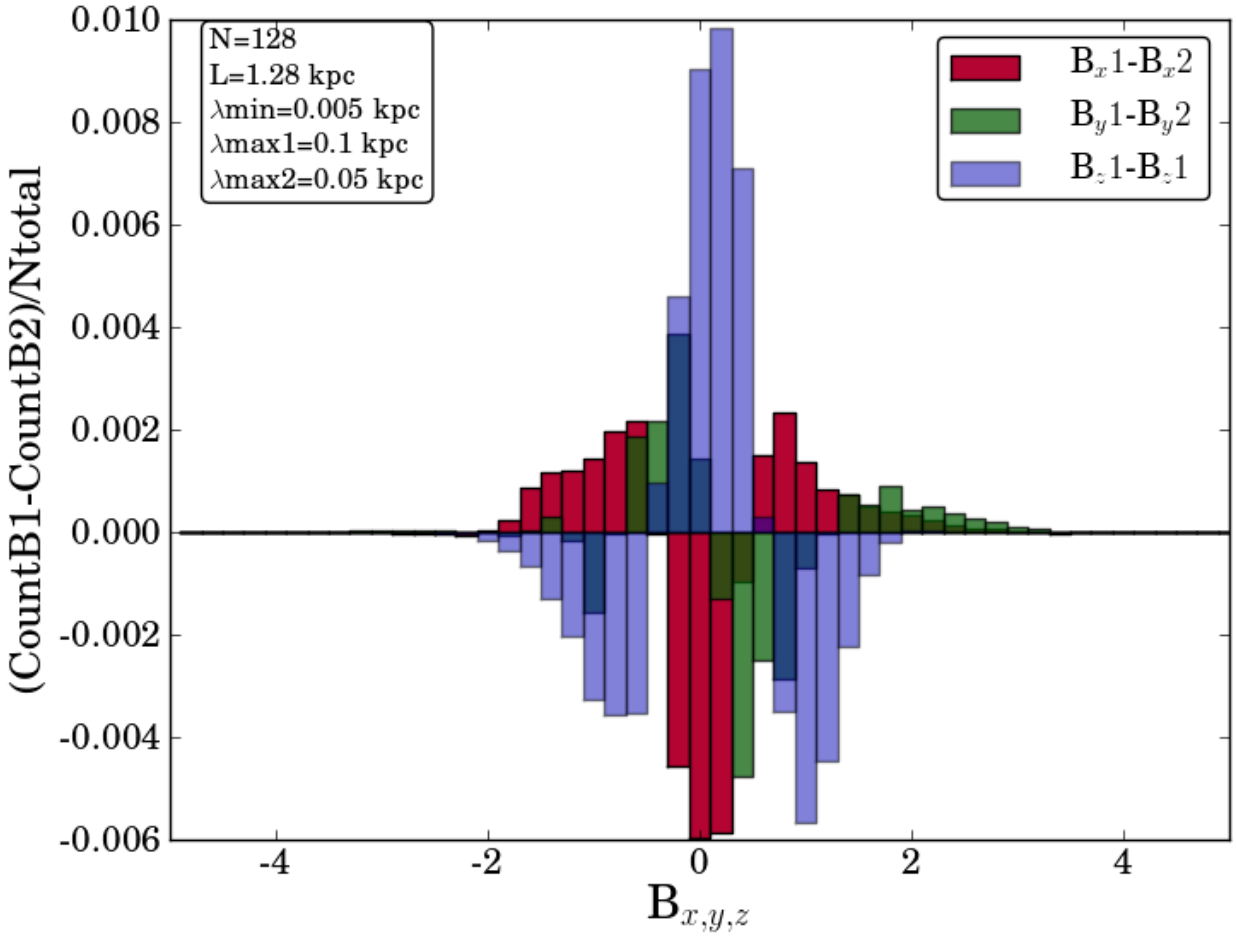

Figure 5.2: Normalized difference between B_x, B_y, B_z histograms of two random field realizations. N=128, L=1.28 kpc, $\lambda_{\rm min}$=0.005 kpc, $\lambda_{\rm max}$=0.05 kpc in the first realization and $\lambda_{\rm max}$=0.1 kpc in the second realiztaion. The ratio of the difference to total count is at most of the order of $\approx 1\%$. The B values in the cube are not scaled with the JF12 parameters therefore they are shown in arbitrary units.

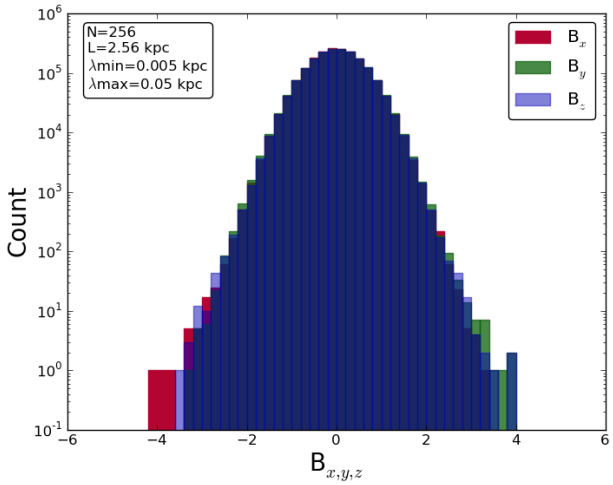

(a) $\lambda_{\max} = 0.05$ kpc

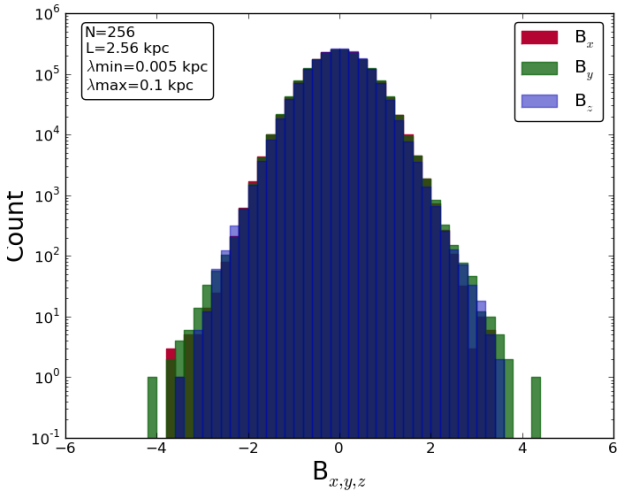

(b) $\lambda_{\max} = 0.1$ kpc

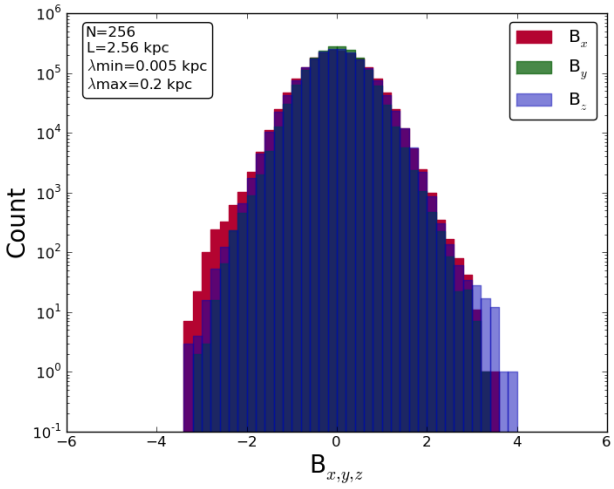

(c) $\lambda_{\max} = 0.2$ kpc

Figure 5.3: Histograms of B_x, B_y and B_z in the cube: N=256, L=2.56 kpc, $\lambda_{\min} = 0.005$ kpc, and (a) $\lambda_{\max} = 0.05$ kpc, (b) $\lambda_{\max} = 0.1$ kpc, (c) $\lambda_{\max} = 0.2$ kpc. The B values in the cube are not scaled with the JF12 parameters therefore they are shown in arbitrary units.

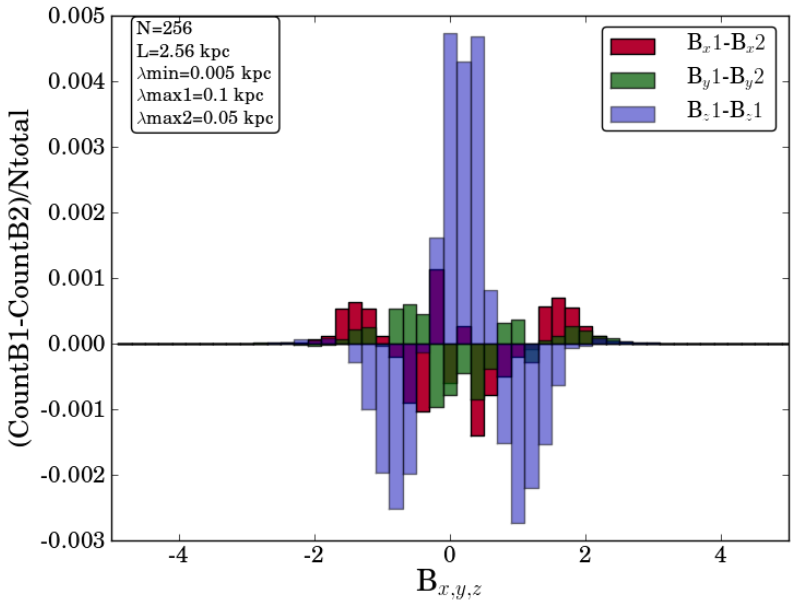

(a) $\lambda_{\rm max1} = 0.1$ kpc and $\lambda_{\rm max2} = 0.05$ kpc

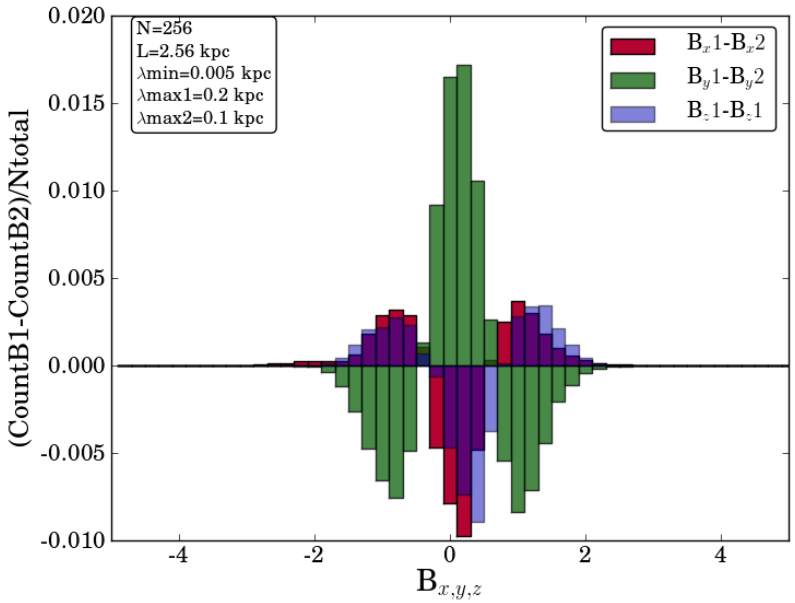

(b) $\lambda_{\rm max1} = 0.2$ kpc and $\lambda_{\rm max2} = 0.1$ kpc

Figure 5.4: Normalized difference between B_x, B_y, B_z histograms of two random field realizations. N=256, L=2.56 kpc, $\lambda_{\rm min}$=0.005 kpc, (a) $\lambda_{\rm max}$=0.05 kpc in the first realization and 0.1 kpc in the second realiztaion and (b) (a) $\lambda_{\rm max}$=0.1 kpc in the first realization and 0.2 kpc in the second realiztaion. The ratio of the difference to total count is at most of the order of $\approx 1\%$. The B values in the cube are not scaled with the JF12 parameters therefore they are shown in arbitrary units.

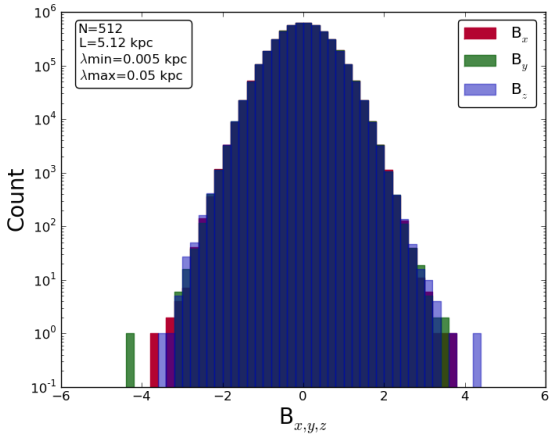

(a) $\lambda_{\max} = 0.05$ kpc

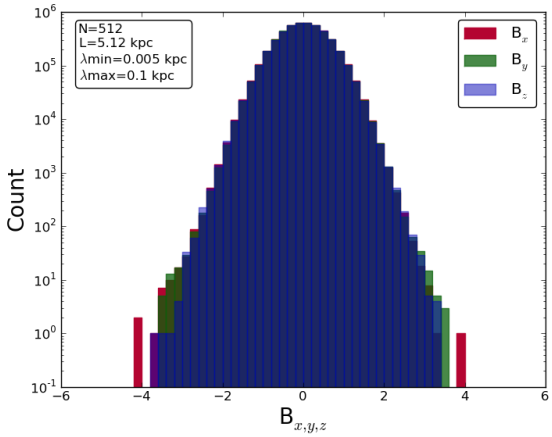

(b) $\lambda_{\max} = 0.1$ kpc

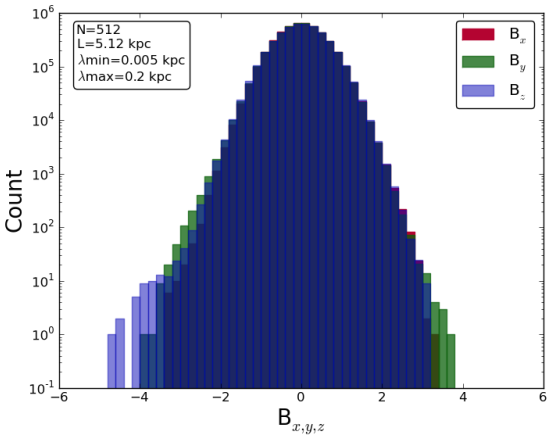

(c) $\lambda_{\max} = 0.2$ kpc

Figure 5.5: Histograms of B_x, B_y and B_z in the cube: N=512, L=5.12 kpc, $\lambda_{\min} = 0.005$ kpc, and (a) $\lambda_{\max} = 0.05$ kpc, (b) $\lambda_{\max} = 0.1$ kpc, (c) $\lambda_{\max} = 0.2$ kpc. The B values in the cube are not scaled with the JF12 parameters therefore they are shown in arbitrary units.

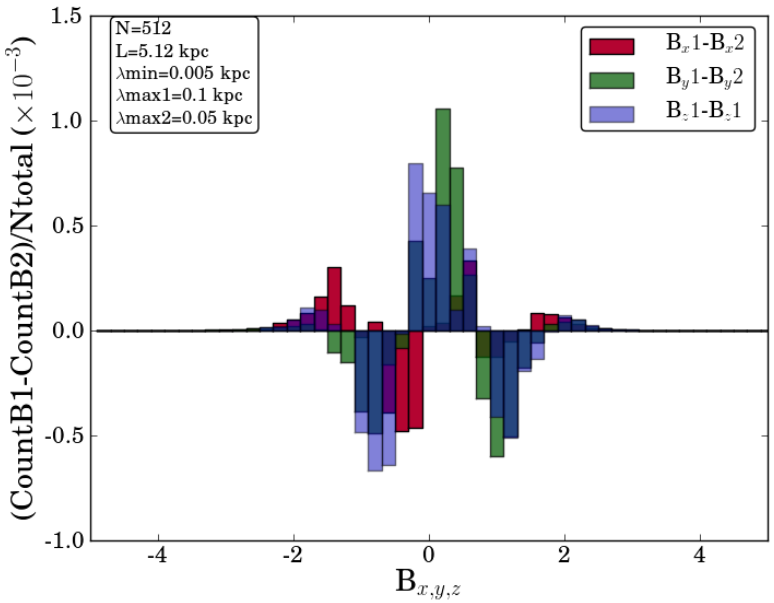

(a) $\lambda_{\rm max1} = 0.1$ kpc and $\lambda_{\rm max2} = 0.05$ kpc

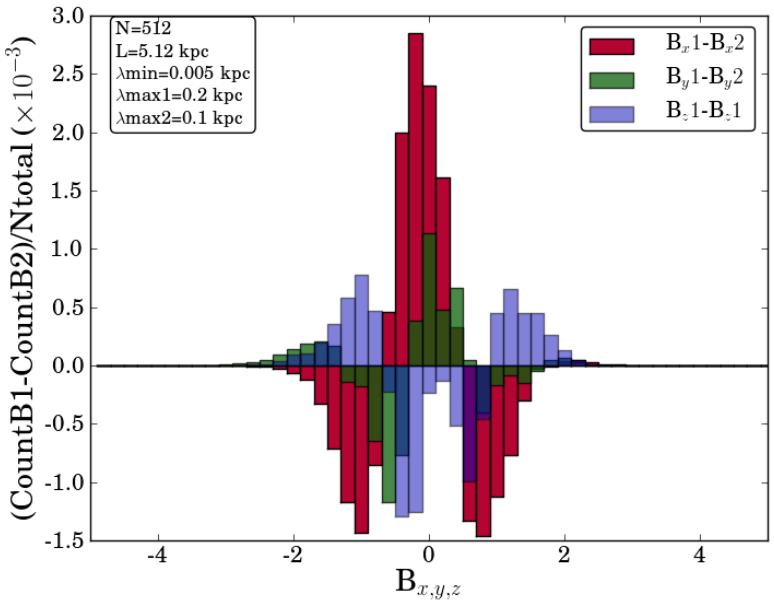

(b) $\lambda_{\rm max1} = 0.2$ kpc and $\lambda_{\rm max2} = 0.1$ kpc

Figure 5.6: Normalized difference between B_x, B_y, B_z histograms of two random field realizations. N=512, L=5.12 kpc, $\lambda_{\rm min}$=0.005 kpc, (a) $\lambda_{\rm max}$=0.05 kpc in the first realization and 0.1 kpc in the second realiztaion and (b) (a) $\lambda_{\rm max}$=0.1 kpc in the first realization and 0.2 kpc in the second realiztaion. The ratio of the difference to total count is at most of the order of $\approx 3\%$. The B values in the cube are not scaled with the JF12 parameters therefore they are shown in arbitrary units.

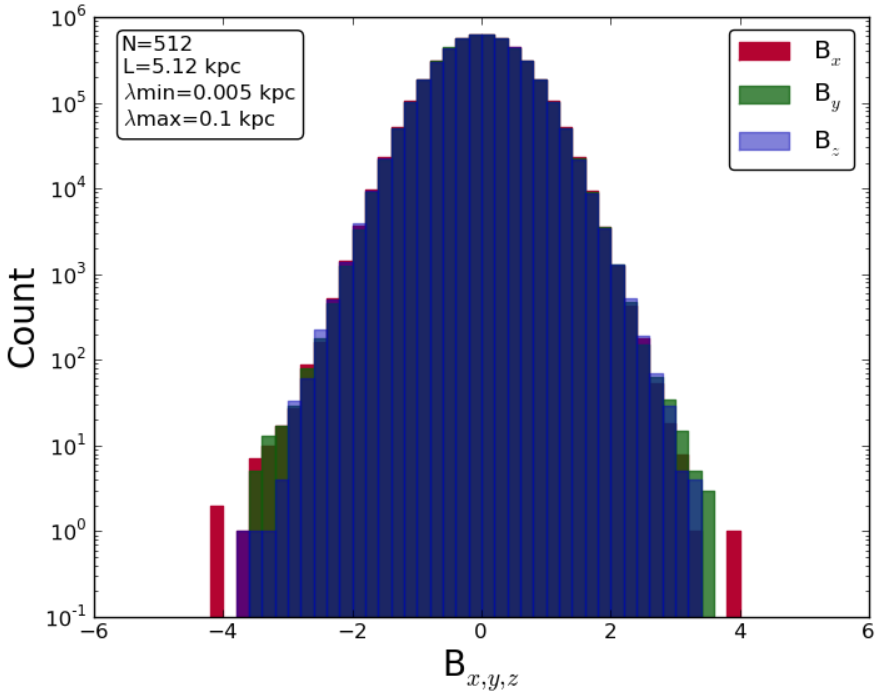

(a) $\lambda_{\rm min} = 0.005$ kpc

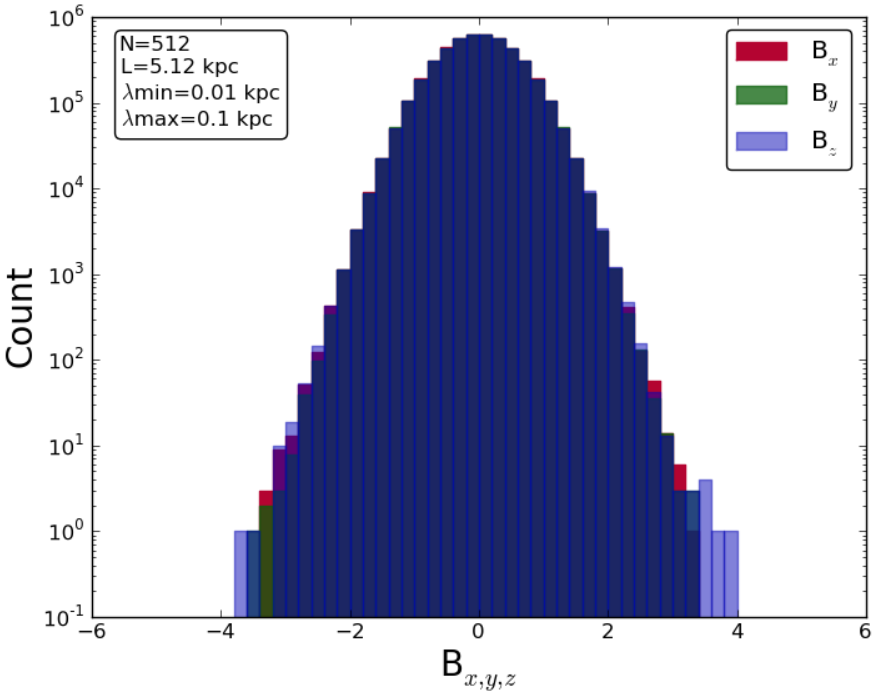

(b) $\lambda_{\rm min} = 0.01$ kpc

Figure 5.7: Histograms of B_x, B_y and B_z in the cube: N=512, L=5.12 kpc, $\lambda_{\rm max} = 0.1$ kpc, (a) $\lambda_{\rm min} = 0.005$ kpc (b) $\lambda_{\rm min} = 0.01$ kpc. The B values in the cube are not scaled with the JF12 parameters therefore they are shown in arbitrary units.

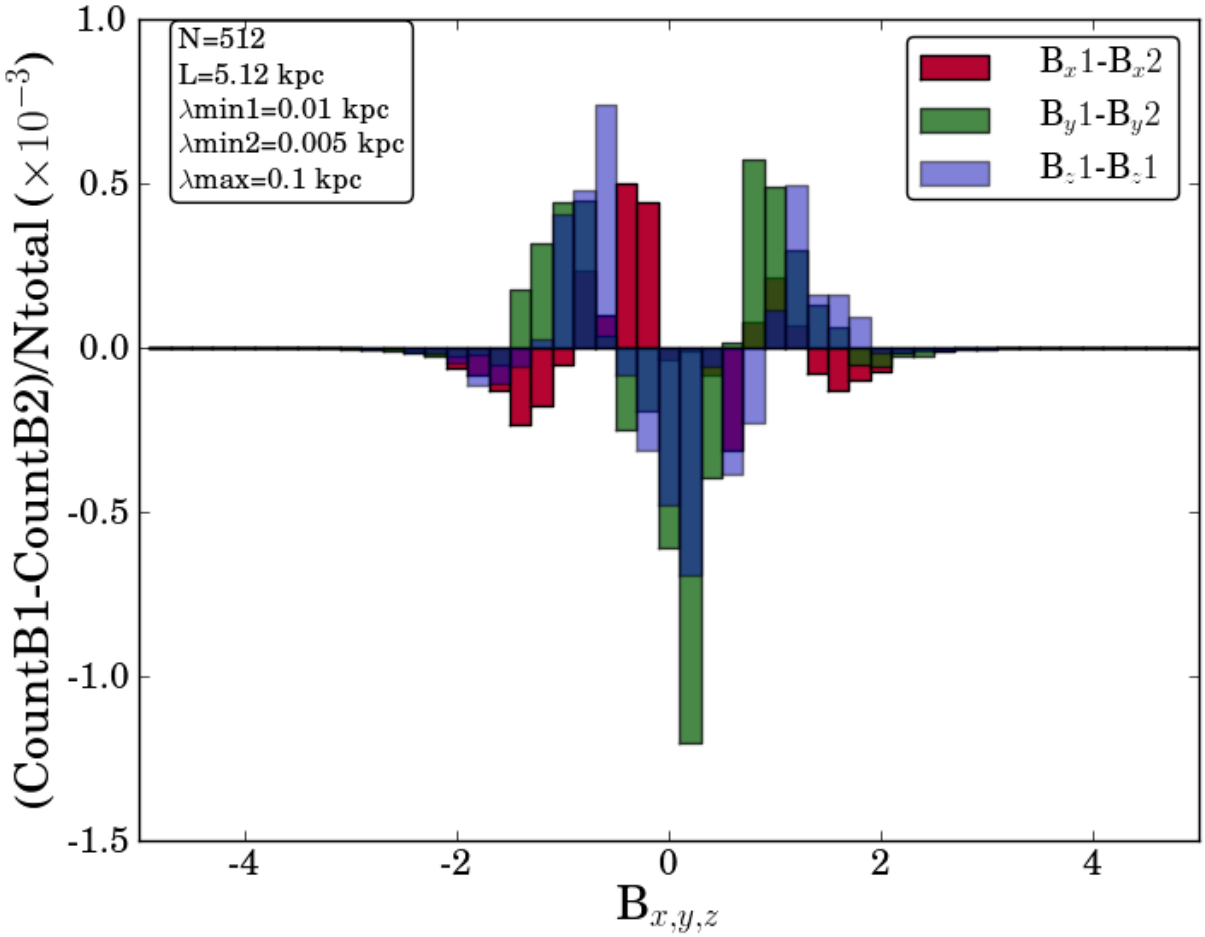

Figure 5.8: Normalized difference between B_x, B_y, B_z histograms of two random field realizations. N=5.12, L=5.12 kpc, $\lambda_{\rm max}$=0.1 kpc, $\lambda_{\rm min}$=0.01 kpc in the first realization and $\lambda_{\rm min}$=0.05 kpc in the second realiztaion. The ratio of the difference to total count is at most of the order of $\approx 1\%$. The B values in the cube are not scaled with the JF12 parameters therefore they are shown in arbitrary units.

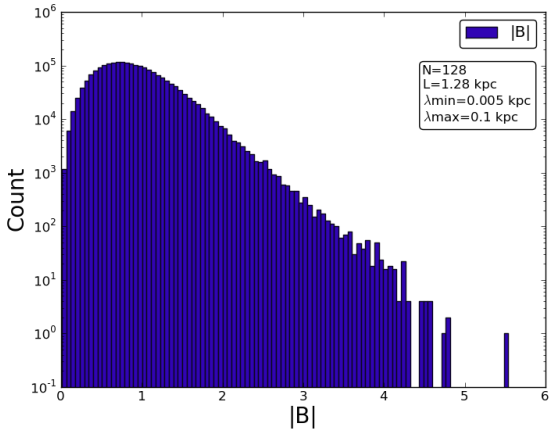

(a) N=128, L=1.28 kpc

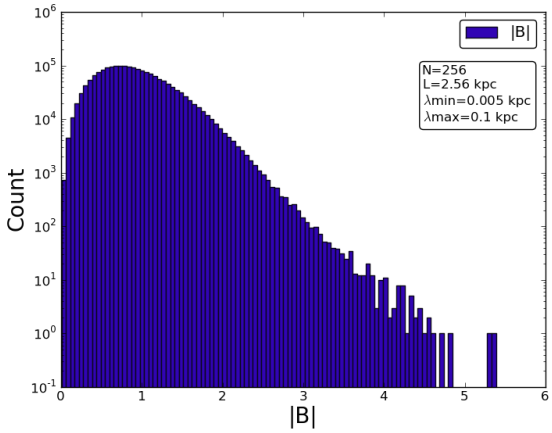

(b) N=256, L=2.56 kpc

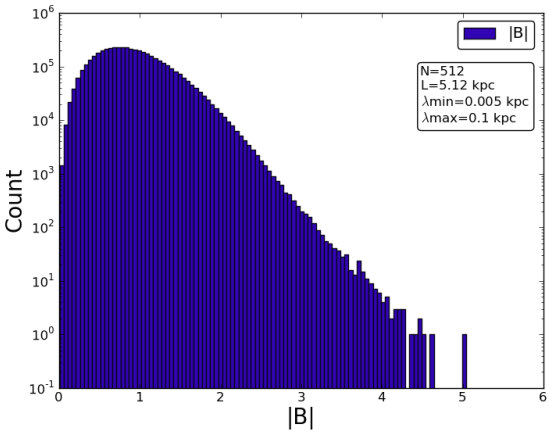

(c) N=512, L=5.12 kpc

Figure 5.9: Histogram of $|\mathbf{B}|$ in a cube is plotted for different values of N and L. In all cases $\lambda_{\rm min}$=0.005 kpc and $\lambda_{\rm max}$=0.1 kpc. The B values in the cube are not scaled with the JF12 parameters therefore $|\mathbf{B}|$ is in arbitrary units.

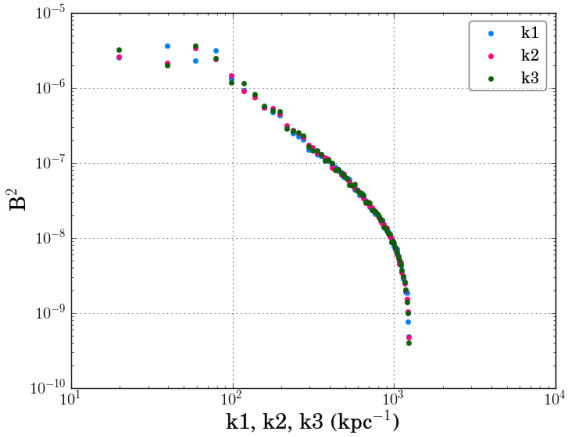

(a) N=128, L=1.28 kpc

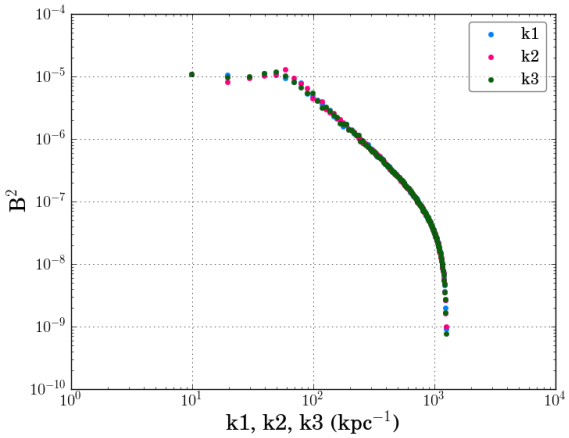

(b) N=256, L=2.56 kpc

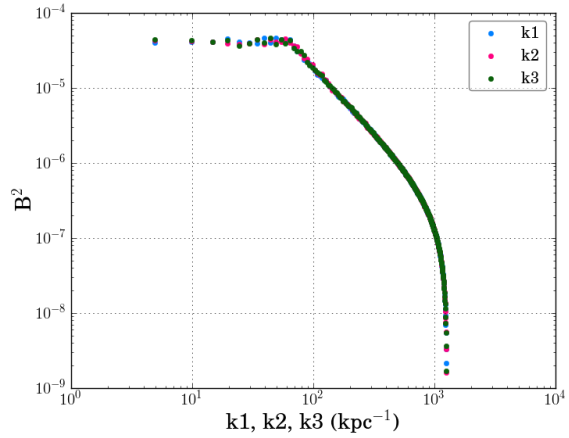

(c) N=512, L=5.12 kpc

Figure 5.10: Power spectrum: B^2 is plotted versus k_1, k_2, and k_3. To plot B^2 versus k_1, B^2 is summed over values at each point in the 2nd and 3rd directions. In all cases $\lambda_{\rm min}$=0.005 kpc and $\lambda_{\rm max}$=0.1 kpc. (a) N=128, L=1.28 kpc, (b) N=256, L=2.56 kpc, and (c) N=512, L=5.12 kpc. The B values in the cube are not scaled with the JF12 parameters therefore B^2 is in arbitrary units.

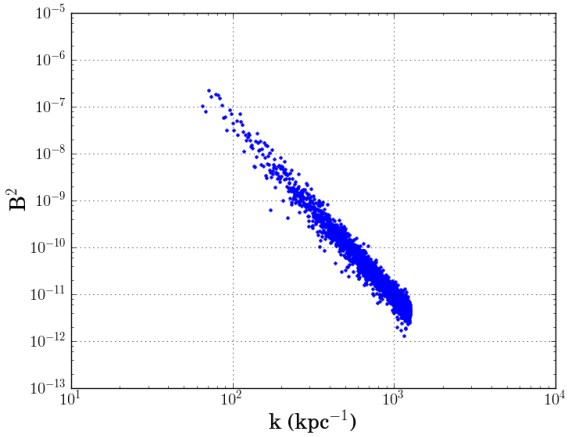

(a) N=128, L=1.28 kpc

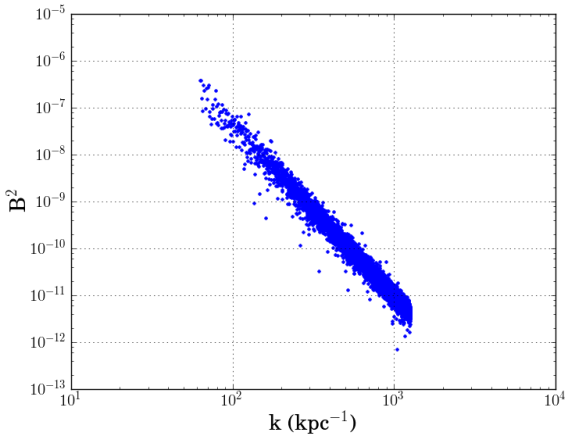

(b) N=256, L=2.56 kpc

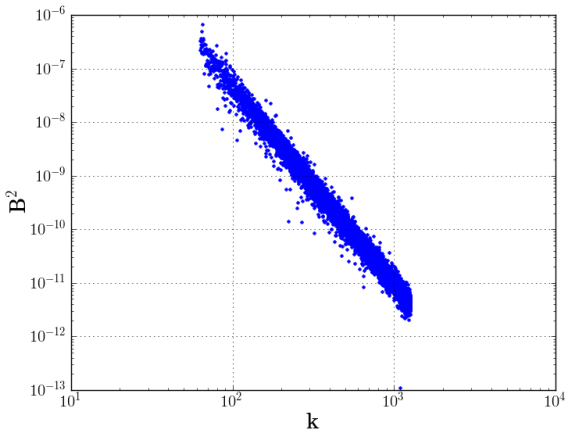

(c) N=512, L=5.12 kpc

Figure 5.11: Power spectrum: B^2 is plotted versus k. B^2 is averaged over values at each point with similar k values. In all cases the $\lambda_{\rm min}$=0.005 kpc and $\lambda_{\rm max}$=0.1 kpc. (a) N=128, L=1.28 kpc, (b) N=256, L=2.56 kpc, and (c) N=512, L=5.12 kpc. The B values in the cube are not scaled with the JF12 parameters therefore B^2 is in arbitrary units.

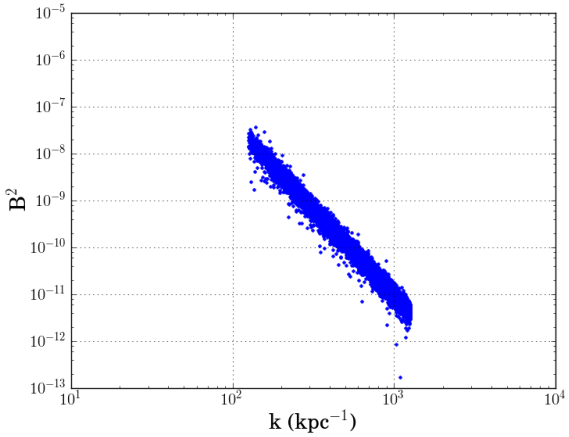

(a) $\lambda_{\max}$=0.05 kpc

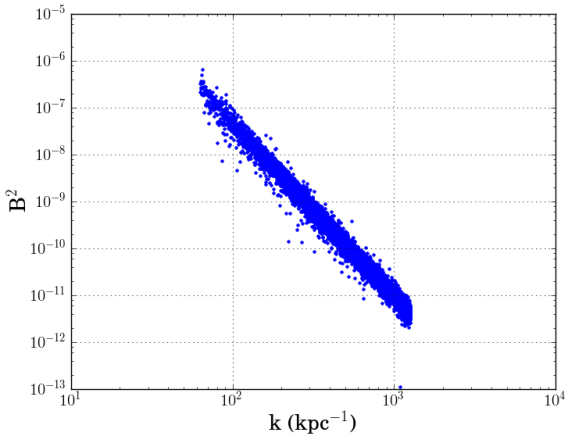

(b) $\lambda_{\max}$=0.1 kpc

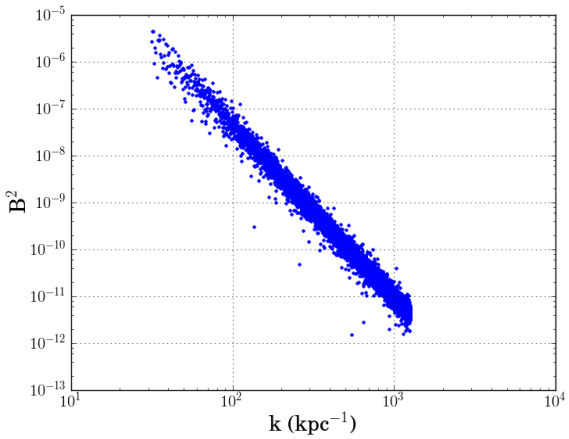

(c) $\lambda_{\max}$=0.2 kpc

Figure 5.12: Power spectrum: B^2 is plotted versus k in a log-log plot. B^2 is averaged over values at each point with similar k values. In all cases N=512, L=5.12 kpc, $\lambda_{\min}$=0.005 kpc and (a) $\lambda_{\max}$=0.05 kpc, (b) $\lambda_{\max}$=0.1 kpc, and (c) $\lambda_{\max}$=0.2 kpc. The B values in the cube are not scaled with the JF12 parameters therefore B^2 is in arbitrary units.

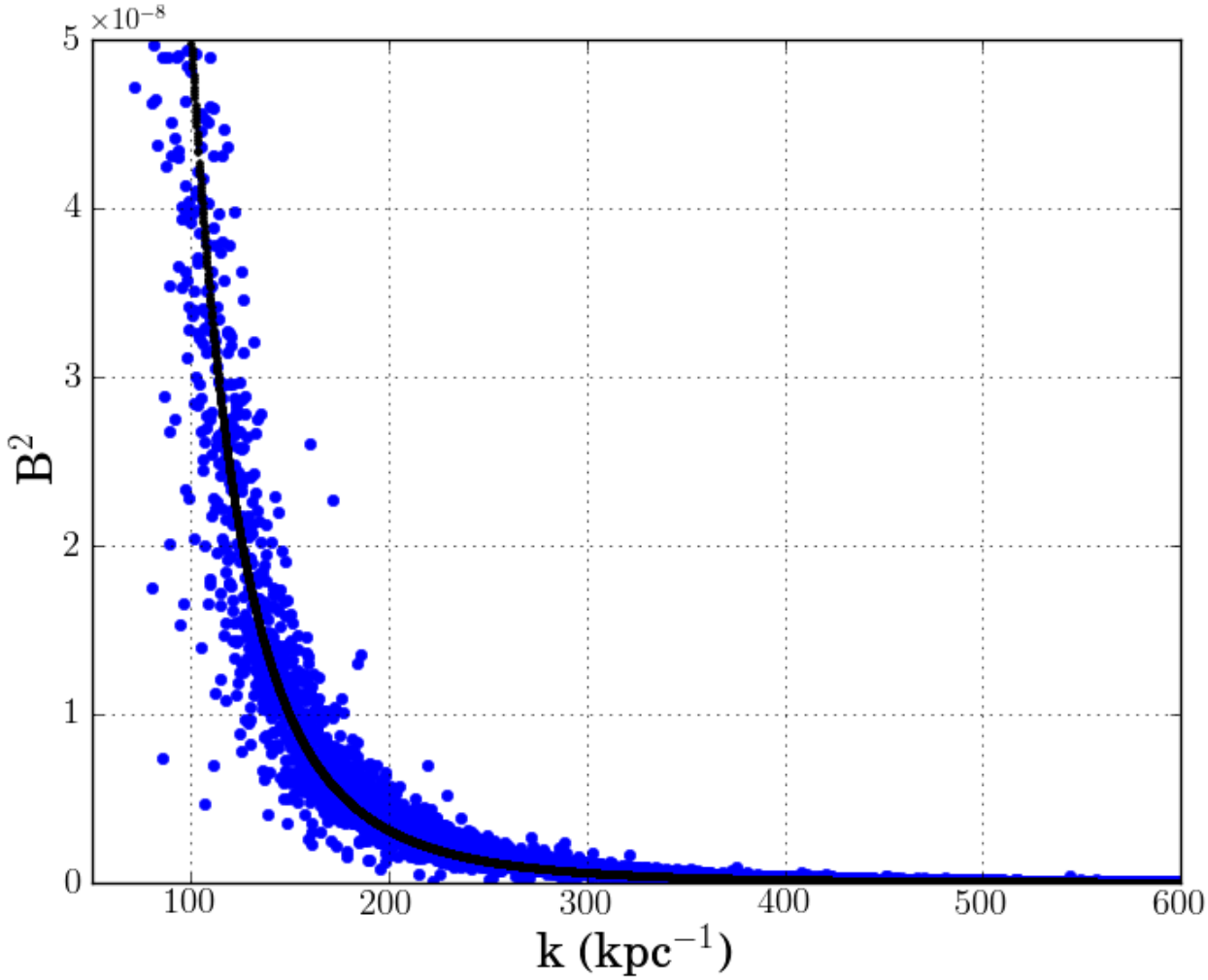

Figure 5.13: The power spectrum follows a Kolmogorov spectrum $\propto k^{-11/3}$. Here part of the histogram is zoomed in and is fitted to $\alpha k^{-11/3}$ for the case of N=512, L=5.12 kpc, $\lambda_{\rm min}$=0.005 kpc and $\lambda_{\rm max}$=0.1 kpc. The B values in the cube are not scaled with the JF12 parameters therefore B^2 is in arbitrary units.

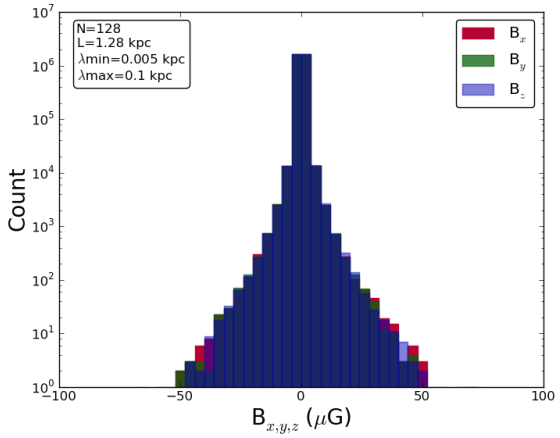

(a) N=128, L=1.28 kpc

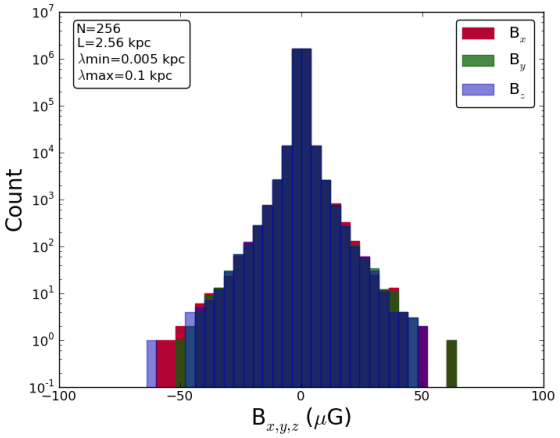

(b) N=256, L=2.56 kpc

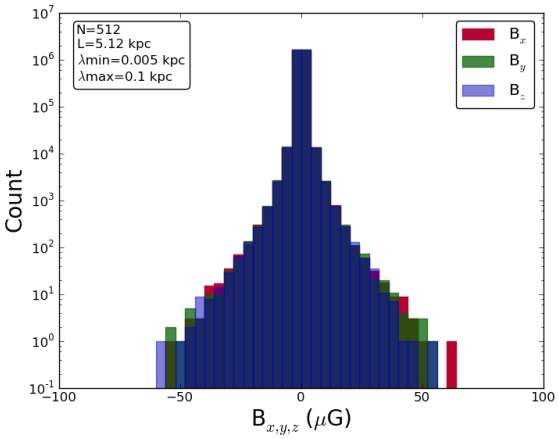

(c) N=512, L=5.12 kpc

Figure 5.14: Histograms of B_x, B_y and B_z in the Galaxy is plotted for different values of N=128, 256, and 512 and L=1.28, 2.56, and 5.12 kpc. In all cases $\lambda_{\rm min}$=0.005 kpc and $\lambda_{\rm max}$=0.1 kpc.

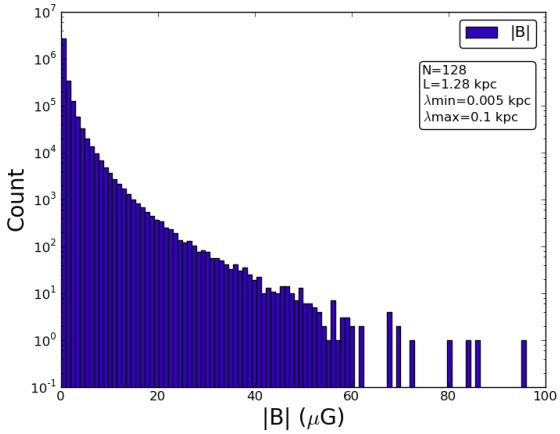

(a) N=128, L=1.28 kpc

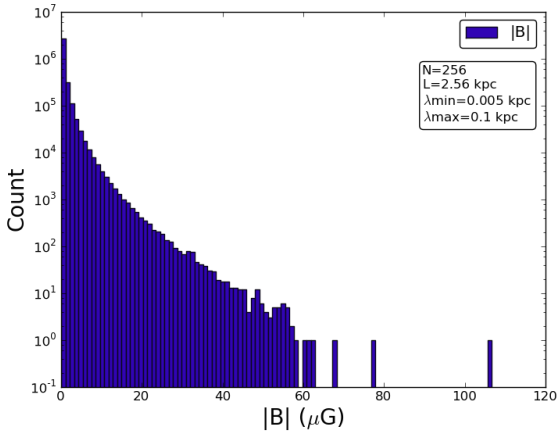

(b) N=256, L=2.56 kpc

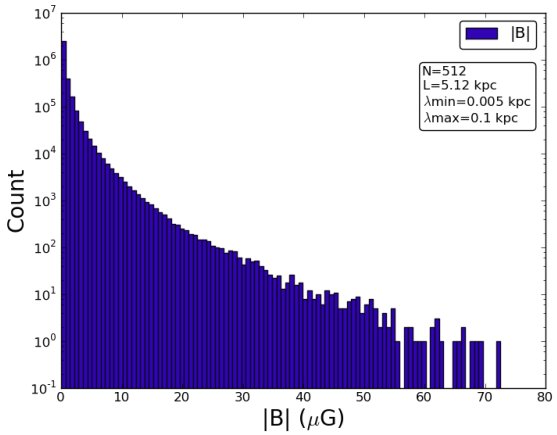

(c) N=512, L=5.12 kpc

Figure 5.15: Histogram of $|\mathbf{B}|$ in the Galaxy is plotted for different values of N=128, 256, and 512 and L=1.28, 2.56, and 5.12 kpc. In all cases $\lambda_{\rm min}$=0.005 kpc and $\lambda_{\rm max}$=0.1 kpc.

6. Tracking Ultra-High Energy Cosmic Rays in the Galactic Magnetic Field

6.1 Introduction

One of the biggest open questions in UHECR physics concerns the sources of these particles. To identify UHECR sources, one needs to consider the effect of UHECR deflection in the Galactic magnetic field (GMF). The deflection magnitude depends on the energy and the charge of the particle. Since the composition of UHECRs is not yet known as a function of energy, I consider rigidity instead of energy in this study. Rigidity (R) is energy divided by charge (E/Ze), that means if energy is in unit of EeV (10^{18} eV) then rigidity is given in unit of EV. Rigidity is a convenient quantity for highly relativistic particles since their Larmor radius is simply R/B.

In general, there are two ways of tracking cosmic rays through the GMF. One is to forward-track a particle from an outside source to detect it at Earth and the other is the reversed procedure, i.e. back-tracking a particle from the Earth to record its exiting velocity direction and location. For both methods I use the *CRT* code, a program to inject and propagate UHECRs from various galactic and extragalactic sources through GMF models. *CRT* uses adaptive Runge-Kutta integration methods to determine the trajectory of a charged particle through a magnetic field according to the relativistic Lorentz force. It allows for the inclusion of user-defined magnetic fields. In Section 6.2, I will detail a study involving forward-tracking cosmic rays through the GMF and in Section 6.3, I will fully describe another study involving the back-tracking method.

6.2 Forward-Tracking Method

In this section, a particle is injected from an extragalactic source and propagates through the GMF until it finally hits the detector centered on Earth. The arrival directions of particles will indicate the observed directions of cosmic rays sent from an extragalactic source to the Earth. The size of the Earth (6400 km) is very small compared to the radius of the

Galaxy (20 kpc), so the probability that a particle hits the Earth is infinitesimally small. Here, I present a new method to increase the efficiency of forward-tracking UHECRs through the GMF. The UHECRs are sent from an extragalactic source to characterize their arrival direction locations and determine if this source can have significant contributions to the observed UHECR events.

To study cosmic rays originating from a single source, I start by sending simulated particles from an injection disk around the source. Since I assume there is no extragalactic magnetic field in this study, the actual injection disk is close to the boundary of the Galaxy, on a line-of-sight to the source. Depending on the size and the distance of the source, I pick a reasonable value for the initial radius of the disk to inject several particles randomly distributed on the injection disk. The initial velocity vectors of the particles are parallel to the observed direction of the source from the Earth. Particles are propagated through the GMF and checked to see if they encounter the detector. The size of the detector also plays an important role in the number of successful detections. Even a large value of 1 pc compared to the real size of the Earth for the radius of the detector will give a negligible number of detections for 5×10^5 injected particles. But I can increase this value (for example to 400 pc) to successfully detect about 1000 events out of the 5×10^5 injected particles.

As a source candidate, I choose Centaurus A in this study. Motivation for why Cen A is an interesting source is deferred to Chapter 7. The GMF model used for propagations is JF12 that is described in Chapter 4. The JF12 model includes a regular component, a random component and a striated random component. The random component used in this section is the one described in Section 4.4.3. The striated component used in this section is described in Section 4.4.2. Here when only the regular and the striated components of the JF12 model are used, it is called JF12-reg and if the complete field model is used it is called JF12. Cosmic rays are injected from a disk of size 8 kpc located at 35 kpc distance from the Earth in the direction of Cen A. Figure 6.1 shows the x-y projection of the initial locations of the detected particles in JF12. The coordinate is such that the z-axis is along the Cen A

line-of-sight direction and the origin is on Cen A. I call this "the injection plane". In this figure, the events have rigidity of 32 EV and the Cen A is shown with a black star at (0,0). The initial injection plane with radius of 8 kpc is called IP0.

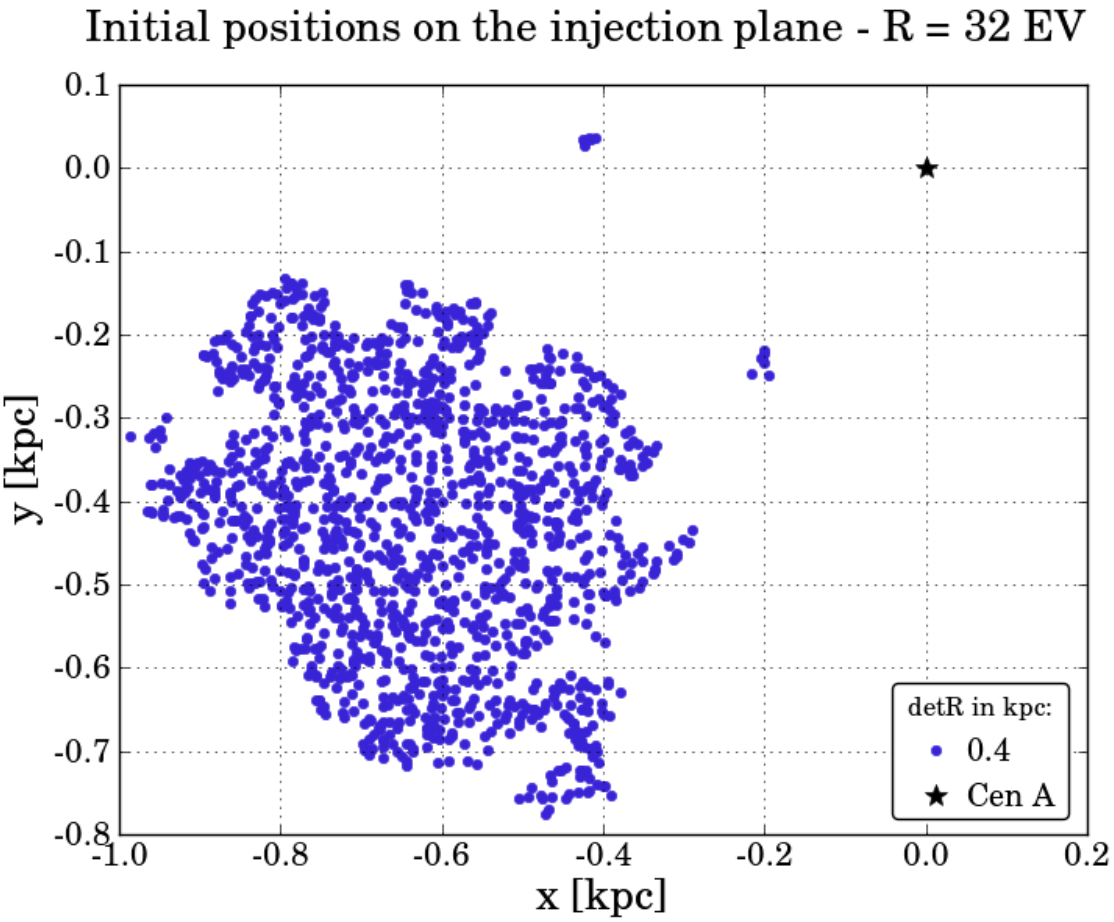

Figure 6.1: The x-y projection of initial positions of observed 32 EV simulated events on the injection plane using detR=0.4 kpc. The black star indicates the location of the center of the Cen A, which is located at (0,0) in this coordinate system.

Although a large detector gives a large number of successful detections, a smaller value better represents reality. The plan is to propagate cosmic rays towards successively smaller detectors by sampling new initial positions within the region of initial positions corresponding to successfully detected events. So far I have the observed arrival directions and the initial positions of about 1000 successful events sent to a detector size (detR) of 0.4 kpc. If I send the particles to a smaller detR, it would not give any successful events from outside of this

region. I limit the initial positions of the successful events on the injection plane. Instead of injecting particles from IP0, I choose random positions inside the region of the initial positions of the detected events on the injection plane (IP1). First, I pick a random number (f) between 0 and 1. Then I pick any two of the successful events, a and b, to find a new location using $(x, y) = f \times (x, y)_a + (1 - f) \times (x, y)_b$. I generate 10^4 of these random events and propagate them to the detector of size detR2. 1000 events are detected out of the total 10,000 which is 50 times more efficient than the first step. I repeat this procedure each time to finally achieve a small desired detR where an image convergence occurs. When the image size is converging, there is no need to decrease the detector size.

In this study, starting with a detR$_i$=0.4 kpc, I go down to detR$_f$=0.002 kpc. At some detR values, I may need less initial particles than 10,000 to detect 1000 of them, depending on the detR and the rigidity of the particles. This method is a relatively efficient way of getting more successful events in less time for small detR. Figure 6.2 shows the injection plane of the successful events with rigidity of 32 EV and different detRs.

To investigate the convergence at small detector sizes, I plot the angular size of the image at each detR taken to be the rms deviation from the image centroid. Figure 6.3 shows the rms values for each detector size for R=32 EV. The rms value becomes smaller than the best resolution at Pierre Auger Observatory ($\sim 0.5^\circ$ at detR=0.002 kpc).

Figures 6.4 and 6.5 show the results of the UHECR deflections in the regular component of the JF12 GMF model for different rigidities. Each plot is for a different rigidity. On the other hand, Figures 6.6 and 6.7 show the results in the complete JF12 model, including the random and striated random field components. Figure 6.8 compares the case of no random field and the complete JF12 model for R=32 EV. When I add the random field, the centroid of the detection is changing by a tiny amount less than 0.01°, but the events are more scattered especially for the images with larger detRs.

The forward-tracking method has some issues that might not be the best way to study the cosmic ray propagation through the GMF from a source. One issue is that it takes a

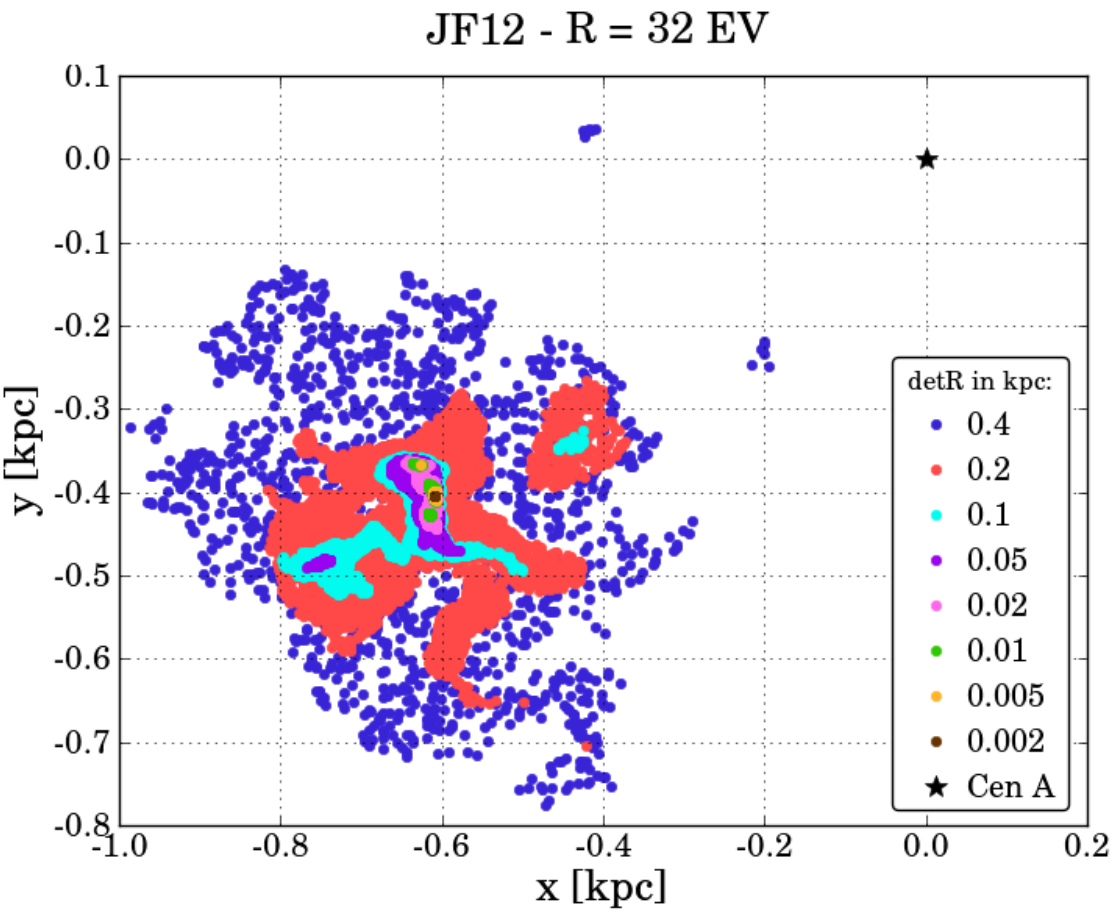

Figure 6.2: The x-y projection of initial positions of successful 32 EV detections on the injection plane for different detR. The black star indicates the location of the center of Cen A, which is located at (0,0).

relatively long time to generate enough events at the first step. Another issue is that I may have neglected some regions by going to the smaller detR, due to low statistics in that region in the first step. The other issue is due to the limit on going to smaller detR. Convergence is observed at detR = 2 pc but this is still too large relative to size of the Earth.

6.3 Back-Tracking Method

Back-tracking is accomplished by following the anti-particle, which means changing the sign of the particle and the initial velocity vector. The propagation of a particle stops when it hits the boundary of the Galaxy, since I have assumed the extragalactic magnetic field is zero in this study. I back-track a fixed number of cosmic rays with a certain rigidity

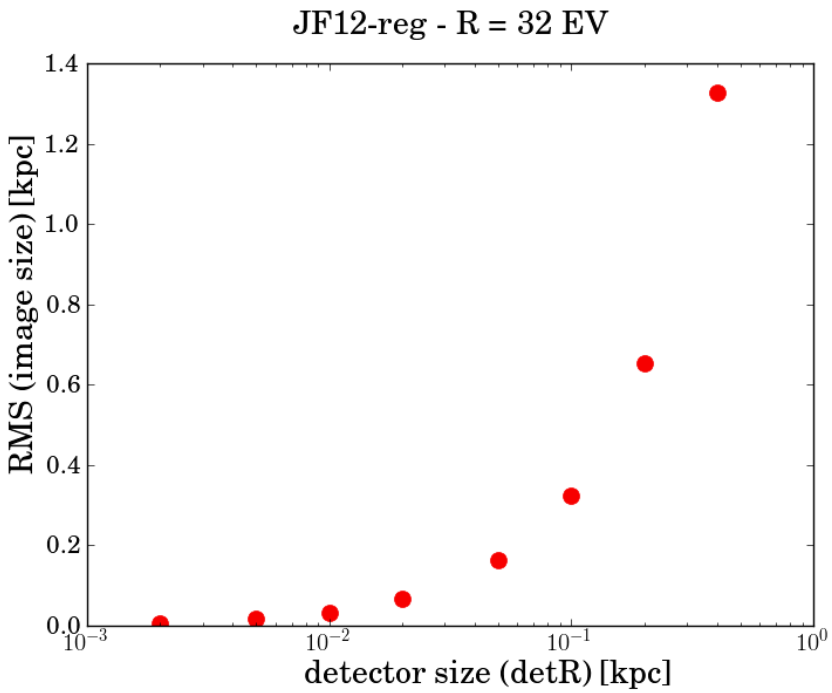

(a) JF12-reg

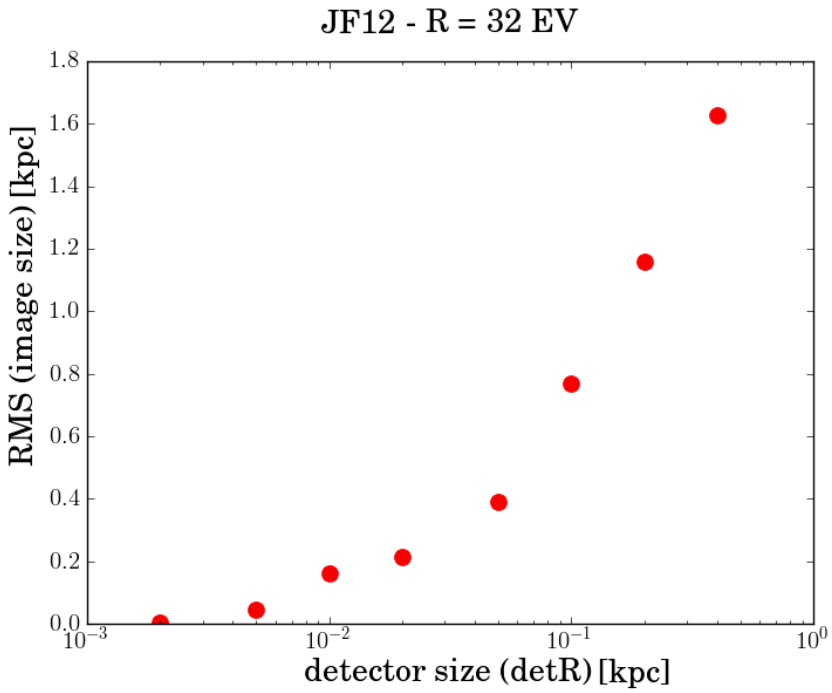

(b) JF12

Figure 6.3: Rms values of the image sizes for each detR at R=32 EV for (a) regular + striated field and (b) regular + striated + random components. A source located at 35 kpc with size 0.1 kpc would appear to span 0.16° as viewed from the Earth.

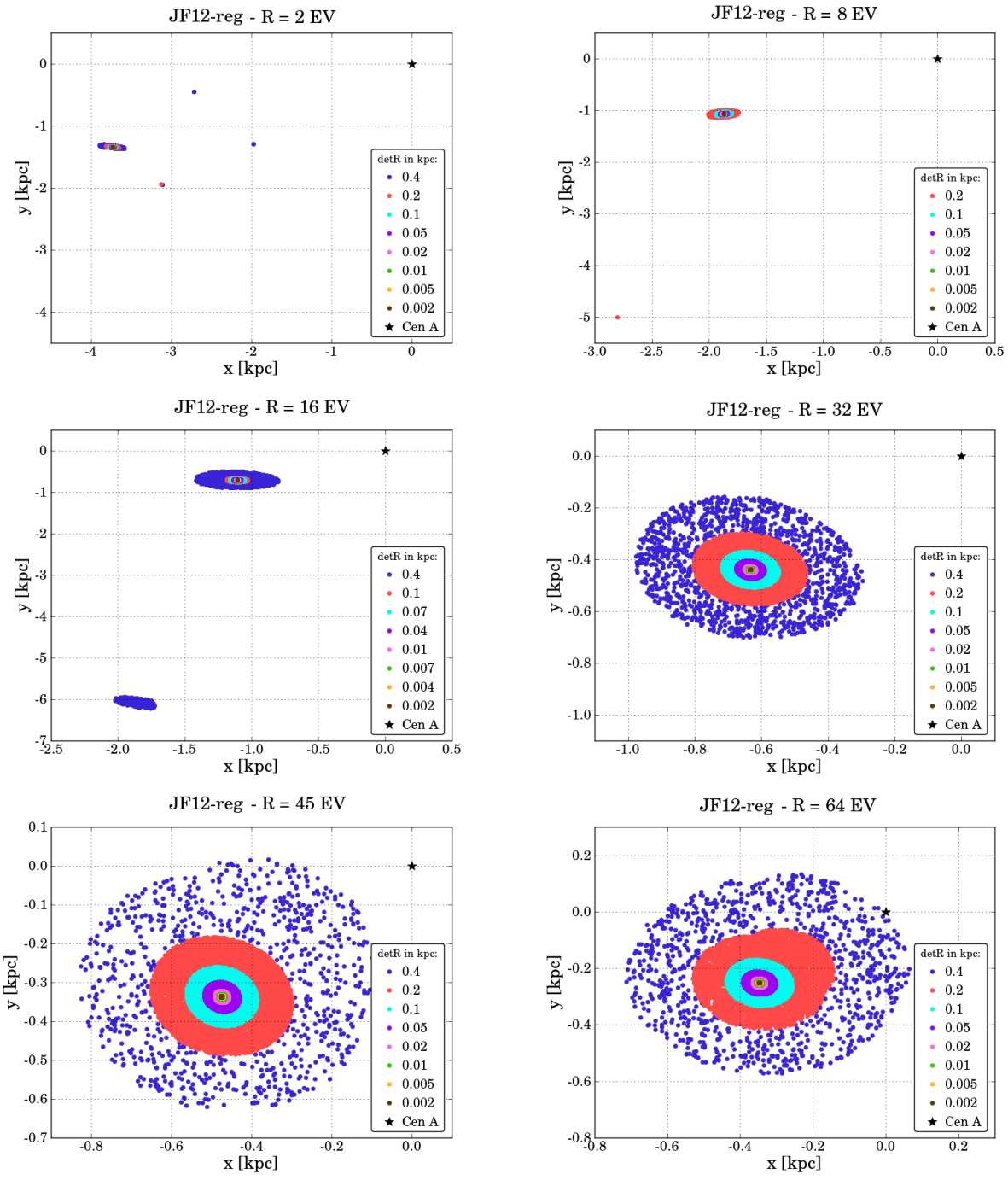

Figure 6.4: The x-y positions of the detected events on the injection disk for different detR using JF12 regular + striated components. The black star indicates CenA.

from isotropically distributed initial locations defined by HEALPix (Gorski et al., 2005). HEALPix is an acronym for Hierarchical Equal Area isoLatitude Pixelization of a sphere, i.e. each pixel on the sphere would cover the same area as the others.

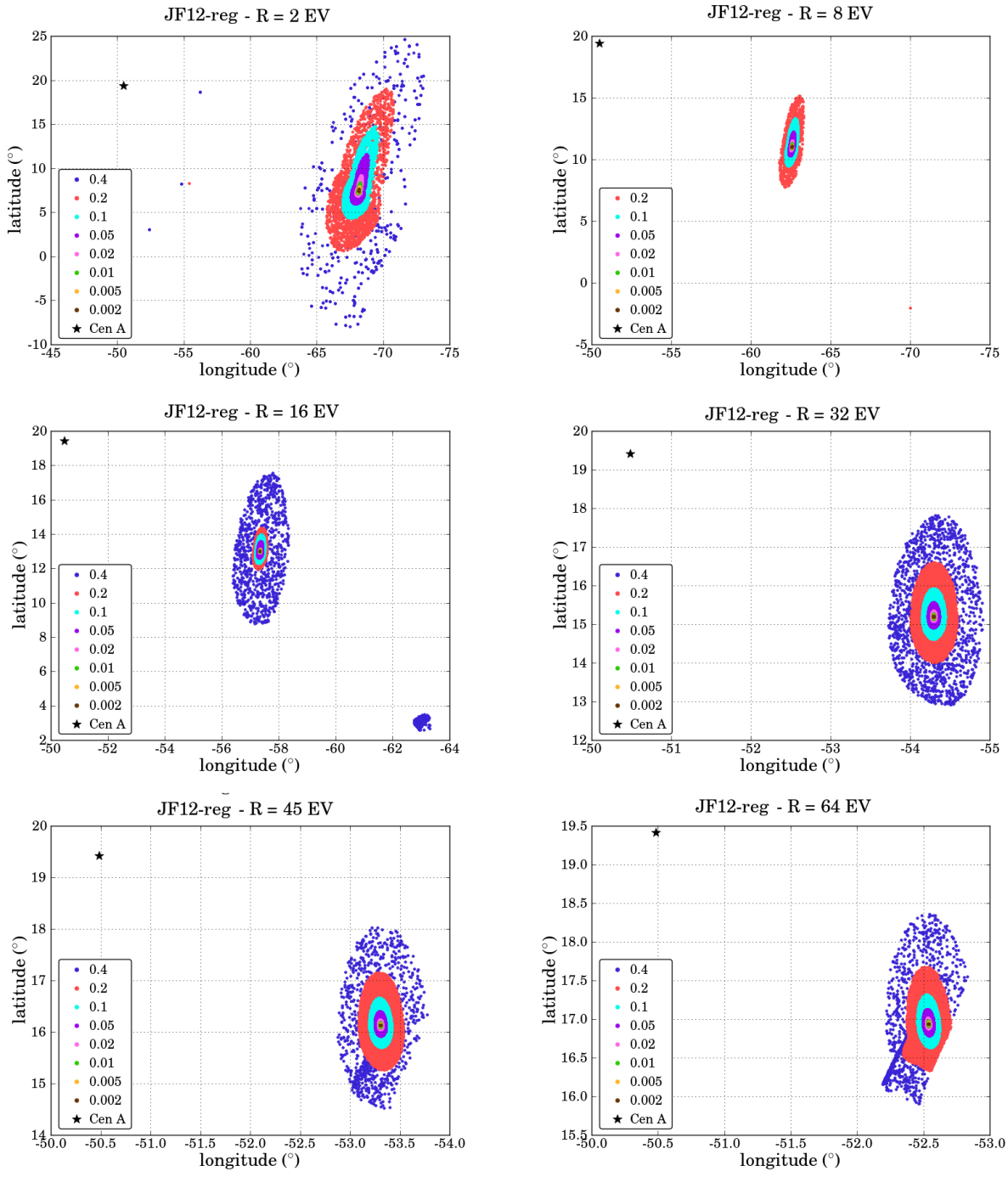

Figure 6.5: The observed arrival directions of the detected events in the Galactic coordinates using JF12 regular + striated components, for different detR.

In my study, I pick HEALPix resolution index 11 (9) that is equivalent to resolution of 8×10^{-4} (1.3×10^{-2}) square-degree, the number of pixels per side of 2048 (512) and total number of pixels of 50,331,648 (3,145,728) in the map. I back-track one particle from the

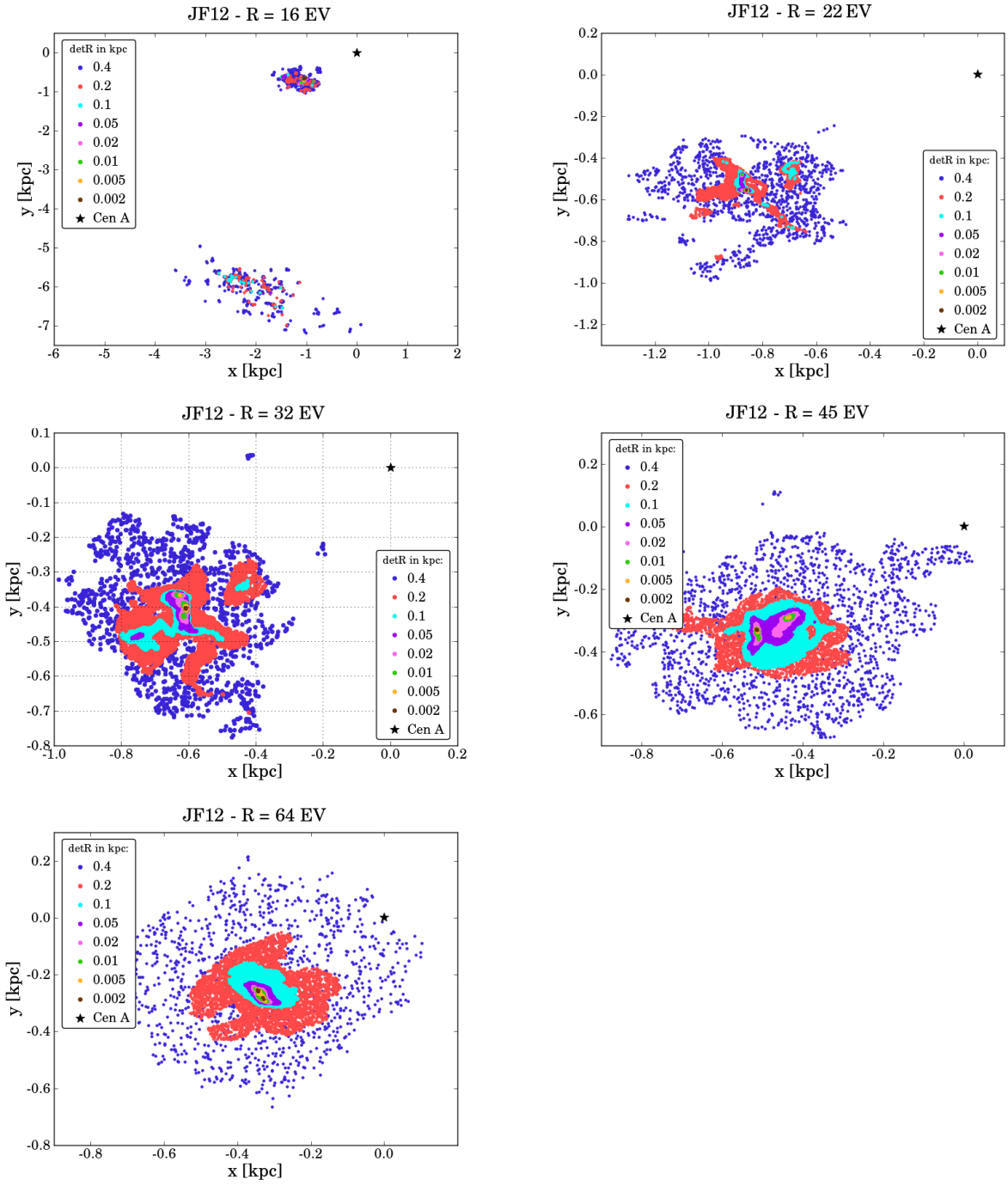

Figure 6.6: The x-y positions of the detected events on the injection disk for different detR using JF12 GMF model.

center of each pixel with a fixed rigidity R. Note that an event with rigidity R, could be a proton with energy R or an iron nucleus with energy $26R$, since the magnetic deflection is proportional to the charge of the particle. Several different rigidities are considered starting

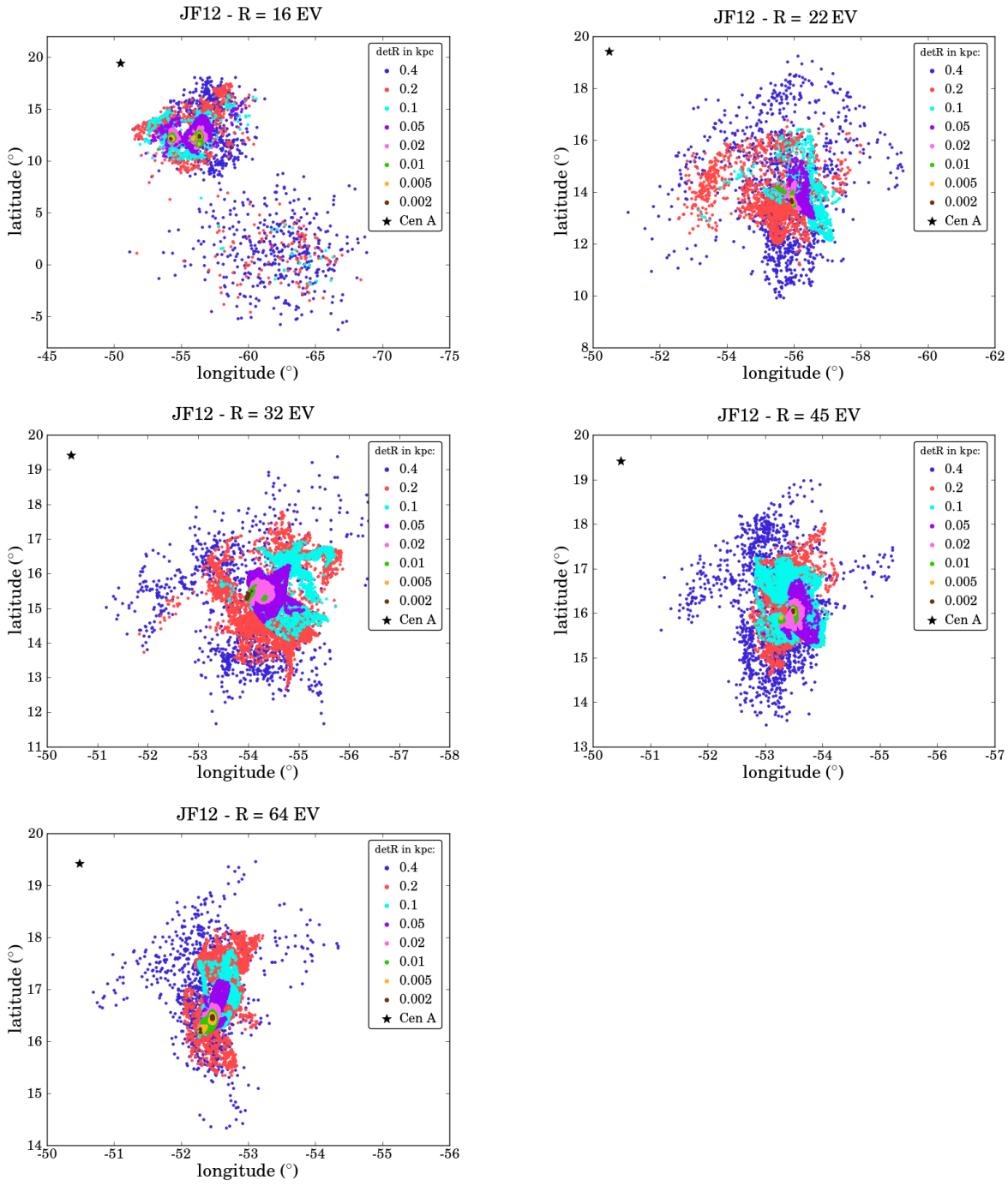

Figure 6.7: The observed direction of the detected events in the Galactic coordinates using JF12 GMF model, for different detR.

with $\log(R_{\rm EV})$=2 (or R=100 EV) and going down to $\log(R_{\rm EV})$=0.3 ($R \simeq 2.0$ EV) in steps of 0.05.

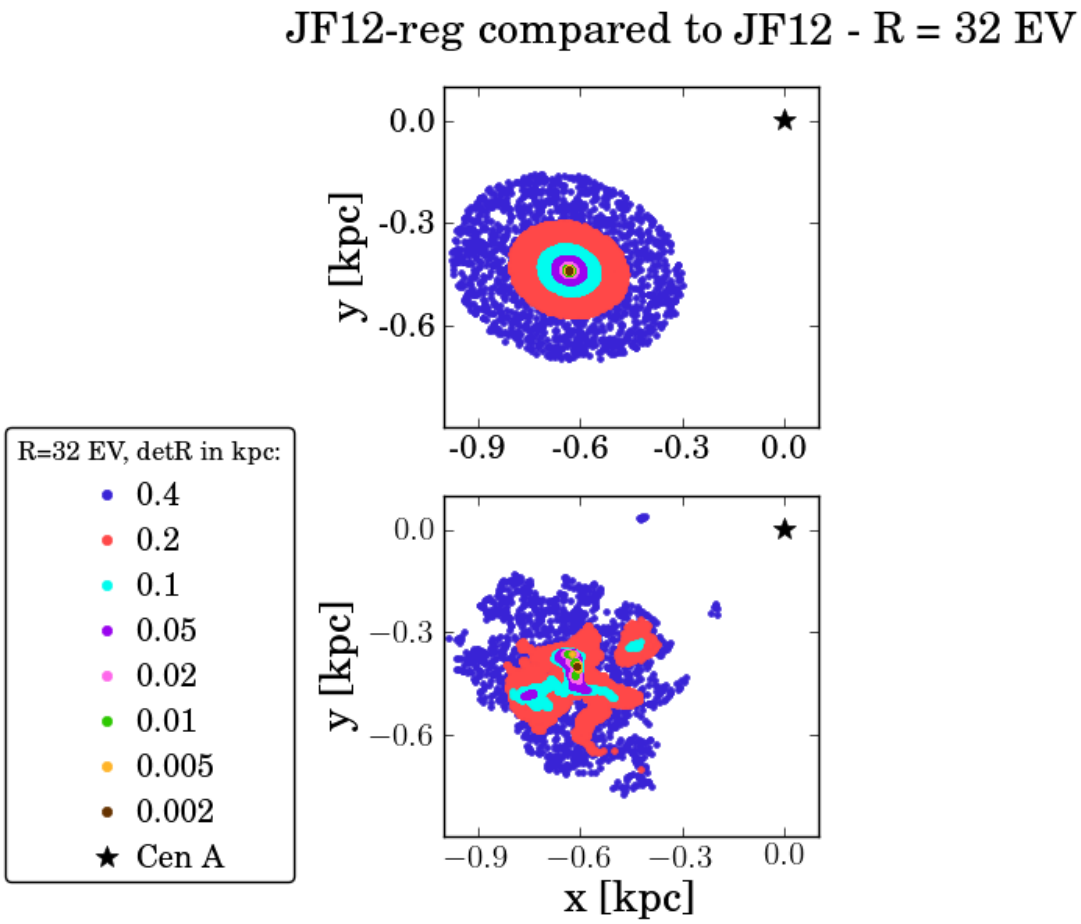

Figure 6.8: The positions of the detected events in (top) regular + striated components of JF12 and (bottom) complete JF12 model.

I plot the source locations of the back-tracked events on a skymap with a smaller resolution to view a better-resolved image of the source distribution. I implement a Mollweide projection (Liddle & Loveday, 2012) and HEALPix resolution index 9 to plot the sky map of the source locations back-tracked from a resolution 11 arrival direction map. As an example, Figure 6.9 shows the sky map of the back-tracked cosmic ray source locations with $\log(R_{\rm EV})$=0.6 ($R \simeq 3.98$ EV) in res=9 in the JF12 regular component (JF12_reg). All sky-plots for different rigidities in the JF12_reg are shown in Figures 6.10–6.14.

These sky maps show different patterns for different rigidities. At higher rigidities, the deflections are not very large, so the source directions do not differ from isotropy, except at the Galactic plane where the fields are stronger. At lower rigidities, however, I see large

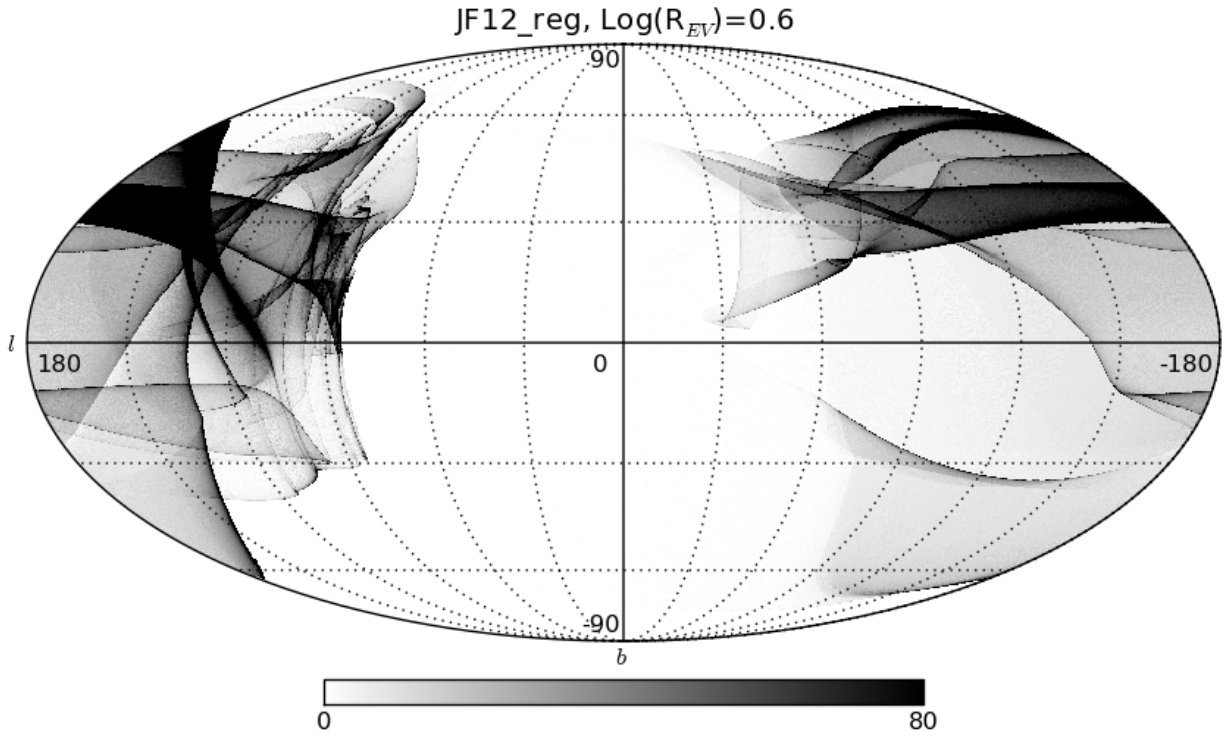

Figure 6.9: Sky map of back-tracked cosmic rays with $\log(R_{\rm EV})$=0.6 in JF12_reg. This map is a Mollweide projection. The horizontal axis shows the Galactic longitude and the vertical axis shows the Galactic latitude. The grey scale represents the particle counts in each HEALPix pixel. Pixels with counts larger than 80 are plotted with a count of 80.

deflections in such a way that some parts of the sky are empty and no cosmic ray is back-tracked to those directions. For instance, at $\log(R_{\rm EV})$=0.6 in Figure 6.9, no proton with energy $\simeq$ 3.98 EeV, and no iron with energy $\simeq$ 103.51 EeV are likely to arrive from directions near $(l, b) = (60^\circ, 25^\circ)$.

Now I would like to see the effect of the random field component on the deflections. I back-track the cosmic rays through the regular component plus one realization of Kolmogorov random field and I call the total field JF12_R1. The parameters of this realization are N=512, L=5120 pc, $\lambda_{\rm min}$=5 pc, and $\lambda_{\rm max}$=100 pc. The random field I use here is generated by the second method of random field implementation described in Chapter 5. Since tracking the particles in random field is computationally expensive, I back-track the cosmic rays in res=9 instead of res=11. I plot the sky maps of back-tracked cosmic rays with $\log(R_{\rm EV})$=2.0, 1.5,

1.0, and 0.5 in JF12_R1 (see Figure 6.15). The maps of res=9 back-tracked cosmic rays are plotted in res=7 to demonstrate the source distributions in a more understandable way.

Comparing each of the sky maps in JF12_R1 with its corresponding sky map in JF12_reg exposes the general qualitative differences between the two maps. However, to better understand the effects of the random field, I pick a few representative source directions and compare the observed arrival directions of events within 1° near each source with and without the random field. Healpix res=1 contains 48 points which could be considered as representative source locations. For smaller rigidities where events are more scattered, I need fewer sources to distinguish the smearing of events from each, so I use res=0 which contains 12 directions. Figure 6.16 compares the random and regular+random field for different positions in the sky. The black crosses are the positions of the 48 sources, the blue regions show the observed arrival directions of events from each source in JF12_reg and the red points are the observed arrival directions of events from each source in JF12_R1. I see that the random field does not deflect the simulated UHECRs by more than a degree for this high rigidity (R=100 EV) over a large portion of the sky and it has larger effects near the Galactic plane.

For lower rigidities, the cosmic rays are deflected more strongly over the sky when I add the random field. Figure 6.17 shows the positions of the 12 sample sources and the observed arrival directions of cosmic rays with $\log(R_{\rm EV})$=1.5 (or R=31.62 EV) from within 1° of each source with and without the random field. The colors of the events match the colors of their sources. Figures 6.18 and 6.19 are similar figures for R=10 and 3.16 EV, respectively.

Although the random field scatters the events compared to the regular field alone, for rigidity of 31.62 EV, events are still within about 10° of the sources for high latitudes ($|b| > 30°$). So, the methods that will be described in Chapter 7 considering the effect of the regular component are still applicable to the events with rigidities down to about 30 EV. The deflection magnitudes are within 10 degrees for R=31 EV. The lower rigidity plots on the other hand show that the events are very strongly scattered. For instance, at R=3 EV, a source at Galactic coordinate of $(l, b) = (135°, 41°)$ deflects cosmic rays all over the

left lower quarter of the sky map, which means deflections as large as 180°. These large deflection angles also exists in the JF12_R1 map, but it deflects the events within a few defined regions, whereas in the random field it is completely smeared over the sky.

Out of all the back-tracking simulations I have made a database that defines the observed arrival directions from each source in the sky with a resolution of better than 0.01°. I use the simulated back-tracking data as a tool for defining sources to study Centaurus A as an UHECR source candidate. The results will be described in the next chapter.

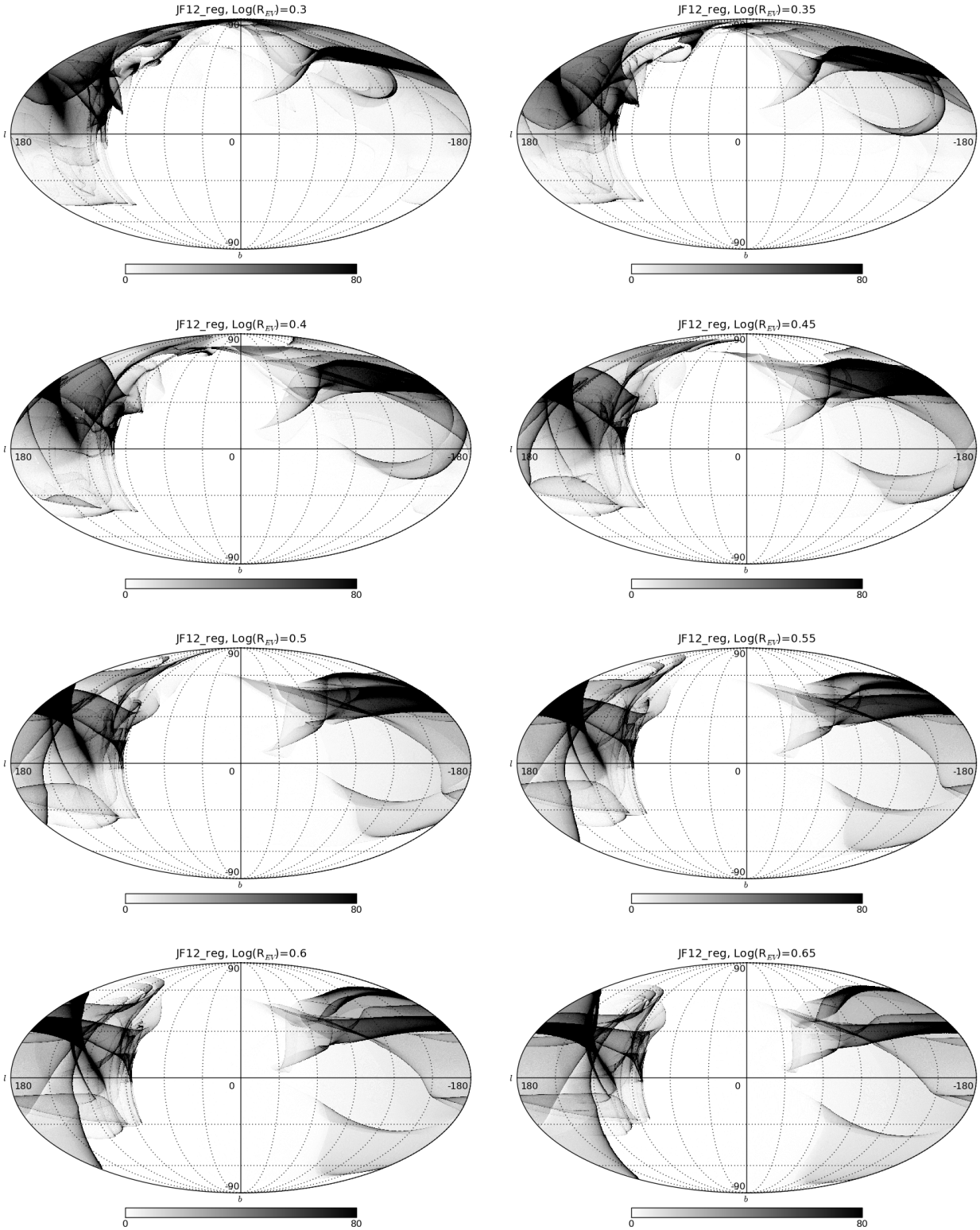

Figure 6.10: Sky maps of the back-tracked cosmic rays in the JF12_reg GMF model. The plots are for $\log(R_{\rm EV})$=0.3, 0.35, 0.4, 0.45, 0.5, 0.55, 0.6, and 0.65, that is equivalent to R=2.0, 2.24, 2.51, 2.82, 3.16, 3.55, 3.98, and 4.47 EV, respectively. The grey scale represents the particle counts in each HEALPix pixel. Pixels with counts larger than 80 are plotted with a count of 80.

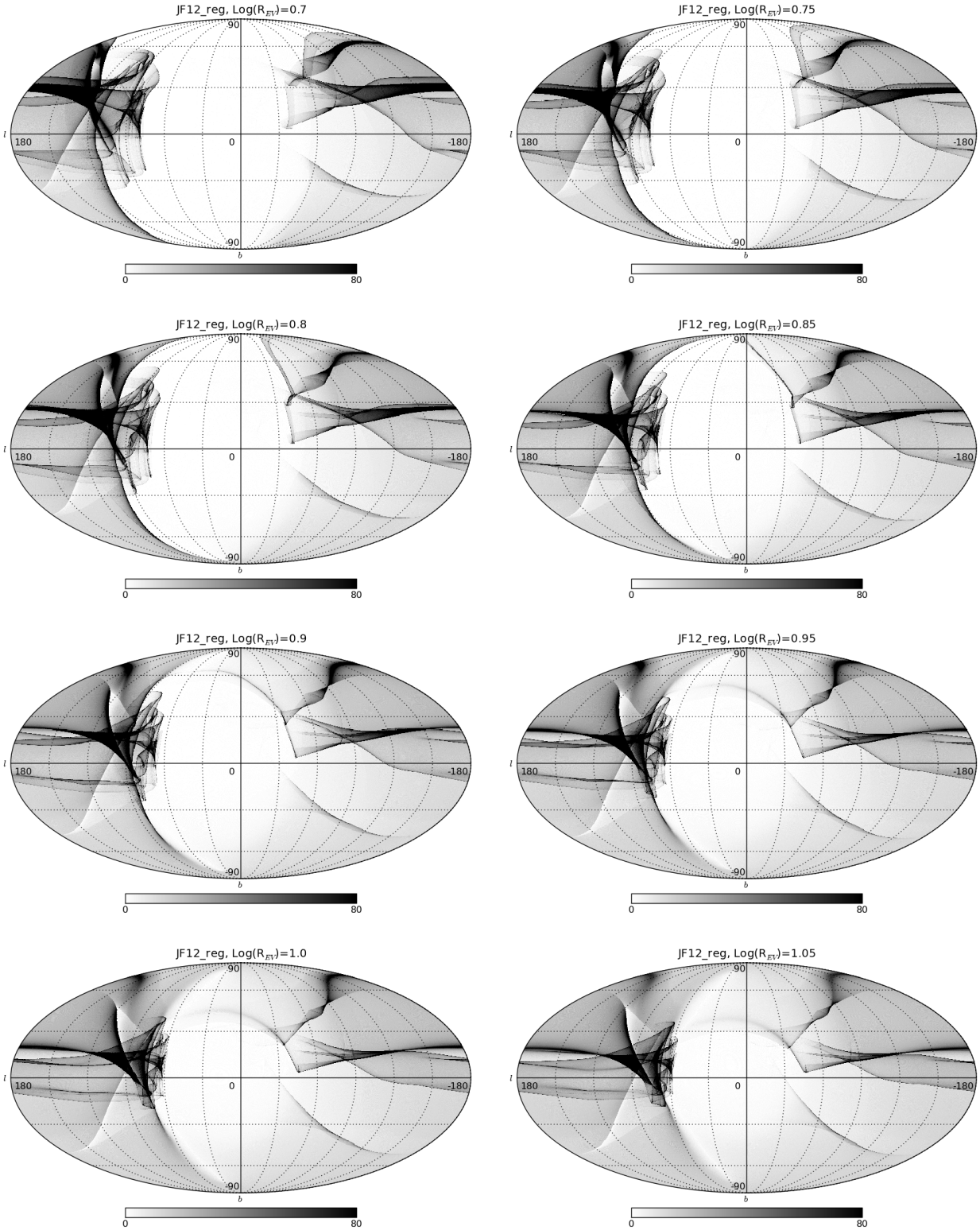

Figure 6.11: Sky maps of the back-tracked particles in the JF12_reg GMF model. The plots are for $\log(R_{\rm EV})$=0.7, 0.75, 0.8, 0.85, 0.9, 0.95, 1.0, and 1.05, that is equivalent to R=5.01, 5.62, 6.31, 7.08, 7.94, 8.91, 10, and 11.22 EV, respectively. The grey scale represents the particle counts in each HEALPix pixel. Pixels with counts larger than 80 are plotted with a count of 80.

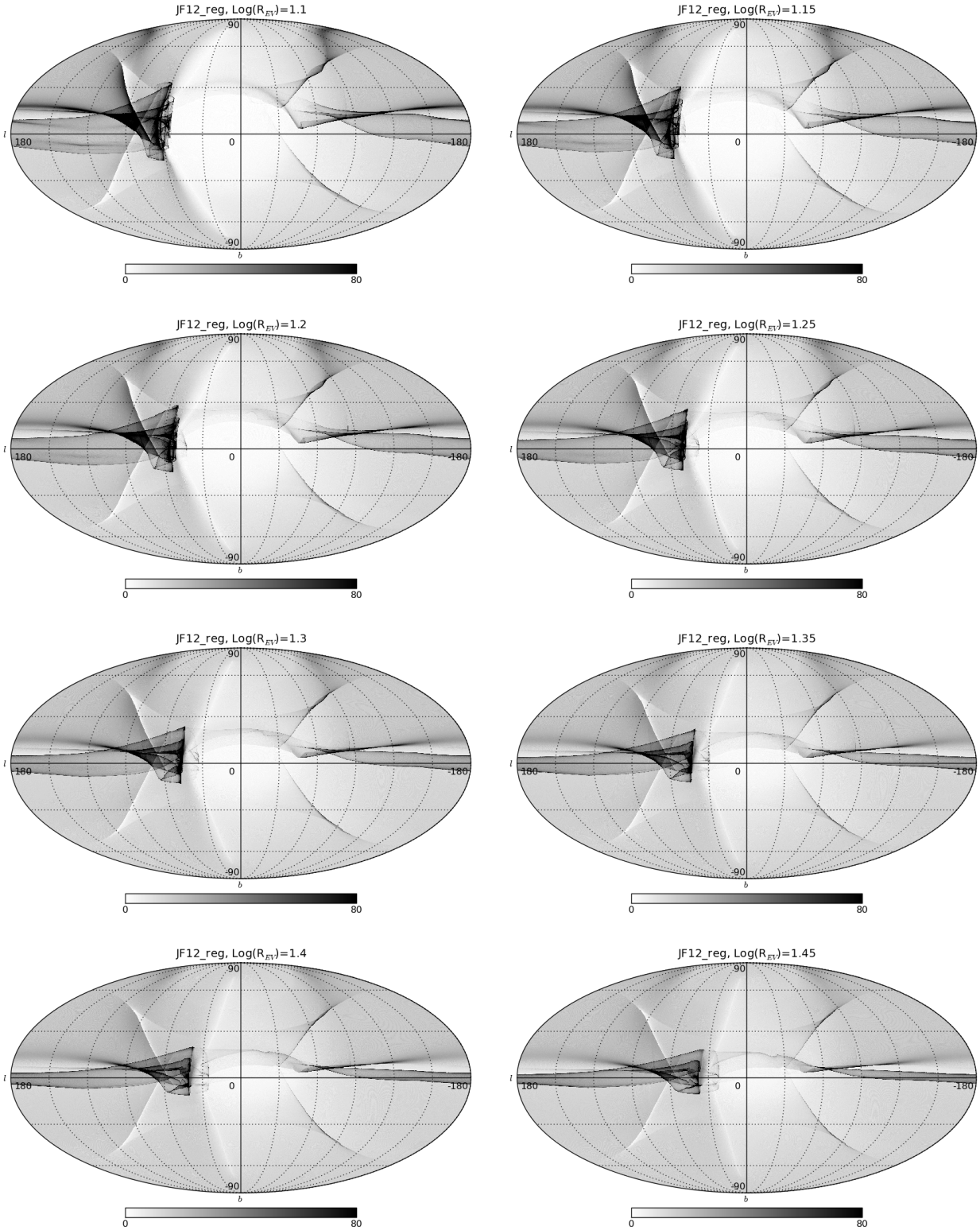

Figure 6.12: Sky maps of the back-tracked particles in the JF12_reg GMF model. The plots are for $\log(R_{\rm EV})$=1.1, 1.15, 1.2, 1.25, 1.3, 1.35, 1.4, and 1.45, that is equivalent to R=12.59, 14.13, 15.85, 17.78, 19.95, 22.39, 25.12, and 28.18 EV, respectively. The grey scale represents the particle counts in each HEALPix pixel. Pixels with counts larger than 80 are plotted with a count of 80.

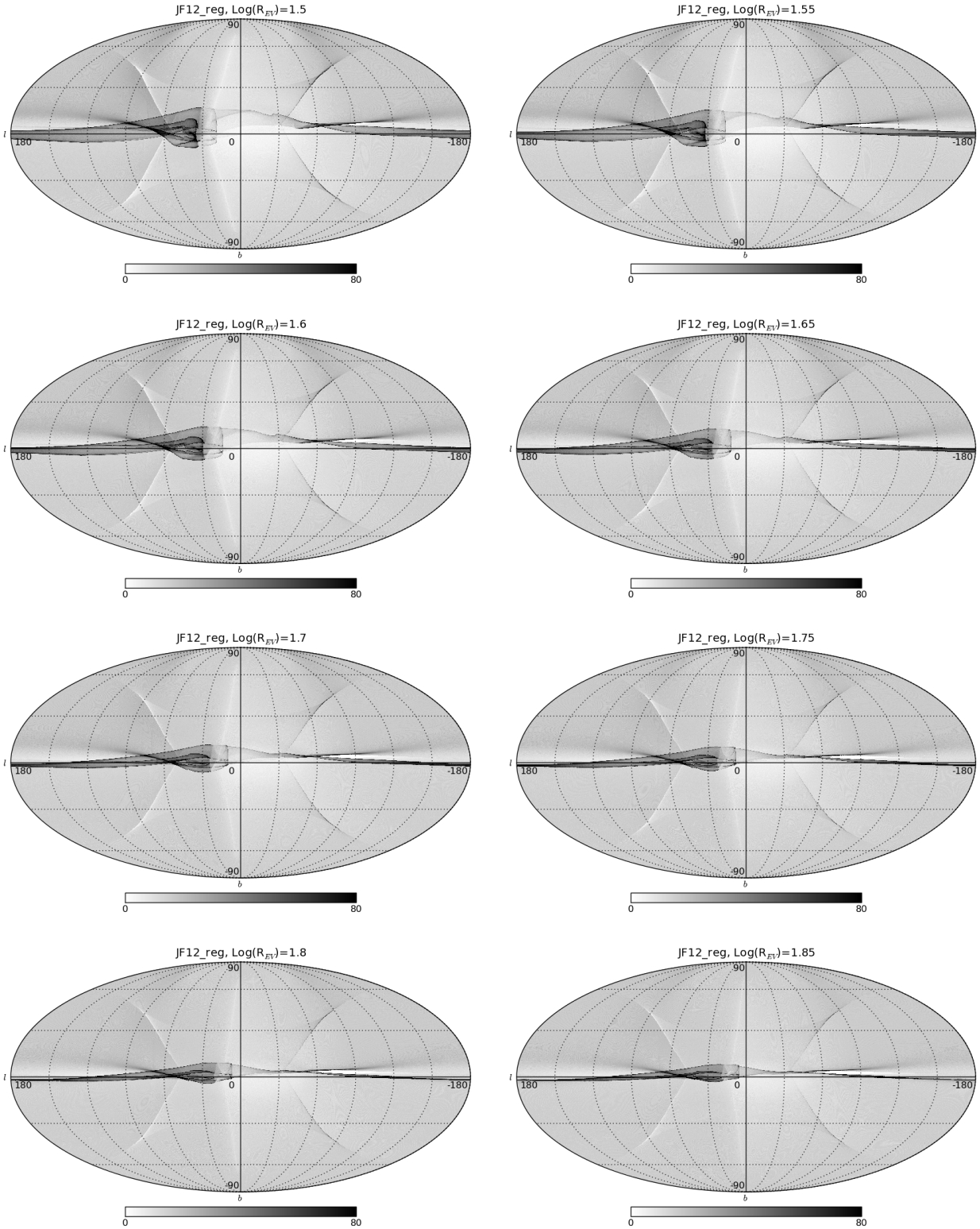

Figure 6.13: Sky maps of the back-tracked particles in the JF12_reg GMF model. The plots are for $\log(R_{\rm EV})$=1.5, 1.55, 1.6, 1.65, 1.7, 1.75, 1.8, and 1.85, that is equivalent to R=31.62, 35.48, 39.81, 44.67, 50.12, 56.23, 63.10, and 70.79 EV, respectively. The grey scale represents the particle counts in each HEALPix pixel. Pixels with counts larger than 80 are plotted with a count of 80.

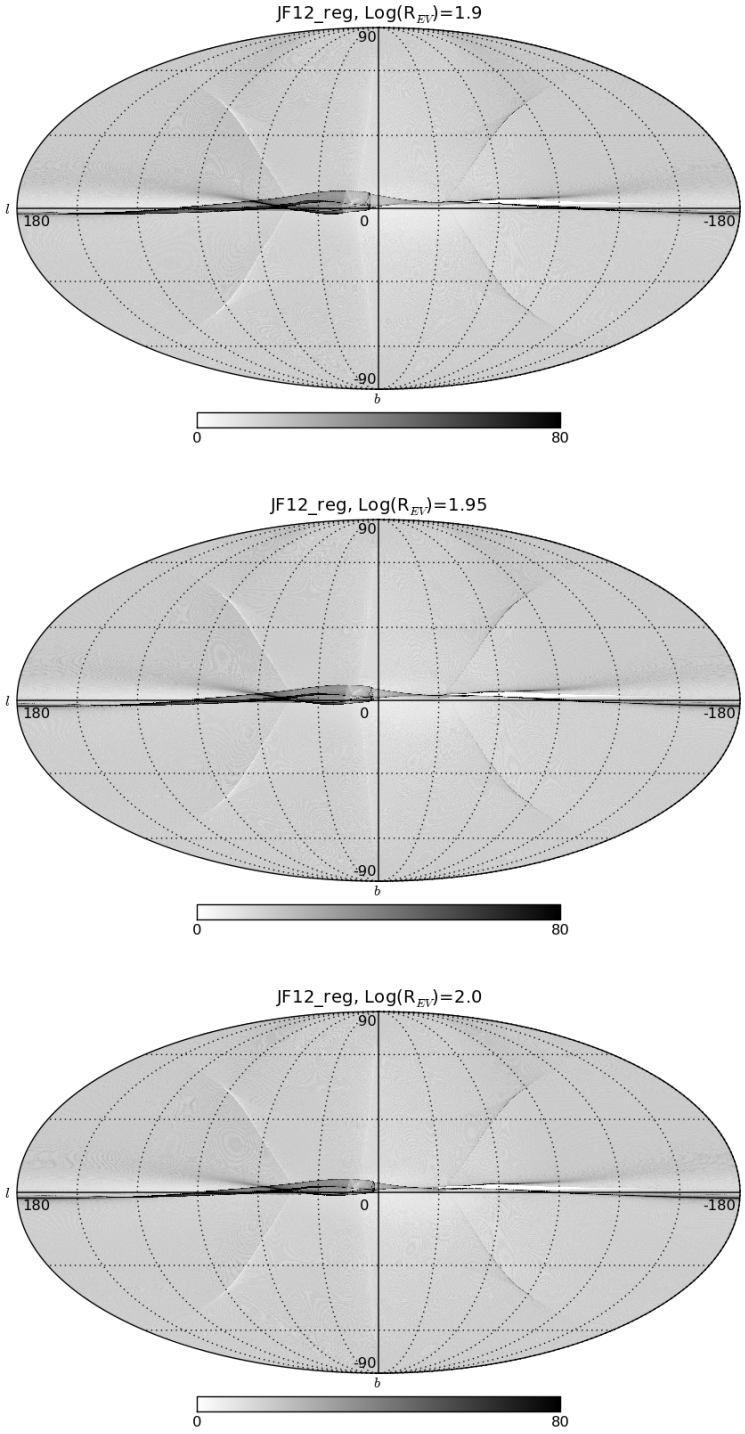

Figure 6.14: Sky maps of the back-tracked particles in the JF12_reg GMF model. The plots are for $\log(R_{\rm EV})$=1.9, 1.95, and 2.0, that is equivalent to R=79.43, 89.13, and 100.0 EV, respectively. The grey scale represents the particle counts in each HEALPix pixel. Pixels with counts larger than 80 are plotted with a count of 80.

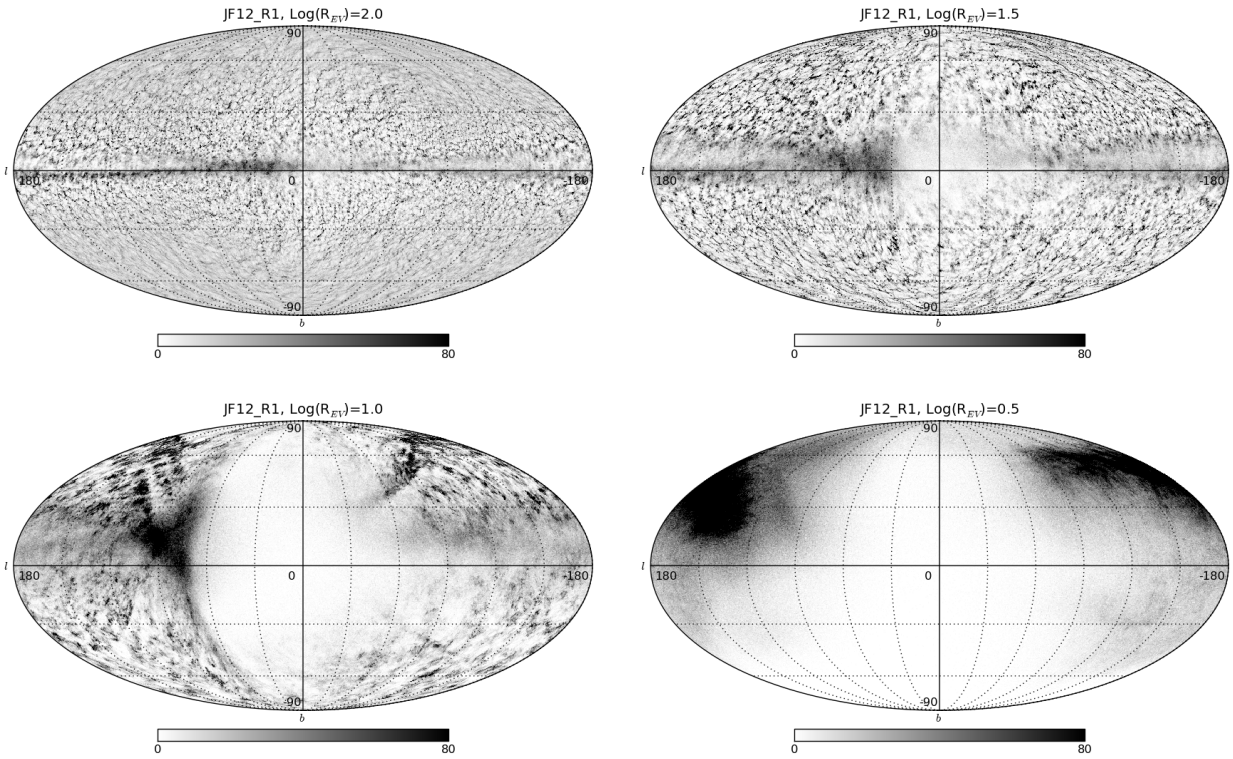

Figure 6.15: Sky maps of the back-tracked particles in JF12_R1 (regular component and random component). The skymap is a HEALPix map with resolution index 7. The plots are for $\log(R_{\rm EV})$=2.0, 1.5, 1.0, and 0.5 (equivalent to R=100, 31.62, 10, and 3.16 EV, respectively).

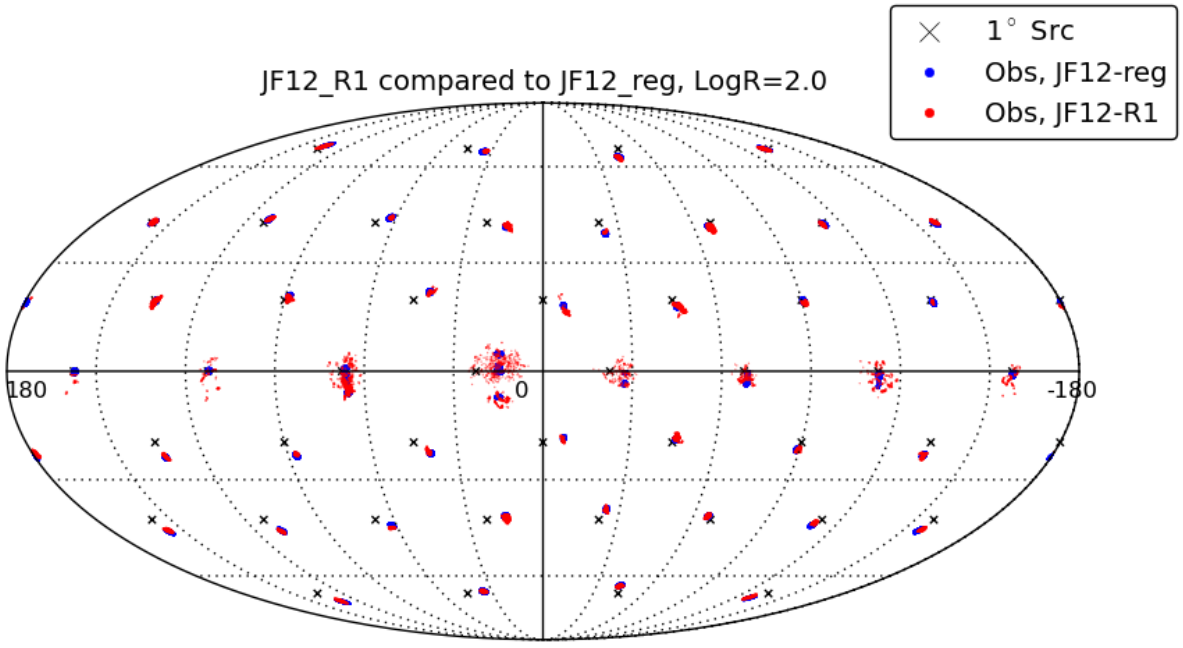

Figure 6.16: The deflections of cosmic rays with R=100 EV are compared in two cases of JF12_reg and JF12_R1.

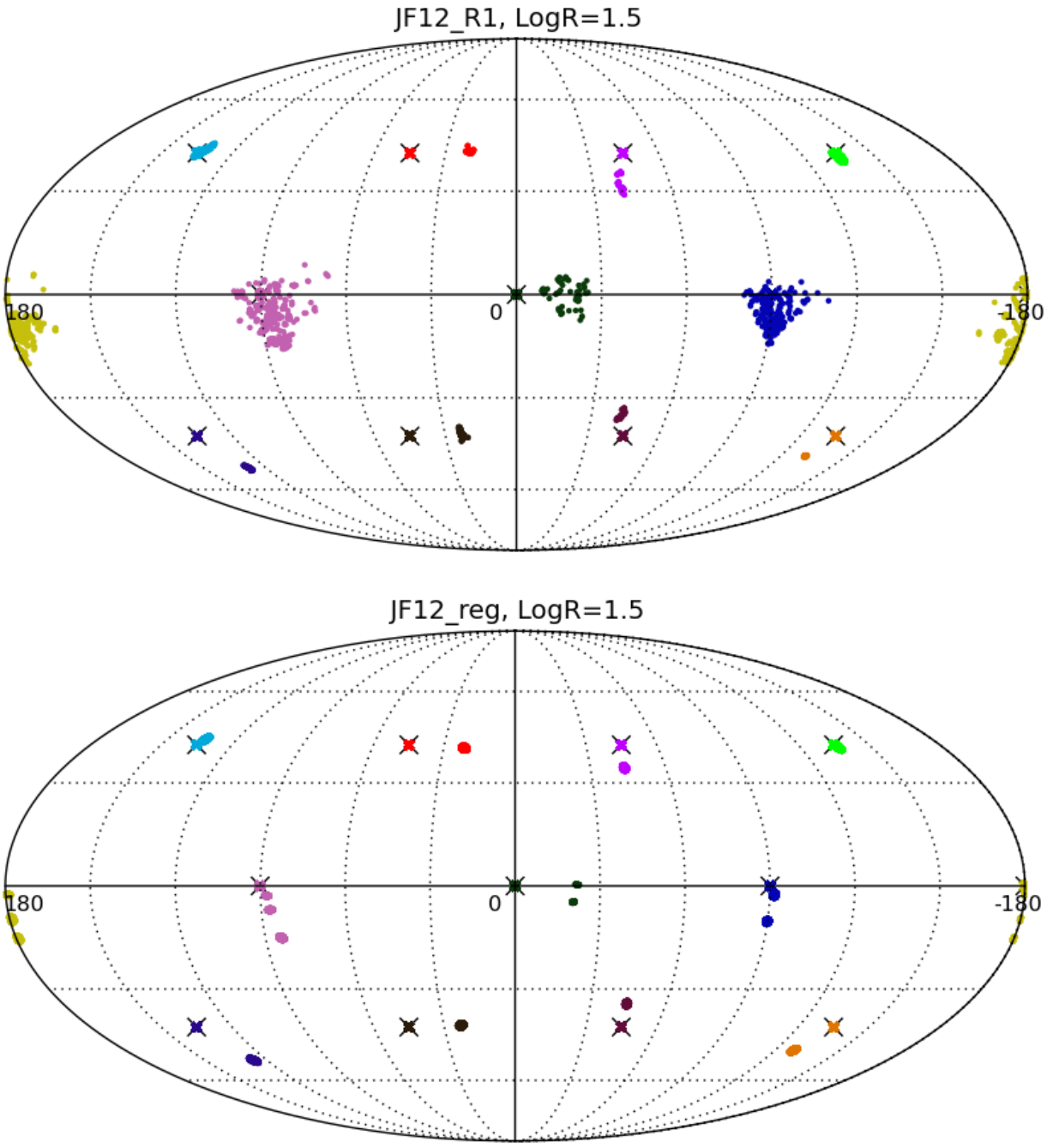

Figure 6.17: The deflections of cosmic rays with R=31.62 EV are compared in two cases of JF12_R1 (top) and JF12_reg (bottom). The colors match between each source and its events.

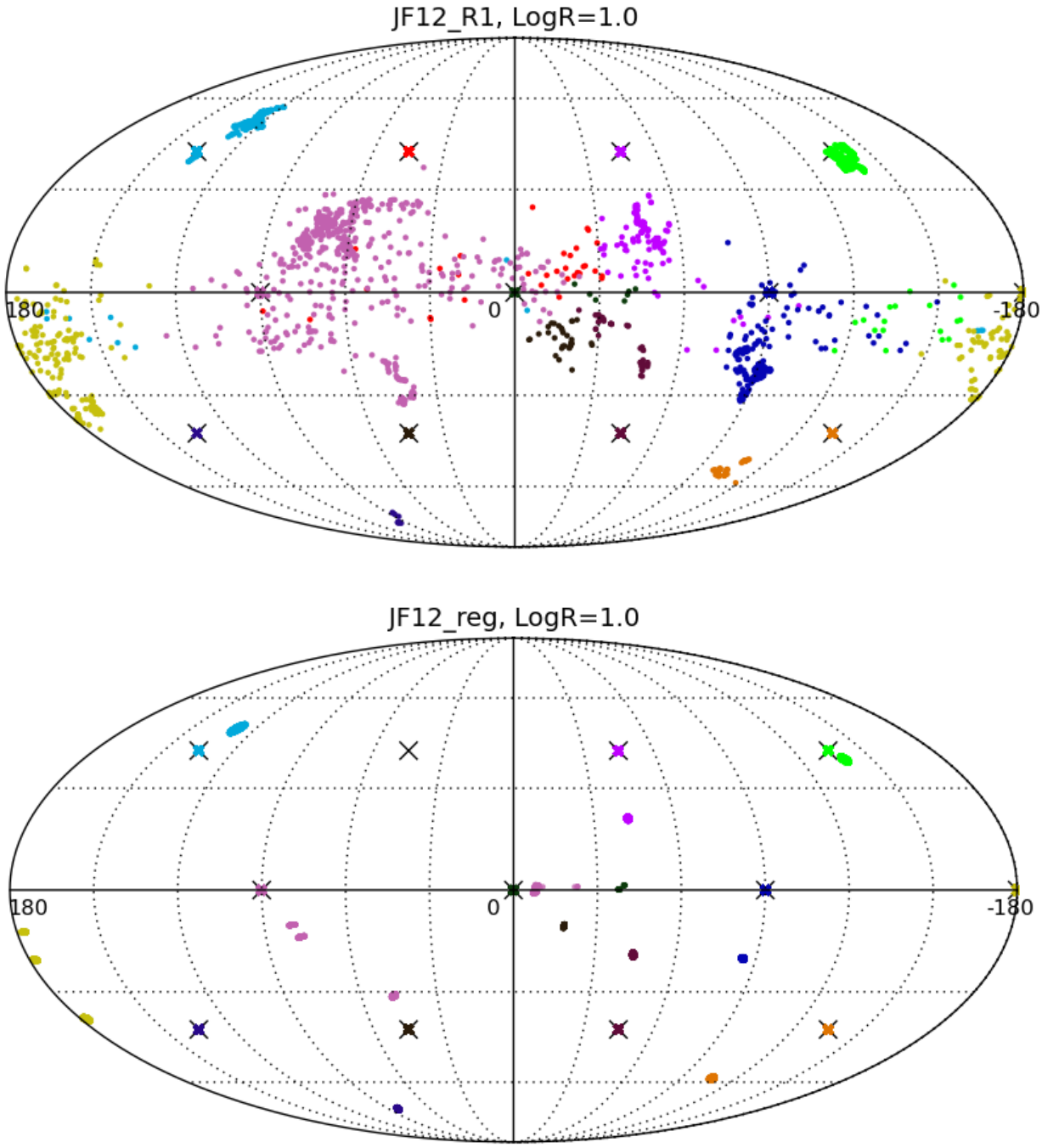

Figure 6.18: The deflections of cosmic rays with R=10 EV are compared in two cases of JF12_R1 (top) and JF12_reg (bottom). The colors match between each source and its events.

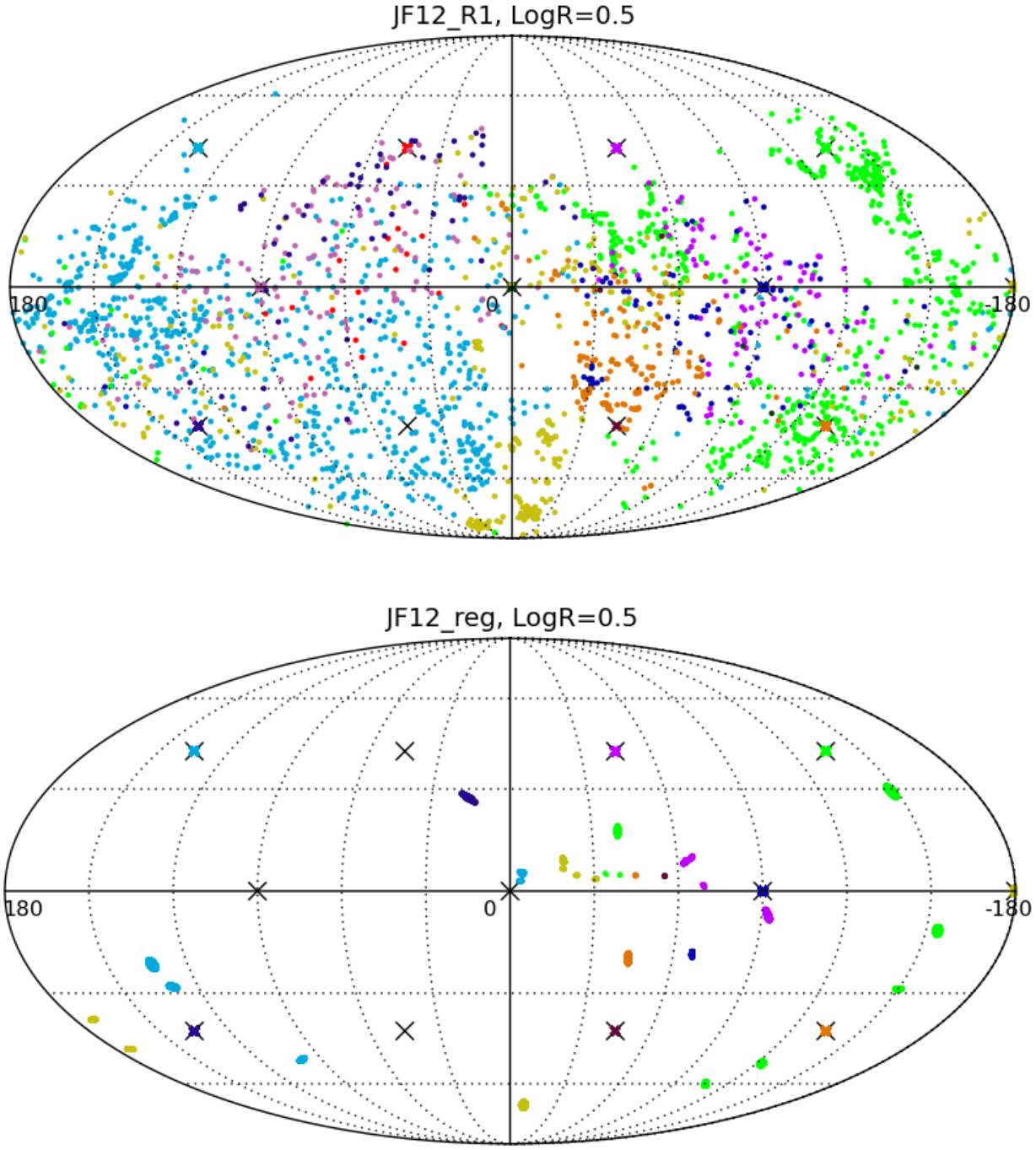

Figure 6.19: The deflections of cosmic rays with R=3.16 EV are compared in two cases of JF12_R1 (top) and JF12_reg (bottom). The colors match between each source and its events.

7. Centaurus A as a Possible Source of Ultra-High Energy Cosmic Rays

7.1 Introduction

The origin of the ultra-high energy cosmic rays (UHECRs) is one of the biggest mysteries of the cosmic ray physics. As discussed in Section 3.3.2, Pierre Auger Observatory has observed a correlation between UHECRs and AGN. Although the correlation fraction in the data has decreased from 69% to 38% between 2007 and 2010, this number is still higher than the expected correlation fraction of isotropically distributed events. Among all of the AGN in the VCV catalog, Centaurus A is the nearest. This galaxy is about 3.8 Mpc away and together with its radio lobes it makes a huge interesting object. Moreover there is an excess in a broad region seen around Cen A in Auger data for energies above 55 EeV. The cumulative number of events as a function of angular separation from Cen A is shown in Figure 7.1. Subtracting an isotropic flux from these numbers produces Figure 7.2.

The observed excess together with Cen A's close distance to Earth provides a motivation to focus our study on this single powerful radio galaxy to determine if it could be a significant source of the observed UHECRs. Since the number of observed events with $E \geq 55$ EeV at Pierre Auger Observatory is not yet large enough to draw any firm conclusions, I need to do large amount of simulations at different energies. One study is to include carefully the effects of the Galactic magnetic field on the trajectory of the charged particles. In addition, if I assume some UHECRs detected at Auger are coming from Cen A, then I can assign charges to those events by comparing their arrival direction with simulations, using their energies and the rigidity of our simulations. This method to be described in Section 7.4, is also based on the explicit assumption that the Galactic magnetic field (GMF) model is an excellent representation of the real GMF. I will consider the most recent GMF model, JF12, to track the UHECRs from and to Cen A to study any directional excess and compare to Auger observations. I first only consider the effects of the regular component of the JF12 GMF model and later I add a randomly oriented field to it.

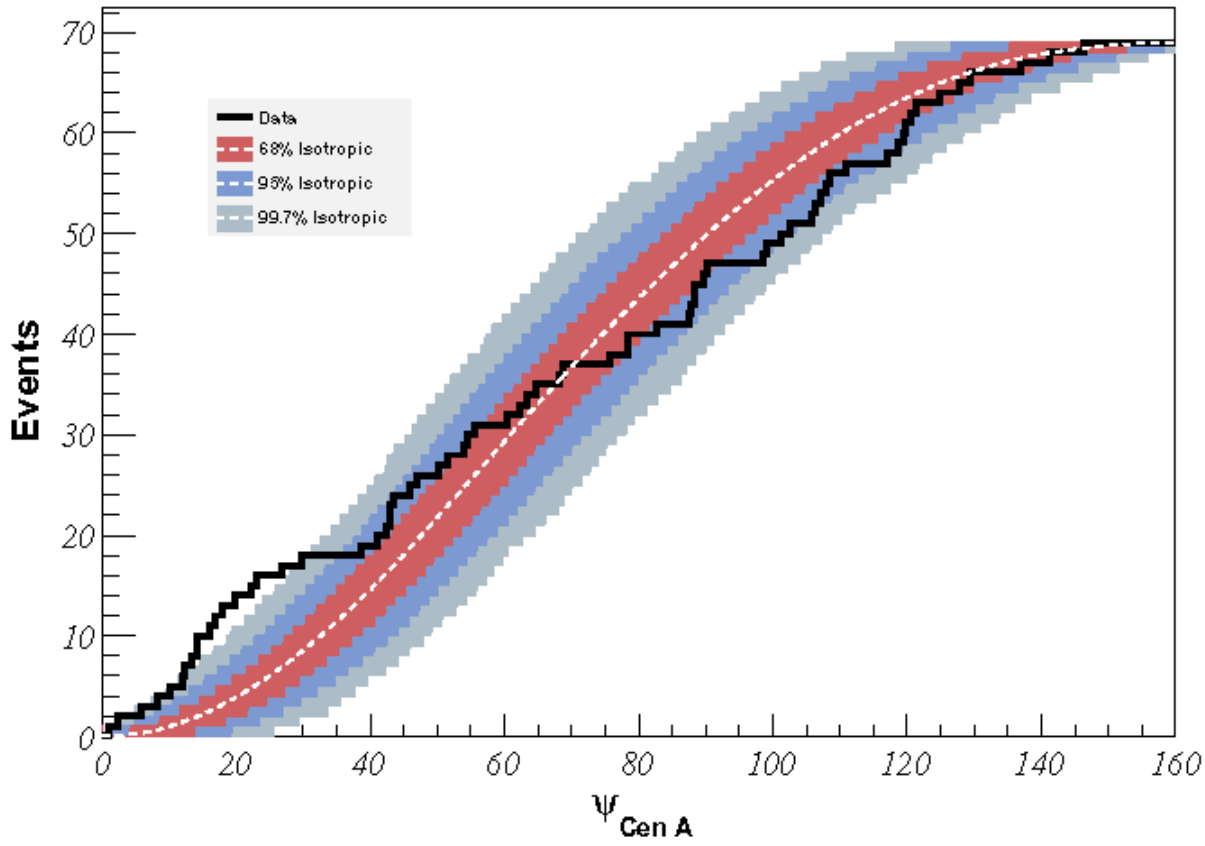

Figure 7.1: Cumulative number of events with $E \geq 55$ EeV as a function of angular distance from the direction of the center of Cen A. The bands show the dispersion expected for an isotropic flux. The plot is taken from (Pierre Auger Collaboration, 2010d).

7.2 Centaurus A

Centaurus A or NGC 5128 (Cen A) is a massive elliptical radio galaxy, in the constellation of Centaurus. It was discovered by Scottish astronomer James Dunlop in 1826. Herschel was the first to note the peculiar nature of NGC 5128 in 1847: "A nebula consisting of two lateral portions and no doubt of a small streak of nebula along the middle of the slit or interval between them, having a star at its extremity" and also "... a very problematical object, and must be regarded as forming a genus apart, since it evidently differs from mere 'double nebulae'..." (Israel, 1998).

Cen A is located at a distance of 3.8±0.1 Mpc (Harris et al., 2013) placing it as the closest radio galaxy to us. It is a unique source that has been studied over the entire electro-

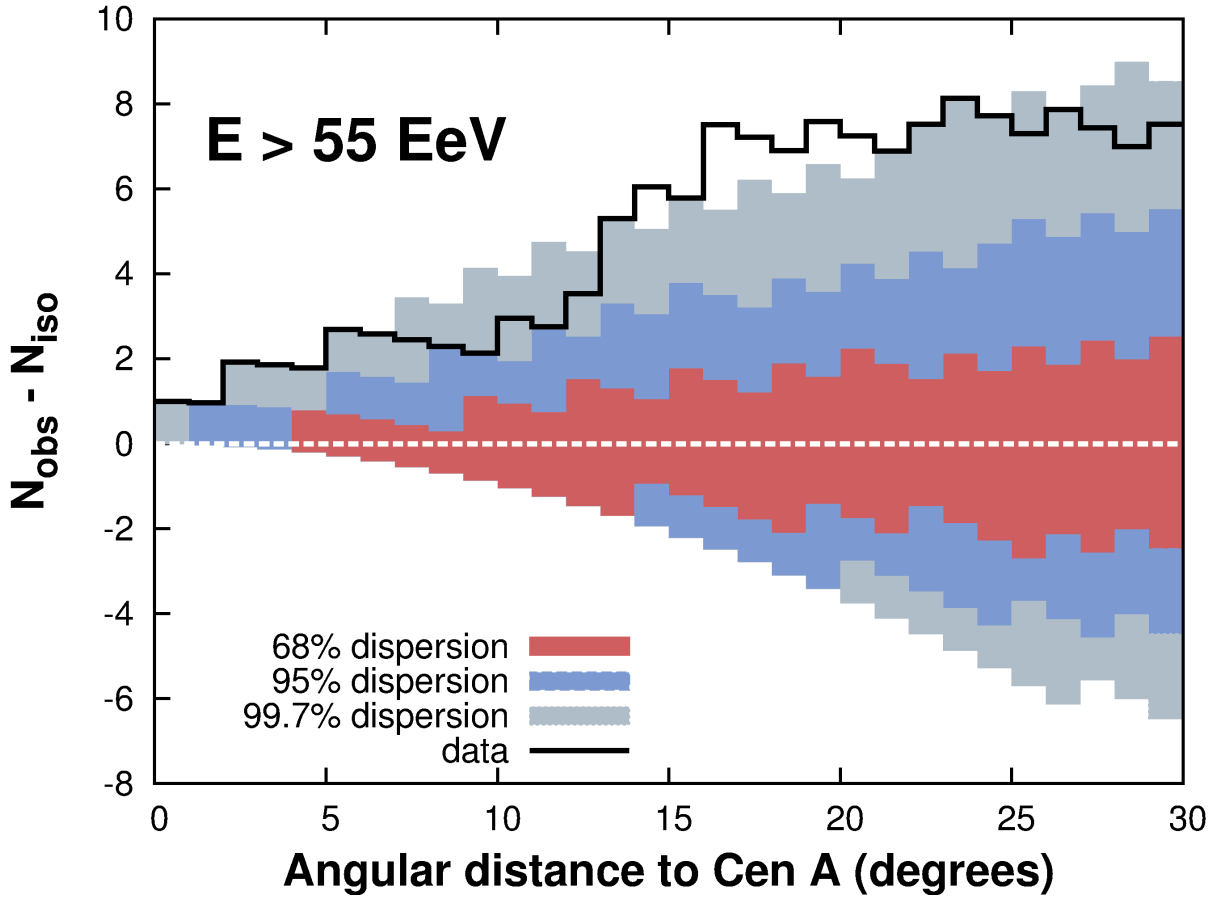

Figure 7.2: Cumulative number of events with $E \geq 55$ EeV (subtracting the average isotropic expectations) as a function of angular distance from the direction of Cen A. The bands correspond to the 68%, 95% and 99.7% dispersion expected for an isotropic flux. The plot is taken from (Pierre Auger Collaboration, 2011).

magnetic spectrum. Cen A is a Fanaroff-Riley class I (Fanaroff & Riley, 1974) radio galaxy with a radio luminosity of $L_{1.4\,\mathrm{GHz}} = 2.3 \times 10^{24}\,\mathrm{W\,Hz^{-1}}$ (Cooper et al., 1965). Cen A has an active galactic nucleus in its center, which ejects relativistic jets: a pair of asymmetric nuclear jets and a pair of inner jets (Feain et al., 2011). The inner jets extend about 1.4 kpc from the center (Burns et al., 1983), where the inner radio lobes extend a further 5 kpc from the nucleus (Clarke et al., 1992). Cen A has also middle and outer lobes that extend about 14 and 500 kpc, respectively.

Figure 7.3 shows a high resolution radio image of Cen A (Feain et al., 2011). As seen from Earth, Cen A has angular dimensions of $8^\circ \times 4^\circ$ that translate to a linear size of 500×200 kpc^2 (Israel, 1998). If it was visible to the eye, it would be about 100 times larger than the full moon in the night sky (Figure 7.4).

7.3 Results of Tracking Ultra-High Energy Cosmic Rays from Centaurus A

In this section, I present the results of propagating UHECRs from Centaurus A to characterize their arrival-direction locus and determine whether Cen A could be a significant source of the UHECR excess reported by Auger. I will also discuss the possibility of assigning charges to Auger data based on the simulations. I use the recent GMF model of Jansson and Farrar (JF12) and the *CRT* code to propagate the UHECRs. First, I will briefly present the results of the forward-tracking method and then devote the rest of the chapter to the more efficient method that is the back-tracking.

7.3.1 Forward-Tracking Simulations

The method to forward-track the UHECRs is described in Section 6.2. Figure 7.5 shows the initial locations of successfully detected cosmic rays with different rigidities on the injection plane. Here the detector size is 2 pc where I started to see convergence in the detection. Figure 7.6 shows the arrival directions of the successful events. In both figures, the circles are the centroids of the regions of successful events in each rigidity. The blue circles are in the presence of the complete JF12 model using the method of generating random field which is described in Section 4.4.3 and the red circles are where no random field is taken into account.

These two plots with their small error bars (the standard deviation of the successful events at each rigidity) show that the regions are more compact than were originally thought. Based on the GMF model and the hypotheses in the current study, there are only a few regions that emit particles at different energies observed at Earth. I conclude Cen A could not be the source of more than a few UHECRs according to these results. But as I said in Chapter 6,

Figure 7.3: High resolution radio image of Cen A at 1.4 GHz showing the inner lobes, the northern middle lobes and the giant outer lobes. Image is the Figure 2 of (Feain et al., 2011).

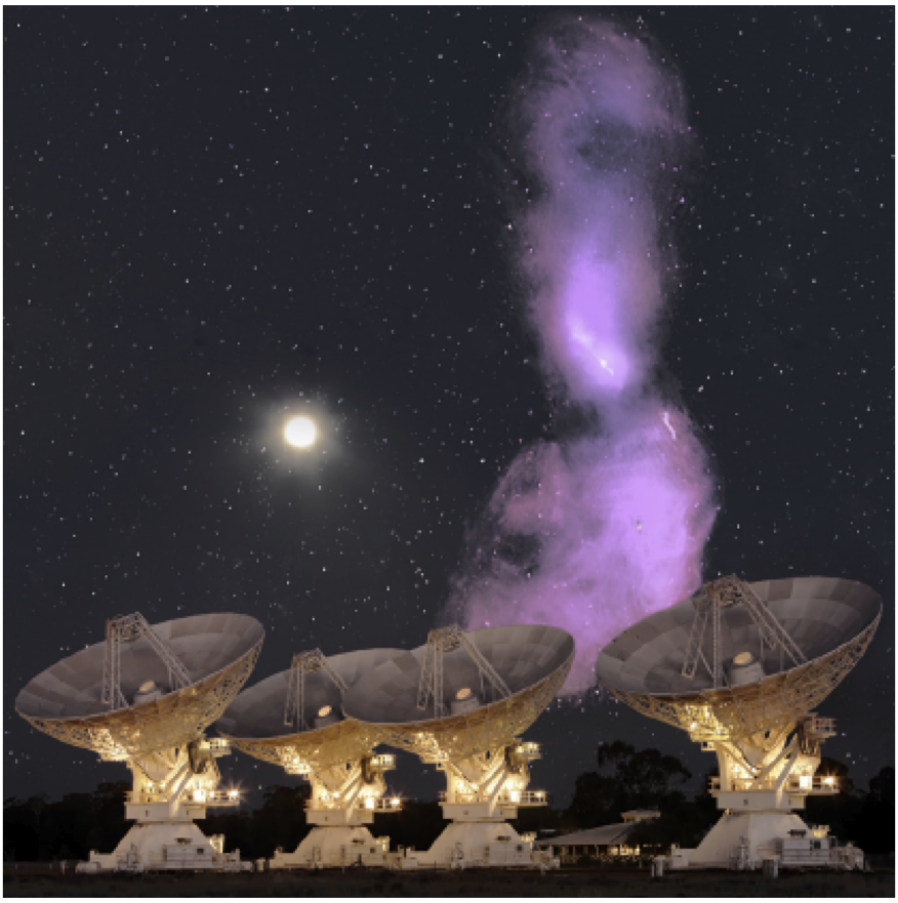

Figure 7.4: Radio image of Cen A compared to the size of the Moon. The Australian Telescope Compact Array (ATCA) is shown in the foreground. Image is from NASA APOD, 13 April 2011.

I am going to rely on a more accurate method, back-tracking the UHECRs to Centaurus A, as described in the next section. Also I will discuss the effect of our recent random field model at the end.

7.3.2 Back-Tracking Simulations

For most of this study, I propagate particles through only the regular component of the GMF. At the end of the chapter, I will discuss the changes due to the presence of an additional Kolmogorov-turbulent field. The method I use to back-track the UHECRs isotropically from the Earth is described in Section 6.3. The back-tracking is done for the whole sky but since I am only interested in the events from Cen A, I must pick events with certain velocity

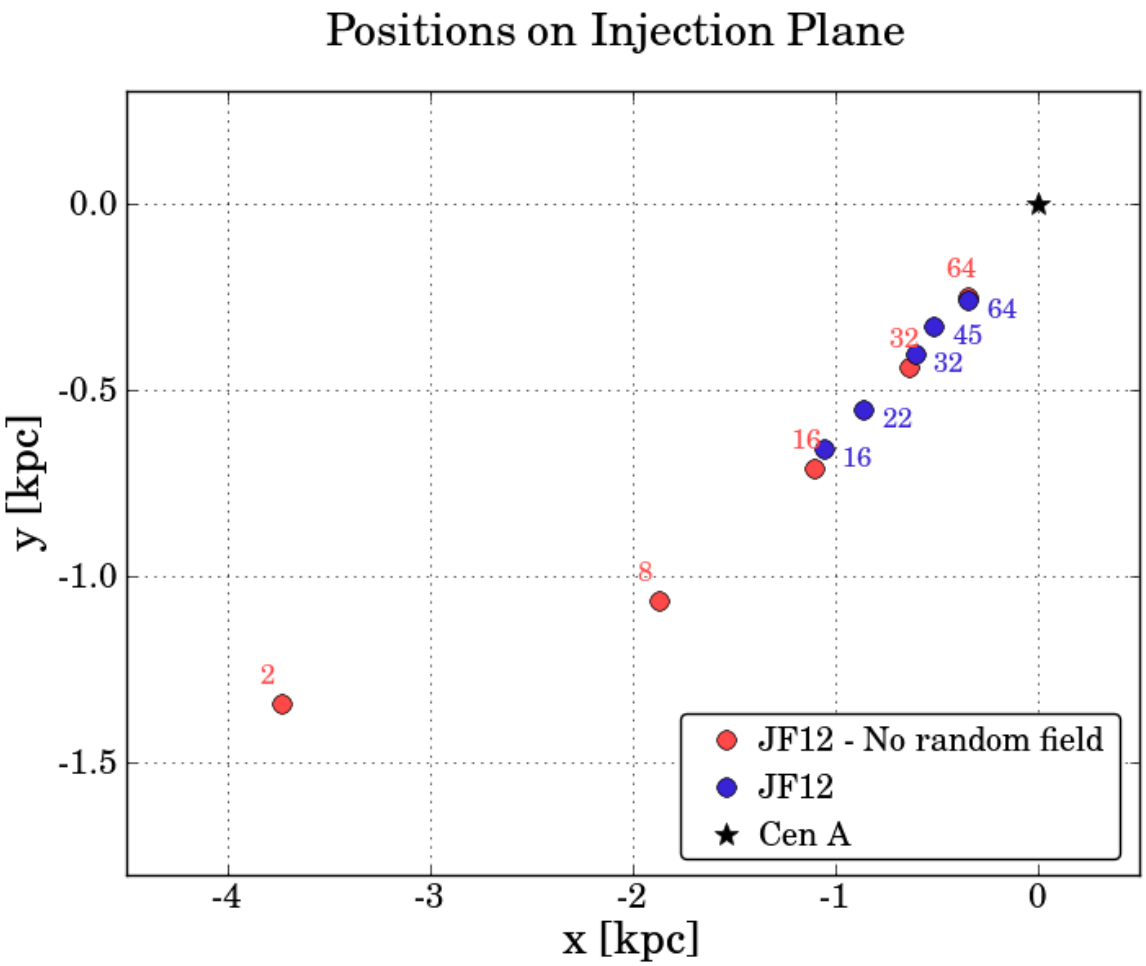

Figure 7.5: Centroids of the simulated events of different rigidities from Cen A on the injection disk. The number on each circle shows the rigidity of the successful events. The blue circles are in the full regular, striated, and random JF12 GMF model whereas the red circles are in the regular + striated components.

directions. Figure 7.7 shows the 1.4 GHz radio image of Cen A in equatorial coordinates. This object is large enough that one can look in separate studies at its different areas that could possibly inject and accelerate UHECRs.

I first look at the center of Cen A and a region with angular size of 3° around it that includes a good portion of the radio galaxy that could be possible emission and acceleration site of UHECRs. Since Cen A is about 3.8 Mpc away from the Earth, the 3° circle would correspond to a distance of about 200 kpc from the center. As I discussed earlier the outer

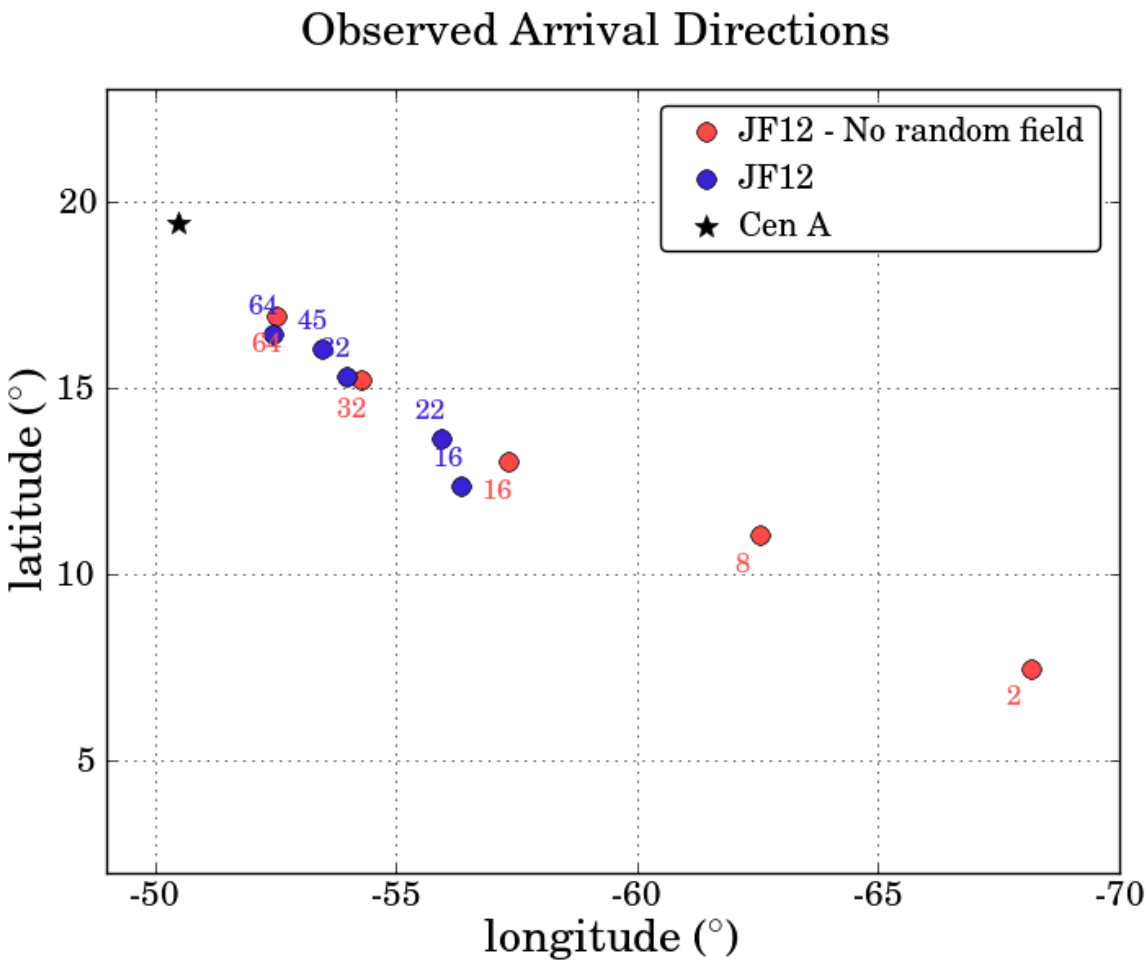

Figure 7.6: Observed arrival directions of the simulated events from Cen A in Galactic coordinates. The number on each circle shows the rigidity of the successful events. The blue circles are in the full regular, striated, and random JF12 GMF model whereas the red circles are in the regular + striated components.

lobes would lie about 500 kpc from the center, thus a value of 200 kpc is a good estimate for possible source regions of accelerating the particles.

In back-tracking method, any particle with a velocity vector pointing to the defined region around Cen A had a starting point on Earth. That makes it possible to do a reverse study and look at the observed arrival directions of the cosmic rays from Cen A and its vicinity. Figure 7.8 shows the observed arrival directions of simulated events from Cen A for different rigidities R with $\log(R_{\rm EV})$=0.3 up to $\log(R_{\rm EV})$=2.0 in steps of 0.05. Each color represents a different rigidity as indicated in the legend. This "snake-like" image has a head

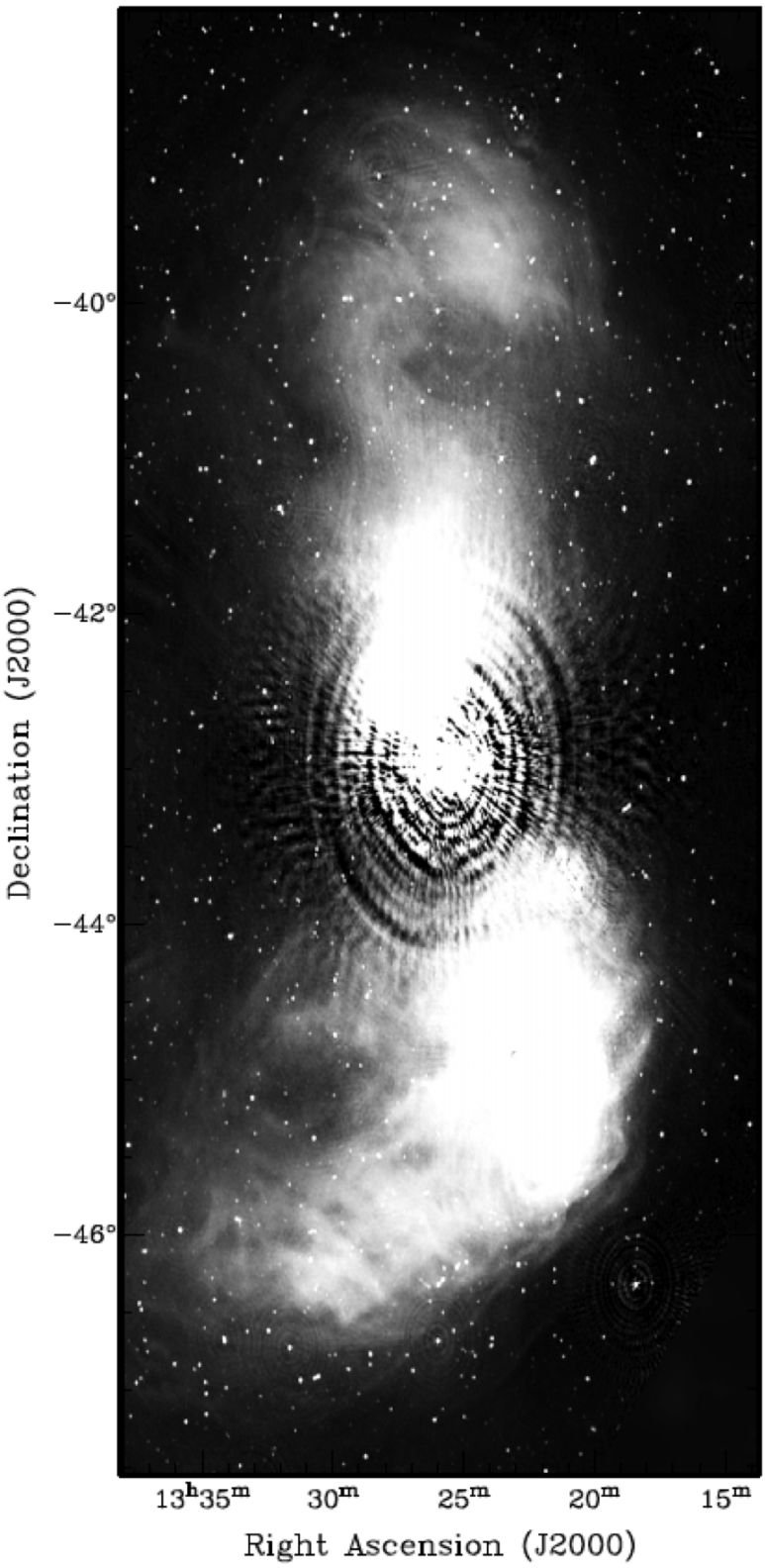

Figure 7.7: 1.4 GHz radio image of Cen A shown in equatorial coordinates. The center of Cen A and its radio lobes are shown here. The northern lobe is at the top of image and the southern lobe is at the bottom. Image is the Figure 3 of (Feain et al., 2011).

located near and pointed towards Cen A (that is the largest simulated rigidity R=100 EV) and the rigidity decreases along the body where the average angular distance from the center of Cen A increases. This is in general compatible with what is expected from the magnetic deflections; the larger the rigidity, the less magnetic deflections. Average deflections become larger with decreased rigidity. At R=17.78 EV, I first see a second region appear separated from the snake-like thread. The number of such regions increases at lowest rigidities, forming small "islands" of particles.

In my analysis, each island is considered as a separate region for calculating the average longitude and latitude and the standard deviations of longitude and latitude. Figure 7.9 shows the centroids of the regions of Figure 7.8. The error bars on the simulated events are the standard deviation of the arrival distribution at each rigidity. These regions show the potential arrival positions of the UHECRs according to their rigidity. It also makes possible a study of other properties of the observed UHECRs, such as mass composition, as will be discussed in the next section.

I also test a region with angular size of 1° near the center of Cen A, in case the sources are actually closer to the center and not located out to about 200 kpc. Figure 7.10 shows the observed arrival directions of the simulated cosmic rays within 1° of center of Cen A.

Another hypothesis is if the northern and southern tips of Cen A radio lobes are the sources. So I separately study the observed directions of the simulated events coming from within 3° near the tips of the northern and southern radio lobes, Figures 7.11 and 7.12. Comparing the arrival directions from center, north and south of Cen A, I find that the general stream of the events are the same, however the appearance of separate regions from the main thread happens at lower rigidities from the northern tip and at higher rigidities from the southern tip.

Having found the arrival direction locations of the simulated events, I can calculate the event fraction within an angle ψ from each Cen A source location (north, center, or south) to compare with the event excess observed at Auger. Here I am only interested in ultra-high

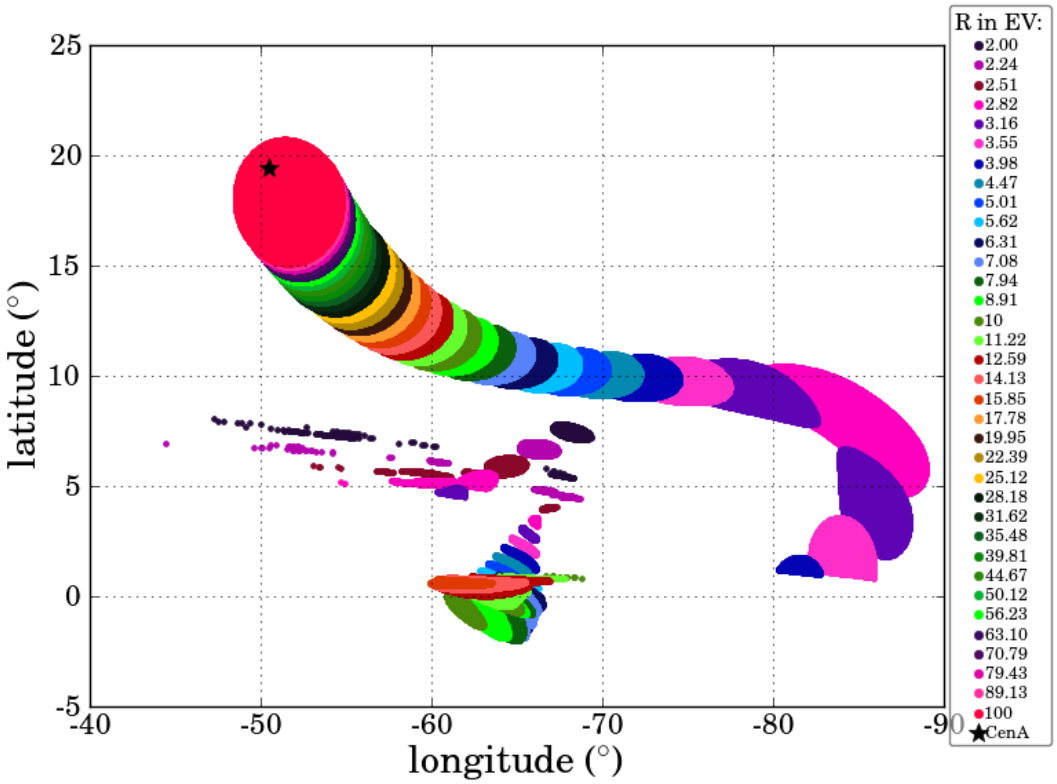

Figure 7.8: Observed directions of the simulated events within 3° of the vicinity of Cen A center shown in Galactic coordinates.

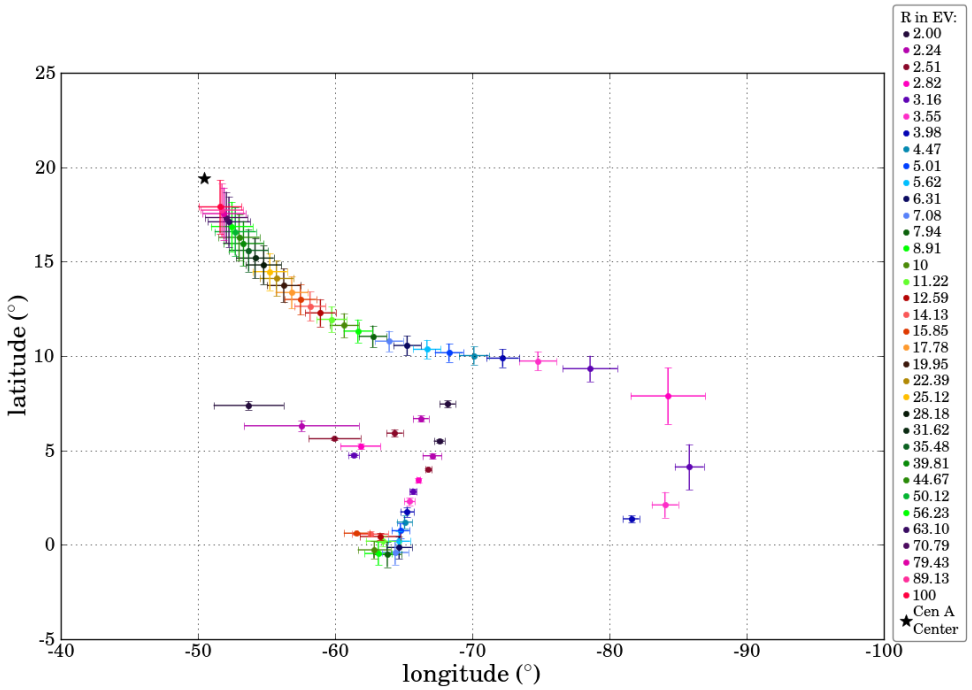

Figure 7.9: Centroids of the observed directions of the simulated events within 3° of the vicinity of Cen A center in Galactic coordinates. The error bars indicate the standard deviation of events with same rigidity.

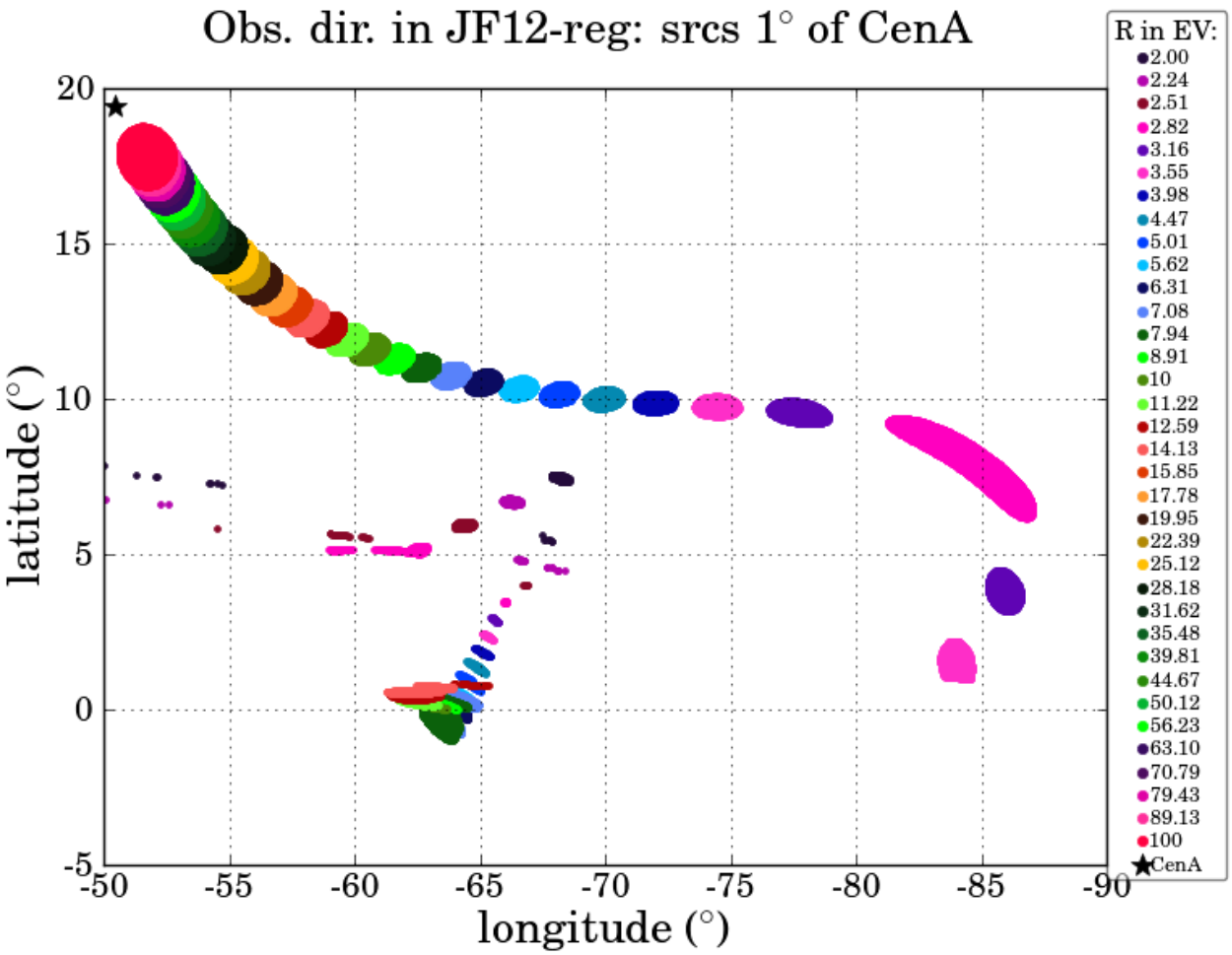

Figure 7.10: Observed directions of the simulated events within 1° of the vicinity of Cen A center in Galactic coordinates.

energy events with energies above 55 EeV. If I assume all the particles are protons, then I only study the events with $R \geq 56.23$ EV. The maximum simulated rigidity will be 100 EV in this case. On the other hand, if the events are all iron nuclei, the minimum rigidity would be $R = E/Z = 55$ EeV / 26 $\approx$ 2.11 EV. The minimum rigidity I can use would be 2.24 EV in this study. I insert an upper limit of 200 EeV ($\approx$ highest energy event ever observed) for the energy of iron events, so our maximum available simulated rigidity for iron candidates would be 7.08 EV.

I plot the normalized cumulative number of protons and iron nuclei with $E \geq 55$ EeV as a function of their angular distances from the direction of Cen A's center in Figure 7.13.

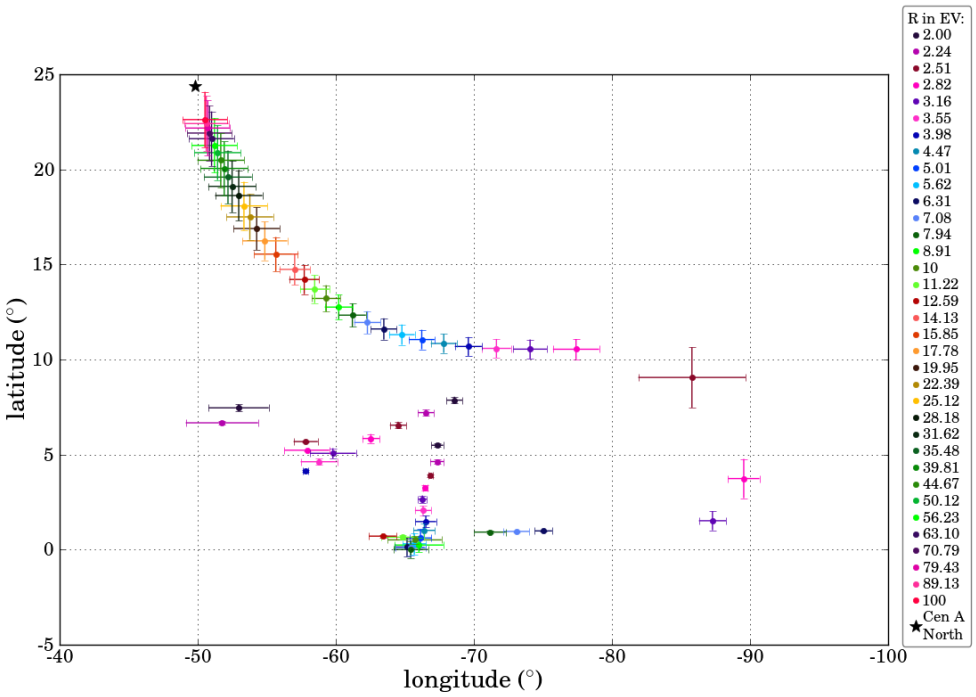

Figure 7.11: Centroids of the observed directions of the simulated events within 3° of the vicinity of the tip of northern radio lobe of Cen A, shown in Galactic coordinates. The error bars indicate the standard deviation of events with same rigidity.

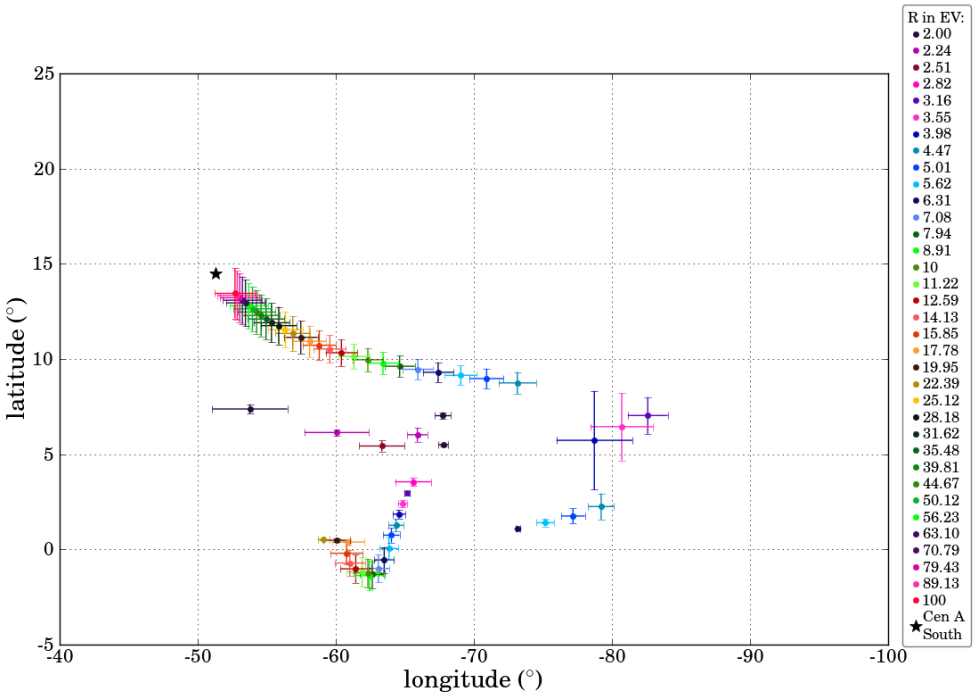

Figure 7.12: Centroids of the observed directions of the simulated events within 3° of the vicinity of the tip of southern radio lobe of Cen A, shown in Galactic coordinates. The error bars indicate the standard deviation of events with same rigidity.

I look at the observed arrival directions up to 45° around Cen A. The simulated events are weighted by Auger exposure (Sommers, 2001) and the energy spectrum (Pierre Auger Collaboration, 2013) to better present the observations. On average, the magnetic deflections of protons are smaller than that for iron nuclei as expected. Adding the proton and iron events together (50% contributions from each), I compare them with the expected isotropic flux. Figure 7.14 shows that there is a visible excess both for protons and iron nuclei above the isotropic expectation.

I repeat this analysis for events within 3° of the northern and southern tips of Cen A radio lobes. The resulting plot is shown in Figure 7.15. This shows that the excess from Cen A exists regardless of the position of the source along the large radio galaxy.

7.4 Mass Composition

As I discussed in Section 7.3, the simulations are done with different rigidities, meaning a 1 EV event can be either a proton with energy of 1 EeV, a Carbon nucleus with energy of 6 EeV, a 26 EeV Iron nucleus or any other element between proton and Iron with $E = RZ$. At Auger, the energy of the particles is measured well, using the energy reconstruction methods described in Sections 3.2.2 and 3.2.4, but not the types of the primary particles. Comparing the real data with simulations could help identify the mass composition of UHECRs. Here I have developed a method described below to determine the mass composition of the UHECRs arriving from Cen A.

7.4.1 Mass Composition Method

Here I take the observed events from Auger data that are arriving from Cen A and compare their arrival directions with the arrival directions of simulated events shown in Figure 7.9. Simply, the idea is to identify the nearest simulated rigidity for each Auger event based on their arrival directions. Suppose an Auger event with a reconstructed energy of 25.41 EeV happens to lie very close to the simulated rigidity of 2 EV (see the red star in Figure 7.16). This means Auger event, if it originated at Cen A, must have a charge equal to 13 in

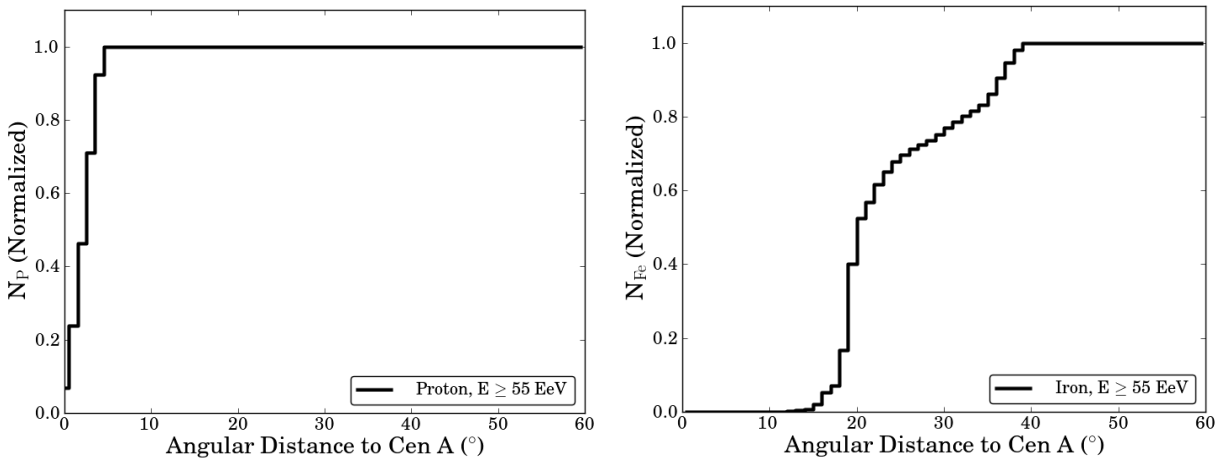

(a) Proton (b) Iron

Figure 7.13: Cumulative number of events with $E \geq 55$ EeV as a function of angular distance from the direction of the center of Cen A for (a) proton and (b) iron.

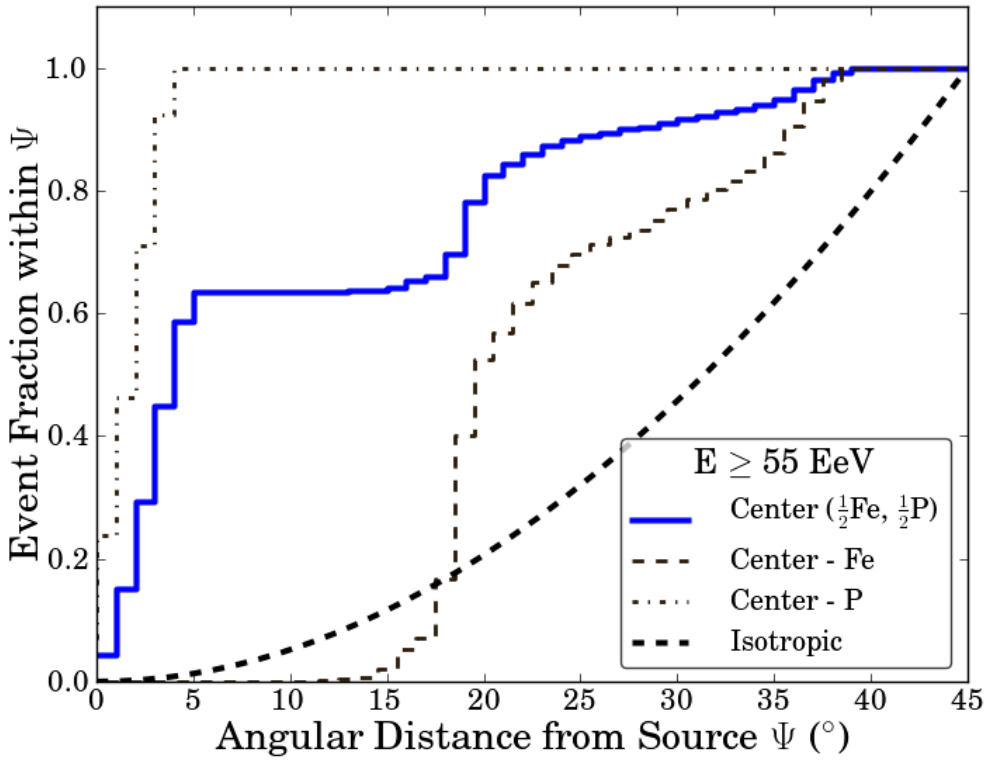

Figure 7.14: Cumulative number of proton and iron events with $E \geq 55$ EeV as a function of angular distance from the direction of the center of Cen A. The thick dashed line shows the expected isotropic flux. The thin dashed line shows only iron events. The dot-dashed line shows only proton events.

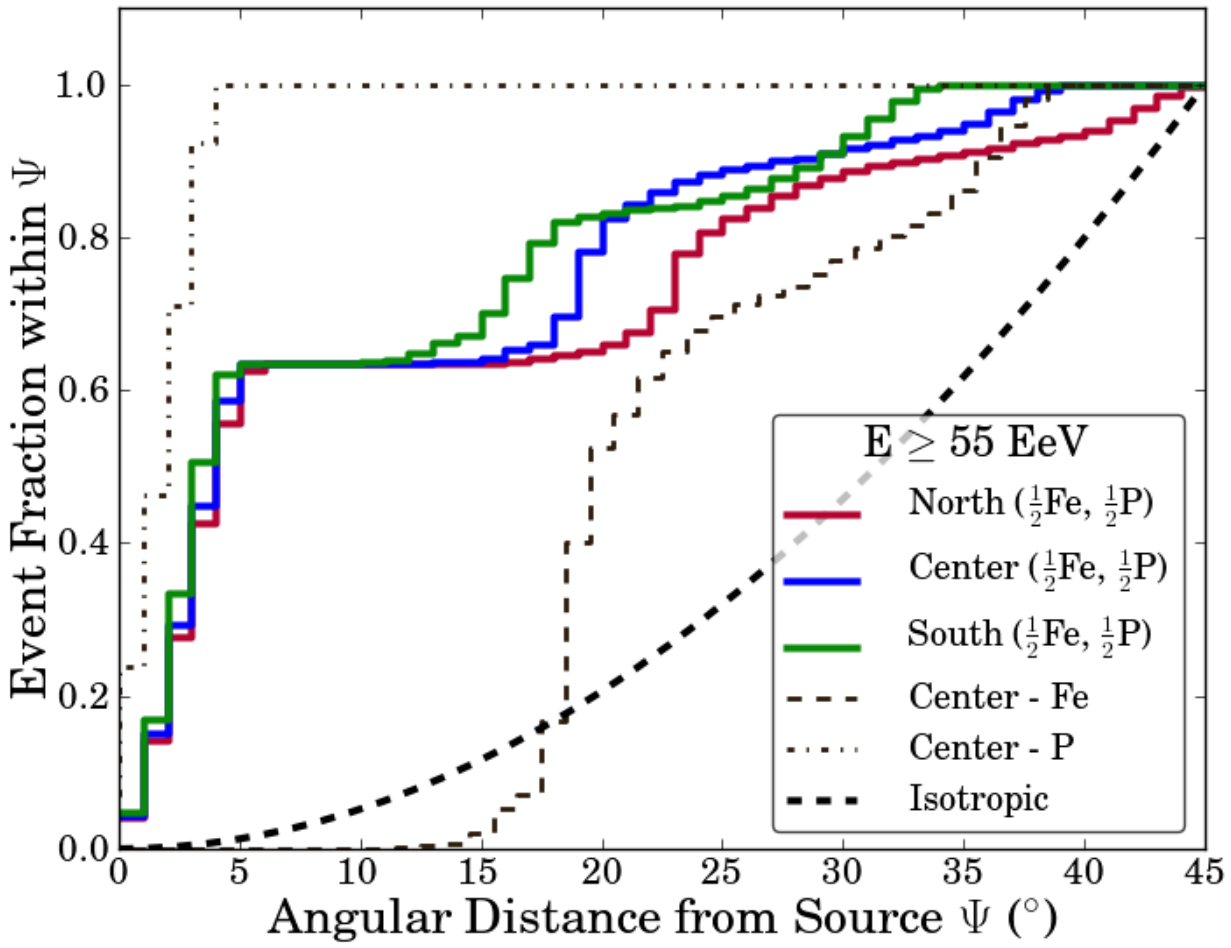

Figure 7.15: The excess of simulated events near Cen A. The observed directions have a separation angle up to 45°. Event excess from center, north, and south of Cen A are shown. The thick dashed line shows the expected isotropic flux. The thin dashed line shows only iron events. The dot-dashed line shows only proton events.

order to be consistent with the simulation. Since the charge is equal to energy over rigidity ($Z = E/R$), an Auger event cannot be assigned any charge in the vicinity of a simulation with rigidity lower than its energy.

The method is as follows: First, I consider a two dimensional Gaussian distribution function around the Galactic coordinates (l, b) of each of the observed events and also around the centroids of the simulated events at each rigidity as shown in Figure 7.17. The function

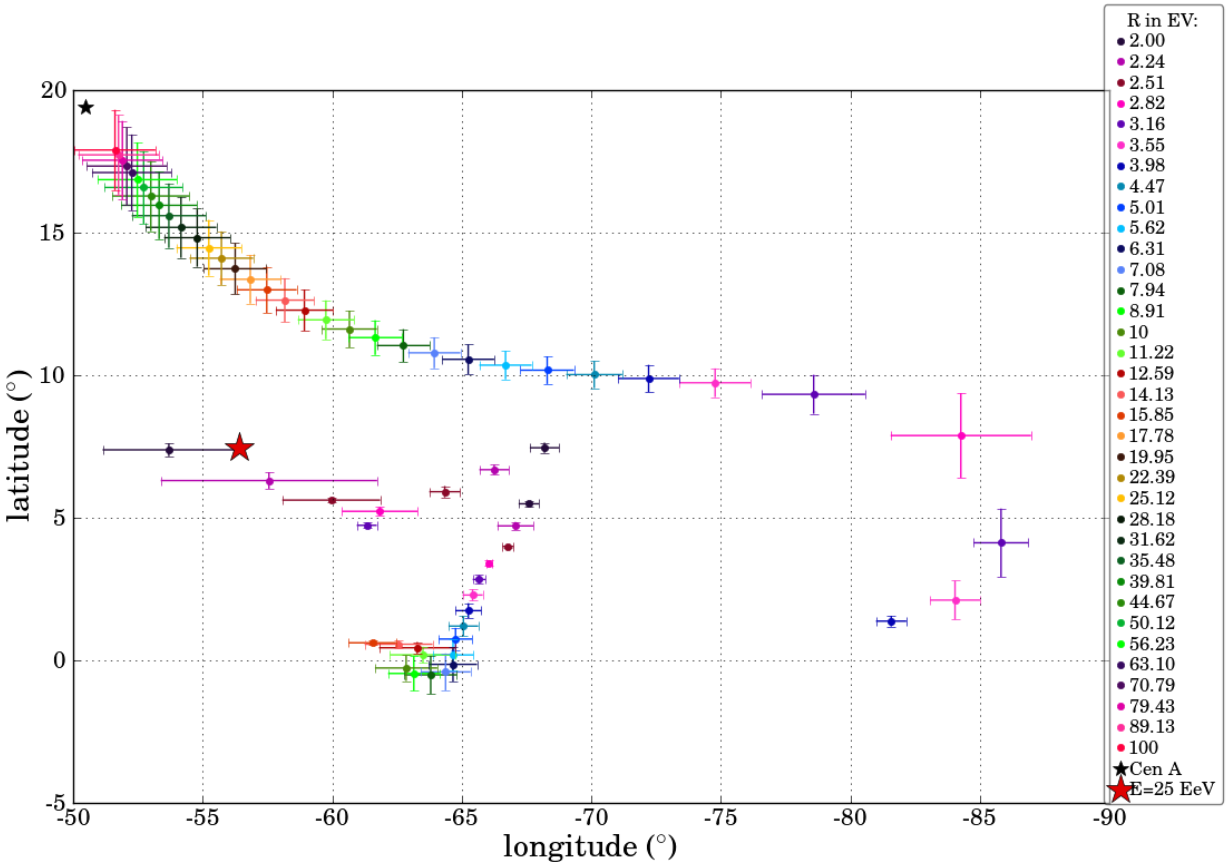

Figure 7.16: An example of the arrival direction of an Auger event near R=2 EV. Centroids of the observed directions of the simulated events within 3° of the vicinity of Cen A are shown. The error bars indicate the standard deviation of events with same rigidity.

is shown in terms of x and y, where $x = l$ and $y = b$:

$$G(x, y, x_0, y_0, \sigma_x, \sigma_y) = \frac{1}{2\pi\sigma_x\sigma_y} \exp\left(-\left(\frac{(x-x_0)^2}{2\sigma_x^2} + \frac{(y-y_0)^2}{2\sigma_y^2}\right)\right). \tag{7.1}$$

The width of the gaussian distribution for simulations is considered to be the standard deviation of the arrival direction distribution of the simulated events at each rigidity, separately for l and b. For a real observed event, the width of the gaussian distribution depends on the position of the event in the Galactic coordinate (l, b). Knowing that Auger angular resolution (σ_γ) is about 1° (Pierre Auger Collaboration, 2013), I can calculate the uncertainties on l and b (σ_l, σ_b) from the formula of calculating the angular separation (γ) between

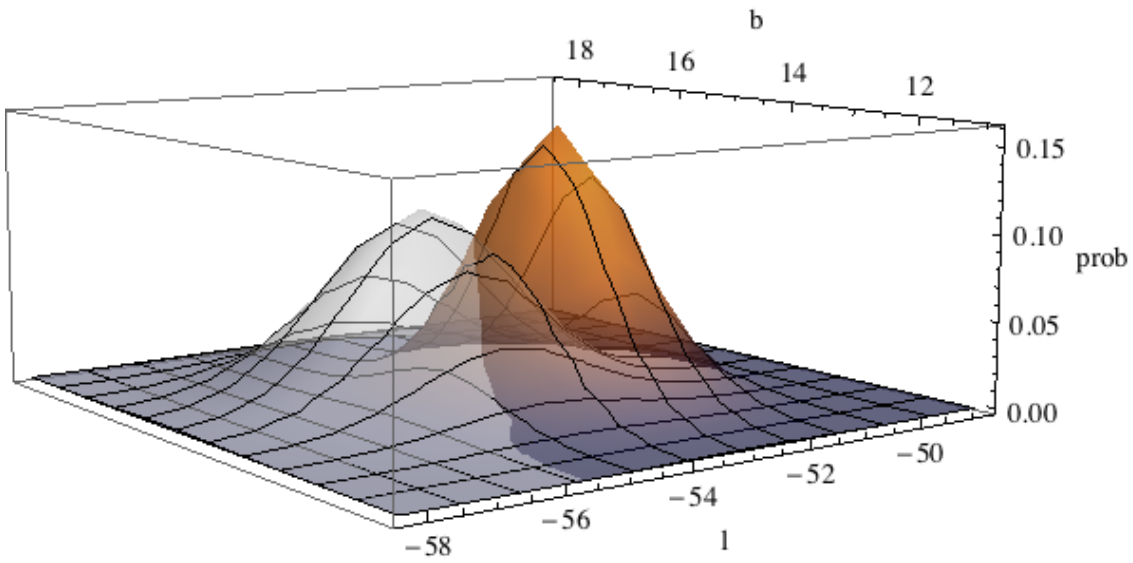

Figure 7.17: Depiction of two overlapping 2-dimensional normalized Gaussian distributions.

two points in Galactic coordinate,

$$\gamma = \cos^{-1}(\cos(b_1)\cos(b_2)\cos(l_1 - l_2) + \sin(b_1)\sin(b_2)). \tag{7.2}$$

I find that σ_b is the same as σ_γ by derivation from the above formula, but σ_l depends on the latitude as in

$$\sigma_l = |\cos^{-1}(\frac{\cos(1)}{\cos^2(b)} - \tan^2(b))|. \tag{7.3}$$

For each of the observed Auger events, I look at the overlap of its two dimensional Gaussian function with each of the simulated centroids with rigidities equal or less than the energy of that event (See Figure 7.18). This way the observed event can possess a charge of 1 or larger in order to agree with any of the simulations ($R = E/Z$). The overlapped volume gives the probability that Auger event has a certain charge that match the simulations. For example if an observation with energy of 16 EeV is closest to simulation of rigidity of 8 EV and the volume under their Gaussian distributions is 90%, I would say this event could be a particle of $Z = 2$ with 90% probability.

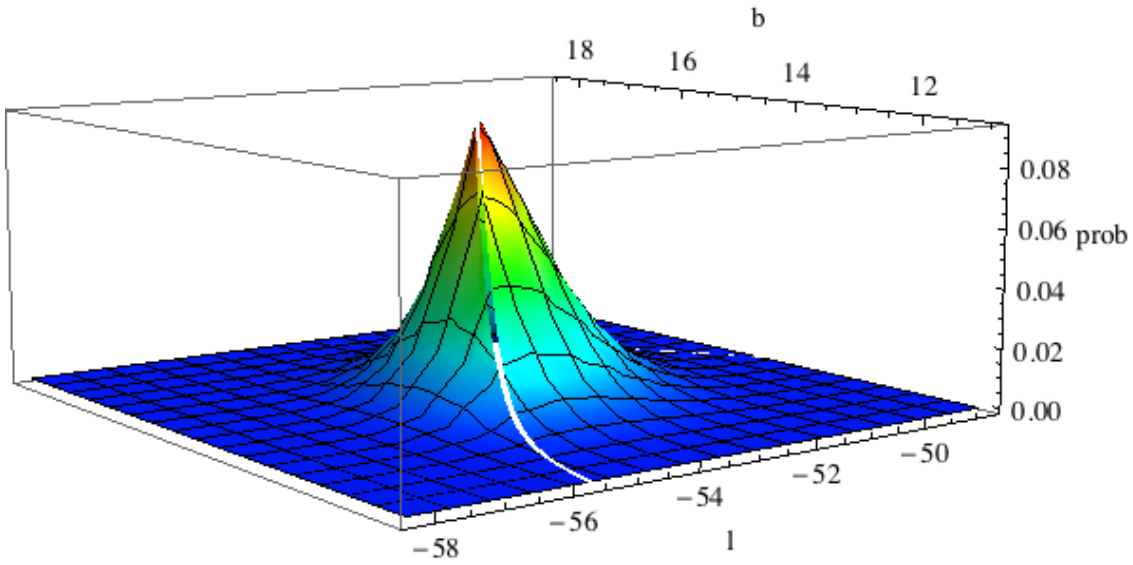

Figure 7.18: Depiction of the product of the two overlapping 2-dimensional normalized Gaussian distributions from Figure 7.17.

Any Auger event in the rectangular window containing the simulated points (giving it $\pm 3\sigma$ space at the boundaries of (l, b) plot) is checked to possibly relate a charge to it. There are two main cuts in this process. The first one is to skip the process at any rigidity that is larger than the energy of Auger particle since the smallest assigned value for charge is 1. The second cut is to skip the rigidities that are separated by more than $3\sigma_{\max}$ in both dimensions (l, b), where $\sigma_{\max}$ is the maximum variance between Auger event and the simulated event.

There are 12370 Auger events with $E \geq 2$ EeV having arrival directions inside the rectangular window defined with $-92.40° \leq l \leq -46.03°$ and $-2.56° \leq b \leq 22.13°$. 1759 Auger events indicate overlap probabilities greater than 10%. Table 7.1 shows the number of events with probabilities larger than the shown values. Figure 7.19 shows the energy histogram of Auger events that correlate with simulations with at least 10% probability. Figure 7.20 shows the assigned charges to those Auger events. The charge versus energy is plotted in Figure 7.21. The error bars on energy is 14% (Pierre Auger Collaboration, 2013). The error bars on charge are derived by smearing the energy and locations of Auger events considering a 1 degree uncertainty on longitude and latitude and 14% uncertainty on the

energy of the events. The method is then re-applied to the smeared events to identify the charge. I plot the average charge in each energy bin in Figure 7.22.

In summary this method can identify the charge of an observed UHECR event. The result is based on the assumption that the hypothesized GMF and source models are true.

Table 7.1: Number of Auger events with overlap probabilities larger than certain values.

Threshold Probability	Number of Events
1	3436
10	1759
20	1012
30	469
40	226
50	123
60	70
70	22
80	2

7.4.2 Method Uncertainty

To check the uncertainty of the charge identification, I apply the method to simulated data with known charges. I consider subsets of events from simulated regions with different rigidities and assume all of them are protons. The energy of each proton would then be equal to its rigidity. Applying the charge identification method may assign a new charge to each event. One would expect to get $Z = 1$ for all of the events. Figure 7.23 shows the histogram of output charges from this method. One can see that this method is efficient in more than 91% of the cases for this example, meaning the reconstructed particles turn out to be protons. The method returns about 8.5% of the events as Helium and only about 0.5% as Lithium.

I repeat the same check for Helium, Nitrogen, and Iron as true charges. I pick these four elements since they are the most interesting astrophysical elements. I plot the distributions of charge differences ($Z_{\text{reconst}} - Z_{\text{true}}$) as shown in Figures 7.24, 7.25, and 7.26. I also plot the reconstructed charge error versus the energy of the events as seen in Figures 7.27, 7.28,

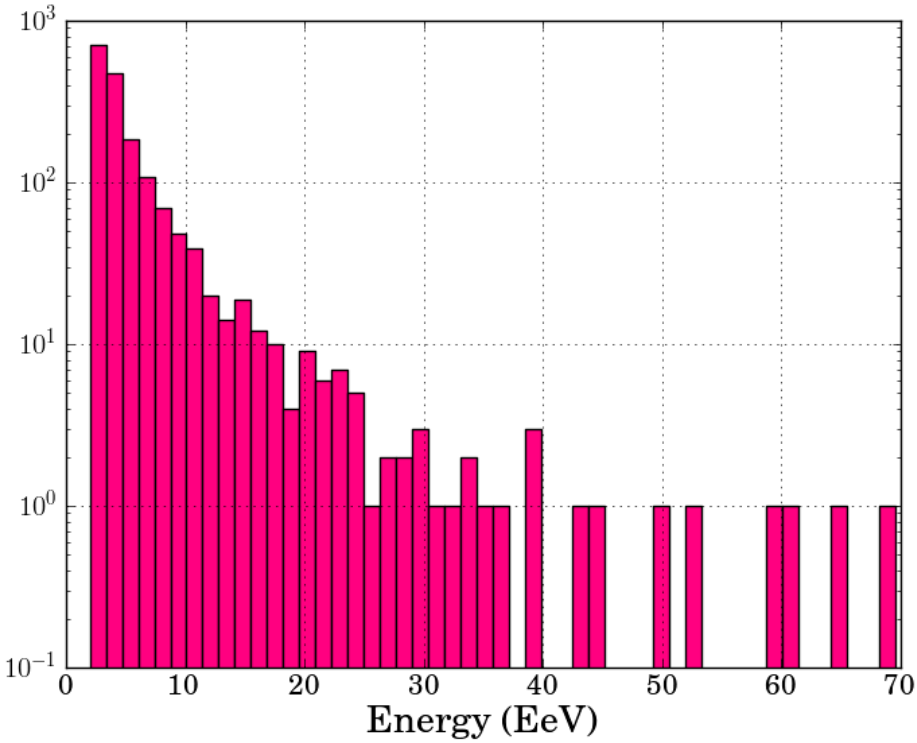

Figure 7.19: Histogram of energy of Auger events with overlap probabilities greater than 10%.

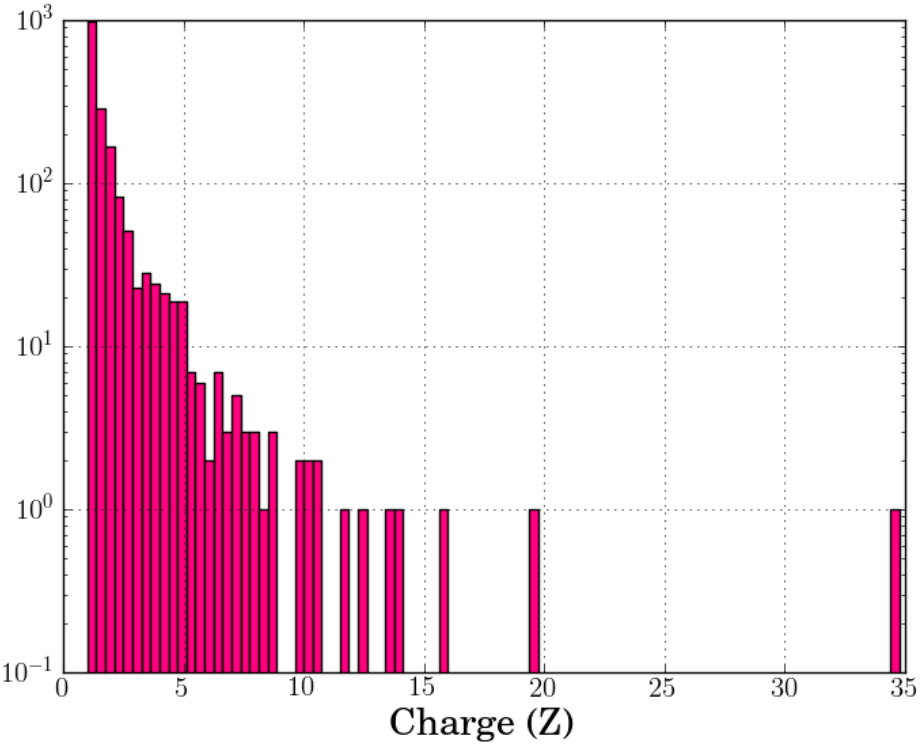

Figure 7.20: Histogram of assigned charges to Auger data around Cen A.

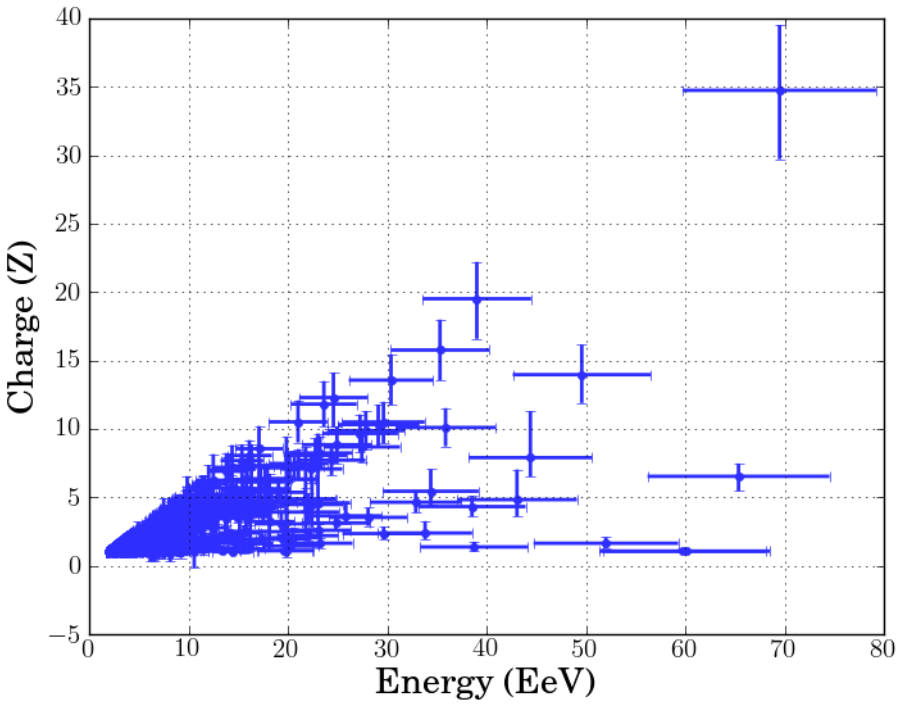

Figure 7.21: Assigned charge to individual Auger events as a function of their energy based on comparison with rigidity simulations assuming the center of Cen A as their source. Only events with overlap probabilities greater than 10% are shown. Uncertainties are derived by assuming 14% and 1° uncertainties in the energy and angular event reconstruction.

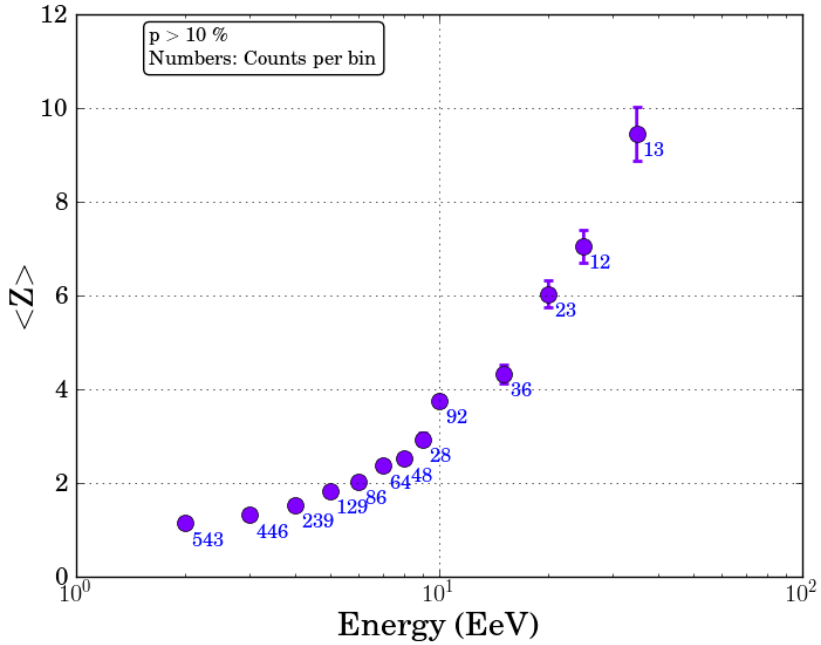

Figure 7.22: Average charge vs. energy in each bin of energy. Bins change by 1 EeV at energies below 10 EeV. Above 10 EeV the bin size is 5 EeV. There is only one bin for all energies above 35 EeV.

7.29, and 7.30. The maximum energy of the simulated events is considered to be 200 EeV to be compatible with the observations. Table 7.2 shows the percentages of reconstructed charges for each primary element. I observe that in all cases, the method of assigning charges to the events works very well; they typically return the same element. The next abundant charge is usually one of the neighbor elements. This study gives us the uncertainty in charge assignment for each Z.

Figure 7.26 and Table 7.2 show that the method selects a few neighbor elements for Iron nuclei, but not all of the neighbors. For instance there is no Co or Mn in this set of data. The reason is related to the limited values of rigidities I have simulated. Since the rigidity range is not continuously simulated and has been performed only for steps of 0.05 in logarithmic scale, the method tends to correlate Auger event to the closest possible rigidity and then round the E/R to find the Z.

Table 7.2: Efficiency of the charge identification method, showing the percentages of reconstructing different elements, given true initial values for charges.

Z_{truth}	$Z_{reconstruct}$	Event Fraction (%)
H	H	91
H	He	8
He	He	68
He	H	10
He	Li	17
He	Be	5
N	N	42
N	C	29
N	O	18
N	F	6
Fe	Fe	63
Fe	V	23
Fe	Cu	11

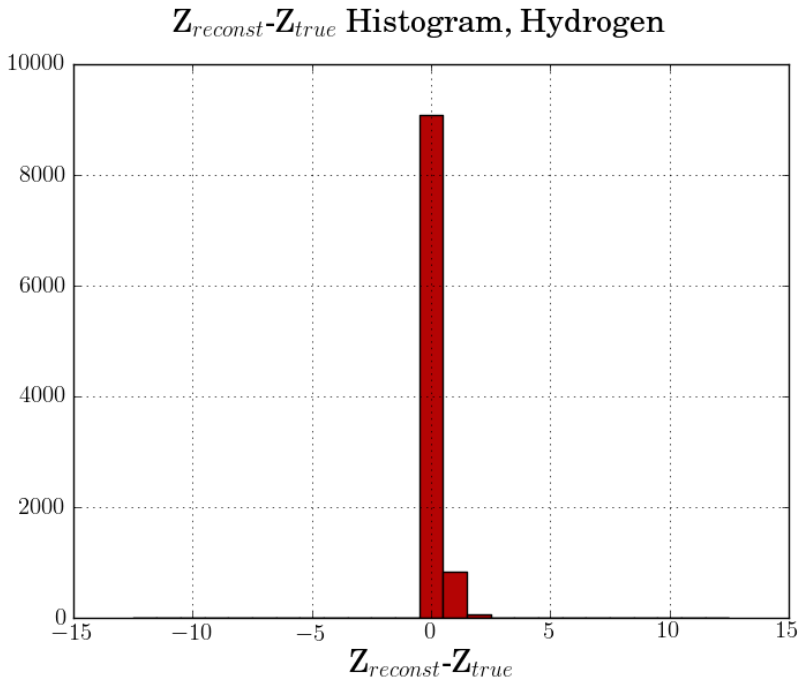

Figure 7.23: Histogram of the difference between reconstructed and the true charges. The events are taken from the simulations performed for different rigidities. They are assumed to be protons before reconstruction with my method. Only events with more than 10% probability are shown.

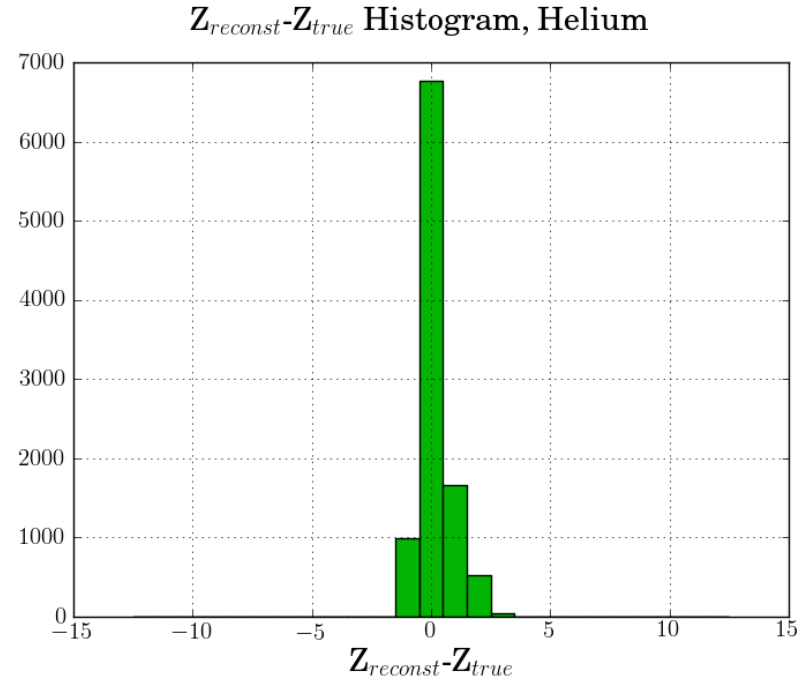

Figure 7.24: Histogram of the difference between reconstructed and the true charges. The events are taken from the simulations done for different rigidities. They are assumed to be Helium nuclei before reconstruction with my method. Only events with more than 10% probability are shown.

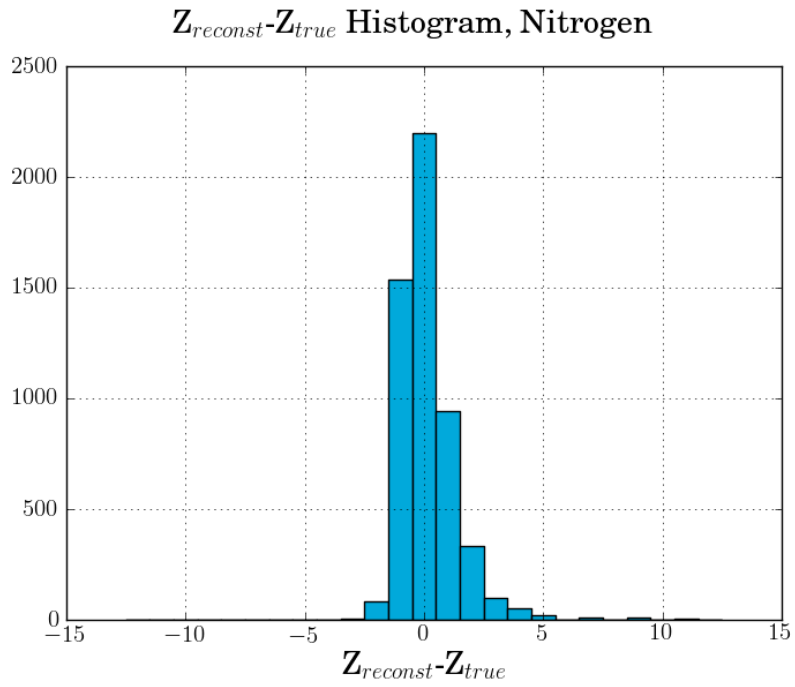

Figure 7.25: Histogram of the difference between reconstructed and the true charges. The events are taken from the simulations done for different rigidities. They are assumed to be Nitrogen nuclei before reconstruction with my method. Only events with more than 10% probability are shown.

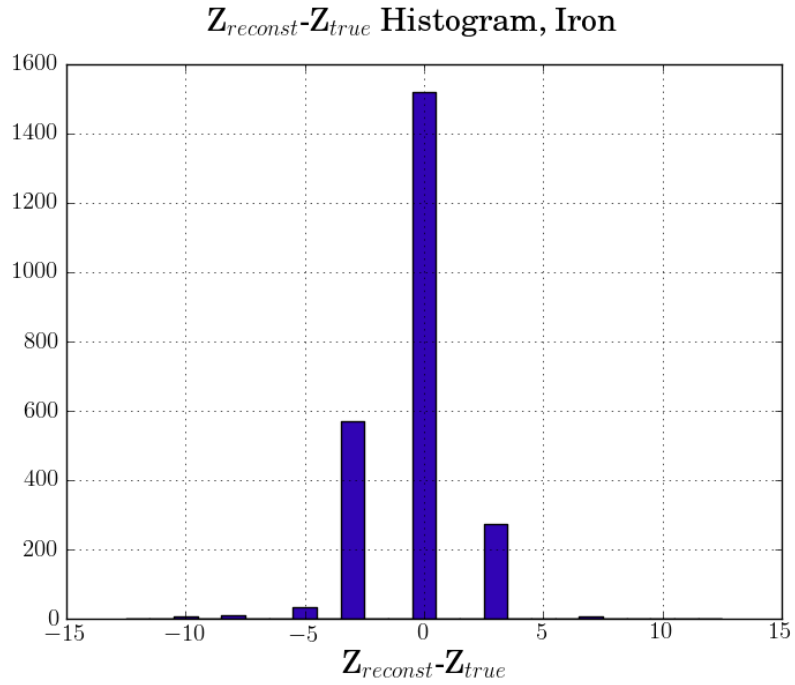

Figure 7.26: Histogram of the difference between reconstructed and the true charges. The events are taken from the simulations done for different rigidities. They are assumed to be Iron nuclei before reconstruction with my method. Only events with more than 10% overlap probability are shown.

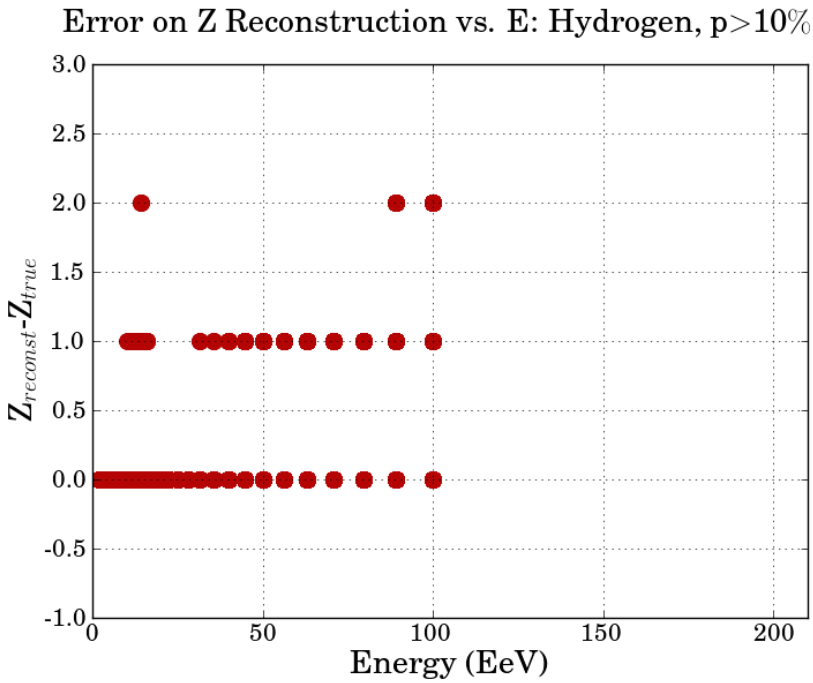

Figure 7.27: Difference between reconstructed and the true charges plotted versus the energy of the events. The events are taken from the simulations done for different rigidities. They are assumed to be protons. Only events with more than 10% overlap probability are shown.

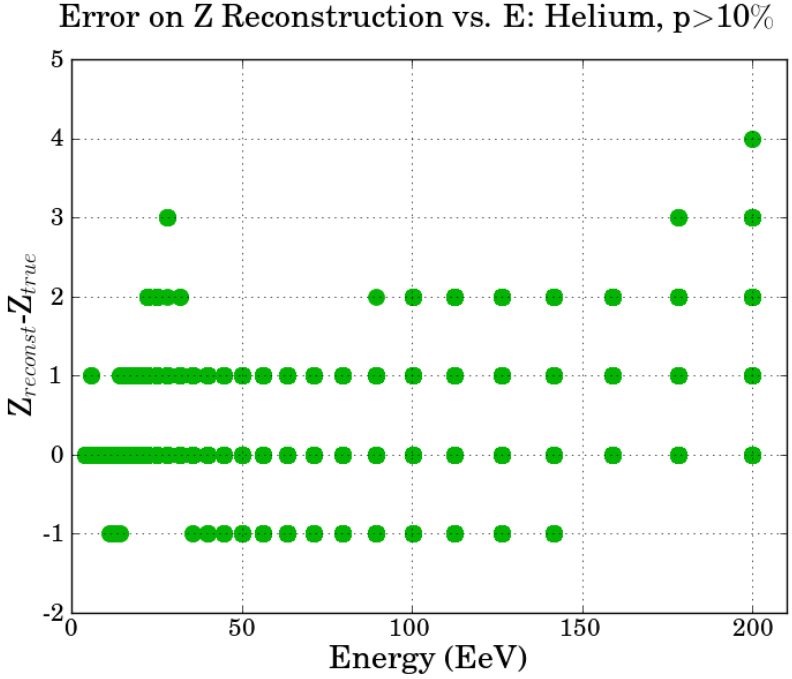

Figure 7.28: Difference between reconstructed and the true charges plotted versus the energy of the events. The events are taken from the simulations done for different rigidities. They are assumed to be Helium nuclei. Only events with more than 10% overlap probability are shown.

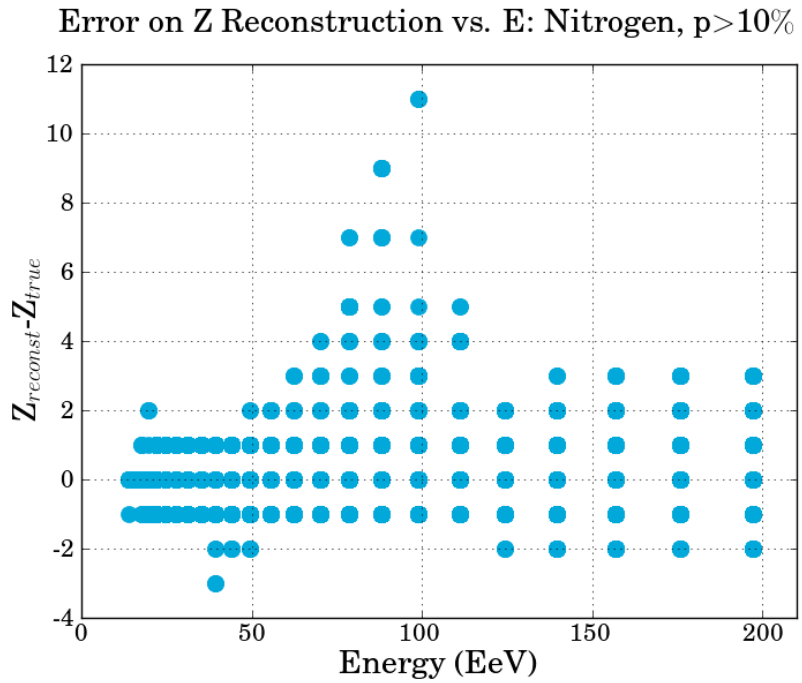

Figure 7.29: Difference between reconstructed and the true charges plotted versus the energy of the events. The events are taken from the simulations done for different rigidities. They are assumed to be Nitrogen nuclei. Only events with more than 10% overlap probability are shown.

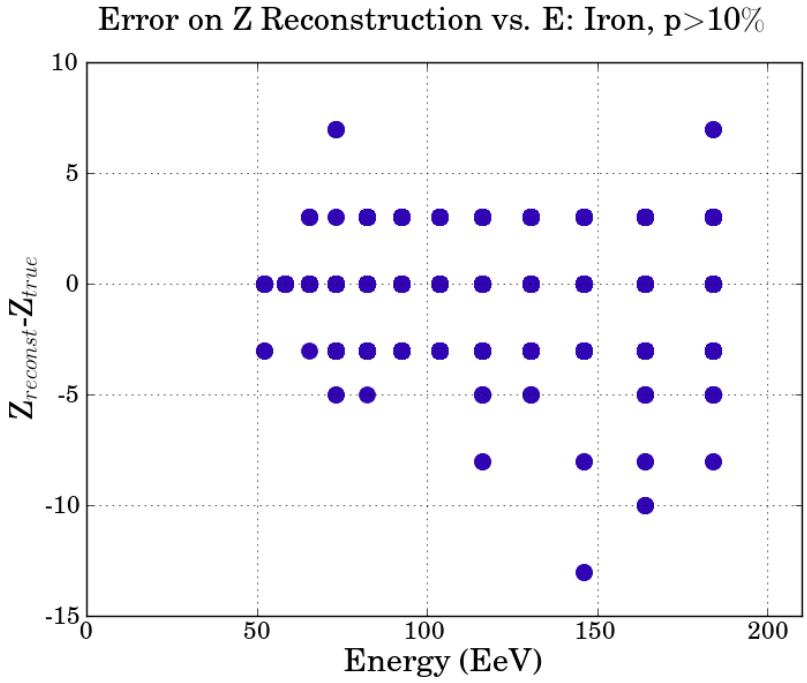

Figure 7.30: Difference between reconstructed and the true charges plotted versus the energy of the events. The events are taken from the simulations done for different rigidities. They are assumed to be Iron nuclei. Only events with more than 10% probability are shown.

7.5 Ultra-High Energy Cosmic Ray Deflections in Jansson-Farrar Galactic Magnetic Field Model Including Random Fields

In this section, I show the results of UHECR propagations from Cen A through the GMF including the random field component in addition to the JF12 regular component. Here I simulate events with $\log(R_{\rm EV})$=0.5, 1.0, 1.5, and 2.0. Figure 7.31 shows the observed arrival directions of the simulated events with R=100 EV in the first random field realization, compared to the case of regular field only. This figure shows the arrival distribution of the events is smeared when I add the random field component but their average deflection is not significantly different than from the regular field only.

I also compare the arrival directions of events with $\log(R_{\rm EV})$=1.5 (R=31.62 EV) in Figure 7.32. I see in this case, the events are more smeared out since they have smaller rigidities, but their average position is not different by more than a few degrees. So at this rigidity, the method of showing the observed events with their average and standard deviation still works and can be applied for study of the event excess and charge assignment. However, at lower rigidities, the deflection magnitudes are very large and the arrival distribution of the events is smeared in such a large region that the method can not be directly applied to them. Figures 7.33 and 7.34 show the observed arrival directions of the events with R=10 and 3.16 EV, respectively.

At the end, I compare the observed arrival directions of simulations from Cen A center in JF12_reg and JF12_R1 in Figure 7.35. This figure shows that for high rigidities (R=100 and 31.62 EV) the centroids of the arrival directions with the random field are not different by more than a few degrees than the regular field only, whereas for low rigidities (R=10 and 3.16 EV) the centroids are separated by a few degrees, but most importantly they are significantly smeared. At high rigidities ($R > 30$ EV in this study), evaluating events using their average angular position and standard deviation still works and can be applied for study of the event excesses and charge assignments. But at lower rigidities these studies are not entirely applicable.

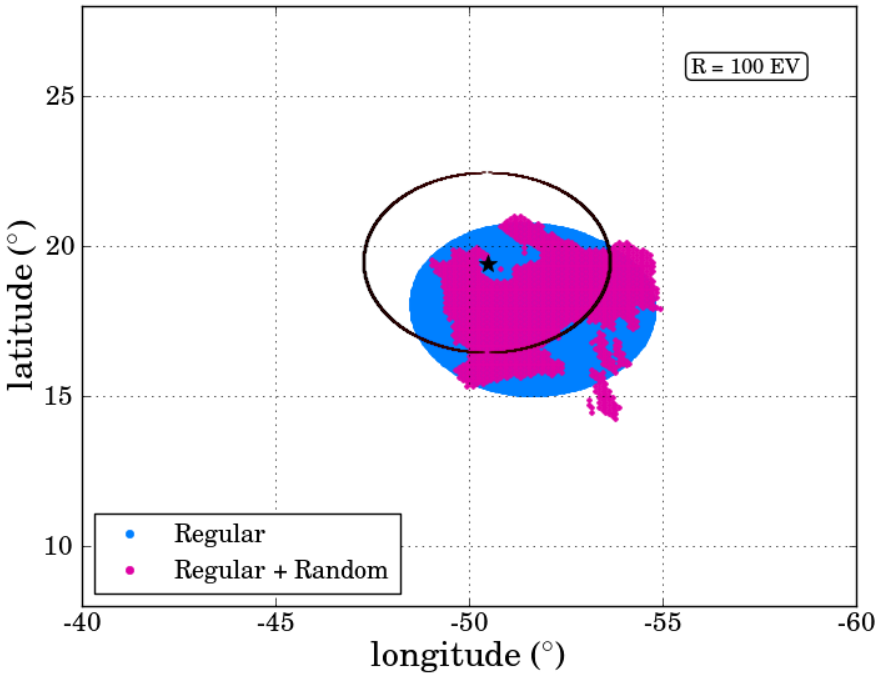

Figure 7.31: Observed arrival directions of the simulated events with R=100 EV within 3° of the vicinity of Cen A center. The blue region relates to events in regular field-only simulation. The black circle shows 3° angular distance from Cen A.

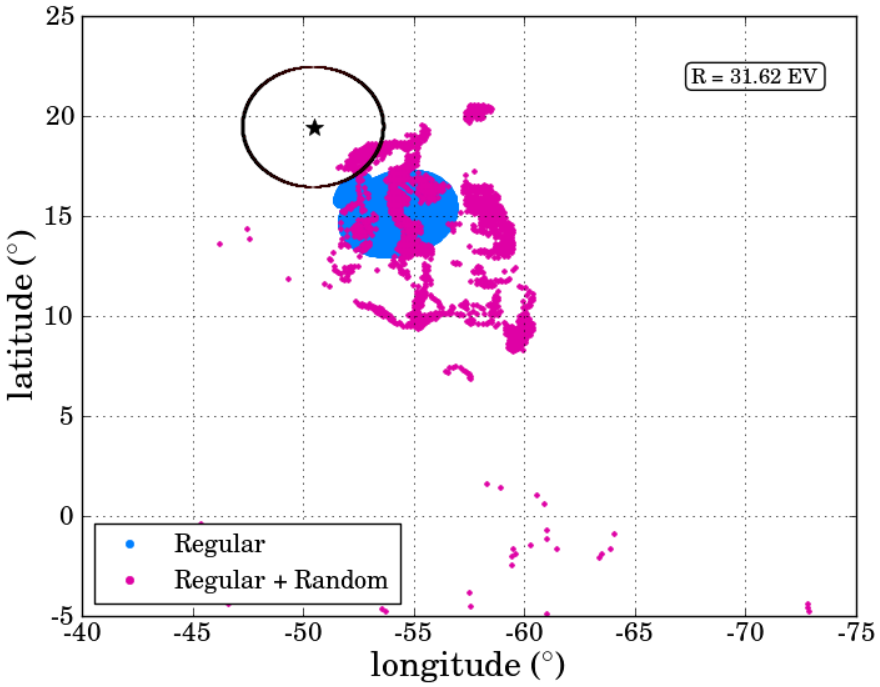

Figure 7.32: Observed arrival directions of the simulated events with R=31.62 EV within 3° of the vicinity of Cen A center. The blue region relates to events in regular field-only simulation. The black circle shows 3° angular distance from Cen A.

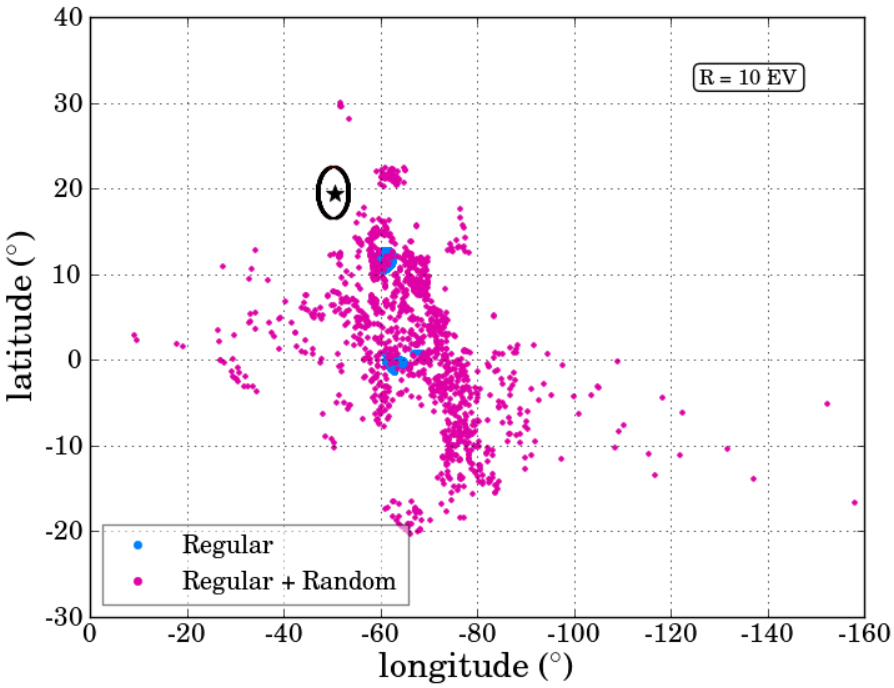

Figure 7.33: Observed arrival directions of the simulated events with R=10 EV within 3° of the vicinity of Cen A center. The blue region relates to events in regular field-only simulation. The black circle shows 3° angular distance from Cen A.

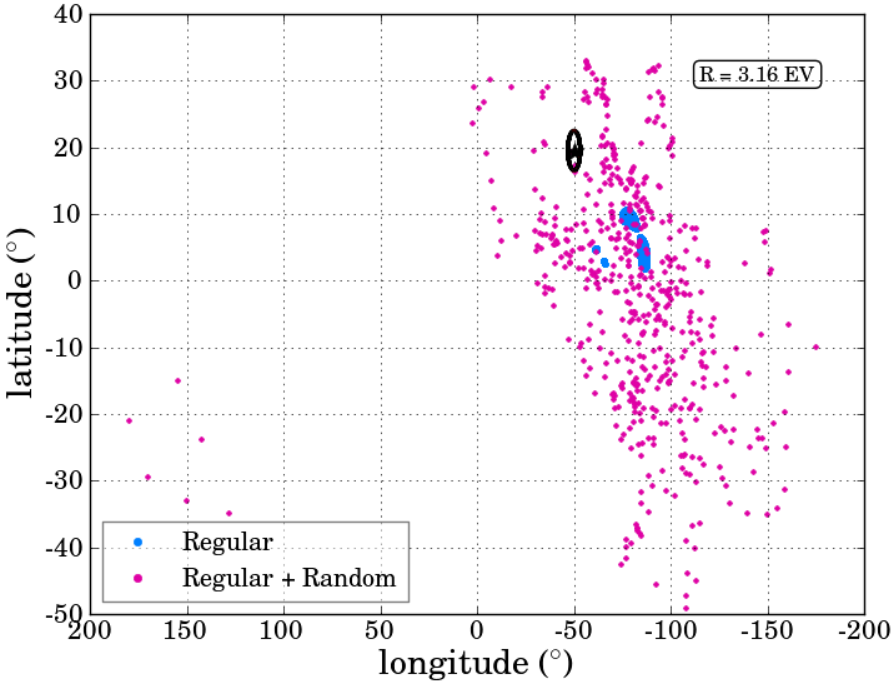

Figure 7.34: Observed arrival directions of the simulated events with R=3.16 EV within 3° of the vicinity of Cen A center. The blue region relates to events in regular field-only simulation. The black circle shows 3° angular distance from Cen A.

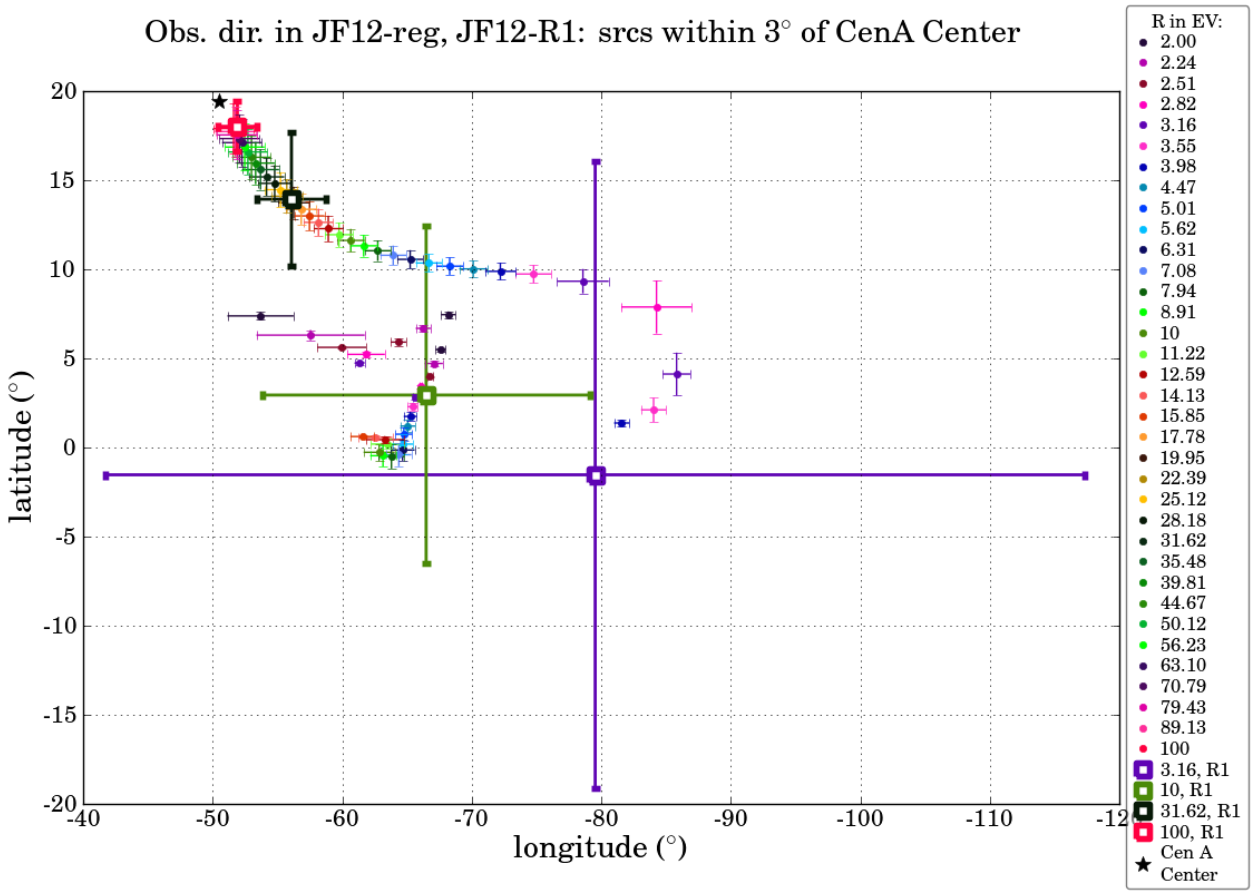

Figure 7.35: Centroids of the observed directions of the simulated events within 3° of the vicinity of Cen A center. The error bars indicate the standard deviation of events with same rigidity. The four squares show the centroids of the simulations in JF12_R1.

8. Conclusions

The study of the propagation of ultra-high energy cosmic rays (UHECRs) through the Galactic magnetic field (GMF) is of great importance in identifying their origin and nature. The calculated magnetic deflections of UHECRs depend strongly on the GMF model used for the propagation studies. The JF12 model is a recent model that has been fitted to the data of more than forty thousand extragalactic rotation measures (the largest fit dataset so far) and the WMAP7 Galactic synchrotron emission map to constrain its parameters. This model fits the observational data better than previous models. In this dissertation, I simulate and propagate UHECRs through this model from an assumed Cen A source to characterize their arrival direction distribution and determine if Cen A could be a significant source of UHECRs.

There are two different methods for tracking cosmic rays through GMF: forwardtracking and backtracking. I have found that the backtracking method is more efficient and accurate than forwardtracking for the following reasons. First, there is the possibility of neglecting some regions that are potentially sources of UHECRs by sequentially decreasing the detector size in forwardtracking studies, due to their low statistics in the first step. In the backtracking method, the particles are selected and tracked isotropically with a high resolution of 8×10^{-4} square-degree pixels. Second, efficiently designed forwardtracking schemes may still take a relatively long runtime to provide the minimum number of successful detections. The third point is specific to my studies. The random field implementation used in the forwardtracking scheme is a simplified model, which was improved to a more realistic Kolmogorov model for the backtracking studies.

Cen A is the nearest AGN to the Earth and together with its huge radio lobes it covers $4^\circ \times 8^\circ$ of the sky. Cen A is a common candidate for source studies. Forwardtracking simulations through only the JF12 regular component have been performed using discrete values of rigidity between 64 and 2 EV. My results indicate that the arrival directions of detected events at each rigidity are highly compact on the sky. This leads to the conclusion

that Cen A could not be the source of more than a few UHECRs for these rigidities under these hypotheses.

Backtracking simulations are performed for similar rigidities including and excluding a specific realization of a random field. In the case of JF12 regular component only, the simulations are done with rigidities of 100 EV down to 2 EV. I select events with Galaxy-exiting velocity directions lying within 3° of the Cen A center. Their arrival directions are plotted for different rigidities which appear to form a "snake-like" image with a head (the 100 EV events) located near and pointed towards the Cen A center. Event rigidities decrease along the body with distance from the Cen A center. This is compatible with previous Galactic magnetic deflection studies. An interesting effect occurs at a rigidity of 17.78 EV, where I observe a second region of arrival directions appearing separated from the snake-like thread. These regions persist and increase in number with lower rigidity, forming small "islands" of arrival directions from the Cen A center. These regions represent potential arrival positions of the UHECRs according to their rigidity under these hypotheses.

An alternative source hypothesis is if the northern and southern tips of the Cen A radio lobes are the sources. Comparing the arrival directions from center, north and south of Cen A, I find that the general stream of the events remains the same, however the appearance of separate regions from the main thread happens at lower (higher) rigidities for the northern (southern) tip source. Also, the bifurcation happens at lower rigidities from northern tip and at higher energies from southern tip. The event fraction as a function of angular distance from each source location (north, center, or south) is calculated and compared with the event excess observed by the Pierre Auger Observatory. Only events with $E \geq 55$ EeV are considered. Arrival directions may be as large as 45° from Cen A for iron nuclei. I consider three scenarios: 100% proton, 100% iron, and 50% contributions from each composition. Results show that there is an excess beyond the isotropic expectation in all three scenarios regardless of the position of the source within Cen A.

I have also developed a method for identifying the mass composition of UHECRs under specific source and GMF hypotheses. Comparisons between Auger observations with simulations of different rigidities leads to the identification of the charges of the events. The nearest simulated rigidity to each Auger event is found based on their overlap probabilities. The charge of each event is then the measured energy divided by the rigidity of the simulated event. The result is based on the assumption that the hypothesized JF 12 GMF and Cen A source models are true.

Finally, I study the effect of adding a realistic Kolmogorov random field component to the JF12 regular component. Simulations including this model are computationally expensive and so I consider only four rigidities: 3.16, 10, 31.62, and 100 EV. The results of propagation do not change significantly at high rigidities, such as 100 EV and 31.62 EV, between the regular-only and regular plus random models. Random field arrival direction distributions are smeared mainly near the Galactic plane but their average deflection is not different by more than a few degrees than the regular field only. At these rigidities, evaluating events using their average angular position and standard deviation still works and can be applied for study of the event excesses and charge assignments. At low rigidities, such as 10 and 3.16 EV, deflection magnitudes are very large and the arrival direction distributions are significantly smeared to the point where these studies become difficult. These results indicate that a 55 EeV iron nucleus is so strongly deflected that it is nearly impossible to identify its source, especially if it is observed to arrive from low Galactic latitudes.

The advantage of studying the propagations separately with and without random field component is that one can compare the results of regular field only with the results of adding a new implementation of random field. The GMF smears the arrival distribution of the events with rigidities above about 30 EV by small amounts in such a way that the source identification is still possible by only studying the effect of JF12 regular component. Our knowledge of Galactic random fields is not yet comprehensive and the results are very

sensitive to the model. Here the modeling is done accurately (to the best of our knowledge), but the new observational data could possibly tune and constrain the model parameters.

References

Ahn, E.-J., Engel, R., Gaisser, T., Lipari, P., & Stanev, T. 2009, Physical Review D, 80, 094003.

Alfvén, H. 1949, Physical Review, 75, 1732.

Anchordoqui, L., Paul, T., Reucroft, S., & Swain, J. 2003, International Journal of Modern Physics A, 18, 2229.

Anderson, C. D. 1933, Physical Review, 43, 491.

Auger, P., Ehrenfest, P., Maze, R., Daudin, J., & Fréon, R. 1939, Reviews of Modern Physics, 11, 288.

Ave, M., Hinton, J., Vázquez, R., Watson, A., & Zas, E. 2002, Physical Review D, 65, 063007.

Baltrusaitis, R., Cady, R., Cassiday, G., et al. 1985, Nuclear Instruments and Methods in Physics Research Section A: Accelerators, Spectrometers, Detectors and Associated Equipment, 240, 410.

Barbosa, H., Catalani, F., Chinellato, J., & Dobrigkeit, C. 2004, Astroparticle Physics, 22, 159.

Beck, R., Poezd, A. D., Shukurov, A., & Sokoloff, D. D. 1994, Astronomy and Astrophysics, 289, 94.

Bergeson, H., Cassiday, G., Chiu, T., et al. 1977, Physical Review Letters, 39, 847.

Beringer, J., Arguin, J. F., Barnett, R. M., et al. 2012, Physical Review D, 86, 010001.

Beuermann, K., Kanbach, G., & Berkhuijsen, E. M. 1985, Astronomy and Astrophysics, 153, 17.

Bird, D. J., Corbato, S. C., Dai, H. Y., et al. 1994, The Astrophysical Journal, 424, 491.

Bolton, J. G., & Wild, J. P. 1957, The Astrophysical Journal, 125, 296.

Burke, D. 2006, http://en.wikipedia.org/wiki/File:Toroidalcoord.png.

Burns, J. O., Feigelson, E. D., & Schreier, E. J. 1983, The Astrophysical Journal, 273, 128.

Chiba, N., Hashimoto, K., Hayashida, N., et al. 1992, Nuclear Instruments and Methods in Physics Research Section A: Accelerators, Spectrometers, Detectors and Associated Equipment, 311, 338.

Clarke, D. A., Burns, J. O., & Norman, M. L. 1992, The Astrophysical Journal, 395, 444.

Cooper, B. F. C., Price, R. M., & Cole, D. J. 1965, Australian Journal of Physics, 18, 589.

Creusot, A. 2012, Nuclear Instruments and Methods in Physics Research Section A: Accelerators, Spectrometers, Detectors and Associated Equipment, 662, S106.

Cronin, J. W., Gaisser, T. K., & Swordy, S. P. 1997, Scientific American, 276, 32.

Dar, A., & De Rújula, A. 2005, Physical Review D, 72, 123002.

Davies, R. D. 1968, Nature, 218, 435.

Davis, Leverett, J., & Greenstein, J. L. 1951, The Astrophysical Journal, 114, 206.

Dolag, K., Grasso, D., Springel, V., & Tkachev, I. 2004, Journal of Experimental and Theoretical Physics Letters, 79, 583.

Dolag, K., Kachelriess, M., Ostapchenko, S., & Tomàs, R. 2011, The Astrophysical Journal, 727, L4.

Dova, M. T. 2003, Nuclear Physics B - Proceedings Supplements, 122, 170.

Ellis, R. S., & Axon, D. J. 1978, Astrophysics and Space Science, 54, 425.

Fanaroff, B. L., & Riley, J. M. 1974, Monthly Notices of the Royal Astronomical Society, 167, 31.

Feain, I. J., Cornwell, T. J., Ekers, R. D., et al. 2011, The Astrophysical Journal, 740, 17.

Fermi, E. 1949, Physical Review, 75, 1169.

Fishman, G. J., & Meegan, C. A. 1995, Annual Review of Astronomy and Astrophysics, 33, 415.

Flückiger, E. O., Kobel, E., Smart, D. F., & Shea, M. A. 1991, Proceedings of the 22nd International Cosmic Ray Conference 1991, 648.

Fraschetti, F. 2008, Philosophical transactions. Series A, mathematical, physical, and engineering sciences, 366, 4417.

Frigo, M., & Johnson, S. G. 2005, Proceedings of the IEEE 93, 2, 216.

Gaensler, B. M., & Johnston, S. 1995, Monthly Notices of the Royal Astronomical Society, 277, 1243.

Gaiser, T. K., & Hillas, A. M. 1977, Proceedings of the 15th International Cosmic Ray Conference 1977, 353.

Giacinti, G., Kachelrieß, M., Semikoz, D., & Sigl, G. 2012, Journal of Cosmology and Astroparticle Physics, 2012, 031.

Glauber, R., & Matthiae, G. 1970, Nuclear Physics B21, 135.

Gold, B., Odegard, N., Weiland, J. L., et al. 2011, The Astrophysical Journal Supplement, 192, 15.

Gorski, K. M., Hivon, E., Bandry, A. J., et al. 2005, The Astrophysical Journal, 622, 759.

Greisen, K. 1966, Physical Review Letters, 16, 748.

Greisen, K., & Wilson, J. G. 1956, Progress in cosmic ray physics. Vol. 3 (Amsterdam: North-Holland.)

Hall, J. S. 1949, Science (New York, N.Y.), 109, 166.

Harari, D., Mollerach, S., & Roulet, E. 1999, Journal of High Energy Physics, 1999, 022.

—. 2000, Journal of High Energy Physics, 2000, 035.

Harari, D., Mollerach, S., Roulet, E., & Sánchez, F. 2002, Journal of High Energy Physics, 2002, 045.

Harris, G. L. H., Rejkuba, M., & Harris, W. E. 2013, Publications of the Astronomical Society of Australia, 27, 457.

Haverkorn, M., Brown, J. C., Gaensler, B. M., & McClure-Griffiths, N. M. 2008, The Astrophysical Journal, 680, 362.

Heitler, W. 1954, Quantum theory of radiation (International Series of Monographs on Physics, Oxford: Clarendon, 1954, 3rd ed.)

Hess, V. F. 1912, Zeitschr Physik, 13, 1084.

Hillas, A. M. 1984, Annual Review of Astronomy and Astrophysics, 22, 425.

Hiltner, W. A. 1949, The Astrophysical Journal, 109, 471.

Israel, F. 1998, Astronomy and Astrophysics Review, 8, 237.

Jansson, R., & Farrar, G. R. 2012a, The Astrophysical Journal, 757, 14.

—. 2012b, The Astrophysical Journal, 761, L11.

JEM-EUSO Collaboration. 2013, Proceedings of the 33rd International Cosmic Ray Conference 2013, 150.

Jones, R. V., & Spitzer, Lyman, J. 1967, The Astrophysical Journal, 147, 943.

Kachelries, M., Serpico, P., & Teshima, M. 2007, Astroparticle Physics, 26, 378.

Kalmykov, N. N., & Ostapchenko, S. S. 1993, Physics of Atomic Nuclei, 56, 346.

Kamata, K., & Nishimura, J. 1958, Progress of Theoretical Physics Supplement, 6, 93.

Kolmogorov, A. 1941, Doklady Akademiia Nauk SSSR, 30, 301.

Kolmogorov, A. N. 1991, Proceedings of the Royal Society A: Mathematical, Physical and Engineering Sciences, 434, 9.

Kuempel, D., Kampert, K. H., & Risse, M. 2008, Astroparticle Physics, 30, 167.

Lattes, C. M. G., Muirhead, H., Occhialini, G. P. S., & Powell, C. F. 1947, Nature, 159, 694.

Letessier-Selvon, A., & Stanev, T. 2011, Review of Modern Physics, 83, 907.

Liddle, A., & Loveday, J. 2012, The Oxford Companion to Cosmology (Oxford University Press.)

Linsley, J. 1963, Physical Review Letters, 10, 146.

Lyne, A. G., & Smith, F. G. 1968, Nature, 218, 124.

Manchester, R. N. 1973, Bulletin of the American Astronomical Society, 5, 35.

Mathewson, D. S., & Ford, V. L. 1970, Memoirs of the Royal Astronomical Society, 74, 139.

Matthews, J. 2005, Astroparticle Physics, 22, 387.

Medina Tanco, G. A., de Gouveia Dal Pino, E. M., & Horvath, J. E. 1998, The Astrophysical Journal, 492, 200.

Mészáros, P. 2002, Annual Review of Astronomy and Astrophysics, 40, 137.

Milgrom, M., & Usov, V. 1995, The Astrophysical Journal, 449, L37.

Mirabal, N., & Oya, I. 2010, Monthly Notices of the Royal Astronomical Society: Letters, 405, 99.

Moisy, F., Tabeling, P., & Willaime, H. 1999, Physical Review Letters, 82, 3994.

Neddermeyer, S. H., & Anderson, C. D. 1937, Physical Review, 51, 884.

Ostapchenko, S. 2006, Nuclear Physics B Proceedings Supplements, 151, 147.

Pierre Auger Collaboration. 2004, Nuclear Instruments and Methods in Physics Research Section A: Accelerators, Spectrometers, Detectors and Associated Equipment, 523, 50.

—. 2007, Science (New York, N.Y.), 318, 938.

—. 2008, Physical Review Letters, 101, 061101.

—. 2009, Astroparticle Physics, 31, 399.

—. 2010a, Physical Review Letters, 104, 091101.

—. 2010b, Nuclear Instruments and Methods in Physics Research Section A: Accelerators, Spectrometers, Detectors and Associated Equipment, 620, 227.

—. 2010c, Nuclear Instruments and Methods in Physics Research Section A: Accelerators, Spectrometers, Detectors and Associated Equipment, 613, 29.

—. 2010d, Astroparticle Physics, 34, 314.

—. 2011, Journal of Cosmology and Astroparticle Physics, 2011, 022.

—. 2012, Physical Review Letters, 109, 062002.

—. 2013, Proceedings of the 33rd International Cosmic Ray Conference 2013, arXiv:1307.5059.

Protheroe, R. J. 1999, Topics in Cosmic-Ray Astrophysics; Horizons in World Physics, 230, 247.

Prouza, M., & Smida, R. 2003, Astronomy and Astrophysics, 410, 1.

Pshirkov, M. S., Tinyakov, P. G., Kronberg, P. P., & Newton-McGee, K. J. 2011, The Astrophysical Journal, 738, 192.

Rao, M. V. S., & Sreekantan, B. V. 1998, Extensive Air Showers (World Scientific.)

Roulet, E. for the Pierre Auger Collaboration. 2011, Talk given at Quarks, Strings and the Cosmos, Hector Rubinstein Memorial Symposium, August 9-11 2010, arXiv:1101.1825.

Settimo, M. 2011, Proceedings of 32nd International Cosmic Ray Conference 2011, 55.

Sokolsky, P. 1989, Introduction of UltraHigh Energy Cosmic Ray Physics (Addison-Wesley.)

Sommers, P. 2001, Astroparticle Physics, 14, 271.

Stanev, T. 1997, The Astrophysical Journal, 479, 290.

Sun, X. H., Reich, W., Waelkens, A., & Enß lin, T. A. 2008, Astronomy and Astrophysics, 477, 573.

Sutherland, M., Baughman, B., & Beatty, J. 2010, Astroparticle Physics, 34, 198.

Takami, H., Yoshiguchi, H., & Sato, K. 2006, The Astrophysical Journal, 639, 803.

Telescope Array Collaboration and Pierre Auger Collaboration. 2013, Proceedings of the 33rd International Cosmic Ray Conference 2013, arXiv:1310.0647.

Teshima, M., Dion, G., Hayashida, N., et al. 1992, Nuclear Physics B - Proceedings Supplements, 28, 169.

Tinyakov, P., & Tkachev, I. 2002, Astroparticle Physics, 18, 165.

Vernov, S., Egorov, T., Efimov, N., et al. 1971, Izv.Akad.Nauk Ser.Fiz., 10, 2098.

Véron-Cetty, M.-P., & Véron, P. 2006, Astronomy and Astrophysics, 455, 773.

Verschuur, G. L. 1969, The Astrophysical Journal, 156, 861.

—. 1979, Fundamentals of Cosmic Physics, 5, 113.

Vietri, M. 1996, Monthly Notices of the Royal Astronomical Society, 278, 1.

Waxman, E. 1995, Physical Review Letters, 75, 386.

Werner, K., Liu, F.-M., & Pierog, T. 2006, Physical Review C, 74, 044902.

Winn, M. M., Ulrichs, J., Peak, L. S., McCusker, C. B. A., & Horton, L. 1986, Journal of Physics G: Nuclear Physics, 12, 675.

Zatsepin, G. T., & Kuz'min, V. A. 1966, Journal of Experimental and Theoretical Physics Letters, 4, 78.

Vita

Azadeh Keivani was born in Tehran, Iran, in 1986. She received her B.S. in Physics from Sharif University of Technology, Tehran, Iran in June 2008. She started her graduate studies at Louisiana State University in August 2008. She earned her M.S. in May 2012 and expects to complete her doctoral degree in December 2013.